INSTABILITY IN BENDING

by

MERVIN SUE-CHU, B. Eng.

A Thesis
Submitted to the School of Graduate Studies
in Partial Fulfilment of the Requirements
for the Degree
Master of Engineering

McMASTER UNIVERSITY
December, 1980

TO MY PARENTS.

MASTER OF ENGINEERING (1980)
(Mechanical Engineering)

McMASTER UNIVERSITY
HAMILTON, ONTARIO

TITLE: Instability in Bending

AUTHOR: Mervin Sue-Chu, B. Eng. (McMaster University)

SUPERVISOR: Dr. J. L. Duncan

NUMBER OF PAGES: xvii, 183

ABSTRACT

Discontinuous yielding in the form of Luder's bands is frequently observed in tensile testing of mild steel sheets. In these materials, instability or kinking may or may not be observed in bending operations and various theories have been proposed to relate the bending and tensile phenomena.

In this work, an extensive experimental investigation was performed on five samples of low carbon sheet steels. The main objective was to develop a new analytical model, based on the uniaxial tensile stress-strain curve that will predict the behaviour of these materials in pure bending. Two models appeared possible and the experiments performed suggested that one of these is an appropriate model for steels of this kind.

ACKNOWLEDGEMENTS

The author would like to express his sincere gratitude to his supervisor, Dr. J. L. Duncan for his continuous guidance, patience and encouragement during the course of this work. Many thanks also to Dr. R. Sowerby and my fellow students for their useful comments and suggestions.

Thanks are also extended to the Department of Mechanical Engineering at McMaster University and the Natural Science and Engineering Research Council for their financial support.

Finally, I would like to thank Dofasco for supplying the test materials and Ms. Linda Hunter for typing this manuscript.

TABLE OF CONTENTS

Page

LIST OF FIGURES

FIGURE CAPTION PAGE

LIST OF TABLES

CHAPTER 1

INTRODUCTION AND DISCONTINUOUS YIELD PHENOMENON

1.1 Introduction

A phenomenon known as coil breaks is occasionally observed when uncoiling sheet steels. In the steel mill, the last stage of processing the sheet is to pass it through a temper mill and to coil it afterwards, generally under some tension. The sheet partially assumes the curvature of the coil but is straightened out again on uncoiling.

However, if the steel has aged in the coil, it may, instead of straightening, form a series of kinks as illustrated in Figure 1.1.

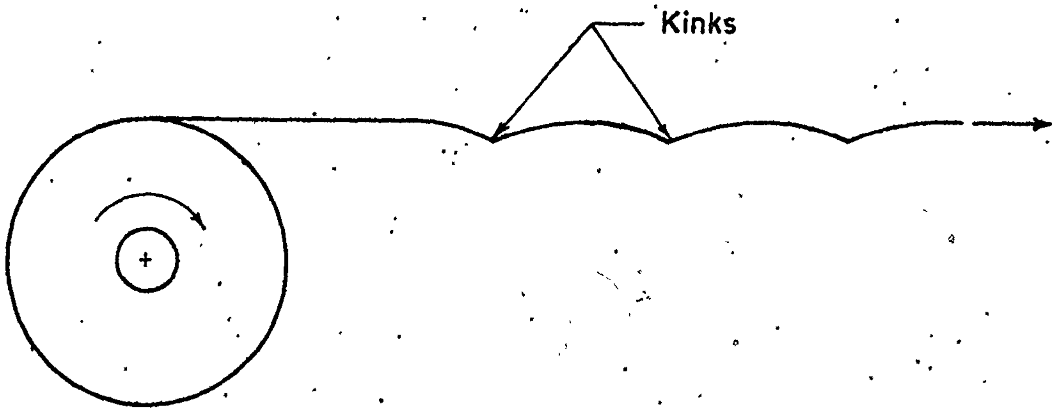

Fig. 1.1 - Illustration of coil forming a series of kinks upon uncoiling.

This behaviour suggests some mechanical bending instability in the sheet and it is known to be associated with discontinuous yielding or Lüder's straining of the material.

Another effect which is sometimes observed, is the appearance of a fine regular marking on the surface. The term microfluting has been used here. There is no apparent kinking or change in thickness of the material but this surface marking can be unacceptable, for example in auto-body outer panels.

Experiments in bending of thick bars and subsequent metallographic examination with Fry's reagent show that initial bending can result from localization of shear strains. A picture of the yielding process for a bar in bending is given by Johnson and Mellor [1].

The kinking effect in sheet steels cannot be explained by the localization of shear strains as deformation occurs on a macroscopic scale. As mentioned before, only discontinuous yielding materials show this effect and the discontinuous yield phenomenon will now be described.

1.2 Discontinuous Yield Phenomenon

This phenomenon has been observed for over a century and was originally found in low carbon steels. It has since been observed in other metals and alloys such as iron [2-8],

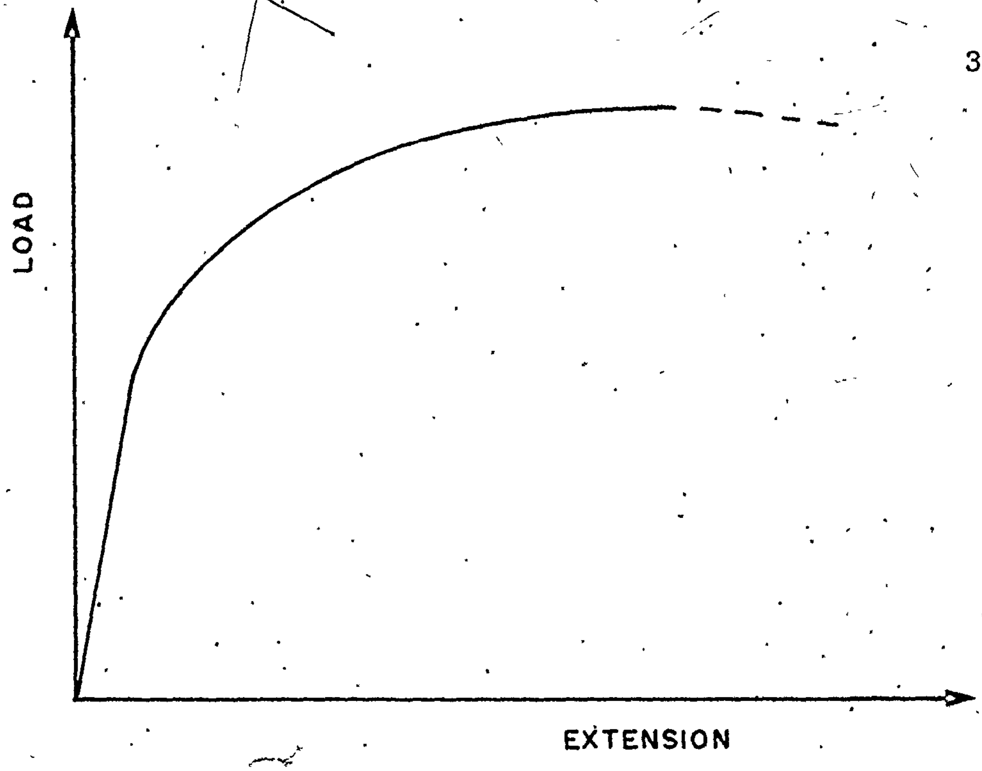

Fig. 1.2 - Typical load-extension curve for homogeneously yielding materials

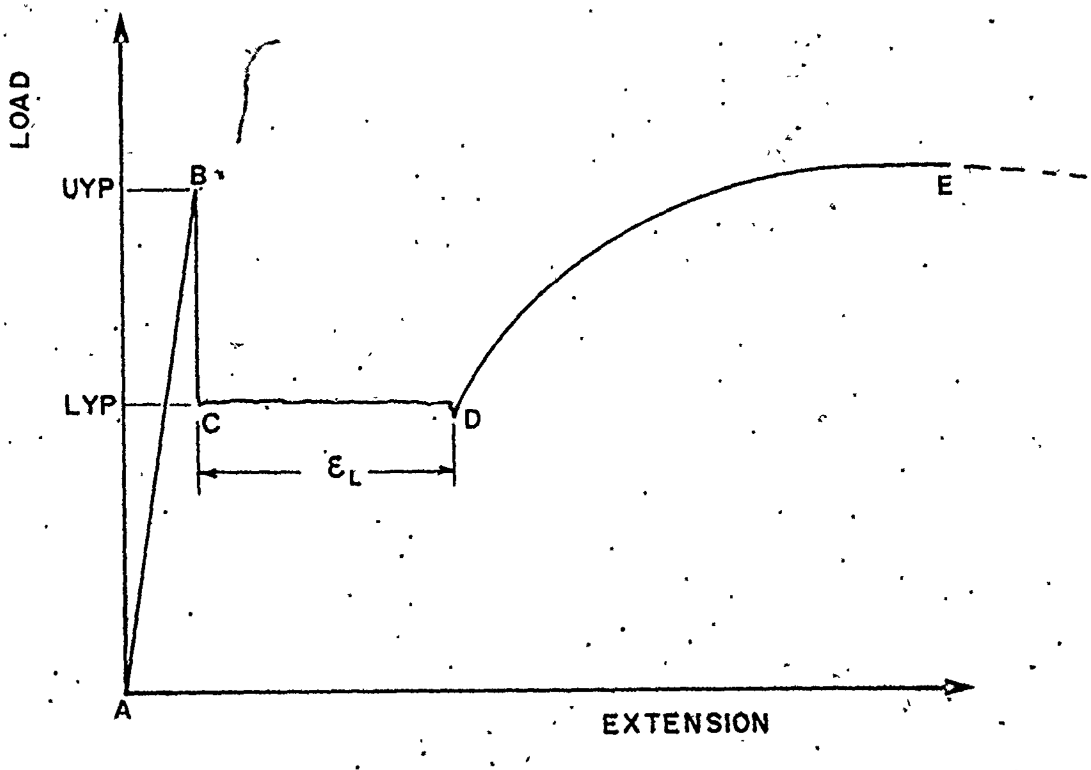

Fig. 1.3 - Typical load-extension curve for discontinuously yielding materials

niobium [9] and aluminum alloys [10-12], however the discontinuous yielding behaviour in aluminum alloys is very different from that of steels.

Materials that do not exhibit the yield point phenomenon show a smooth and gradual transition from the elastic to plastic stage of deformation. Figure (1.2) shows a typical tensile load-extension curve for such materials.

Materials that yield inhomogeneously, especially low carbon steels, exhibit the yield point phenomenon. They show a localized, heterogeneous type of transition from the elastic to plastic stage of deformation and a typical load-extension curve from a tensile test is shown in Figure 1.3. From A to B, the deformation is totally elastic and obeys Hooke's law. At point B, the material reaches its upper yield point (UYP) and the load suddenly drops to point C with the simultaneous appearance of the first Lüder's band. Now, the material ahead of the band is still elastic and if an extensometer is used to measure the strain, no extension is recorded beyond point C until the band has propagated into the gauge length of the extensometer. Thereafter, the band spreads throughout the specimen at an approximately constant load; the plateau CD is known as the lower yield point (LYP). It should be noted that the extensometer measures an average extension over the gauge length and is the sum of plastically and elastically deformed sections within the gauge length. After point D, no further extension is again recorded until the band has spread throughout the length of the specimen. Thereafter, the deformation becomes macroscopically homogeneous and is given by the curve DE. The length CD is known as the yield point elongation or Lüder's strain, ε_L. The value of the Lüder's strain is dependent on many factors, such as strain rate [2, 13-15], grain size [4, 16-18] and temperature [19].

A mechanism used to explain the discontinuous yielding behaviour in the tensile test is given by Cottrell and Bilby [20]. This is given in terms of the dislocation theory and was based on the idea that dislocation sources were locked or pinned by solute atoms. So, in order for the dislocations to be pulled apart from the solute atoms and become mobile, a large force has to be applied. This is the origin of the upper yield point. Once the dislocations become mobile, slip can occur rapidly at a lower applied force - the lower yield point.

In steels, the yield point is associated with small amounts of interstitial or substitutional impurities. It has been shown by Low and Gensamer [21] that removing either C or N from low carbon steels will eliminate the YPE. However, if a very small amount (0.001 %) of either of these elements was returned, the yield point will reappear.

Although the dislocation pinning mechanism seems to explain the behaviour in steels, it could not be used in explaining the yield point phenomenon in materials which have a very low dislocation density. One such material is Li F crystal [22]. Therefore, pinning of dislocations by impurities is only one case of the yield point behaviour. To account for discontinuous yielding in low dislocation density materials, other models have been proposed [22, 23].

1.3 Scope of the Present Work

The aim of this study has been to undertake a detailed experimental study of discontinuous bending in low carbon sheet steels and to develop an analytical model to predict the behaviour of these materials in terms of their tensile stress-strain curve.

In the pure bending of sheet metal exhibiting the yield point phenomenon, sometimes the material has a "kinking" effect just after the elastic limit. When "kinking" occurs, a plot of bending moment versus curvature would show a drop in moment. From the theoretical models that have been suggested so far, this does not occur and developing a model which would predict this effect would be very useful for understanding manufacturing processes that involve pure bending. The development and theory of two models are presented in Chapter IV.

An experimental rig was built to test specimens in pure bending. The experimental results obtained are compared with the theoretical results from the proposed model that seems to be more appropriate. Also, for two materials, the theoretical results are compared with the results generated from previous models. These models are presented in Chapter II.

CHAPTER II

PREVIOUS MODELS OF DISCONTINUOUS BENDING

2.1 Introduction

The phenomenon of discontinuous yield in materials has been widely studied by many investigators, however, there still seems to be some controversy about the exact explanation of this unique material behaviour.

Since the tensile test is the simplest and most universal test of material behaviour, much of the work has been done using this test and many models have been proposed. A very good summary of the work done in tensile testing is given by Moon [24].

In the tensile test, Lüder's bands form and propagate throughout the length of the specimen. These bands can be observed visually and their characteristics and description are well documented [14, 25, 26].

In addition to the tensile test, discontinuous yield behaviour has been observed and studied in torsion [27], reverse tension-compression [28-30] and bending.

Since this thesis deals with discontinuously yielding materials in bending, the work that has been done so far in this area will now be presented.

2.2 Present State of Discontinuous Yielding in Bending

As early as 1899, Ewing [31] suggested that the form of the stress distribution across the section of a mild steel beam in bending just after the yield point should be as shown in Figure 2.1.

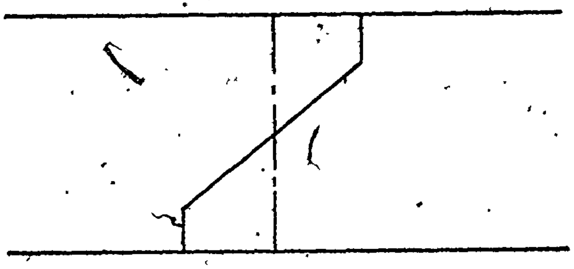

Fig. 2.1 - Stress distribution for a mild steel beam in the elastoplastic region as suggested by Ewing [31].

However, at that time, little or no attention had been given to the yield point phenomenon of mild steel and there was no mention of the difference between the upper and lower yield points in this stress distribution. It is now clearly established that discontinuously yielding materials such as annealed mild steel exhibit an upper and lower yield point.

During the last seventy years, several models have been proposed to explain the discontinuous yielding behaviour of materials in the elastoplastic range. All these models assume that plane sections before bending remain plane and from this assumption, the strain distribution across a rectangular section is as shown in Figure

2.2. Therefore, the strain is proportional to the distance

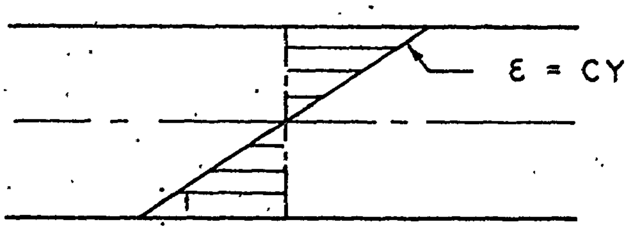

Fig. 2.2 - Strain distribution across a rectangular section

from the neutral axis and the proportionality constant, C is equal to the 1/R where R is the radius of curvature of the bent beam.

The first theoretical model was suggested by Robertson and Cook [32] in 1913 after tensile tests confirmed the existence of an upper and lower yield point. The stress distribution for this model is shown in Figure 2.3(a) and was based on the assumption that the stress in each longitudinal fibre of the beam, after reaching the upper yield value, drops to the lower value and remain constant as the material yields through the depth of the section. The experimental and theoretical moment-deflection curves are shown in Figure 2.4. In their theoretical analysis, curves were generated for different stress reductions.

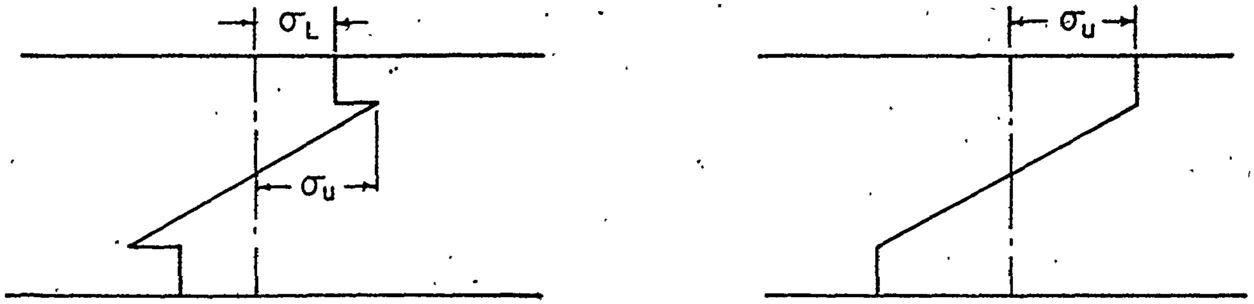

(a) – ROBERTSON & COOK (b) – MUIR & BINNIE

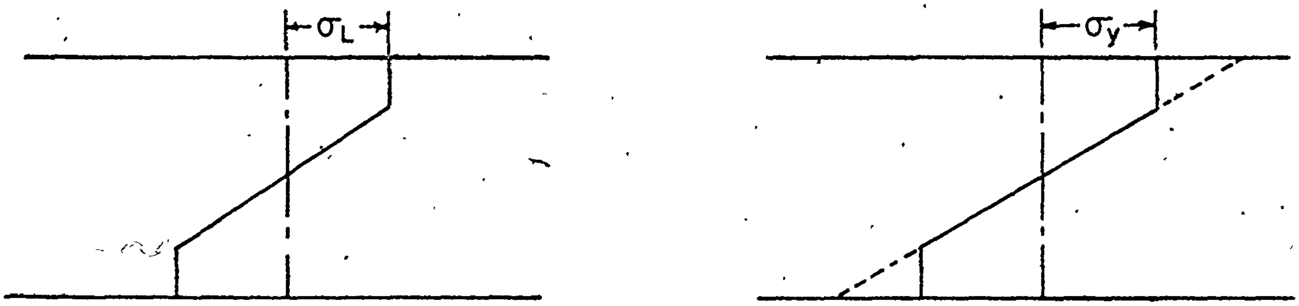

(c) – NADAI (e) – KUNTZE

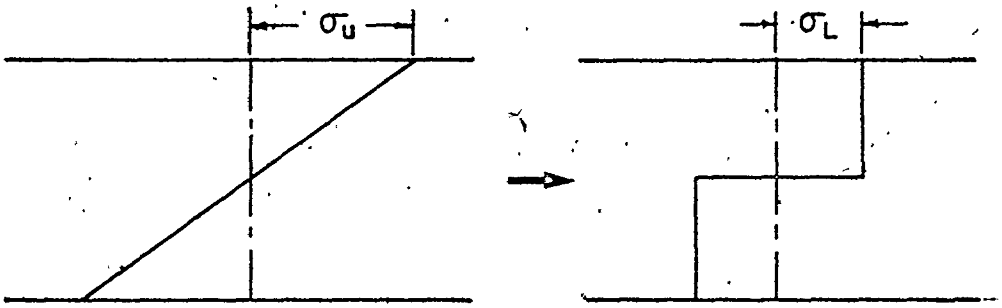

(d) – PRAGER

Fig. 2.3 - Stress distributions for discontinuously yielding materials as suggested by various investigators

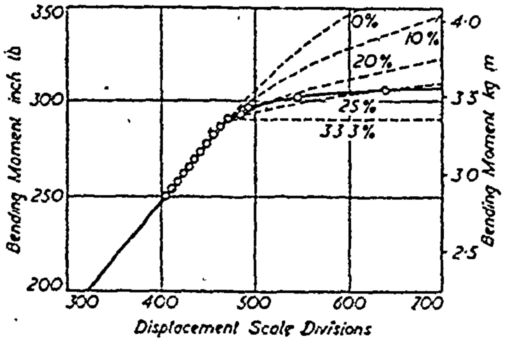

Fig. 2.4 - Experimental and theoretical moment-deflection curves obtained by Robertson and Cook [32]

In 1926, Muir and Binnie [33], suggested the stress distribution shown in Figure 2.3(b). This model was developed from experiments by Kennedy [34] and is based entirely on the value of the upper yield stress. They could not accept that there can be a sudden drop in stress at the onset of yield. Their argument to support this model was that since yielding is brought about by slip along maximum shear stress planes, the stress that initiates this slip is the upper yield and thus, this should be the stress upon which the plastic theory should be based.

Nadai [35] proposed the next model in 1931. The stress distribution is shown in Figure 2.3(c) and it became known as the "classical theory". This model is similar to that of Muir and Binnie except that the plastic theory is now based on the value of the lower yield stress.

This model is very simple and would give conservative results if used in design calculations.

In 1933, Prager [36] proposed the model shown in Figure 2.3(d). This was based on experimental results of Thum and Wunderlich [37], who found that the maximum elastic moment was greater than that calculated from the "classical" theory and closer to that of the fully plastic moment. This led Prager to believe that yielding of the extreme fibres and collapse of the member are coincident. He believed that the function of the upper yield point is to keep the member in the elastic region when the bending moment is less than the plastic moment but as soon as the applied bending moment is equal to the plastic moment, the whole section of the member suddenly becomes plastic. That is to say, the member is either totally elastic or totally plastic.

Also in 1933, Kuntze [38] suggested the stress distribution shown in Figure 2.3(e). The assumption being made here is that the extreme fibres do not yield until the tensile yield stress is reached at a certain depth in the beam. This depth was referred to as "the centre of resistance".

Of the theories proposed, those of Prager and Kuntze were called the "new theories" and the one by Robertson and Cook was referred to as the "old theory". Both of these have found some support by later investigators.

The theory given by Nadai can be disregarded as experimental moment-curvature curves by all investigators show that yielding was always above that deduced from the Nadai model. This would seem to show conclusively that yielding of the material occurs at a stress greater than that given by the lower yield.

Of all the research carried out with discontinuously yielding materials in bending, most investigators [27, 39-41] supported the "old theory" and only a few have supported the "new theories" [42, 43] and the "classical theory" [44, 45].

The "old theory" has been very useful in predicting the collapse loads in structural analysis but there is still doubt about it representing the actual physical behaviour of materials, with yield point elongation, subjected to pure bending in the elastoplastic range. Experimental results presented so far have been for specimens with thicknesses greater than 0.2". These results show no drop in moment after the elastic limit has been exceeded and it would be interesting to know whether these models can be applied to cold rolled sheet metal, which is used in sheet-metal forming operations.

CHAPTER III

DISCONTINUOUS YIELD IN TENSILE TEST

In a uniaxial tensile test, a typical true stress-true strain curve for a discontinuous yielding material is as shown in Figure 3.1.

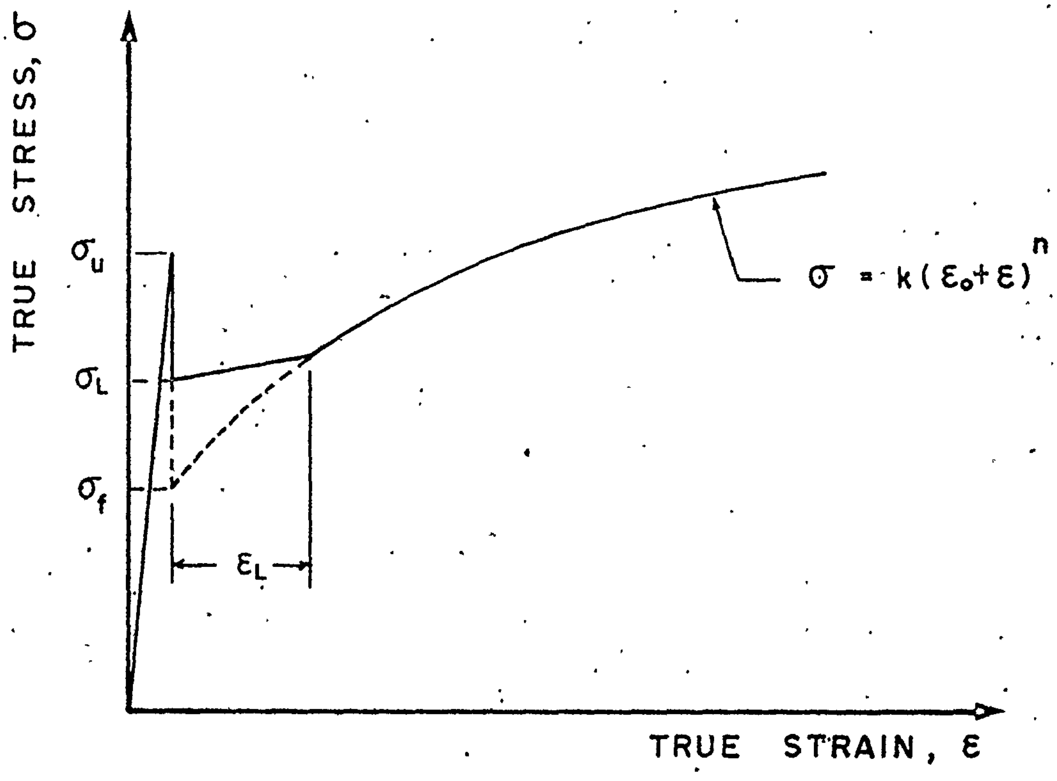

Fig. 3.1 - Typical true stress-true strain curve in a tensile test

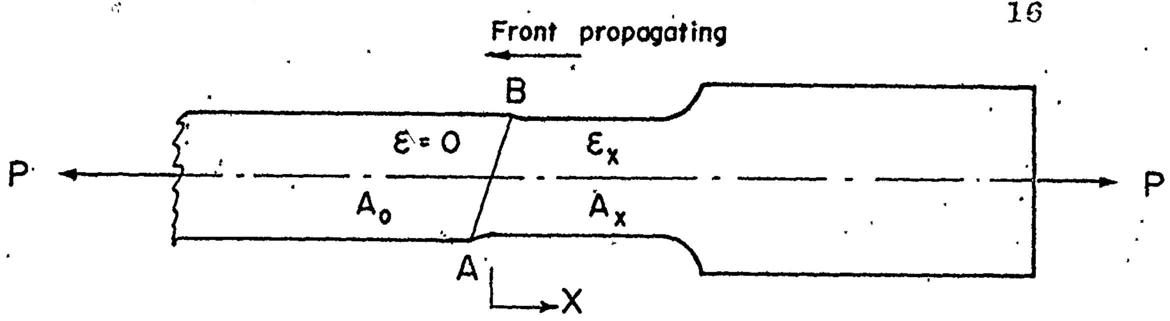

Fig. 3.2 - Illustration of tensile specimen after Lüder's front has propagated some distance

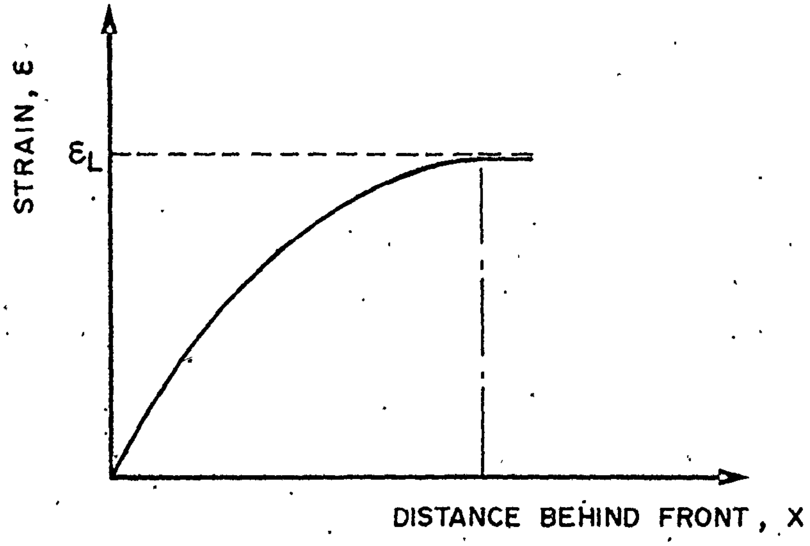

Fig. 3.3 - Strain distribution behind the Lüder's front

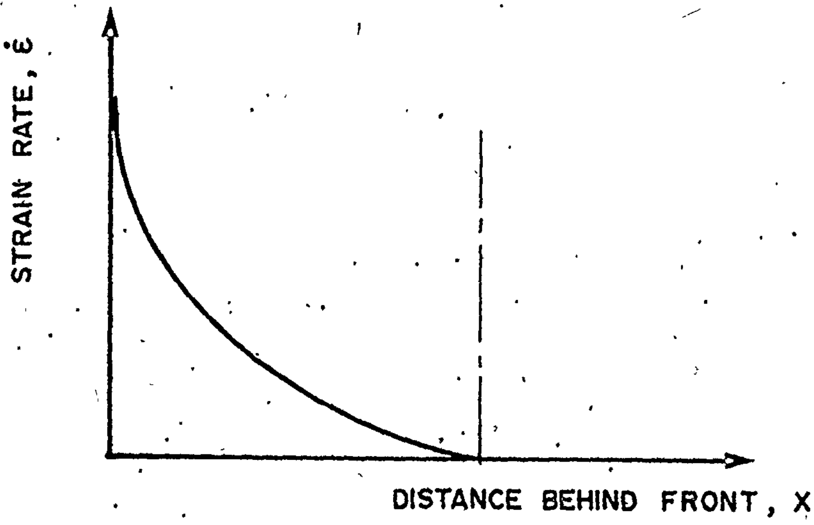

Fig. 3.4 - Strain rate distribution behind the Lüder's front

σ_u = upper yield stress or generation stress

σ_L = lower yield stress or propagation stress

σ_f = flow stress for uniform flow at zero strain rate

ε_L = Lüder's strain or yield point elongation

The strain hardening portion of the curve is fitted to an equation of the form: $\sigma = K(\varepsilon_o + \varepsilon)^n$ and the flow stress σ_f is obtained by back extrapolation of this curve to the value of the maximum elastic strain.

Figure 3.2 shows the geometry of a tensile specimen after a Lüder's front AB has propagated some distance into the gauge length. Ahead of the front, the strain is always zero and behind the front, the strain rises to the Lüder's strain ε_L. The strain distribution is shown in Figure 3.3 and Figure 3.4 shows the corresponding strain rate distribution.

During the propagation of the front, the load P remains relatively constant and every element must be in equilibrium. The equilibrium equation is derived by assuming that the strain rate is small and therefore inertia terms can be neglected. Hence, at every cross-section the transmitted force is the same.

(i.e.) $P = \sigma_L A_o = \sigma_x A_x = \text{Constant}$ (3-1)

where A_o = original cross-sectional area

Now, $A_x = A_o \exp(-\varepsilon_x)$ (3-2)

Therefore, $\sigma_x = \dfrac{P}{A_x} = \dfrac{P}{A_o \exp(-\varepsilon_x)}$ (3-3)

But, $\dfrac{P}{A_o} = \sigma_L$ (3-4)

Hence, $\sigma_x = \sigma_L \exp(\varepsilon_x)$ (3-5)

By plotting equation (3-5) on a stress, strain, strain rate space, the equilibrium conditions give the surface shown in Figure 3.5.

From the material behaviour point of view, the stress-strain relationship at constant strain rate is as shown in Figure 3.6. By plotting a number of these sections in a stress, strain, strain rate space results in the surface shown in Figure 3.7.

The strain rate hardening behaviour of mild steel has not yet been unequivocally established and different authors employ different constitutive relations. One which is used is:

$$\sigma = K(\varepsilon_o + \varepsilon)^n \dot{\varepsilon}^m \qquad (3\text{-}6)$$

where m is the strain rate sensitivity index and typically has a value less than 0.01 as compared with approximately 0.2 for the strain hardening index n. Equation (3-6) has various drawbacks and here we do not choose any particular relation but illustrate the surface as having a small but positive gradient in the strain rate $\dot{\varepsilon}$ direction.

Now, every point on the Lüder's front must be represented by a point on the equilibrium surface as well as one on the surface representing the material behaviour. Therefore, the points of intersection of these two surfaces will satisfy both conditions. Hence, superimposing Figure 3.5 on Figure 3.7 results in the diagram shown in Figure 3.8 where the intersection of the two surfaces is along AB. At B, the strain rate is maximum and this occurs when the displacement x = 0. At point A, the strain rate is zero and the strain value is equal to the Lüder's strain ε_L. Now, the material surface is sloping upwards and since the strain rate must decrease from maximum to zero, it is conceivable that it will decrease smoothly along the path indicated by the arrows in Figure 3.8. This gives the equilibrium surface for a tensile test and it represents the path taken during the inhomogeneous deformation of each element. Thus, in this way, the Lüder's band propagate throughout the specimen.

It will be appreciated that there are numerous objections to this simplified model of Lüder's straining. The principal difficulty is that the portrayal of the material properties as a surface in the stress, strain, strain rate space implies the strain ε is a state variable. This is certainly not the case and the resistance to flow σ depends not only on the instantaneous plastic process but also on the prior history of the material. In steel at room temperature, the flow stress in continuous plastic deformation depends more on the accumulated plastic work than on any other single factor and the simplified model is useful conceptually, if not entirely correct quantitatively.

If we consider the projection of the strain path on the stress, strain rate plane, then the picture is as shown in Figure 3.9. The jump from $\sigma = \sigma_u$, $\varepsilon = \dot{\varepsilon} = 0$ to $\sigma = \sigma_L$, $\varepsilon = 0$, $\dot{\varepsilon} = \dot{\varepsilon}_B$ is assumed to occur instantaneously and hence is only shown by an arbitrary dotted line. We note that straining never occurs at $\sigma = \sigma_L$ and $\dot{\varepsilon} = 0$; hence σ_L is a stress associated with $\dot{\varepsilon}_B$. Therefore, it is not surprising that the lower yield stress σ_L is very sensitive to the applied extension rate and the strain rate distribution curve as shown in Figure 3.4 is probably dependent, amongst other things, on the applied extension rate.

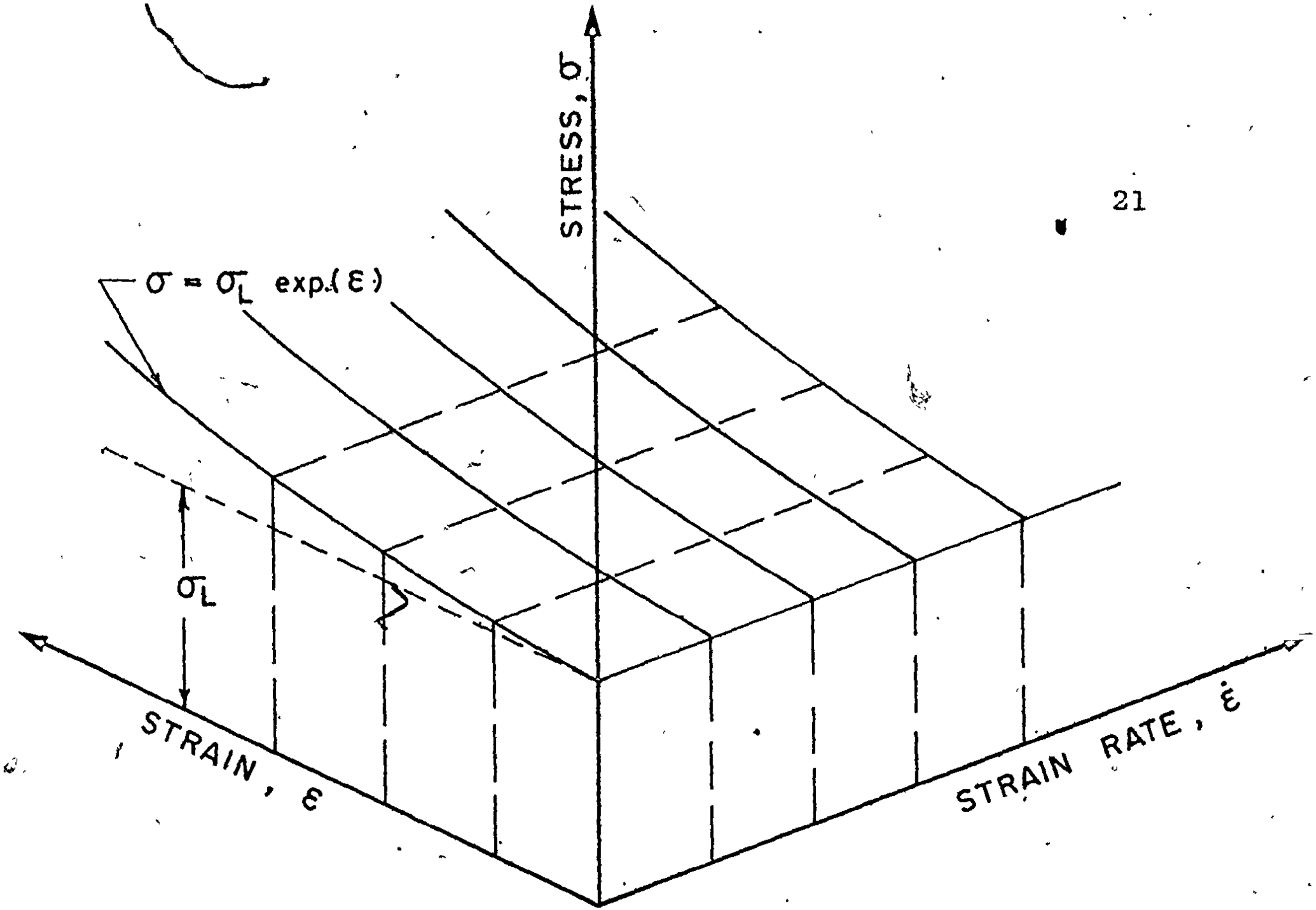

Fig. 3.5 - Illustration of stress, strain, strain rate surface from equilibrium conditions

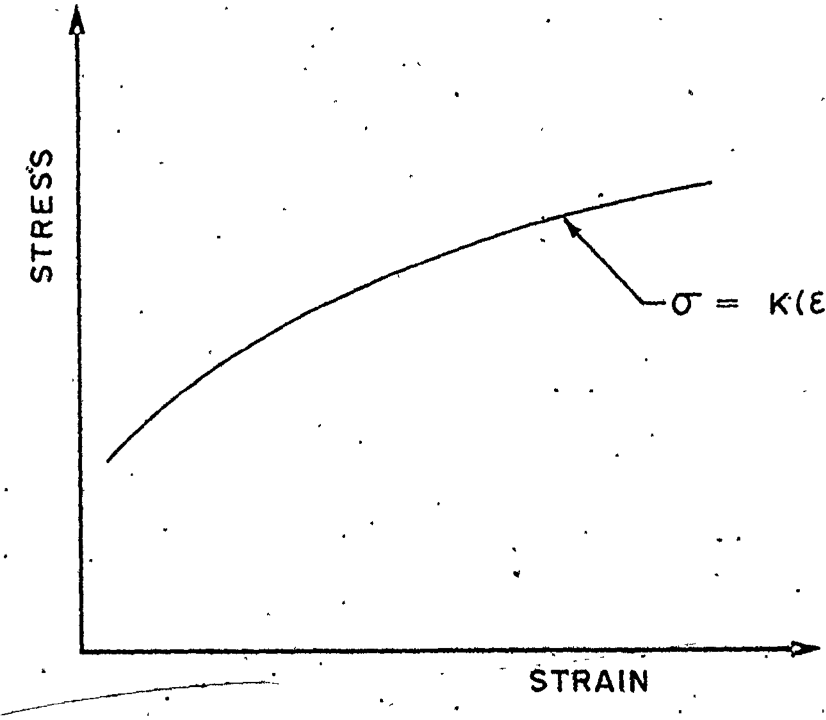

Fig. 3.6 - Stress-strain relationship from the material behaviour point of view

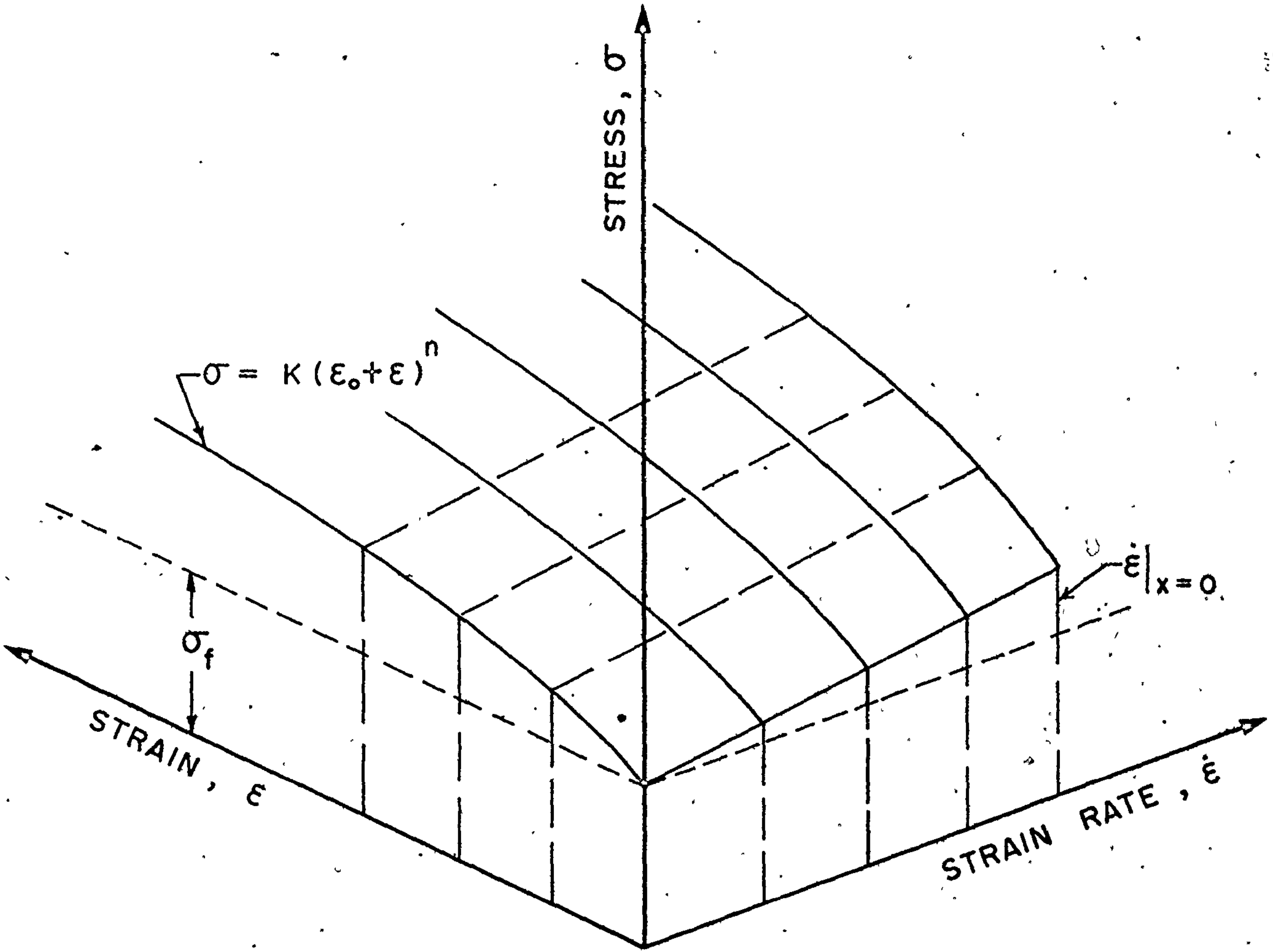

Fig. 3.7 - Illustration of stress, strain, strain rate surface from the material behaviour point of view

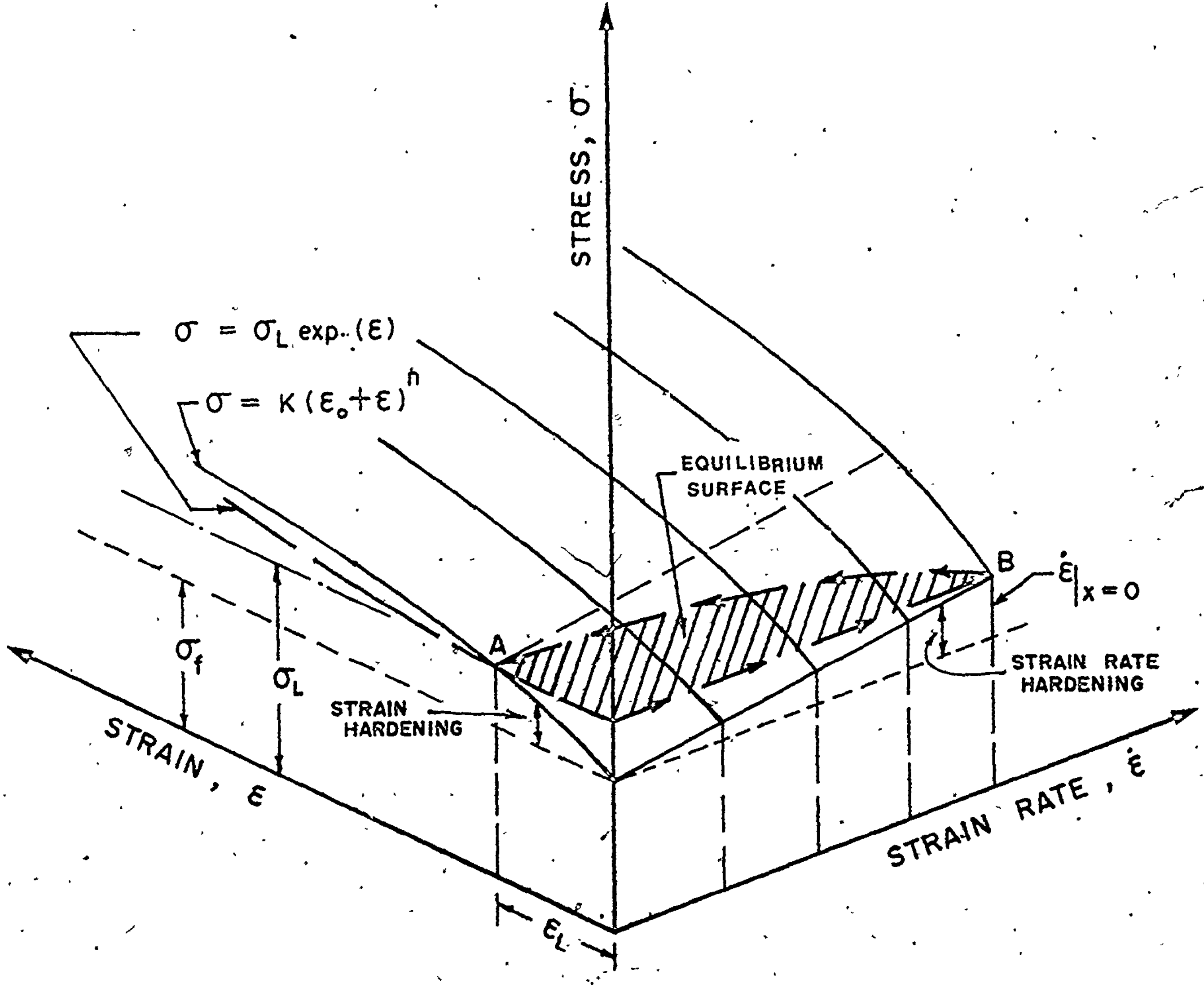

Fig. 3.8 - Illustration of equilibrium surface for a tensile test

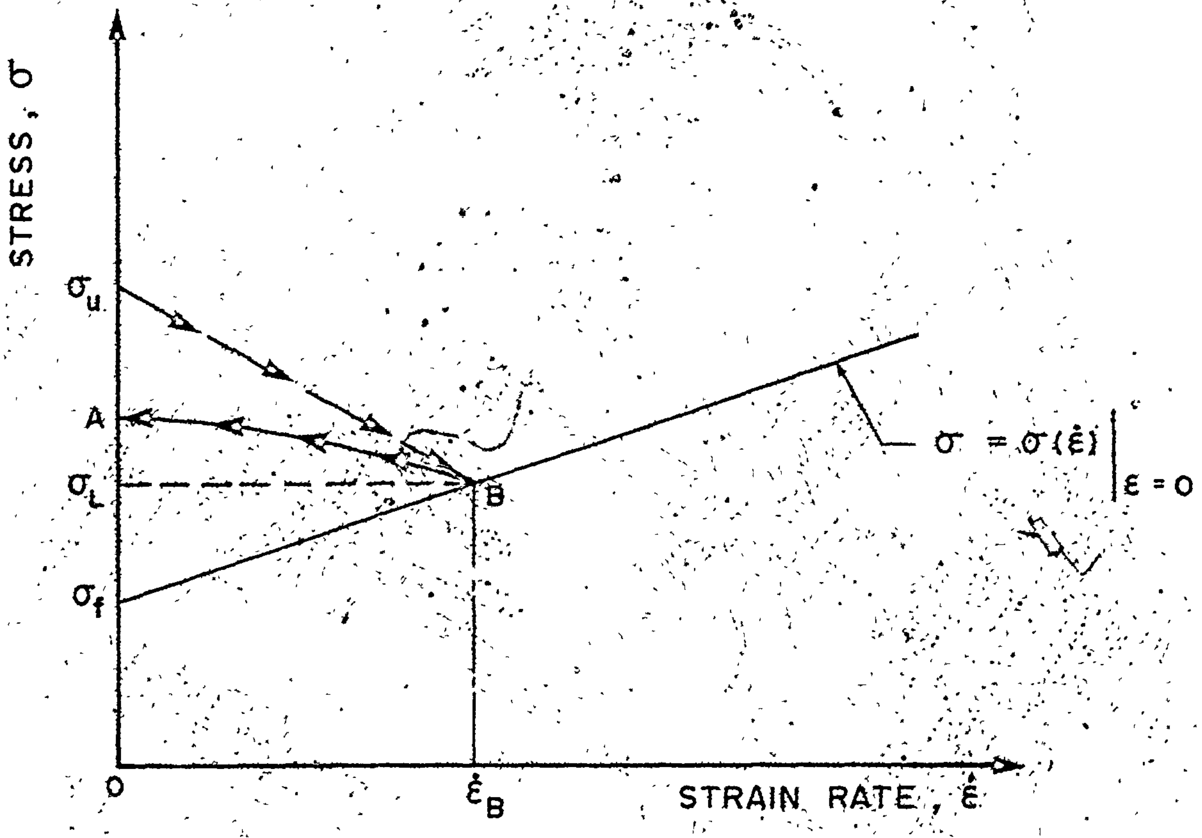

Fig. 3.9 - Projection of the strain path on the stress, strain rate plane

CHAPTER IV

MODELLING

4.1 Analytical Modelling of a Discontinuous Yielding Material in Pure Bending

In this type of modelling, certain assumptions are made about the strain condition and a macroscopic approach to the equilibrium equations is used. From the model, theoretical curves are generated to indicate the behaviour of the material.

In the pure bending of a specimen, the outer surface is essentially in tension and the inner surface in compression. In the development of the model, the following assumptions will be made.

1) All longitudinal elements bend into circular arcs having a common centre of curvature.

2) Plane sections before bending remain plane after bending.

3) The stress-strain curves in tension and compression are identical.

From the second assumption, the strain distribution in a rectangular cross-section specimen is given by $\varepsilon = y/R$

where R is the radius of curvature.

For a material bent to the elastic limit at the outer fibres, the stress distribution for a rectangular section is shown in Figure 4.1 where σ is equal to the yield stress in a continuously yielding material. The stress-strain curve for such a material is shown in Figure 1.2. For a discontinuous yielding material, it is proposed that σ is equal to the upper yield stress or generation stress σ_u.

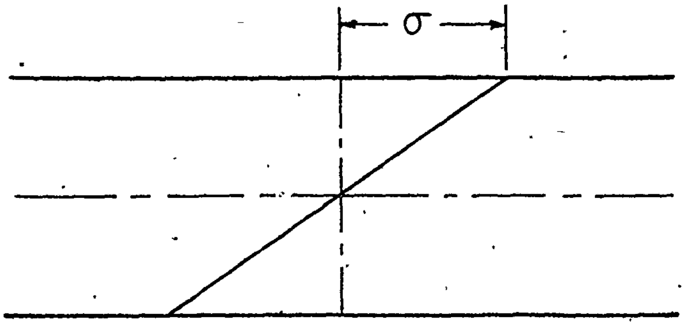

Fig. 4.1 - Stress distribution up to elastic limit for a specimen with rectangular cross-section

For pure bending of a discontinuous yielding material in the elastic region, the profile of the specimen is as shown in Figure 4.2 with the angle θ increasing as the radius of curvature R_E decreases.

At the onset of yielding, the outermost fibres of the material undergo plastic deformation and in-

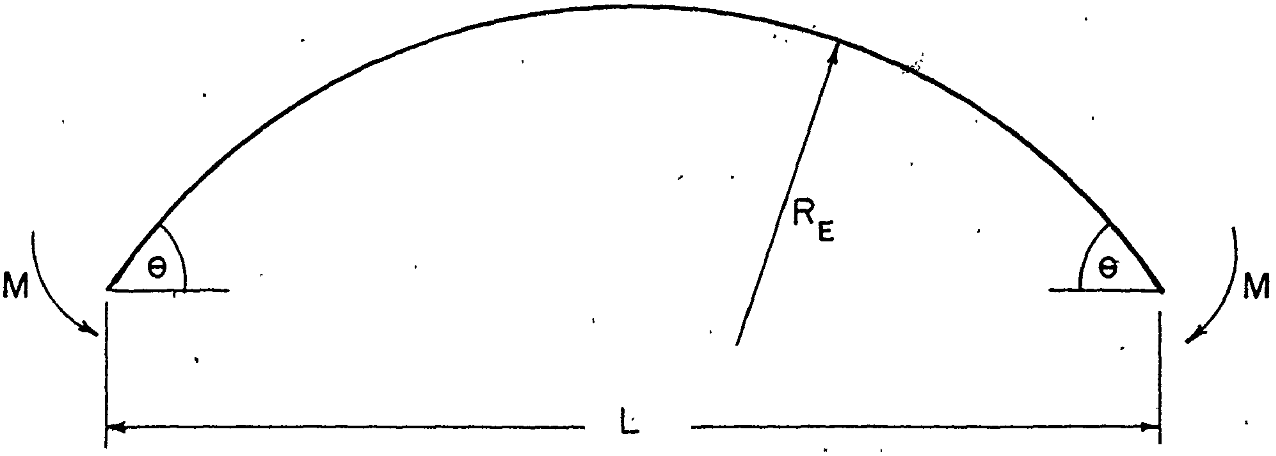

Fig. 4.2 - Profile of rectangular specimen bent up to the elastic limit

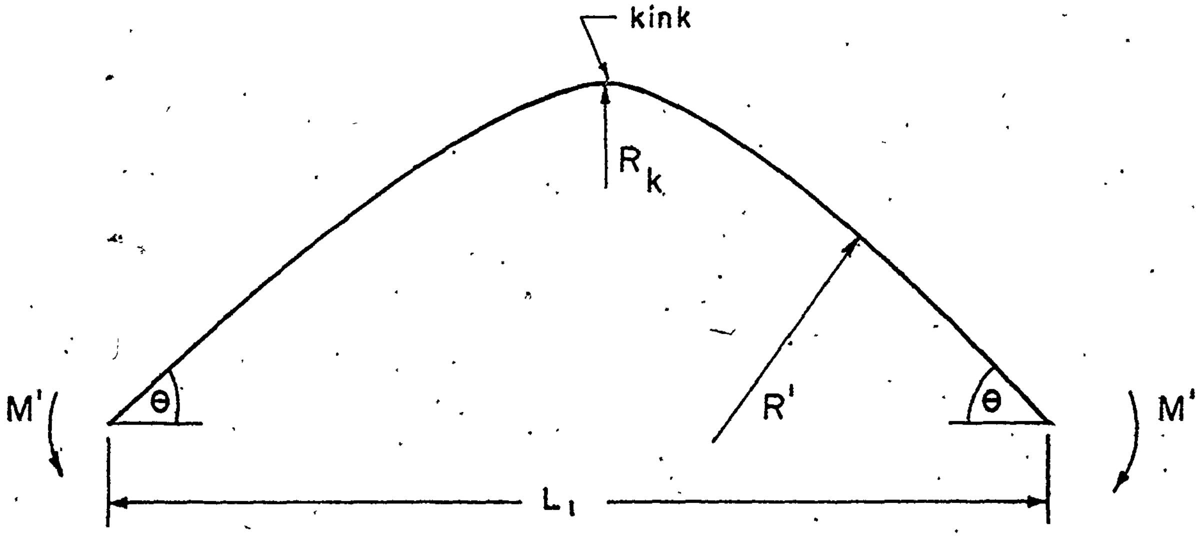

Fig. 4.3 - Profile of rectangular specimen showing instability or kinking

stability in bending may or may not occur. If a material shows instability, at the point of kinking, a drop in load is normally recorded and the resultant profile of the specimen is that shown in Figure 4.3 where the bending moment M' is less than the maximum elastic moment. Also, in the region of instability, the radius of curvature R_k is always less than R' which is the radius of curvature in the elastic region of the specimen.

To model this behaviour, the stress distribution across the section must be developed. It is assumed that the intrinsic stress-strain relationship is as developed in Chapter III and represented by Figure 3.1. In bending beyond the elastic limit, the peak stress in the elastic zone for an elastic-plastic interface is a matter of speculation. Some investigators have suggested it is the generation stress σ_u while others have stated it is the propagation stress σ_L. From the literature, this was never resolved and therefore, two models will be suggested here. In Model I, the peak elastic stress is equal to the generation stress σ_u. This implies that even after yielding of the outermost fibres, each inner longitudinal fibre stresses up to the generation stress σ_u before it begins to yield. In Model II, after the outermost fibres yield at the upper yield stress σ_u, the material continues to yield at the propagation stress σ_L. The stress distri-

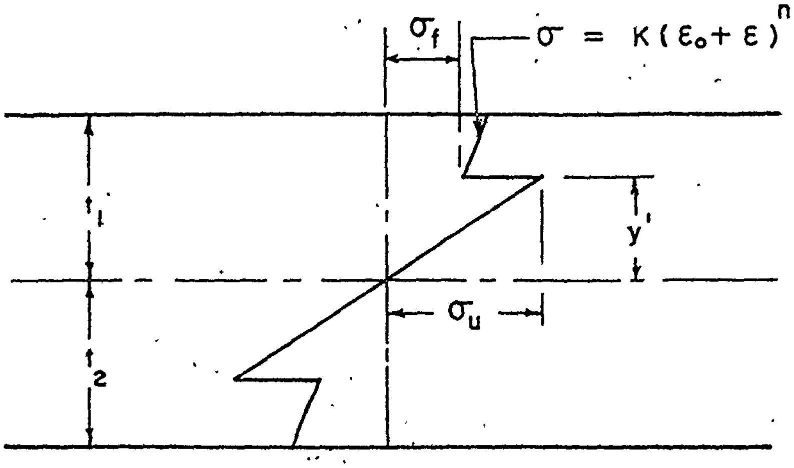

Fig. 4.4 - Stress distribution across rectangular section according to Model I

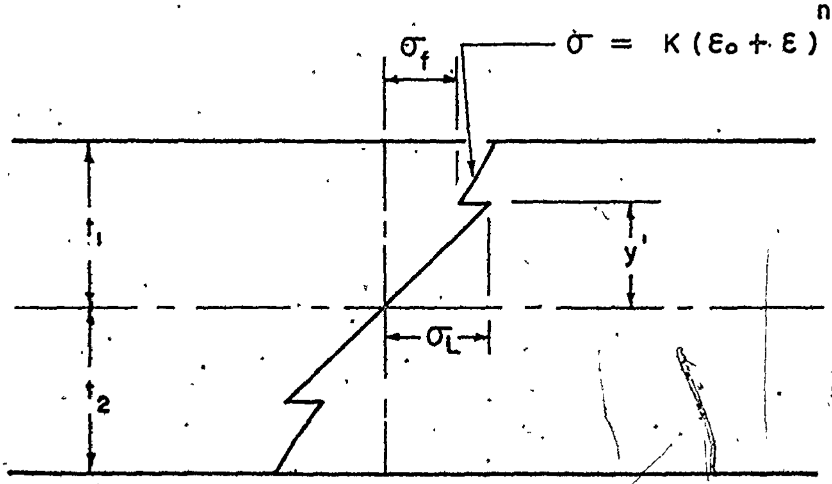

Fig. 4.5 - Stress distribution across rectangular section according to Model II

butions for Model I and Model II are shown in Figures 4.4 and 4.5 respectively.

Although both models are not equally plausible, the theoretical analysis will be made for both so that the theoretical curves can be compared with the experimental results.

4.2 Theoretical Analysis

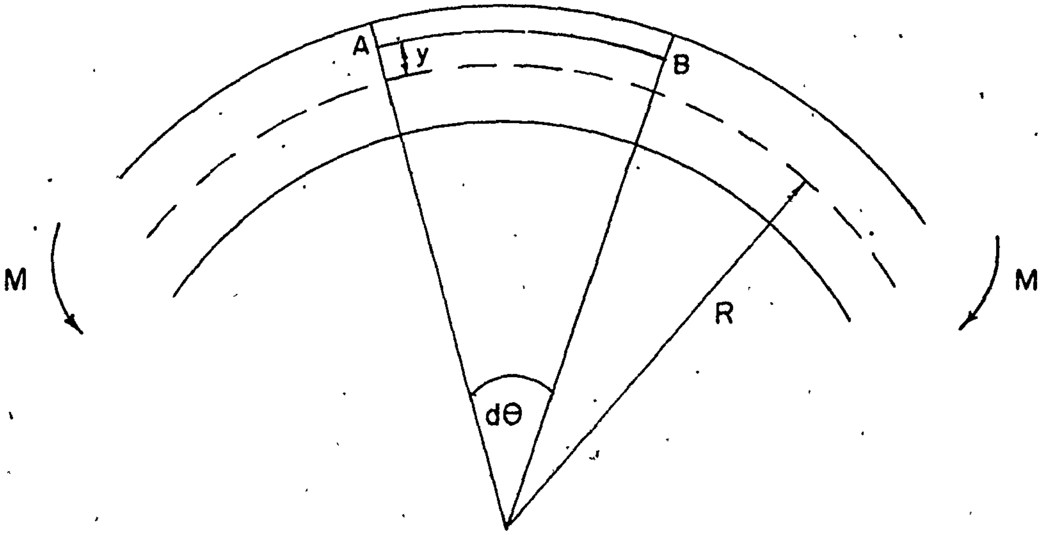

Consider a beam in pure bending, (shown schematically above) subjected to a bending moment M and at a radius of curvature R at the neutral axis. The strain in the longitudinal fibre AB, a distance "y" from the neutral axis is given by:

$$e = \frac{\delta l}{l_o} = \frac{y d\theta}{R d\theta} = \frac{y}{R} \qquad (4-1)$$

The bending moment M is calculated from:

$$M = \int_A \sigma \cdot y \, dA \tag{4-2}$$

and for a beam with rectangular cross-section of width "b" and thickness "t",

$$M = 2b \int_{-t_1}^{t_2} \sigma \cdot y \, dy \tag{4-3}$$

where t_1 and t_2 are the distances from the neutral axis of the extreme fibres.

It will be assumed that $t_1 = t_2 = t/2$ and that the position of the neutral axis does not change during deformation. Therefore, the bending moment can be rewritten by:

$$M = 2b \int_{0}^{t/2} \sigma \cdot y \, dy \tag{4-4}$$

For Models I and II, the stress up to the elastic limit is:

$$\sigma = \sigma_u \frac{y}{(t/2)} \; ; \; 0 \leq y \leq t/2$$

and since the material is totally elastic, Hooke's law is obeyed.

Therefore, $\sigma = Ee = \frac{Ey}{R}$ (4-5)

Substituting for σ in equation (4-4),

$$M^{I,II} = 2b \int_0^{t/2} \frac{Ey}{R} \cdot y \, dy$$

$$= 2b \frac{E}{R} \int_0^{t/2} y^2 \, dy \qquad (4\text{-}6)$$

This gives on integrating and simplifying,

$$M^{I,II} = \frac{Ebt^3}{12} \cdot \frac{1}{R} \quad ; \quad R \geq R_E \qquad (4\text{-}7)$$

For the beam bent in the elastoplastic range, the stress distribution for <u>Model I</u> can be expressed by:

$$\sigma = \frac{y}{y'} \sigma_u \quad ; \quad 0 \leq y \leq y'$$

$$\sigma = K (\varepsilon_o + \varepsilon)^n \qquad (4\text{-}8)$$

$$= K (\varepsilon_o + y/R)^n \quad ; \quad y' < y \leq t/2$$

where it is assumed $\varepsilon \approx e = y/R$ and y' is the distance from the neutral axis of the elastic-plastic interface.

Substituting for σ in equation (4-4), the bending moment in the elastoplastic region according to Model I is:

$$M^I = 2b\left[\frac{\sigma_u}{y'}\int_0^{y'} y^2\,dy + K\int_{y'}^{t/2}\left(\varepsilon_o + y/R\right)^n \cdot y\,dy\right] \qquad (4\text{-}9)$$

Integrating and simplifying,

$$M^I = 2b\left[\sigma_u\frac{(y')^2}{3} + \frac{KR}{(n+1)}\left\{\frac{t}{2}\left(\varepsilon_o + \frac{t}{2R}\right)^{n+1} - y'\left(\varepsilon_o + \frac{y'}{R}\right)^{n+1} \frac{- R\left(\varepsilon_o + \frac{t}{2R}\right)^{n+2} + R\left(\varepsilon_o + \frac{y'}{R}\right)^{n+2}}{(n+2)}\right\}\right] \qquad (4\text{-}10)$$

Now, $y' = \frac{\sigma_u R}{E}$

Therefore, the relationship between bending moment and radius of curvature from Model I is given by:

$$M^I = 2b\left[\frac{\sigma_u^3 R^2}{3E^2} + \frac{KR}{(n+1)}\left\{\frac{t}{2}\left(\varepsilon_o + \frac{t}{2R}\right)^{n+1} - \frac{\sigma_u R}{E}\left(\varepsilon_o + \frac{\sigma_u}{E}\right)^{n+1} \frac{- R\left(\varepsilon_o + \frac{t}{2R}\right)^{n+2} + R\left(\varepsilon_o + \frac{\sigma_u}{E}\right)^{n+2}}{(n+2)}\right\}\right] \qquad (4\text{-}11)$$

From Model II, when the material is in the elastic-plastic range, the stress distribution can be expressed by:

$$\sigma = \frac{y}{y''}\,\sigma_L \quad ; \quad 0 \leq y \leq y''$$

$$\sigma = K\,(\varepsilon_o + y/R)^n \quad ; \quad y'' < y \leq t/2 \qquad (4\text{-}12)$$

Substituting for σ in equation (4-4),

$$M^{II} = 2b\left[\int_0^{y''} \sigma_L \frac{y^2}{y''}\,dy + \int_{y''}^{t/2} K\left(\varepsilon_o + \frac{y}{R}\right)^n \cdot y\,dy\right] \qquad (4\text{-}13)$$

Now, $y'' = \dfrac{\sigma_L R}{E}$ and on integrating and simplifying,

$$M^{II} = 2b\left[\frac{\sigma_L^{\,3} R^2}{3E^2} + \frac{KR}{(n+1)}\left\{\frac{t}{2}\left(\varepsilon_o + \frac{t}{2R}\right)^{n+1} - \frac{\sigma_L R}{E}\left(\varepsilon_o + \frac{\sigma_L}{E}\right)^{n+2} - \frac{R\left(\varepsilon_o + \frac{t}{2R}\right)^{n+2} + R\left(\varepsilon_o + \frac{\sigma_L}{E}\right)^{n+2}}{(n+2)}\right\}\right] \qquad (4\text{-}14)$$

4.3 Plane Strain Bending

Equations (4-11) and (4-14) give the relationship between M and R in elastoplastic bending under plane stress conditions. However, if the ratio of width to thickness is large, the test is one of plane strain which is the strain condition normally associated with pure bending of sheet-metal.

Since the aim is to use the uniaxial tensile stress-strain curve in the theoretical analysis, it is necessary to develop the relationship between the uniaxial tensile and plane strain stresses and make modifications to the bending moment equations derived so far.

The relationship between uniaxial and plane strain stresses for both the elastic and plastic conditions are developed in Appendix A.

For Models I and II, when the material is bent up to the elastic limit, the plane strain bending moment M_{PS} is given by:

$$M_{PS}^{I,II} = \frac{Ebt^3}{12R} (\phi) \quad ; \quad R \geq R_E \qquad (4\text{-}15)$$

When the material is bent beyond the elastic limit, the plane strain bending moment from Model I is:

$$M_{PS}^{I} = 2b\left[\frac{\sigma_u^{3} R^{2}}{3E^{2}} \phi + \frac{KR}{(n+1)}\left\{\frac{t}{2}\left(\varepsilon_o + \frac{t}{2R}\right)^{n+1} - \frac{\sigma_u R}{E}\left(\varepsilon_o + \frac{\sigma_u}{E}\right)^{n+1} - \frac{R\left(\varepsilon_o + \frac{t}{2R}\right)^{n+2} + R\left(\varepsilon_o + \frac{\sigma_u}{E}\right)^{n+2}}{(n+2)} (PPSC)\right\}\right] \tag{4-16}$$

From Model II,

$$M_{PS}^{II} = 2b\left[\frac{\sigma_L^{3} R^{2}}{3E^{2}} \phi + \frac{KR}{(n+1)}\left\{\frac{t}{2}\left(\varepsilon_o + \frac{t}{2R}\right)^{n+1} - \frac{\sigma_L R}{E}\left(\varepsilon_o + \frac{\sigma_L}{E}\right)^{n+2} - \frac{R\left(\varepsilon_o + \frac{t}{2R}\right)^{n+2} + R\left(\varepsilon_o + \frac{\sigma_L}{E}\right)^{n+2}}{(n+2)} (PPSC)\right\}\right] \tag{4-17}$$

In equations (4-16) and (4-17), $R < R_E$, ϕ and PPSC are the elastic and plastic plane strain correction factors. These values can be calculated from equations (A-11) and (A-27) respectively.

CHAPTER V

EXPERIMENTATION

5.1 Materials

For this work, the materials used were:

1) Rimmed steel - A
2) Rimmed steel - B
3) Rimmed steel - C
4) Mild steel
5) HSLA steel

The rimmed steels were of different thicknesses and may also have different compositions. All the steels exhibited the yield point elongation (YPE) and were aged different amounts to vary the YPE. With rimmed steel-B in the as received condition, the Lüder's strain was approximately 6% and in order to achieve smaller values, the material was temper rolled approximately 2% and subsequently aged. This temper rolled steel will be denoted as Rimmed-B' in the text. The ageing temperature for most of the tests was 100°C.

The mild and HSLA steels in the as received condition were almost fully aged and further ageing did not show a large increase in Lüder's strain.

For all materials, no chemical composition analysis or metallographic studies were undertaken, but they were all industrially produced materials with compositions typical for the generic description.

5.2 Tensile Tests

Tensile tests were performed on all materials after their different heat treatment. The heat treatment was the same as that done for the equivalent bend test specimens.

The tensile specimens were carefully machined on a Tensile Kut machine and the testing was done on a 10,000 lbf. capacity Instron machine. The cross-head speed for all tests was 0.1 inch/minute.

The extension was monitored by means of a 1" gauge length Instron extensometer and the autographic load-extension curve was continuously plotted for each test. Tests were stopped when the maximum load was clearly exceeded. The stress-strain curves for all materials in the as received condition are shown in Figure 5.1. True stress-true strain curves for all tests are given in Appendix E. From these curves, the material parameters K, ε_o and n were obtained by a least square fit of each curve, beginning just beyond the YPE region and ending at the point of maximum load. The heat treatment and mechanical properties for all test materials from tensile testing are summarized in Tables I(a) - I(f).

Also, from tensile testing, the r-values (r_o and r_{90}) for each material were obtained so that the plastic plane strain correction factor (PPSC) could be calculated. The r-value is the measure of anisotropy of the material and is equal to the ratio of width strain to thickness strain. For thin specimens, normally the longitudinal and width strains are measured instead since it is difficult to measure the thickness strain accurately and by assuming constancy volume of material, the r-value can be determined from:

$$r = \frac{e_w}{e_t} = \frac{\ln (w_o/w_f)}{\ln (t_o/t_f)} = \frac{\ln (w_o/w_f)}{\ln (w_f l_f/w_o l_o)} \qquad (5\text{-}1)$$

where: w_o = original width
t_o = original thickness
l_o = original length
w_f = final width
t_f = final thickness
l_f = final length

Since the r-value is a function of strain, values were calculated at strains of 10-20%, the first value always being taken after the yield point elongation and in calculating the plastic plane strain correction factor from equation (A-28), the average r-values were used. Table II gives the r-values at 0^{o} and 90^{o} to the rolling direction for all test materials and Table III gives the values of the plastic plane strain correction factor (PPSC) for each material.

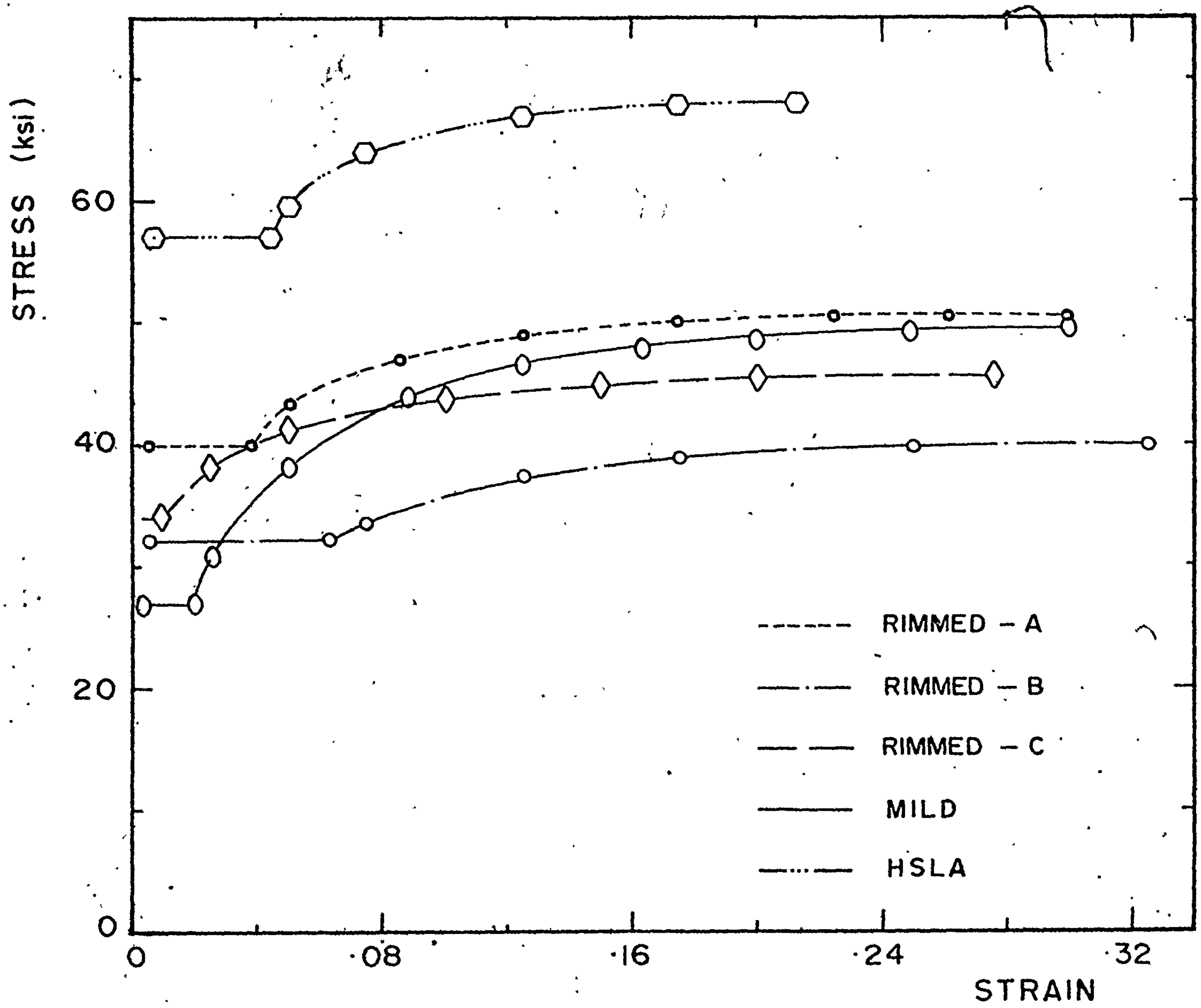

Fig. 5.1 – Uniaxial tensile stress-strain curves for test materials in the as received condition

TABLE I(a)

Heat treatment and mechanical properties for Rimmed steel-A
(t = 0.034")

Heat treatment		σ_u	σ_L	YPE	K	ε_o	n
Temp. (°C)	Time (hrs)	(ksi)	(ksi)	(%)	(ksi)		
---	---	42.33	37.92	3.1	87.612	0.0022	0.218
100	0.50	42.44	39.15	3.63	88.972	0.0023	0.232
100	1.00	42.65	40.62	3.75	88.332	0.0069	0.232
100	5.00	43.35	41.57	4.13	88.452	0.0008	0.226
100	13.25	48.47	42.47	4.50	88.518	0.004	0.225
100	13.75	45.00	42.64	4.88	91.183	0.0153	0.247
100	14.25	45.24	42.28	5.15	86.754	0.0036	0.222
100	14.75	49.02	42.78	5.50	86.625	0.0038	0.217
100	15.75	49.73	42.12	5.63	88.654	0.0031	0.226
100	18.00	46.60	44.44	6.60	92.317	0.0317	0.268

TABLE I(b)

Heat treatment and mechanical properties for Rimmed steel-B
(t = 0.04")

Heat treatment		σ_u	σ_L	YPE	K	ε_o	n
Temp. (°C)	Time (hrs)	(ksi)	(ksi)	(%)	(ksi)		
---	---	43.37	32.13	6.0	75.465	0.0	0.278
200	0.75	42.23	33.62	7.8	78.170	0.0	0.279
215	0.50	44.27	33.97	6.8	76.326	0.0	0.256
270	1.00	48.14	32.24	7.0	77.256	0.0	0.281

TABLE I(c)

Heat treatment and mechanical properties for Rimmed steel-B
(t = 0.039")

Heat treatment		σ_u	σ_L	YPE	K	ε_o	n
Temp. (°C)	Time (hrs)	(ksi)	(ksi)	(%)	(ksi)		
---	---	28.71	27.95	0.85	76.08	0.0132	0.250
100	0.25	35.01	33.24	2.4	76.18	0.028	0.252
100	0.50	36.65	34.88	3.4	76.52	0.030	0.258
100	1.00	41.65	36.66	4.1	76.32	0.028	0.240
100	1.50	42.85	38.35	6.2	77.49	0.050	0.266
100	2.00	41.84	37.34	6.5	77.62	0.042	0.271

TABLE I(d)

Heat treatment and mechanical properties for Rimmed steel-C (t = 0.058")

Heat treatment		σ_u	σ_L	YPE	K	ε_o	n
Temp (^oC)	Time (hrs)	(ksi)	(ksi)	(%)	(ksi)		
---	---	35.40	34.06	0.75	76.636	0.0134	0.207
100	2.0	44.28	41.52	3.75	81.225	0.0733	0.276
100	4.0	45.45	41.74	3.88	80.335	0.0509	0.248
100	13.0	46.64	42.80	4.00	81.341	0.0872	0.284
100	19.5	44.94	40.64	5.10	77.184	0.0565	0.255
100	23.0	45.52	42.47	6.75	80.991	0.112	0.323

TABLE I(e)

Heat treatment and mechanical properties for Mild steel
(t = 0.056")

Heat treatment		σ_u	σ_L	YPE	K	ε_o	n
Temp. (°C)	Time (hrs)	(ksi)	(ksi)	(%)	(ksi)		
---	---	28.09	27.04	1.80	95.770	0.0	0.288
100	2	28.38	25.62	1.82	90.889	0.0	0.281
100	4	27.68	25.74	1.84	89.540	0.0	0.273
100	23	27.71	27.01	1.86	90.945	0.0	0.278
100	36	27.53	26.29	1.87	93.434	0.0	0.294

TABLE I(f)

Heat treatment and mechanical properties for HSLA steel
(t = 0.076")

Heat treatment		σ_u	σ_L	YPE	K	ε_o	n
Temp. (°C)	Time (hrs)	(ksi)	(ksi)	(%)	(ksi)		
---	---	71.29	57.11	4.25	114.037	0.0	0.195
225	8	60.38	55.91	5.0	113.66	0.0	0.208

TABLE II: r-values for test materials

Material	Orientation to RD	Extension (%)	r	$\bar{r}$
Rimmed steel-A	0°	10	0.85	0.91
		15	0.92	
		20	0.97	
	90°	10	1.20	1.18
		15	1.18	
		20	1.17	
Rimmed steel-B	0°	10	0.82	0.87
		15	0.83	
		20	0.96	
	90°	10	1.69	1.79
		15	1.78	
		20	1.89	
Rimmed steel-C	0°	10	1.34	1.35
		15	1.35	
		20	1.36	
	90°	10	1.77	1.80
		15	1.79	
		20	1.83	
Mild steel	0°	10	0.74	0.75
		15	0.76	
	90°	10	0.87	0.92
		15	0.97	
HSLA steel	0°	10	0.58	0.60
		15	0.62	
	90°	10	1.26	1.27
		15	1.28	

TABLE III

Plastic plane strain correction factor (PPSC) for test materials

Material	PPSC
Rimmed steel-A	1.16
Rimmed steel-B	1.19
Rimmed steel-C	1.26
Mild steel	1.12
HSLA steel	1.12

5.3 Bend Tests

5.3.1 Experimental Bending Rig

In order to check the validity of the theoretical models developed in Chapter IV, the experimental rig shown schematically in Figure 5.2 was built. The rig subjects the specimen to pure bending and consists essentially of four rollers. The two outer rollers being at an equal distance from the inner ones. To reduce friction, the rollers were mounted in roller bearings. The rig was designed such that the distances between the inner rollers and outer rollers could vary from 3-3/4" to 6-3/4" and 5-3/4" to 8-3/4" respectively.

For testing, the rig was attached to the Instron machine and the complete experimental arrangement is shown in Figure 5.3.

5.3.2 Experimental Procedure

Bending specimens of geometry shown in Figure 5.4 were carefully machined so that the shoulders fitted between the inner rollers of the rig. The geometry of the specimen was such that instability would occur in the reduced section instead of at the rollers.

To check whether the rig works, a preliminary test was done using AKDQ steel. This is a continuously yielding material which always form a uniform curvature in bending even after the elastic limit. The results obtained from this test is presented in Appendix C. Also, using AKDQ steel and by means of a spherometer arrangement attached to the rig as shown in Figure 5.3, the calibration curve between radius of curvature and cross-head extension was obtained. This is given in Appendix B.

For each material, both tensile and bend specimens were heat treated together so that they would presumably have the same mechanical properties. The bend specimens were approximately aligned at right angles to the rollers and tested at a cross-head speed of 0.1 inch/minute. The autographic load-crosshead extension curve was continuously plotted and the test was stopped whenever kinking of the specimen occurs. However, the chart was left on to record the drop in load as a function of time. A typical load-crosshead extension curve is shown in Figure 5.5 and the data from this curve is used to calculate the bending moment and curvature. The method of calculating these parameters is given in Appendix D. The experimental observations and results are presented in Chapter VI.

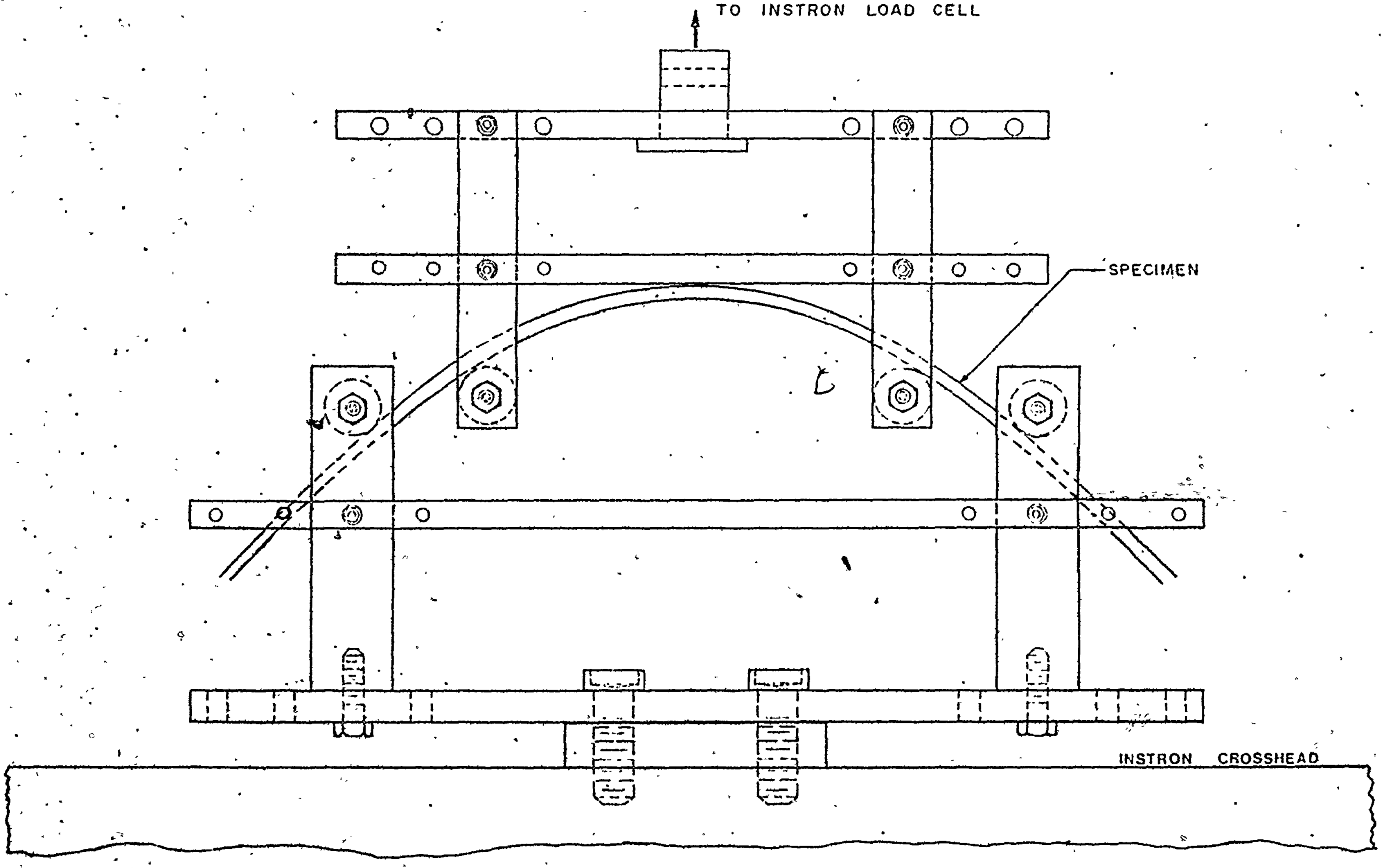

Fig. 5.2 - Schematic diagram of experimental bending rig

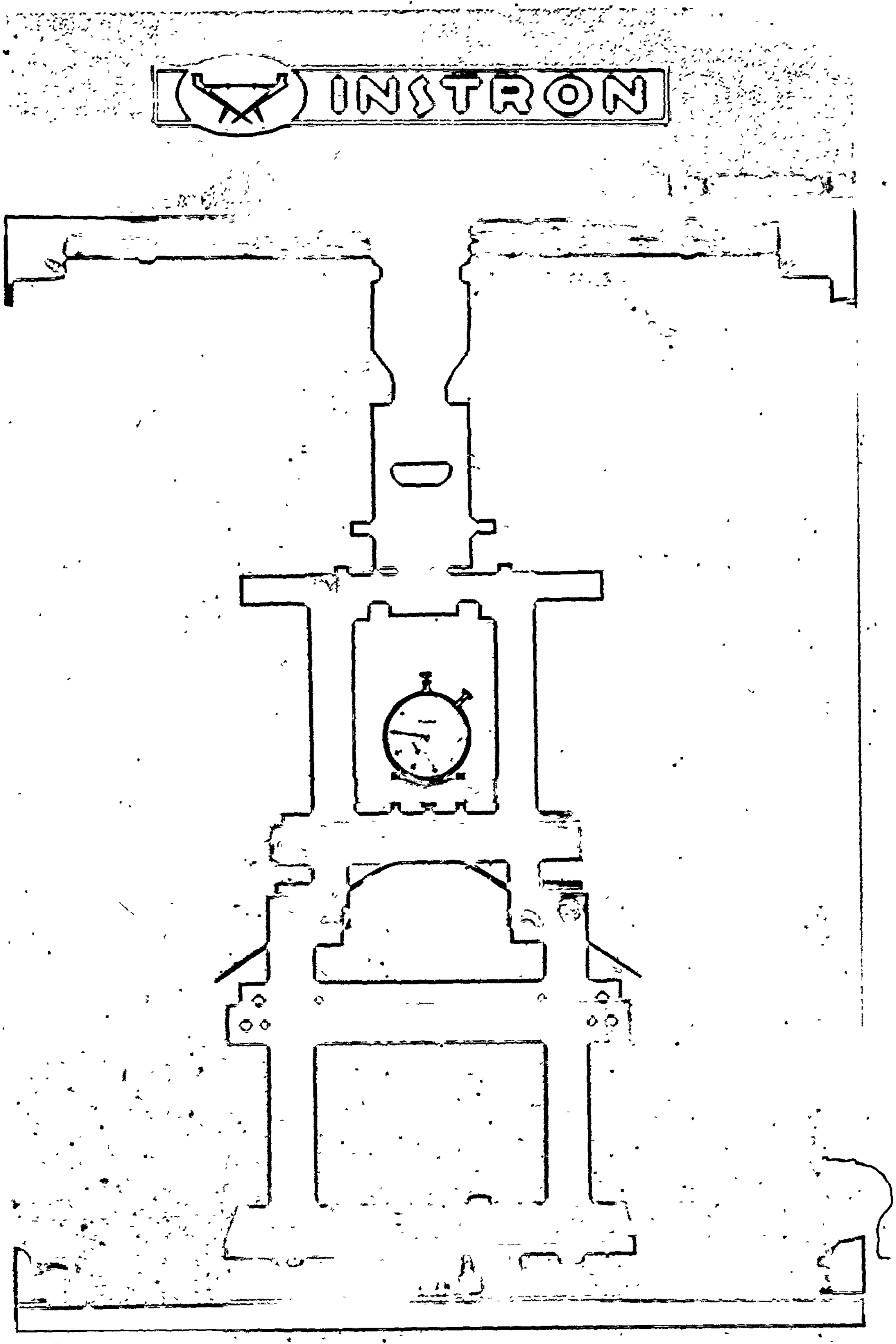

Fig. 5.3 - The complete experimental bending arrangement.

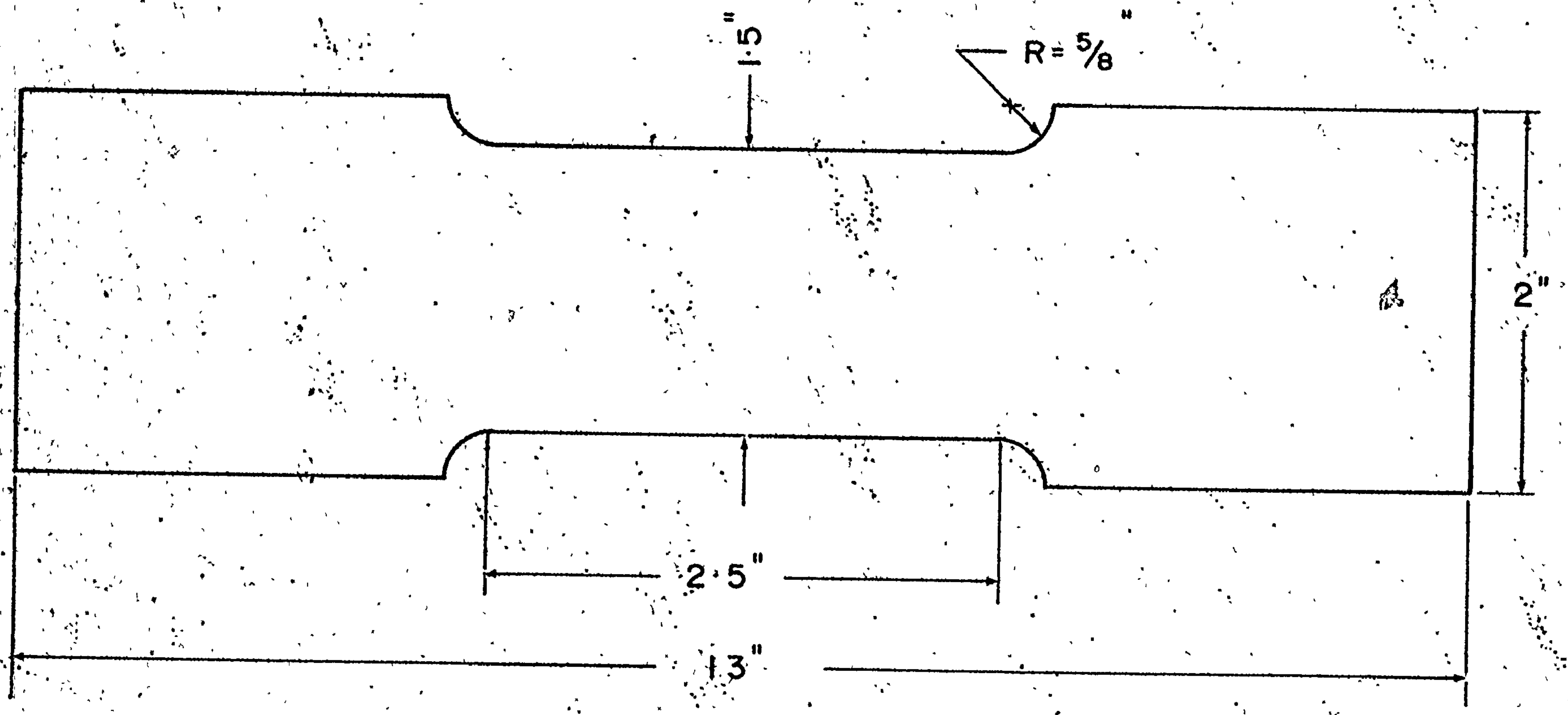

Fig. 5.4 - Geometry of bending specimen

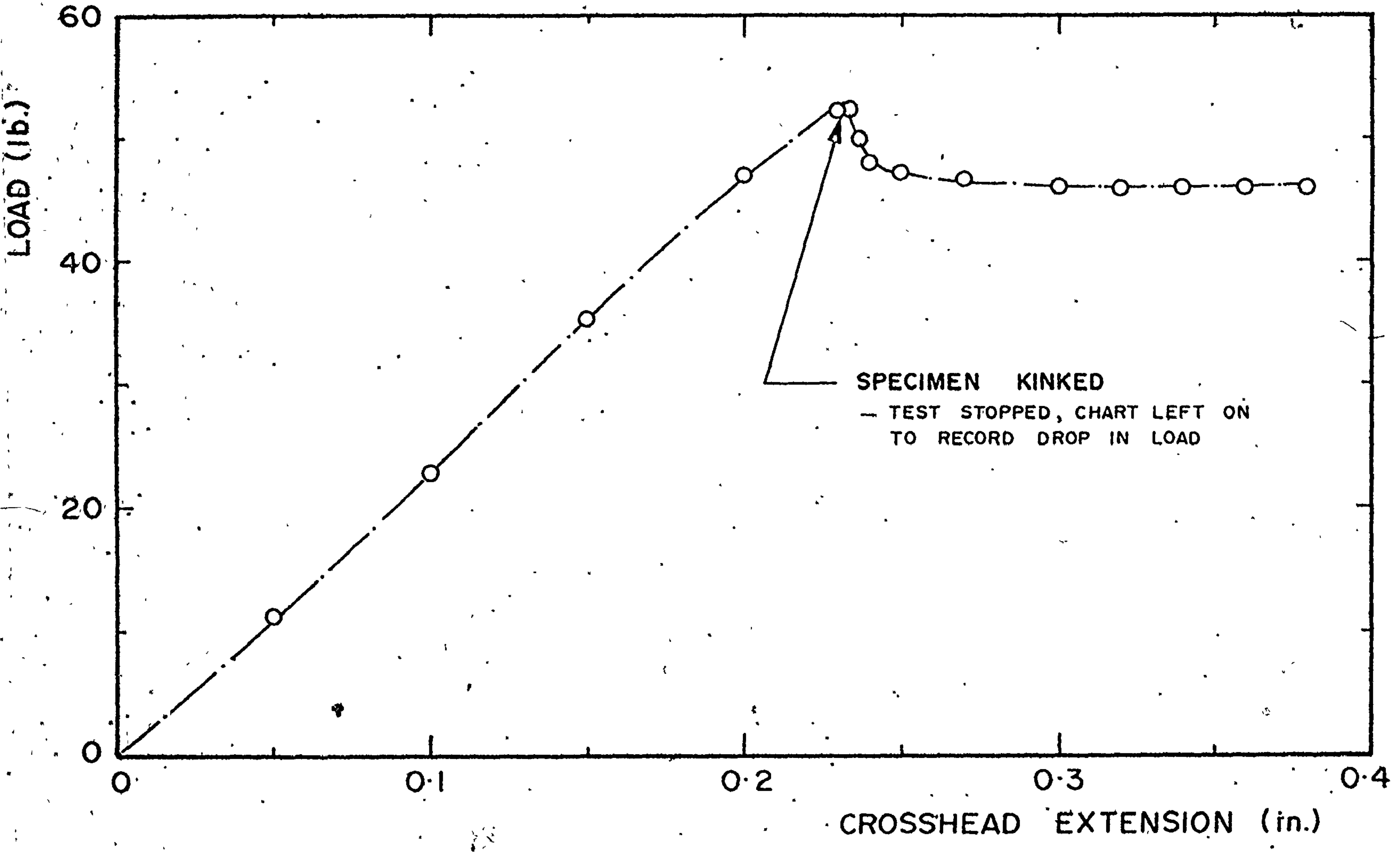

Fig. 5.5 - Typical load-crosshead extension curve for material showing instability in bending

CHAPTER VI

RESULTS AND DISCUSSION

6.1 Experimental Bending Results

A brief description of the bending behaviour of each material and a sample set of experimental results are given in this chapter.

When Rimmed steel-A was tested in the as received condition, no kinking of the specimen occurred and a stable bend was made. Figure 6.1(a) shows the specimen after testing and Figure 6.2(a) gives the experimental moment-curvature diagram. A sample of this material was aged at 100°C for 13.75 hours and a kinking of the specimen occurred on bending beyond the elastic limit. This kinking effect can be seen in Figure 6.1(b) and the experimental bending moment-curvature relation is shown in Figure 6.2(b).

The experimental results for Rimmed steel-B in the as received condition is given in Figure 6.2(c). The specimen kinks in post elastic bending and this effect was also observed with subsequent ageing. When this material was temper rolled and tested, no kinking occurred. With ageing of the temper rolled material (Rimmed steel-B'), the Lüder's strain was recovered but the specimen did not kink. However, a fine regular marking was observed on both surfaces. Figure 6.1(d) shows a photograph of a heat treated specimen and Figure 6.2(d) gives the experimental results for the material, heat treated at 100°C for 1.5 hours.

The experimental results for Rimmed steel-C in the as received and heat treated (100°C for 23 hours) conditions are given in Figures 6.2(e) and 6.2(f). No kinking of the material was observed and the profile of one of the aged specimens is shown in Figure 6.1(e).

For Mild and HSLA steels, both materials kinked in the as received condition and the experimental results obtained are given in Figures 6.2(g) and (h) respectively. The profiles of these tested specimens are shown in Figures 6.1(f) and (g).

From the experimental results, the value of the upper yield stress can be calculated since the bending moment M is proportional to the curvature up to the elastic limit. This stress value is one of plane strain and by dividing by ϕ, which is given by equation (A-11), the equivalent uniaxial tensile upper yield stress can be obtained. These values are given in Table IV which also shows the calculated values of the flow stress, σ_f.

Experimental moment-curvature results for all other tests are given in Appendix F. These are compared

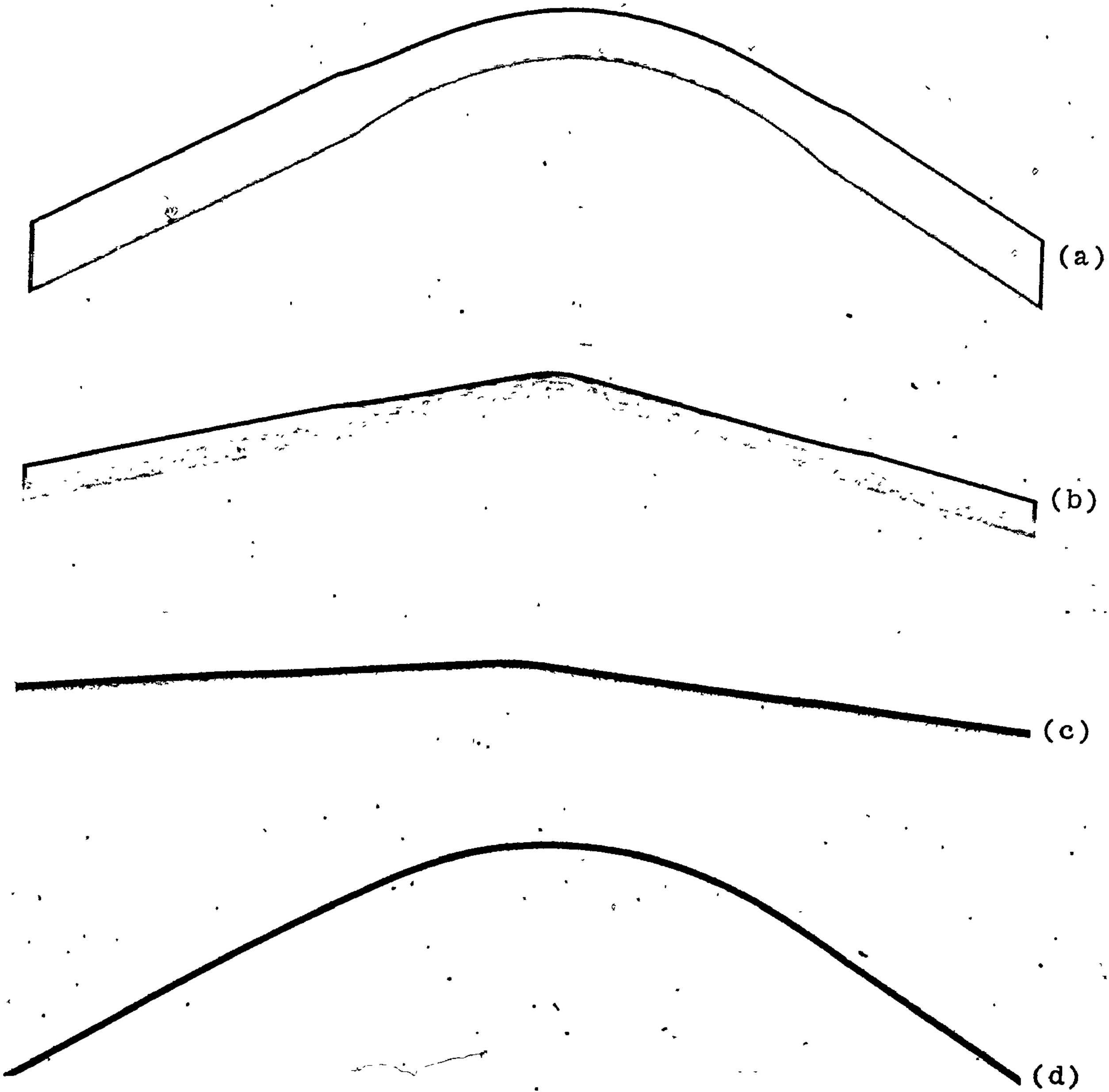

Fig. 6.1 - Profile of tested bend specimen for:

a) Rimmed steel-A in the as received condition
b) Aged Rimmed steel-A
c) Rimmed steel-B in the as received condition
d) Aged Rimmed steel-B'

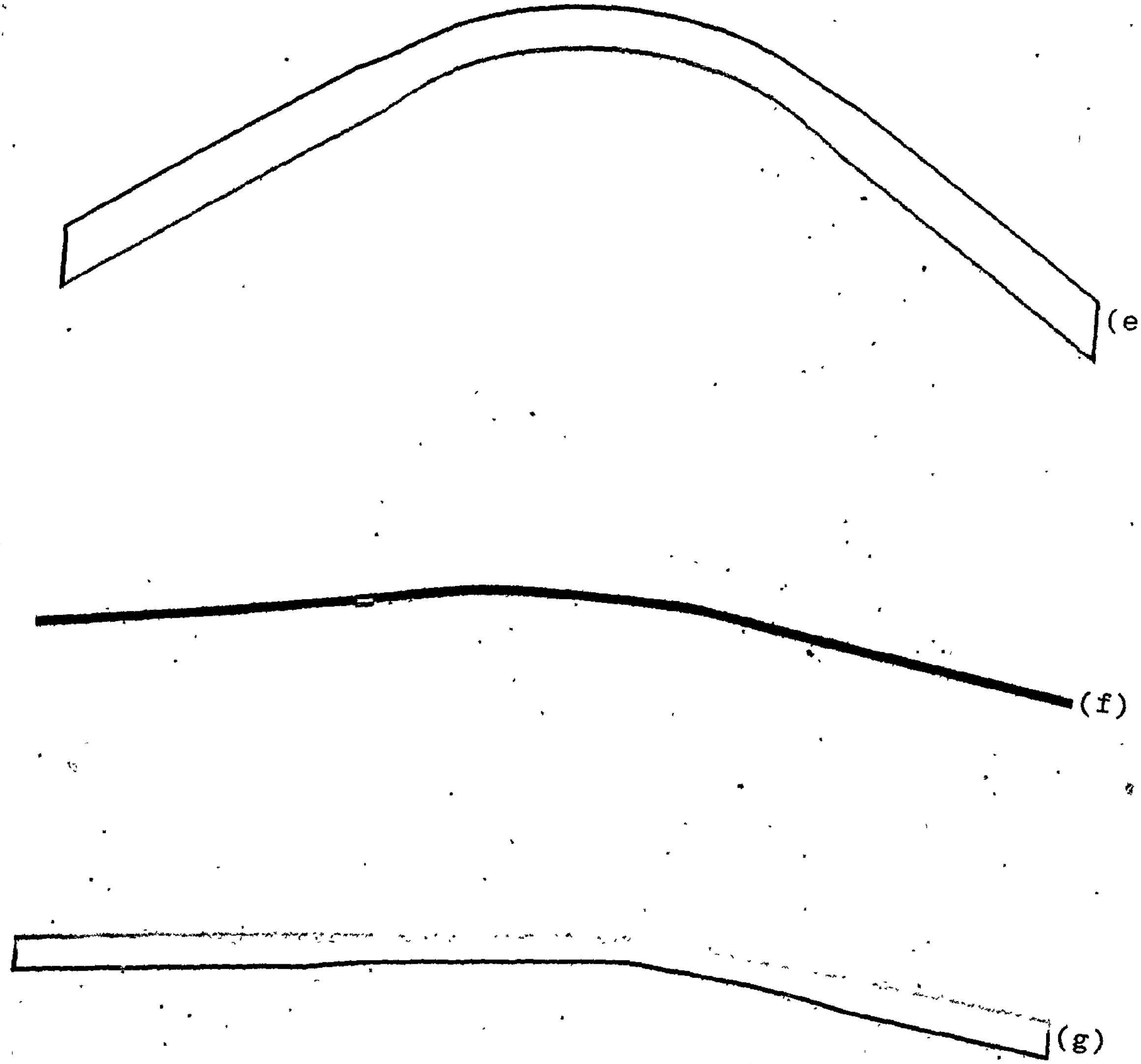

Fig. 6.1 - Profile of tested bend specimen for:
e) Aged Rimmed steel-C
f) Aged Mild steel
g) HSLA steel in the as received condition

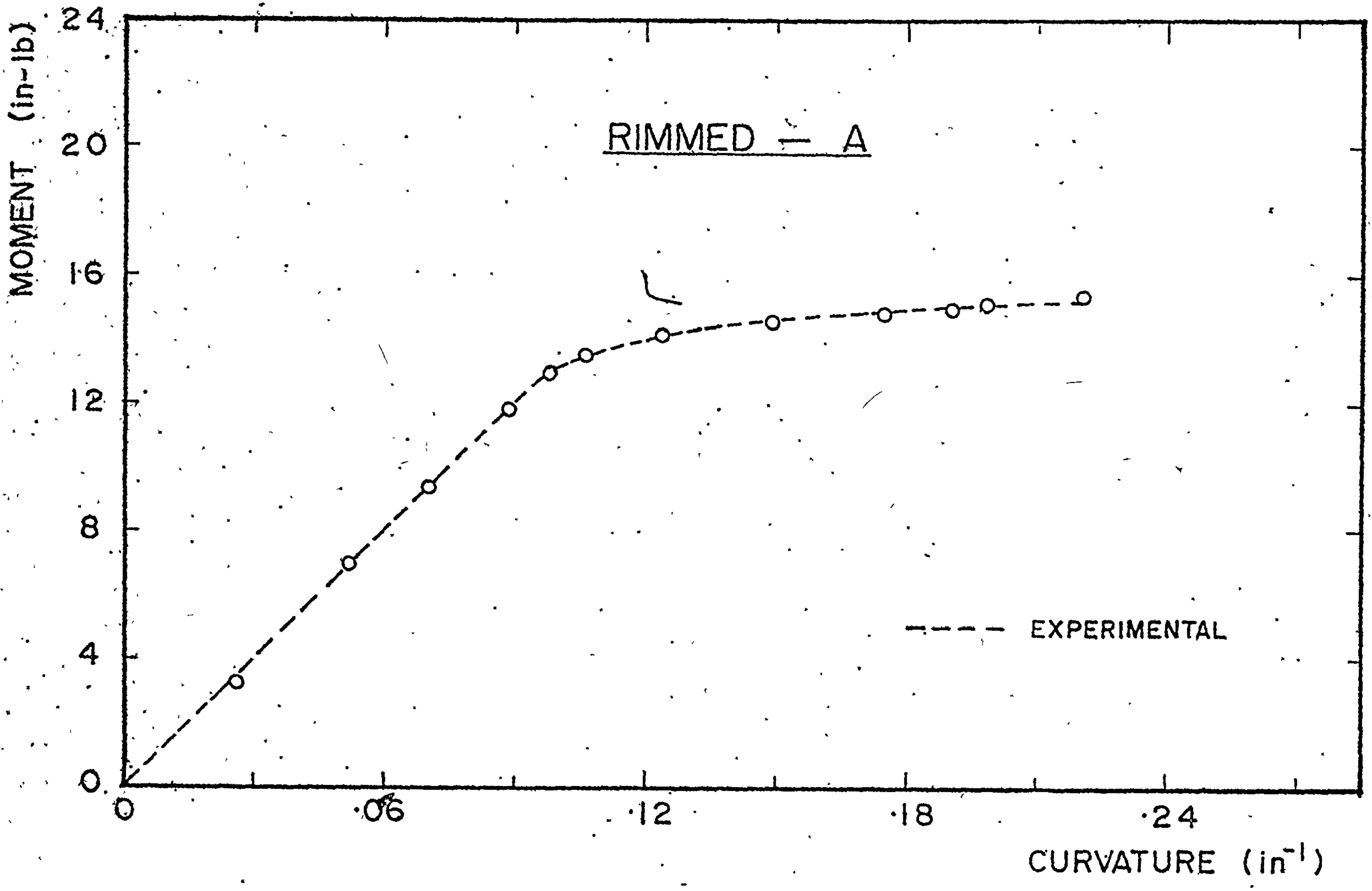

Fig. 6.2(a) - Experimental moment-curvature diagram for Rimmed steel-A in the as received condition

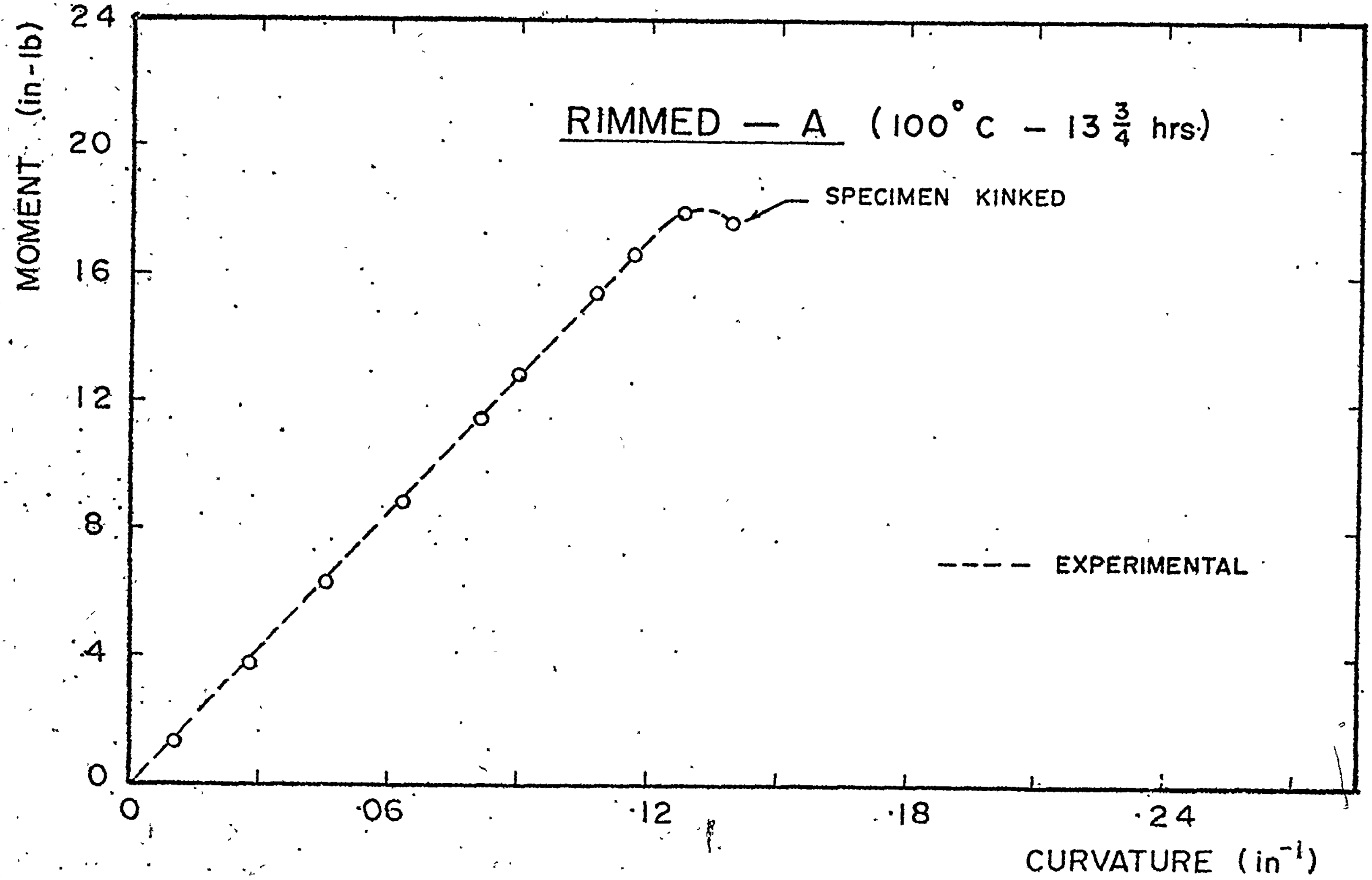

Fig. 6.2(b) - Experimental moment-curvature diagram for Rimmed steel-A, aged at 100°C for 13.75 hours

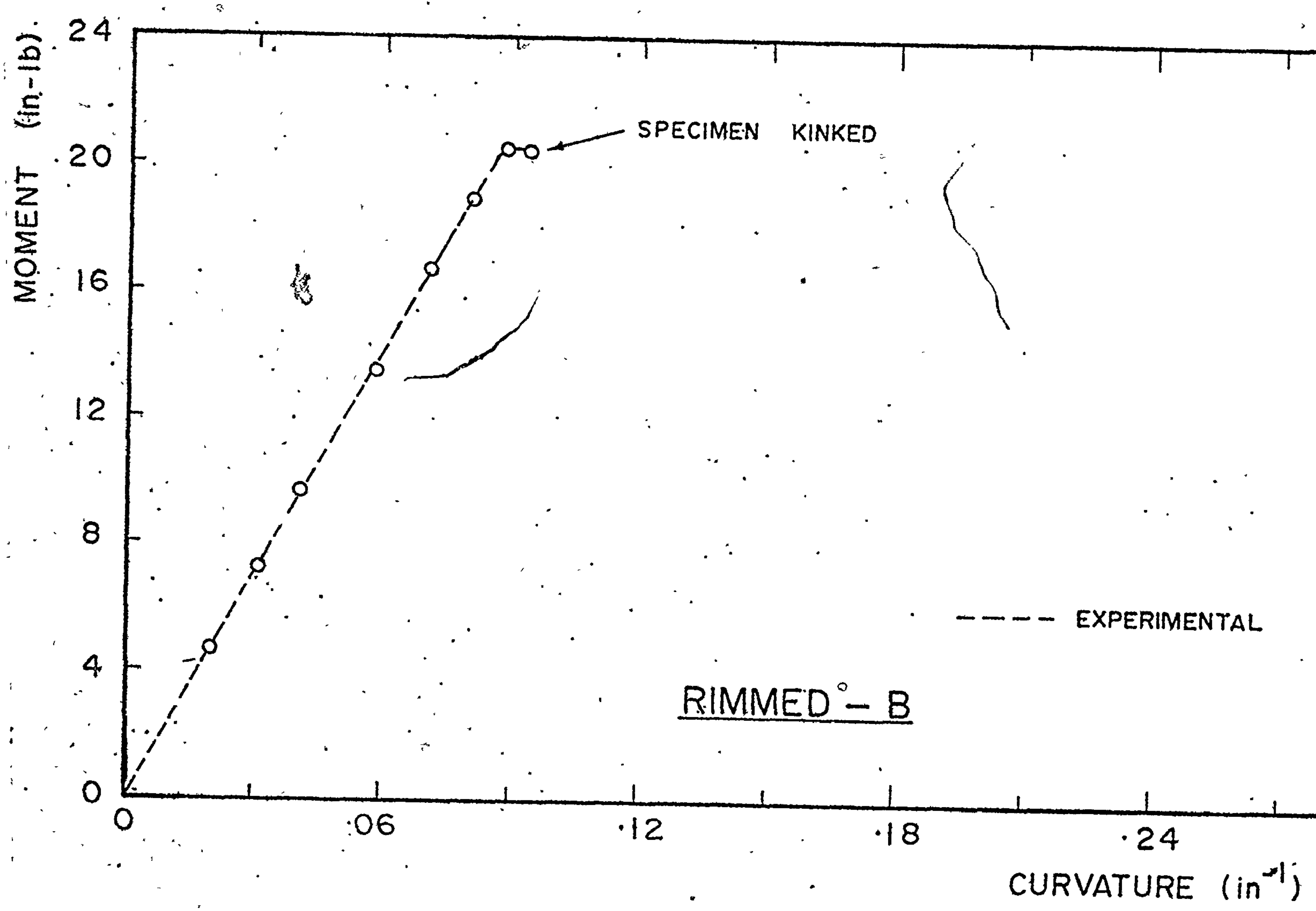

Fig. 6.2(c) - Experimental moment-curvature diagram for Rimmed steel-B in the as received condition

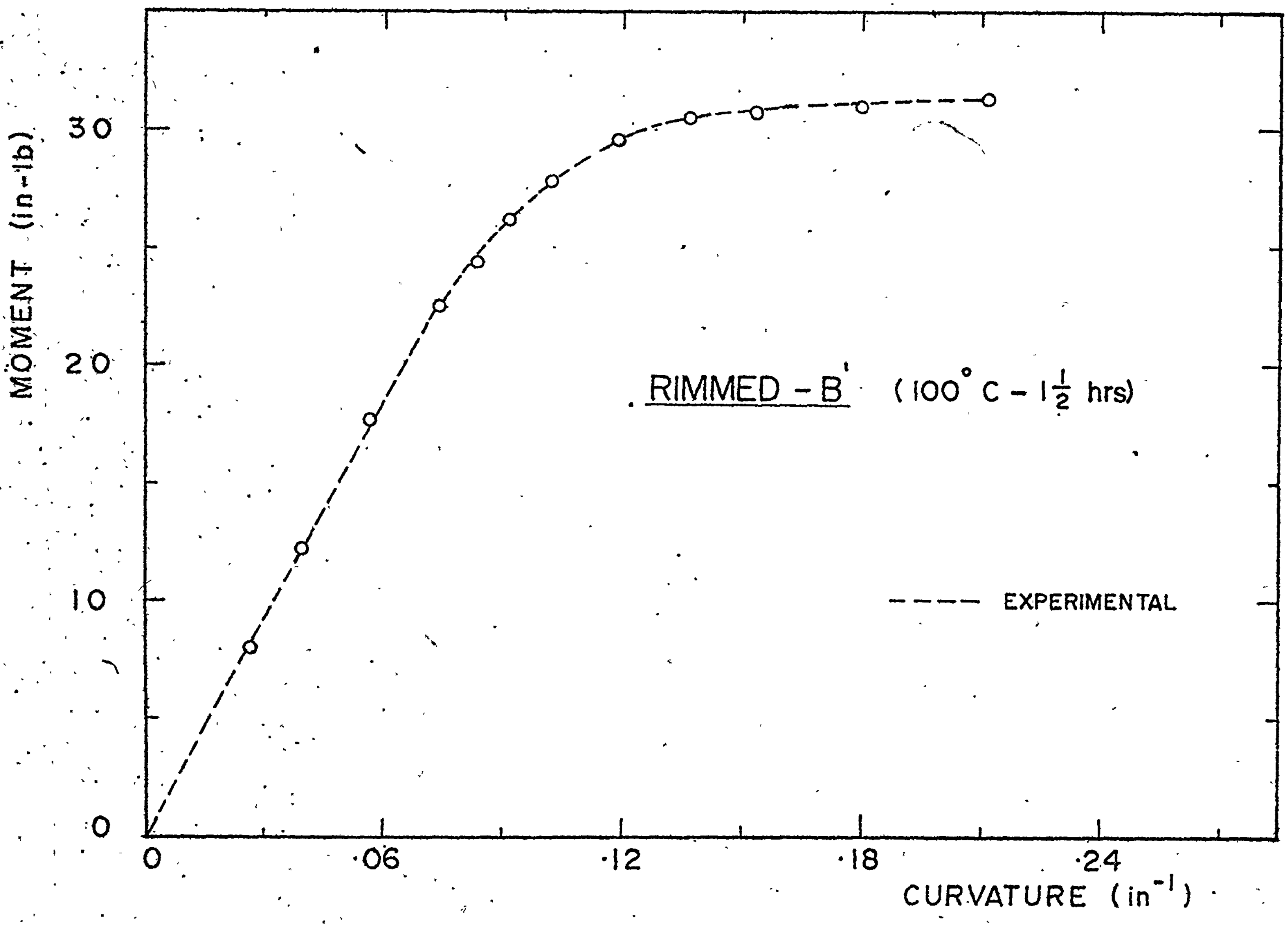

Fig. 6.2(d) - Experimental moment-curvature diagram for Rimmed steel-B', aged at 100°C for 1.5 hours

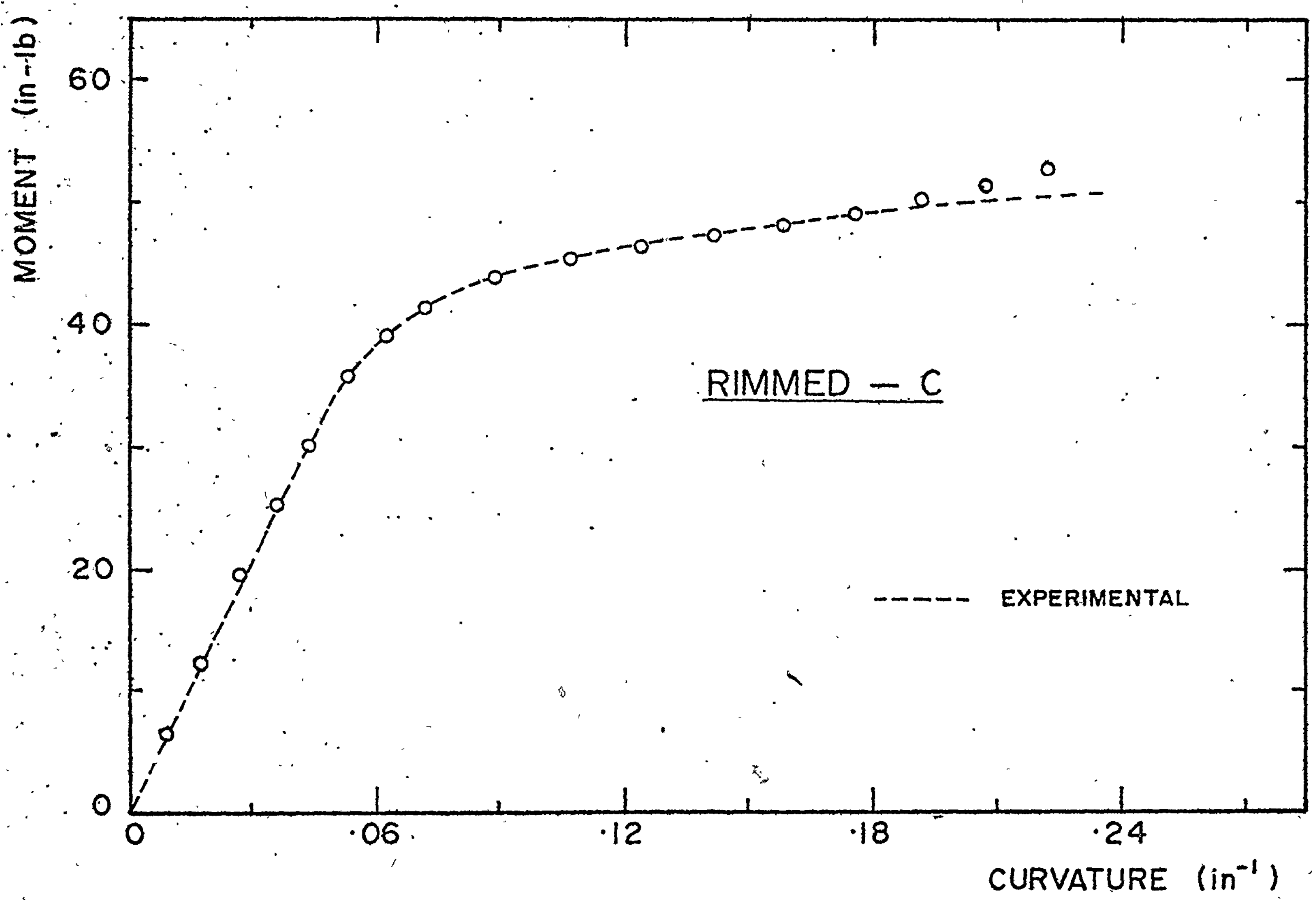

Fig. 6.2(e) - Experimental moment-curvature diagram for Rimmed steel-C in the as received condition

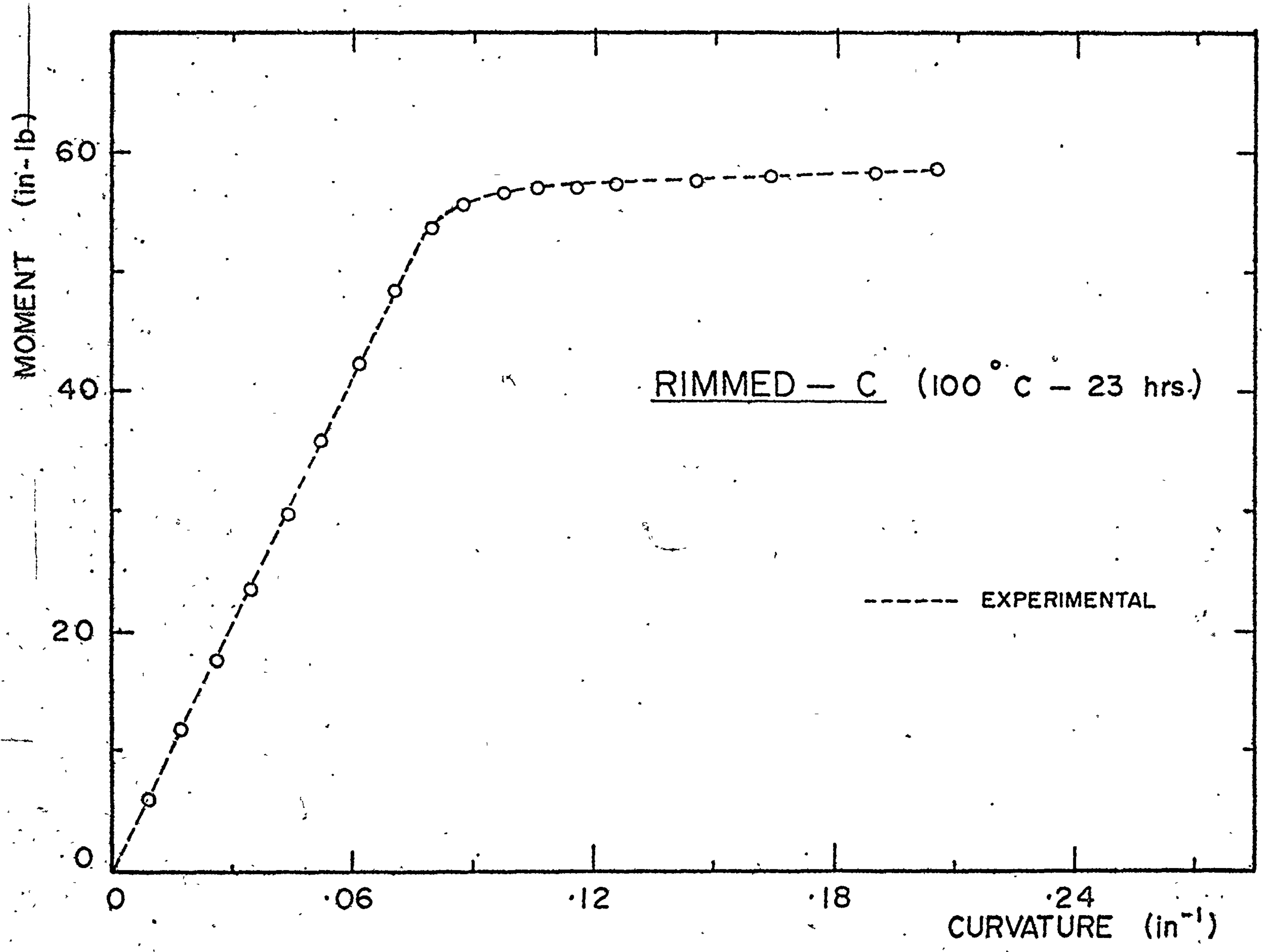

Fig. 6.2(f) - Experimental moment-curvature diagram for Rimmed steel-C, aged at 100°C for 23 hours

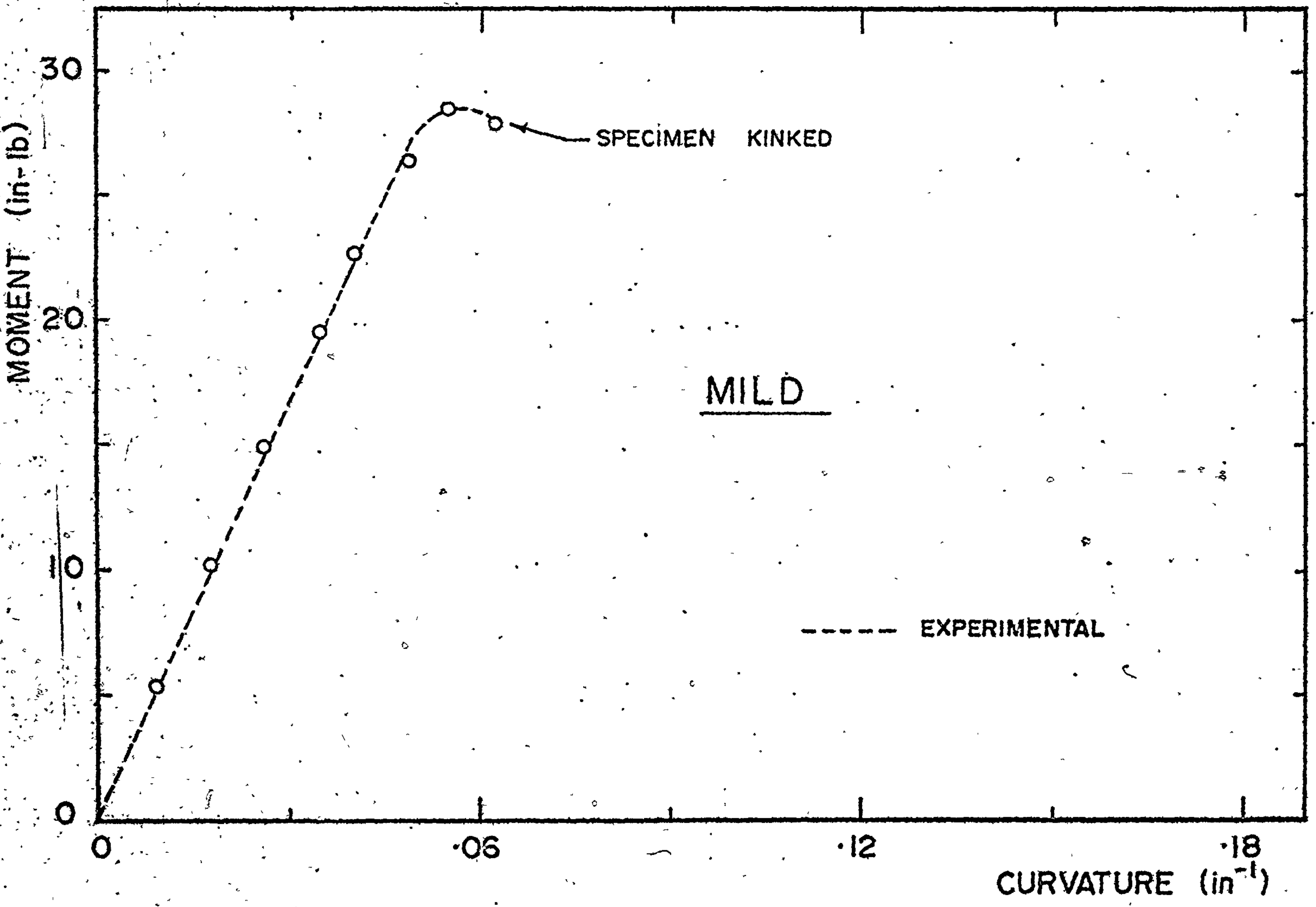

Fig. 6.2(g) - Experimental moment-curvature diagram for Mild steel in the as received condition

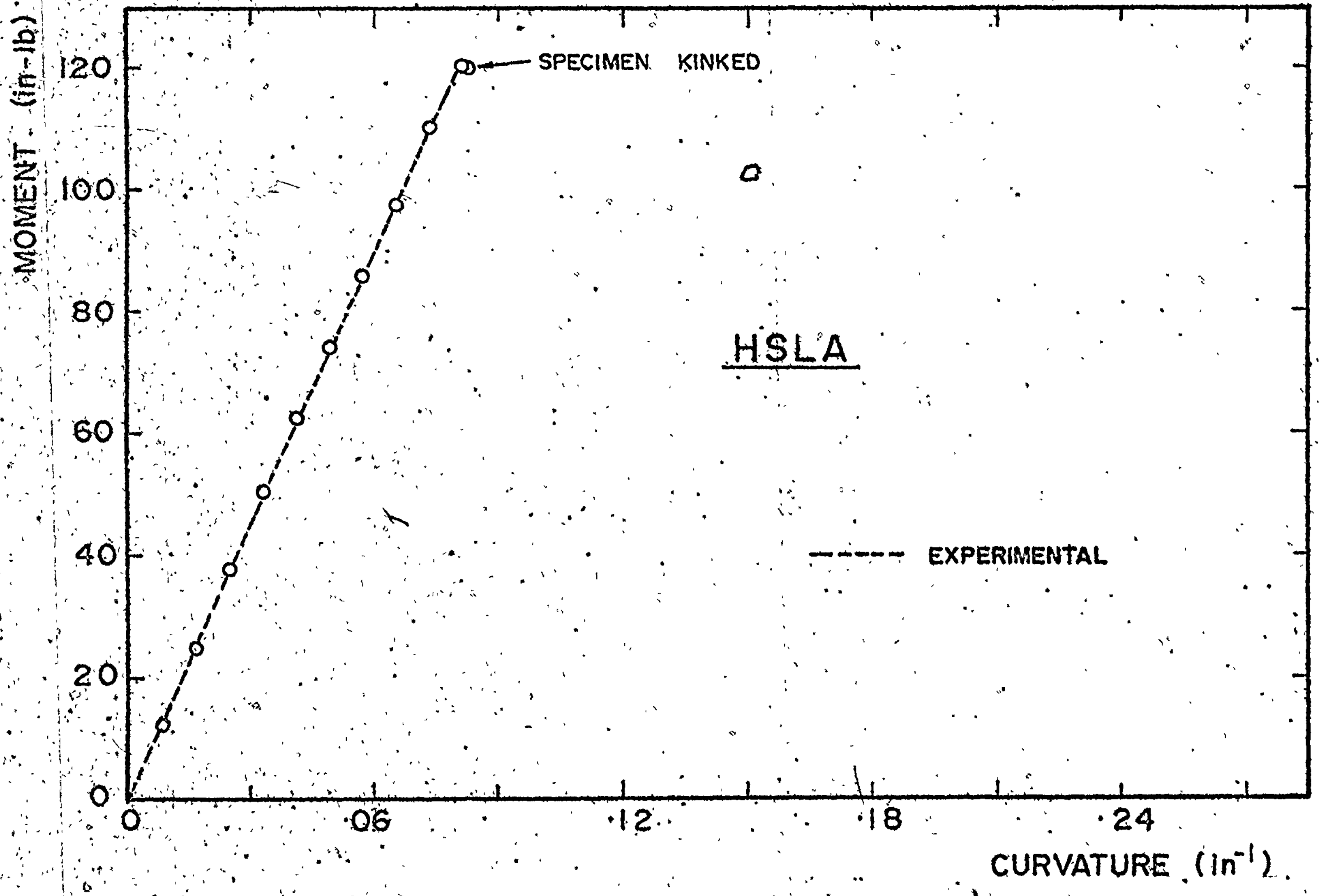

Fig. 6.2(h) – Experimental moment-curvature diagram for HSLA steel in the as received condition

TABLE IV

Flow stress values σ_f and calculated values of the upper yield stress σ_u from bend tests

(a) Material: Rimmed steel-A (t = 0.034")

Heat Treatment		σ_u (ksi)	σ_f (ksi)
Temp.(°C)	Time (hrs)		
---	---	41.89	25.69
100	0.5	52.75	24.80
100	1.0	54.36	29.39
100	5.0	59.30	23.39
100	13.25	59.97	28.00
100	13.75	60.11	33.48
100	14.25	60.21	27.45
100	14.75	60.40	28.37
100	15.75	61.69	26.96
100	18.00	62.16	37.23

(b) Material: Rimmed steel-B (t = 0.04")

Heat Treatment		σ_u (ksi)	σ_f (ksi)
Temp.(°C)	Time (hrs)		
---	---	47.81	12.59
200	0.75	48.83	13.03
215	0.50	50.49	14.88
270	1.00	51.58	12.91

(c) <u>Material</u>: Rimmed steel-B (t = 0.039")

Heat Treatment		σ_u (ksi)	σ_f (ksi)
Temp. (°C)	Time (hrs)		
---	---	28.62	26.24
100	0.25	34.59	31.26
100	0.50	36.85	31.29
100	1.00	38.86	32.71
100	1.50	39.69	35.17
100	2.00	40.49	33.16

(d) <u>Material</u>: Rimmed steel-C (t = 0.058")

Heat Treatment		σ_u (ksi)	σ_f (ksi)
Temp. (°C)	Time (hrs)		
---	---	37.03	31.96
100	2.0	53.15	36.95
100	4.0	54.97	38.72
100	13.0	58.31	40.94
100	19.5	59.56	37.47
100	23.0	61.48	40.09

(e) <u>Material</u>: Mild steel (t = 0.056")

Heat treatment		σ_u (ksi)	σ_f (ksi)
Temp.(°C)	Time (hrs)		
---	---	33.47	13.52
100	2	34.30	13.55
100	4	35.24	14.19
100	23	36.54	14.08
100	36	36.98	13.37

(f) <u>Material</u>: HSLA steel (t = 0.076")

Heat treatment		σ_u (ksi)	σ_f (ksi)
Temp.(°C)	Time (hrs)		
---	---	78.33	35.75
225	8	80.96	33.21

with the theoretical results from the proposed model that best agrees with the experimental observations.

6.2 Effect of Ageing on the Upper Yield Stress

The effect of ageing on the value of the upper yield stress for Rimmed-A, Rimmed-B', Rimmed-C and Mild steels are shown in Figures 6.3(a) to 6.3(d) respectively. Here, the values of σ_u from the tensile and bend tests are compared. The graphs reveal that the magnitude of σ_u from the bend test is, in almost all cases, greater than that obtained from the tensile test. Also, the values from the bend tests increase with ageing time which is expected, whereas the values from the tensile test are scattered. From Figure 6.3(b), which shows the results for the temper rolled material Rimmed steel-B', the tensile upper yield stress values are larger for some tests. This may be due to the residual stresses in the tensile and bend test specimens being different since the specimens were machined from sheets which may not have been rolled under the same conditions.

The magnitude of the upper yield stress at a particular strain rate from a tensile test depends on:

i) the rigidity of the testing machine

ii) the alignment of the specimen in the grips

and iii) the radius of the fillets on the specimen.

For instance, upper yield stress values between 1.4 and 1.6 times the lower yield stress values have been obtained [27]. However, to achieve such values, the specimens have to be very carefully machined and truly aligned in the grips. Unfortunately, in this work, such precautionary measures were not possible.

6.3 Effect of Ageing on the Lüder's Strain

Figures 6.4(a) to 6.4(d) show the effect of ageing on the value of Lüder's strain for Rimmed-A, Rimmed-B, Rimmed-C and Mild steels respectively. In these graphs, the values of ε_L, obtained from tensile tests are compared with the values obtained from the curve fit parameters. These values are determined by finding the intersection of the curve generated from the curve fit values with the experimental tensile true stress-true strain curve. The graphs show that the magnitude of the Lüder's strain, ε_L generally increases with ageing time. This is expected since ageing increases both upper and lower yield stress values and from the model presented for the tensile test in Chapter III, an increase in lower yield stress will result in an increase in Lüder's strain. The comparison of observed and calculated values shows that the calculated values are less than those obtained from experiments. This is because the curve fit is not good in the region just after the yield point elongation where the material has a higher hardening rate.

From Figure 6.4(a), there is not much of an increase in Lüder's strain until the material, Rimmed steel-A has been aged for over 13 hours. An examination of the lower yield stress values in Table I(a) also shows that the stress value hardly increases until ageing has exceeded 13 hours. Thus, this confirms that the magnitude of the Lüder's strain is directly dependent on the value of the lower yield stress.

6.4 Comparison of Proposed Models with Experimental Results

In Chapter IV, the stress distributions and theoretical analyses of two models (Models I and II) were presented. In order to determine which model is preferable the theoretical results computed from both will be compared with the experimental results of a test that shows no instability when bent beyond the elastic limit. Rimmed steel-A in the as received condition will be used here since this material has approximately 3% Lüder's strain and shows no kinking. In the theoretical analysis, the value of the upper yield stress σ_u from the bend test will be used along with the lower yield stress value from the tensile test. Also, it will be assumed that Young's modulus of elasticity E is equal to 30 x 10^6 psi and

Poisson's ratio ν is equal to 0.3.

Figure 6.5 shows the comparison of the experimental and theoretical results for the material. It can be seen that the results from Model I are in good agreement with the experimental results in that no kinking of the material is predicted. The curve from Model II shows a drop in moment after the elastic limit which indicates kinking and as stated before, this does not occur. An examination of other test results show that the results obtained from Model I are more agreeable with experimental results than those from Model II. Therefore, on this basis, Model I seems to be the more plausible model. Another reason why this is so is due to the fact that the strains in bending are very small compared with the Lüder's strain, hence the strain rates are probably very low and can be considered to be nearly zero. As noted in Chapter III, the lower yield stress σ_L is associated with a high strain rate which is unlikely to be reached in the bending experiment. Therefore, the whole bending behaviour can be roughly characterized by the stress-strain curve for the section at a strain rate $\dot{\varepsilon} = 0$. For this reason, the lower yield stress does not seem to be a relevant parameter and since Model II is based on this value, it can be argued that failure to represent the material behaviour in bending is reasonable. Hence, for all tests, the experimental results will be compared with the theoretical curve generated from Model I.

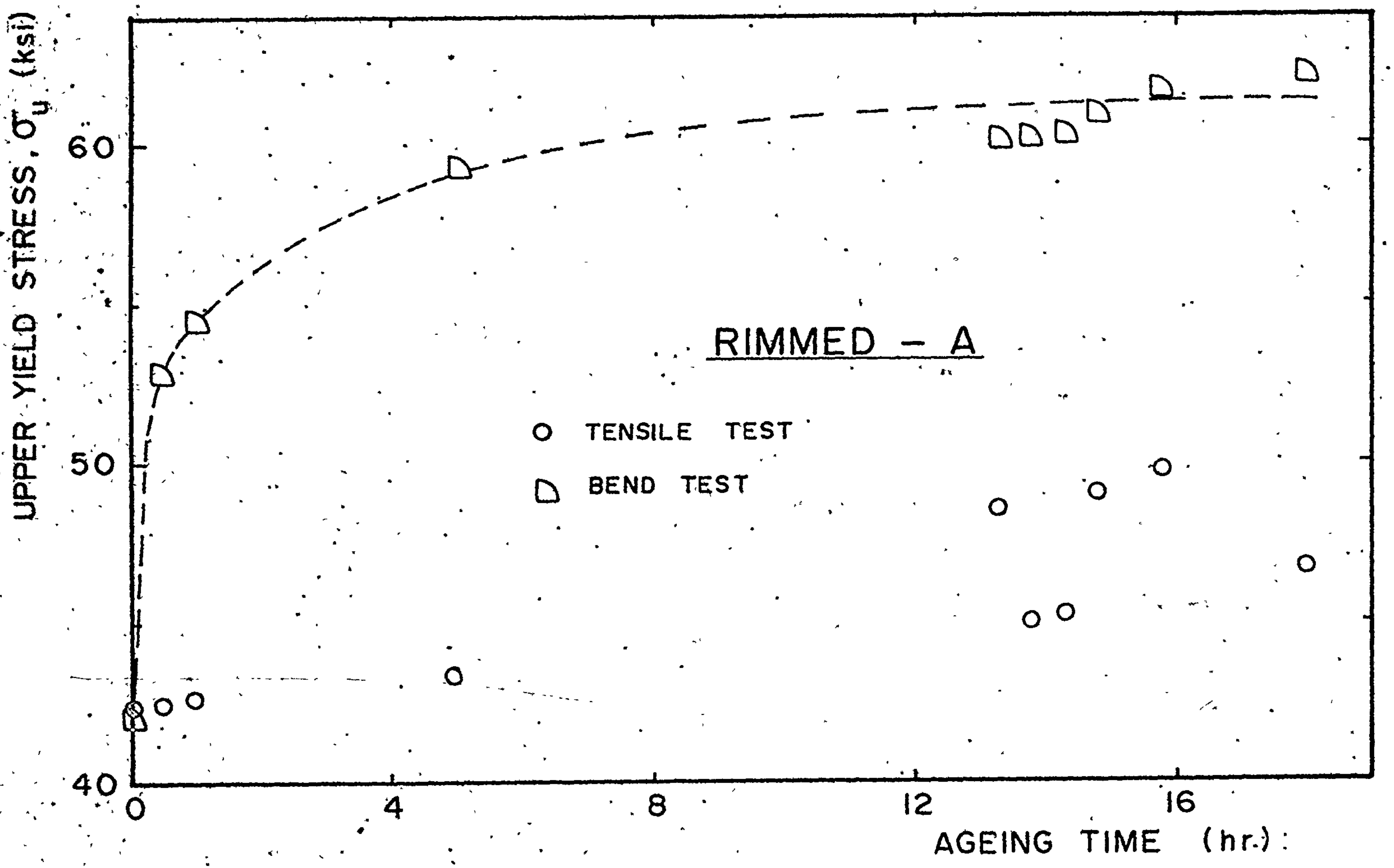

Fig. 6.3(a) - The effect of ageing on the upper yield stress value for Rimmed steel-A

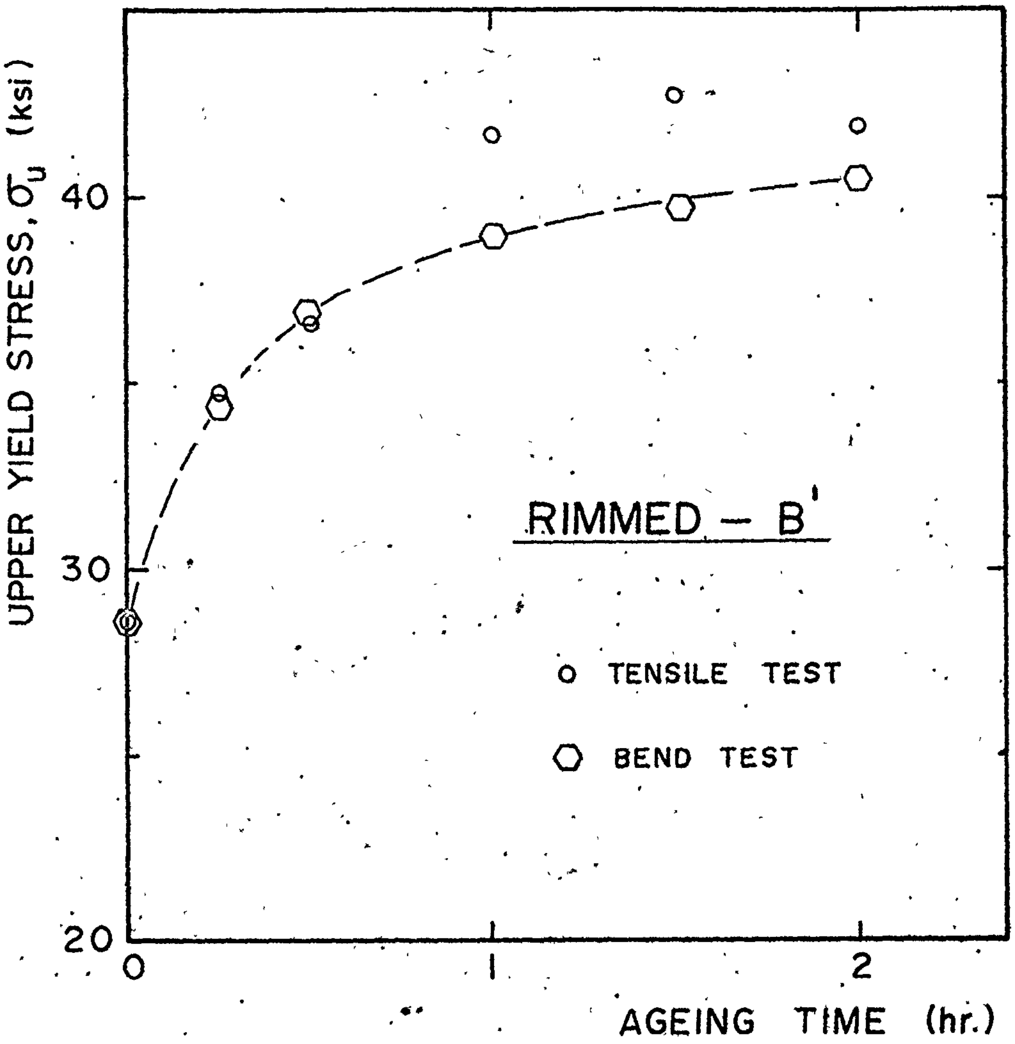

Fig. 6.3(b) - The effect of ageing on the upper yield stress value for Rimmed steel-B'

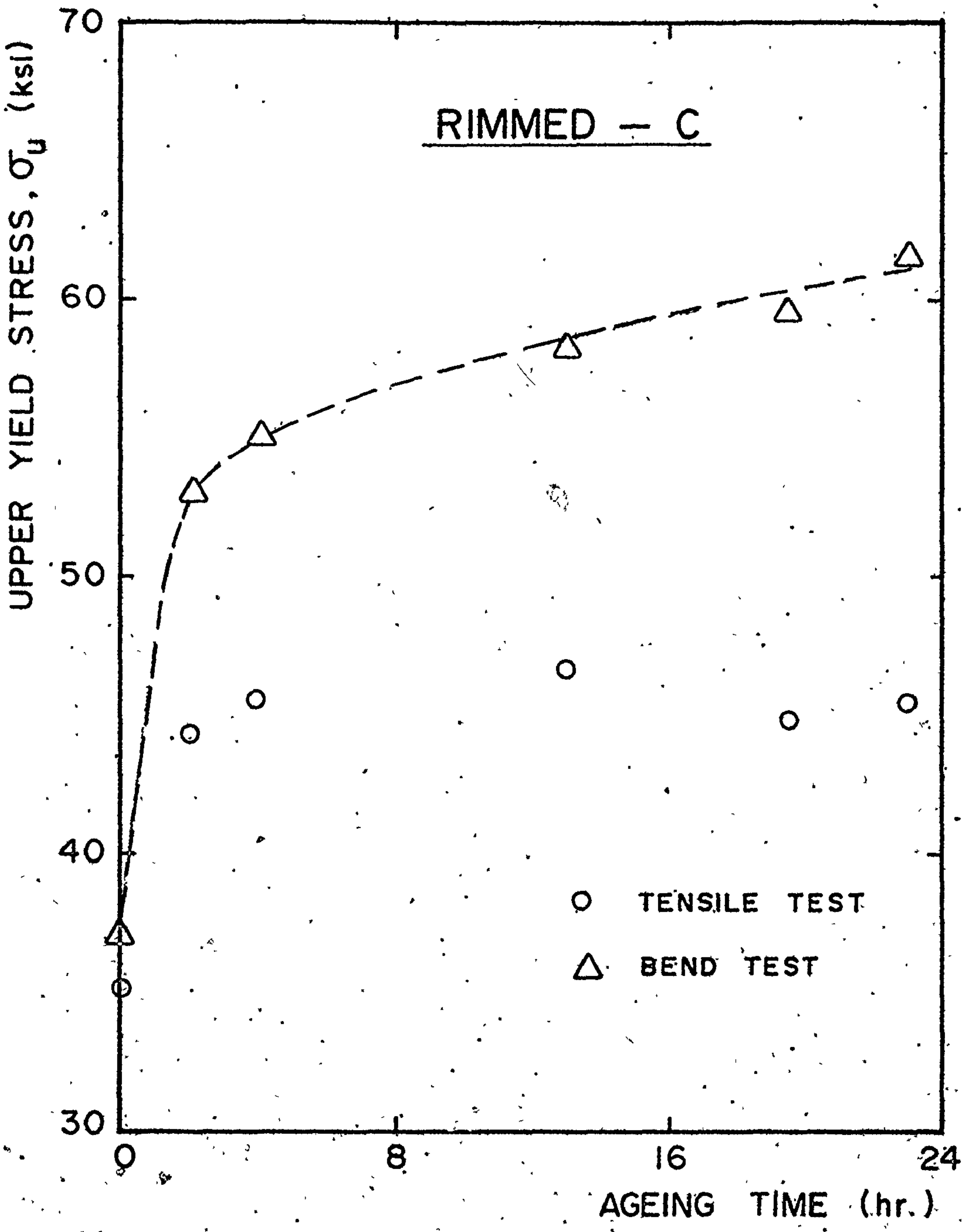

Fig. 6.3(c) - The effect of ageing on the upper yield stress value for Rimmed steel-C

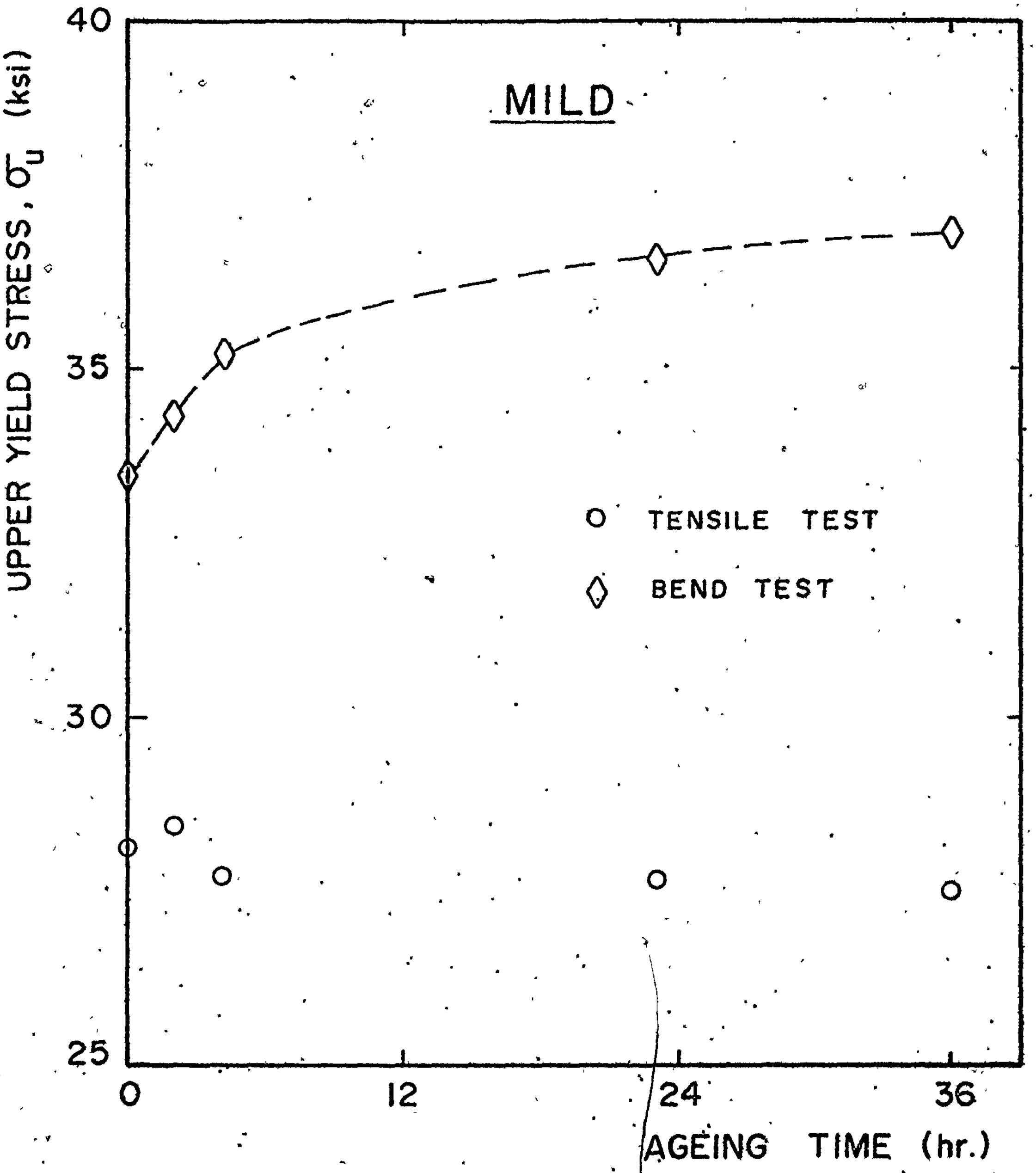

Fig. 6.3(d) - The effect of ageing on the upper yield stress value for Mild steel

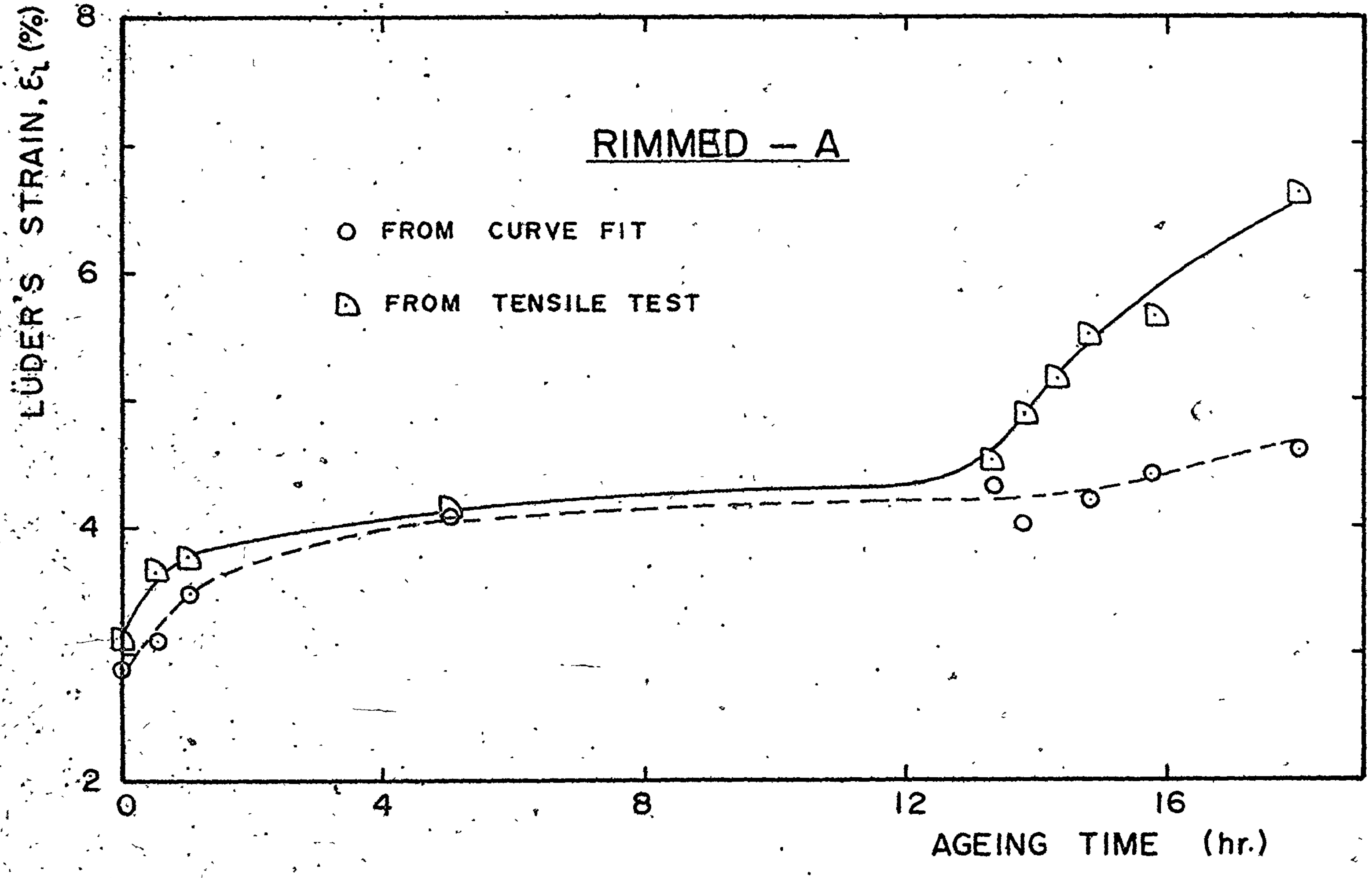

Fig. 6.4(a) - The effect of ageing on the Lüder's strain value for Rimmed steel-A

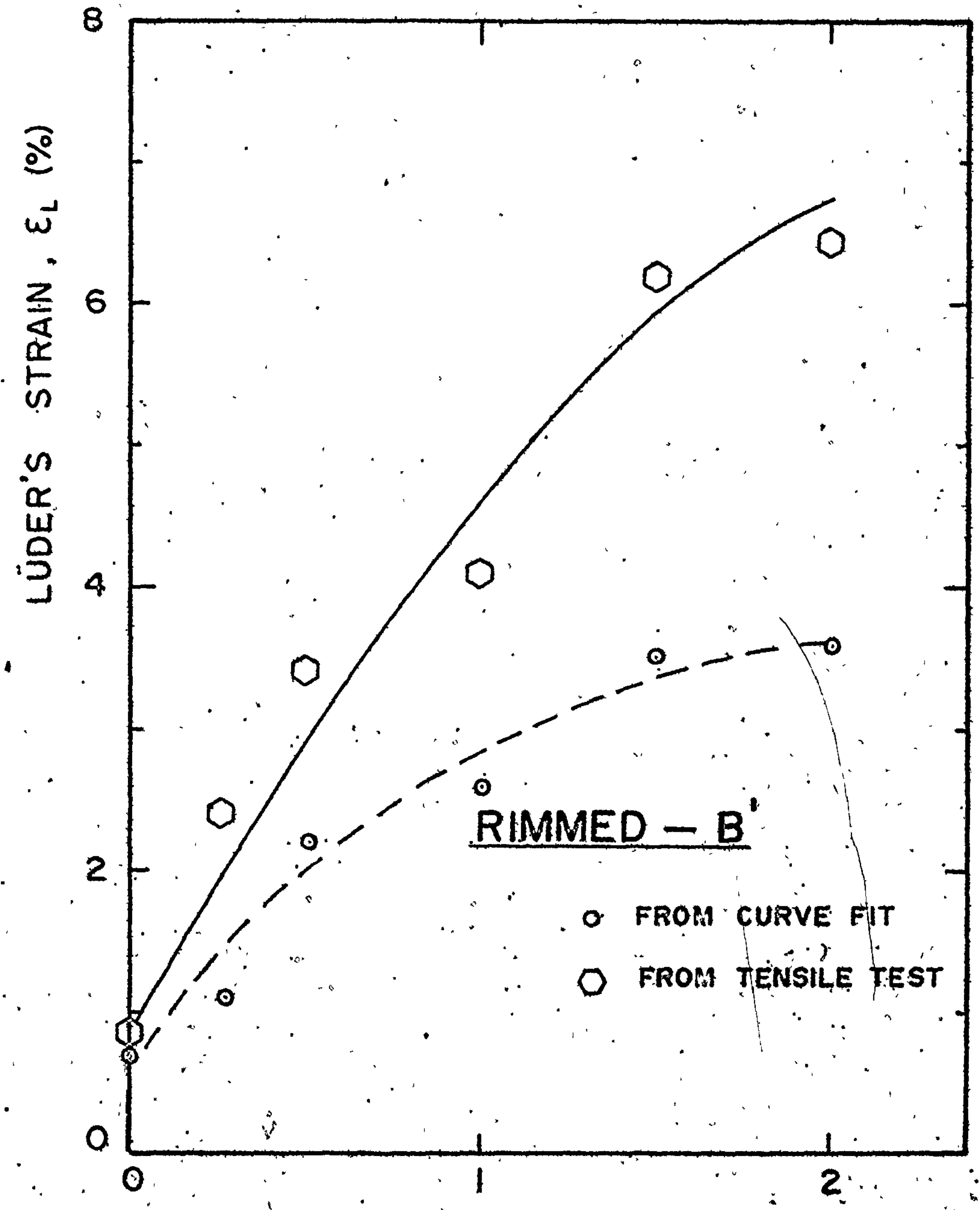

Fig. 6.4(b) - The effect of ageing on the Lüder's strain value for Rimmed steel-B'

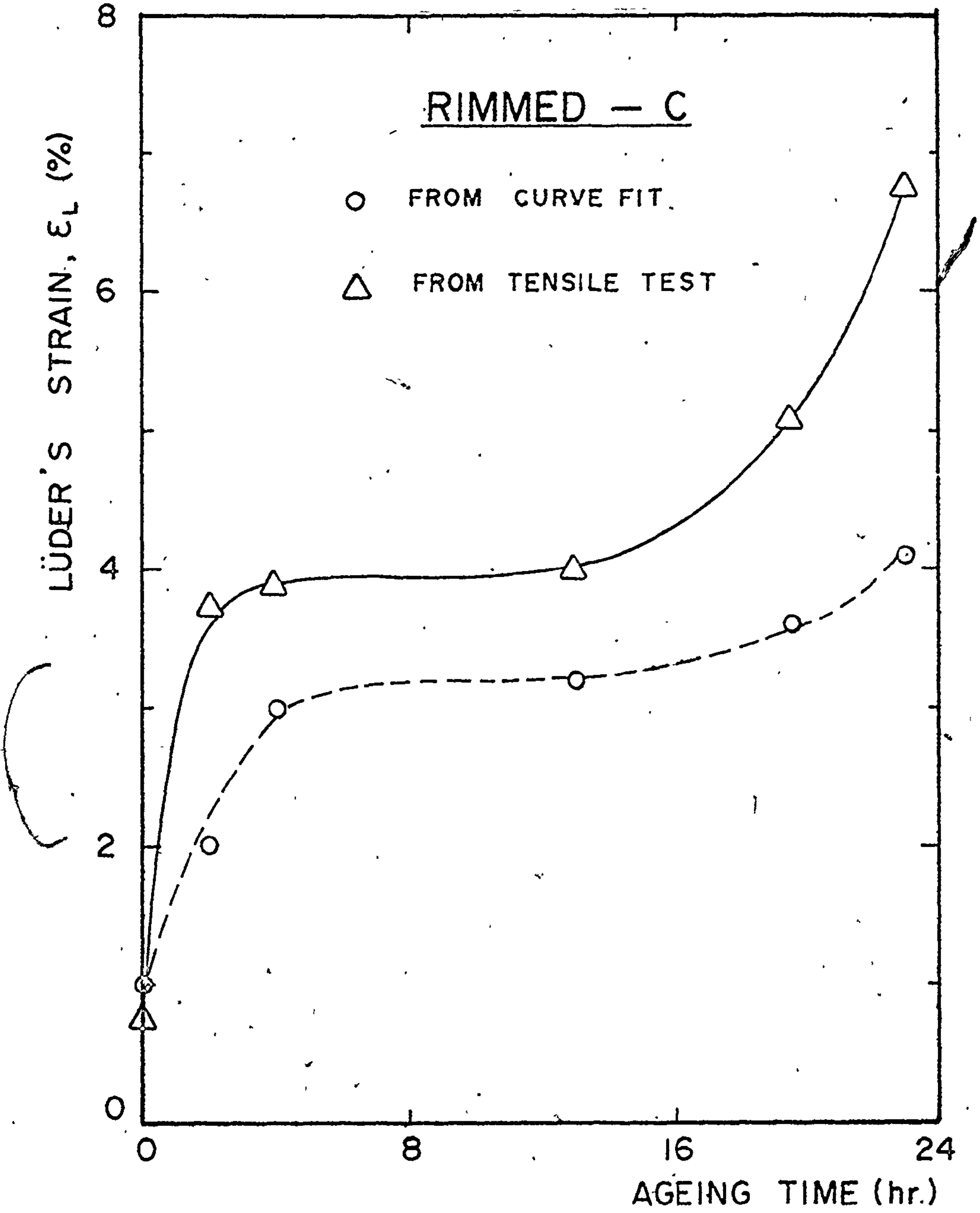

Fig. 6.4(c) - The effect of ageing on the Lüder's strain value for Rimmed steel-C

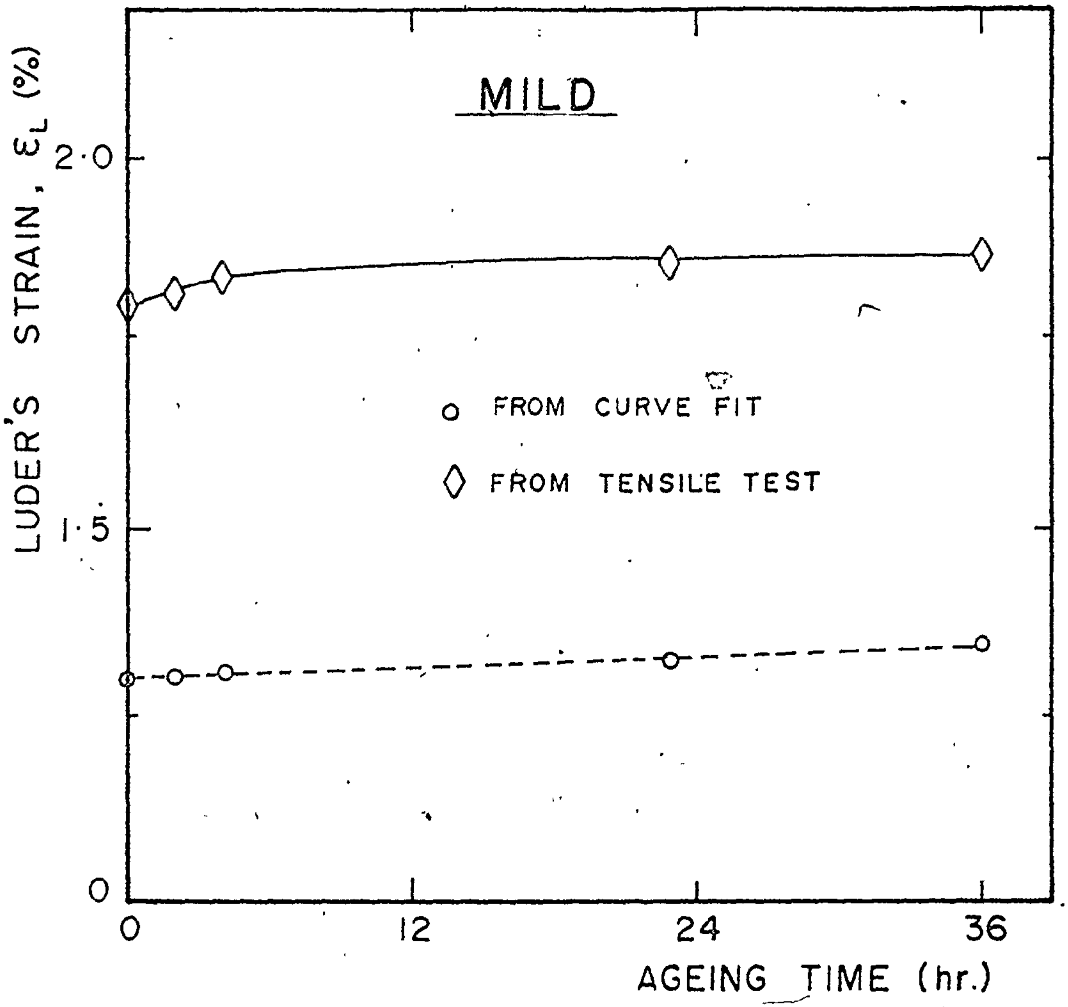

Fig. 6.4(d) - The effect of ageing on the Lüder's strain value for Mild steel

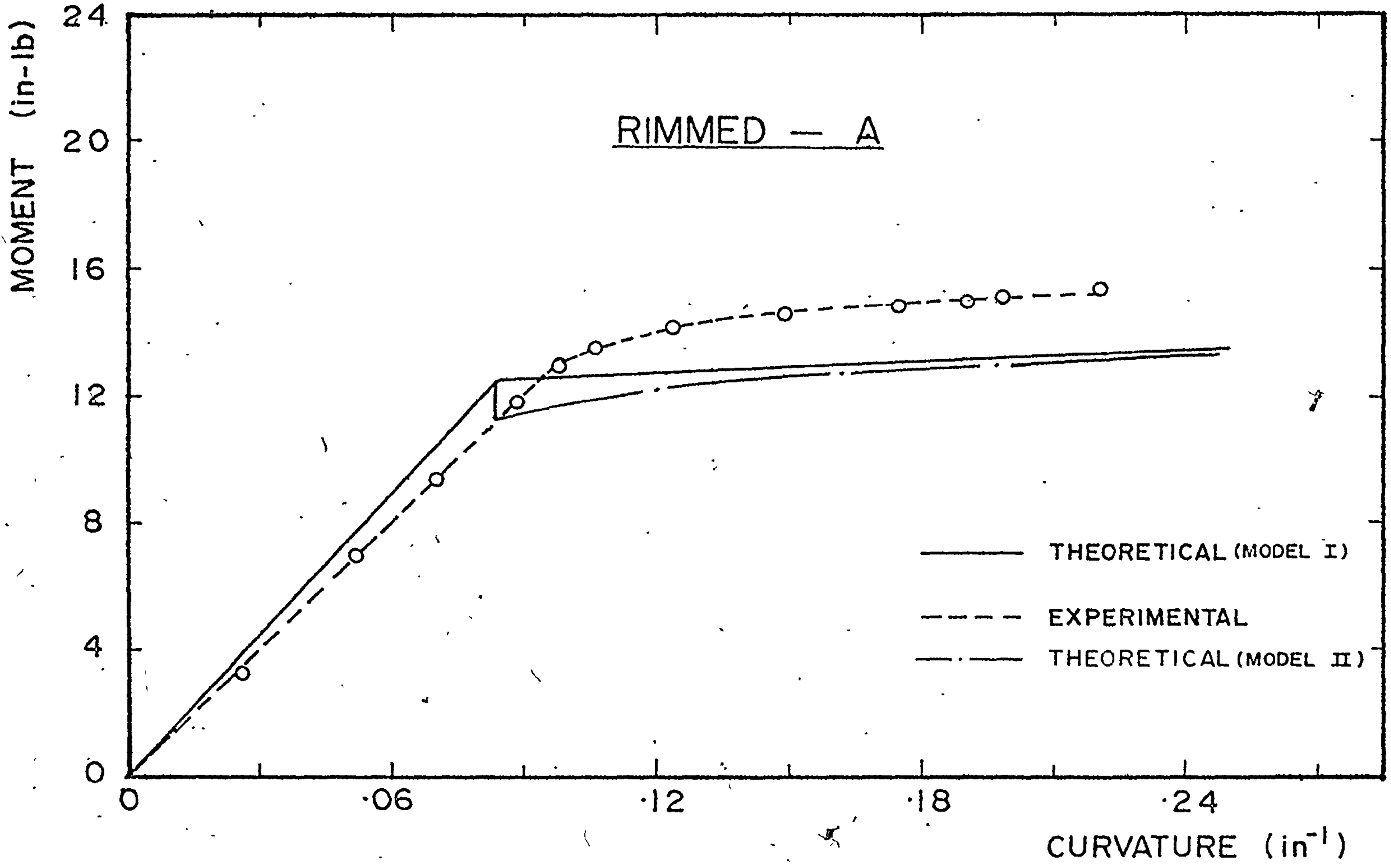

Fig. 6.5 - Comparison of experimental results with the theoretical curves generated from Models I and II for Rimmed steel A in the as received condition

6.5 Discussion

Figures 6.6(a) - 6.6(h) show the comparison of the experimental results presented in section (6.1) with the theoretical results obtained from the stress distribution given by Model I. The comparison of experimental results from other tests are given in Appendix F. In the generation of the theoretical curves, the values of σ_u from the bend test will be used since, for the reasons already given, the values from the tensile test may not be reliable. Also, Young's modulus of elasticity E is assumed to be 30 x 10^6 psi and Poisson's ratio ν is equal to 0.3.

The theoretical results in all cases are in good agreement with experimental observations in that whenever kinking of the specimen is observed, this is predicted by Model I. For some theoretical analyses, tensile tests had to be re-performed since the tensile and curve fit parameters were found to be unreliable.

Upon closer examination of the moment-curvature diagrams, there is a discrepancy in slopes of the theoretical and experimental results in the elastic region. One reason for this may be due to the value of Young's modulus of elasticity E not being the assumed value. Another reason is that the specimens may not be truly in plane strain in the bending experiment.

In the elastoplastic region, the experimental and theoterical curves can only be compared when the test does not show kinking. When the specimen kinks, the curvature changes rapidly and further experimental data could not be obtained. From the curves that can be compared, the error between experimental and theoretical results is within 20%. This discrepancy may be due, in addition to the reasons already given, on the degree of accuracy in the curve fit of the tensile true stress-true strain curve and the assumptions made in the theoretical analysis. One of which is Hill's theory for anisotrophy in the plastic region which assumes that the stress-strain relations in tension and compression are the same. This is not necessarily correct.

From the analysis, the material parameter that seems to determine whether kinking of the material can be predicted is the value of $(\sigma_u - \sigma_f)$. This can be seen in Figure 6.7 where the value of σ_u from the tensile test is used in the theoretical analysis. The graph shows that the theoretical elastic bending moment is much less than the experimental value and also, kinking of the material is not predicted. Therefore, an accurate value of σ_u is necessary for predicting the behaviour of discontinuously yielding materials in pure bending and in calculating bend force and springback values. If a low value of σ_u is used, these values will be underestimated since they depend essentially on the moment to bend the sheet.

Since the value of $(\sigma_u - \sigma_f)$ was found to control the instability of the sheet in bending, this value should be kept to a minimum in order to achieve stable bends. One way of doing this is to temper roll the material. However, if the rolled material is allowed to age, although stable bends may be made, surface markings may appear on the material surface as observed with Rimmed steel-B'. The reason why the rolled material can be bent smoothly may be due to the residual stress left in the material.

The value of Lüder's strain does not indicate whether kinking will occur. This can be seen from a comparison of the values from Mild and aged Rimmed-C steels. For mild steel, ε_L is about 1.8% and kinking occurs, whereas Rimmed steel-C has a value greater than 6% and the material shows no instability. However, an examination of the experimental moment-curvature results for the aged material shows that there is not a large increase in bending moment after the elastic limit. This may be an indication that the material is almost at the point of kinking.

The comparison of results from Model I with the results obtained from the stress distributions suggested by Robertson and Cook, Muir and Binnie, Prager and Nadai are shown in Figures 6.8(a) and (b) for two materials. These are Rimmed steel-A, aged at 100^{O}C for 1 hour and Rimmed steel-C in the as received condition. As already stated, aged Rimmed steel-A shows kinking whereas Rimmed steel-C does not kink.

It can be seen that only the proposed model, Model I predicts the behaviour of both materials. The model by Prager always shows instability since it is assumed that the material is either totally elastic or plastic. The models by Muir and Binnie, Robertson and Cook and Nadai do not predit any instability for the aged Rimmed steel-A since the bending moment always increases with curvature. However, of these models, the one by Robertson and Cook may predict instability if the value of $(\sigma_u - \sigma_L)$ is large enough. From all the tests that show kinking, this value was not large enough for the Robertson and Cook model to predict kinking.

For Rimmed steel-C, the curves from Robertson and Gook's model and Model I are comparable since there is not much difference between the calculated flow stress value and the value of the lower yield stress. In this case, the model by Robertson and Cook will show good agreement with experimental results.

Therefore, from the comparison of theoretical results and on the basis of good agreement of results from Model I with experimental observations for all tests, Model I seems to be better in predicting the behaviour of discontinuously yielding materials in pure bending.

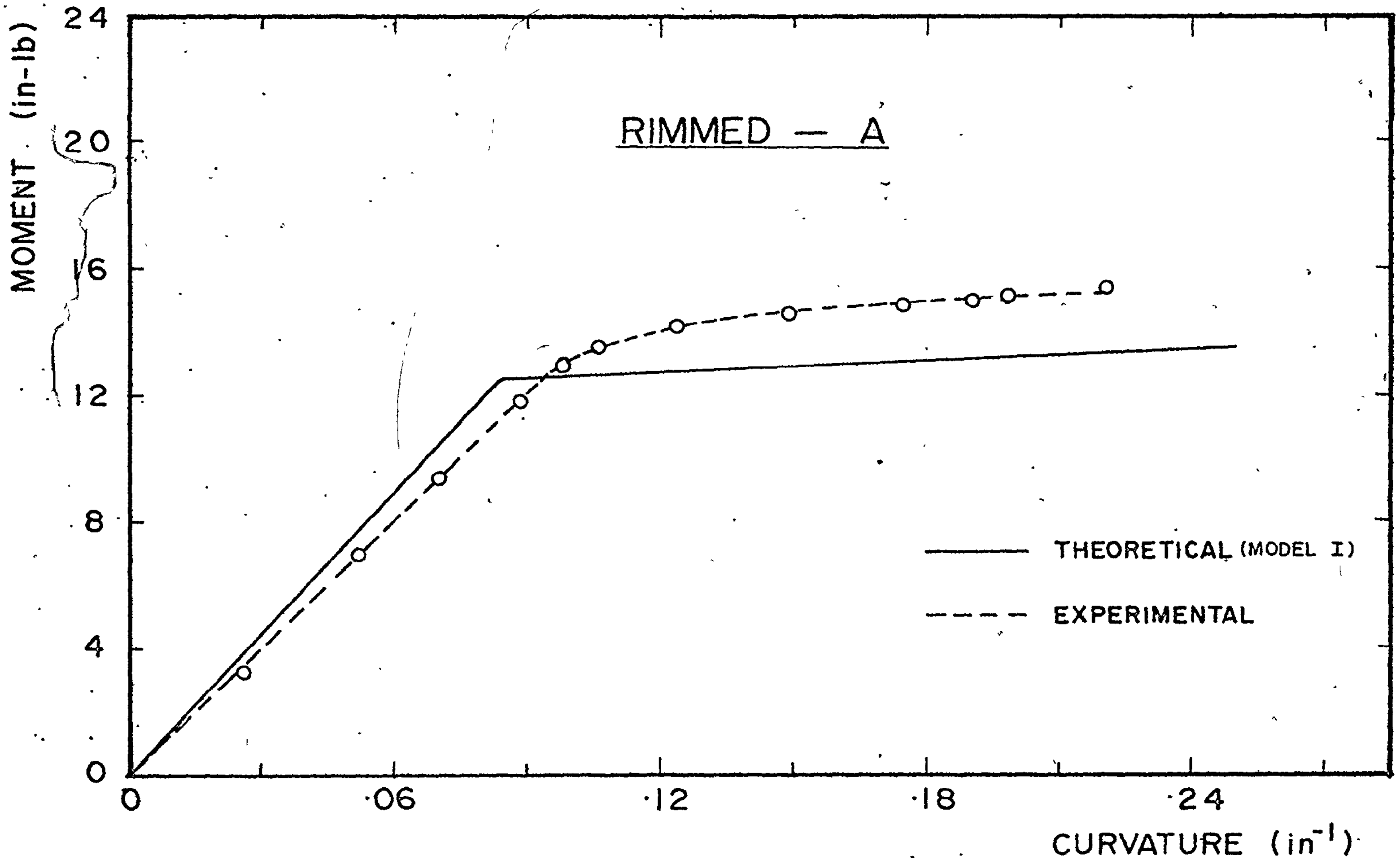

Fig. 6.6(a) - Comparison of experimental moment-curvature results with the theoretical curve from Model I for Rimmed steel-A in the as received condition

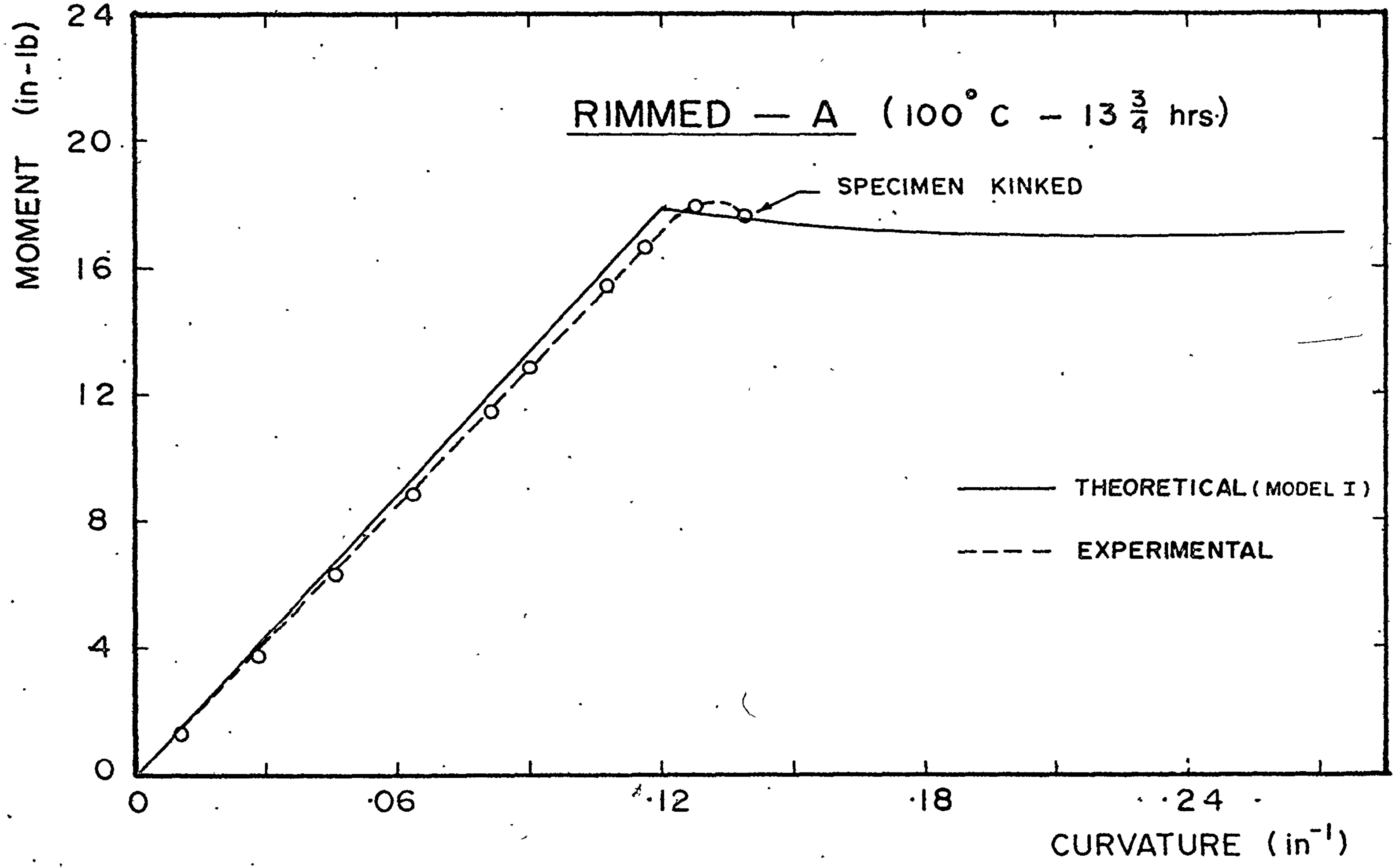

Fig. 6.6(b) - Comparison of experimental moment-curvature results with the theoretical curve from Model I for Rimmed steel-A, aged at 100°C for 13.75 hours

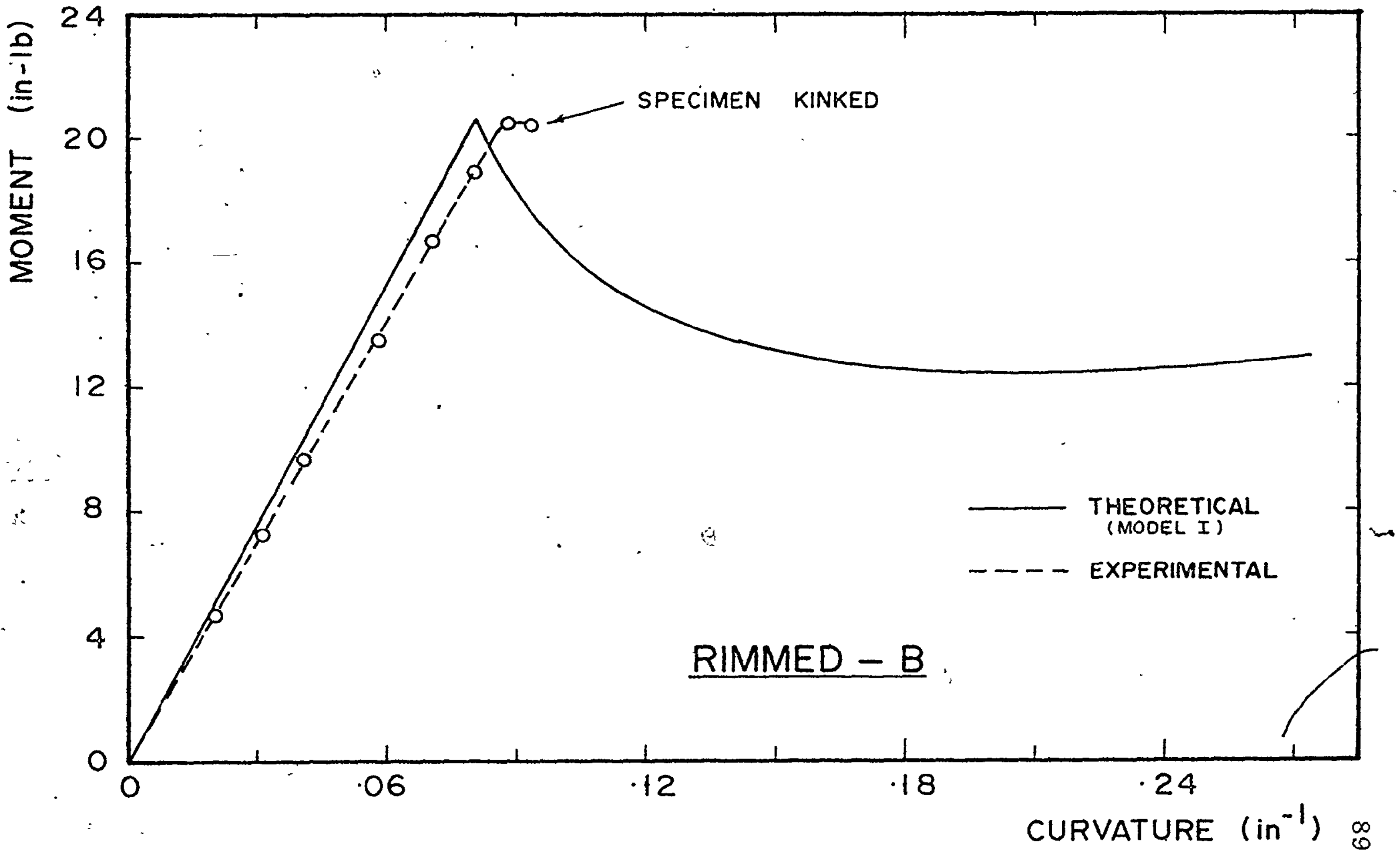

Fig. 6.6(c) - Comparison of experimental moment-curvature results with the theoretical curve from Model I for Rimmed steel-B, in the as received condition

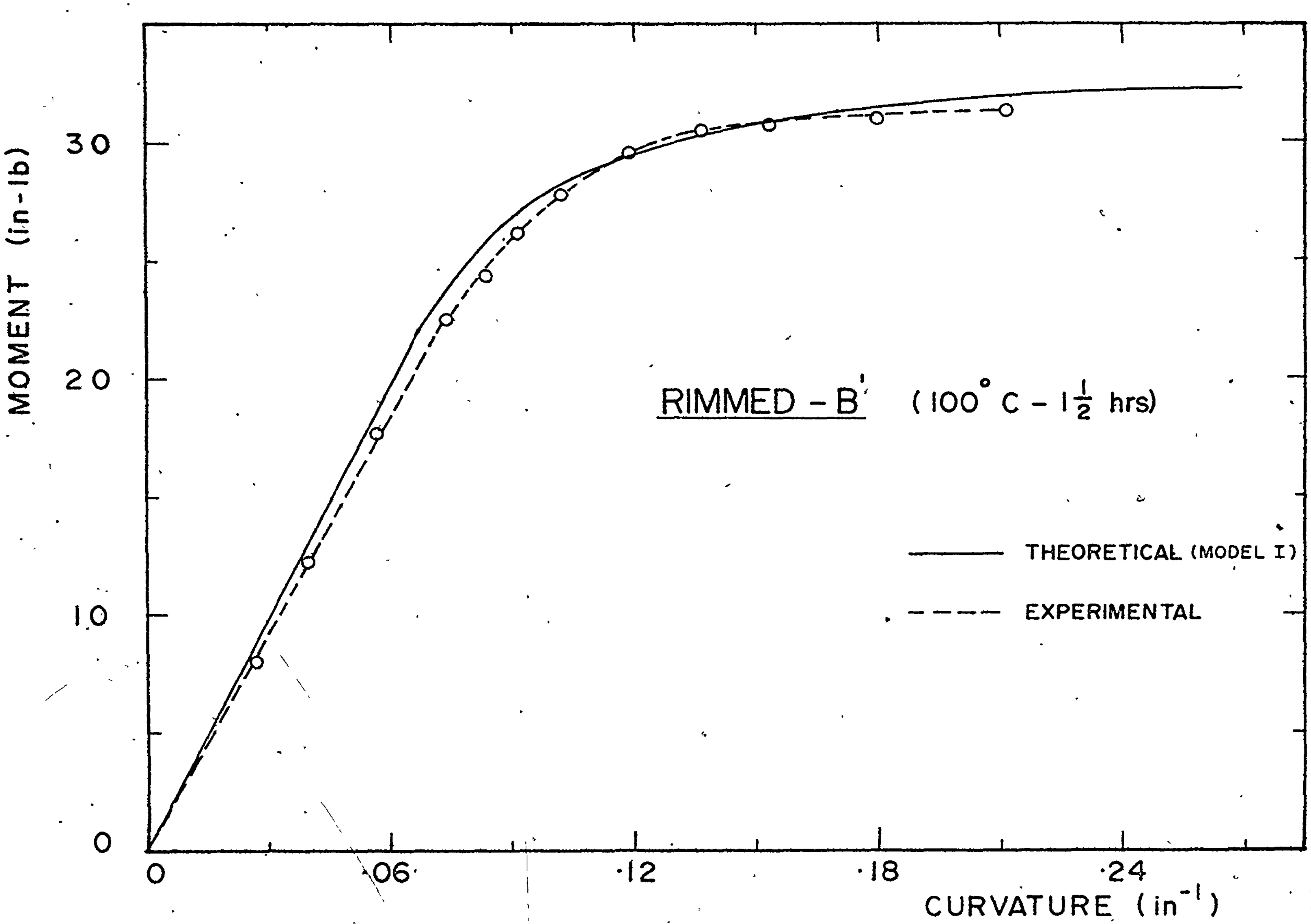

Fig. 6.6(d) - Comparison of experimental moment-curvature results with the theoretical curve from Model I for Rimmed steel-B', aged at 100°C for 1.5 hours

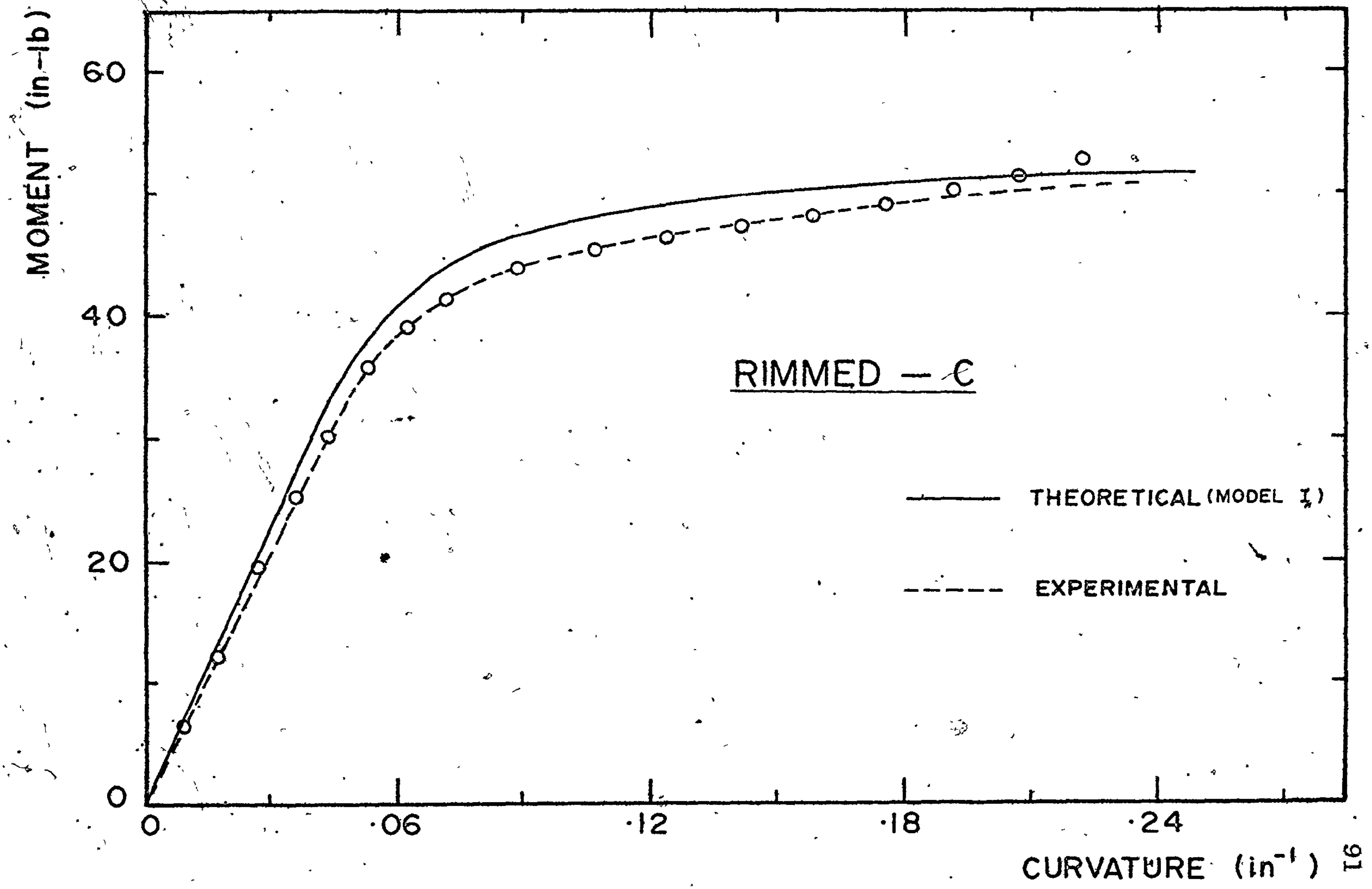

Fig. 6.6(e) - Comparison of experimental moment-curvature results with the theoretical curve from Model I for Rimmed steel-C in the as received condition

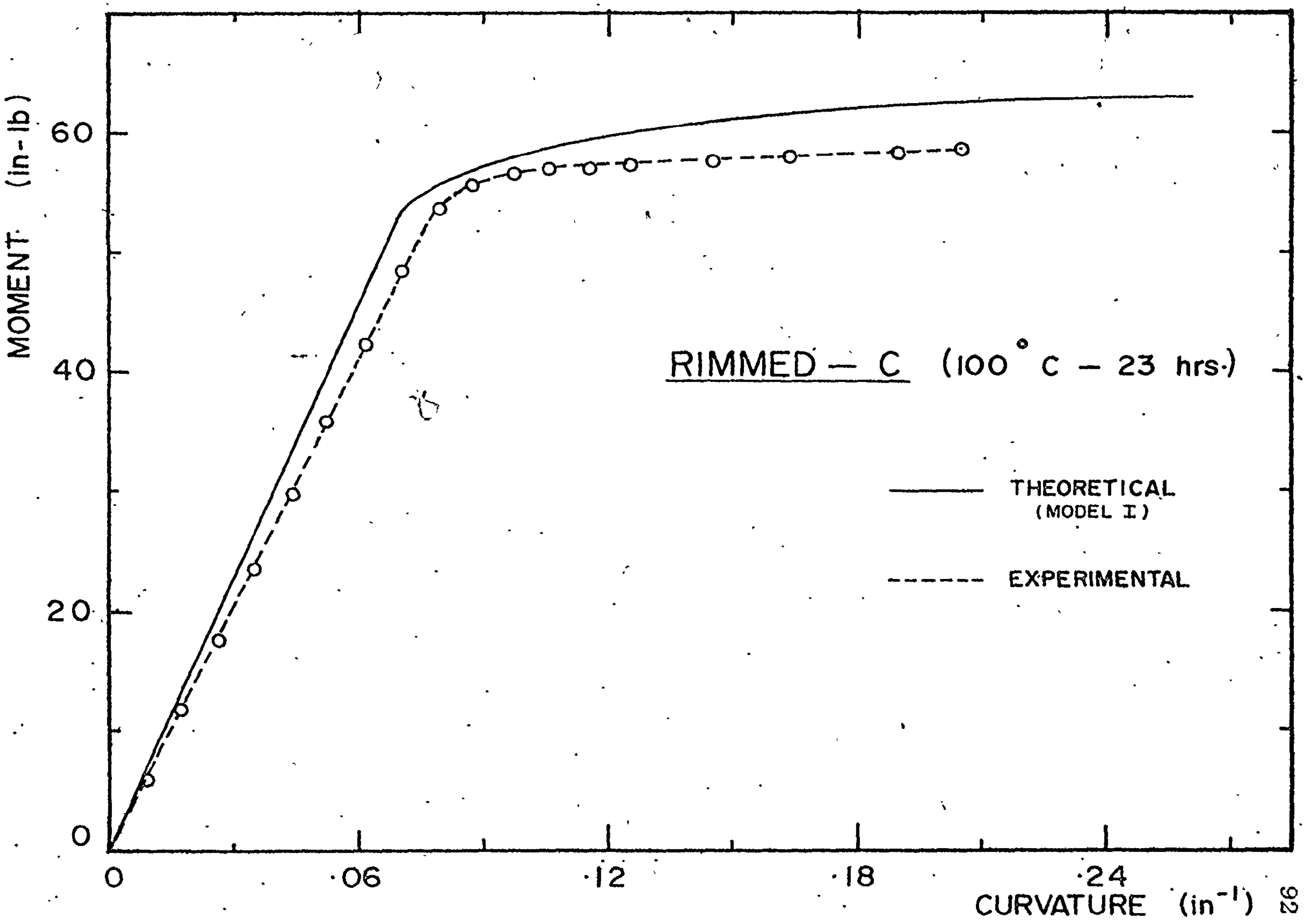

Fig. 6.6(f) - Comparison of experimental moment-curvature results with the theoretical curve from Model I for Rimmed steel-C, aged at 100°C for 23 hours

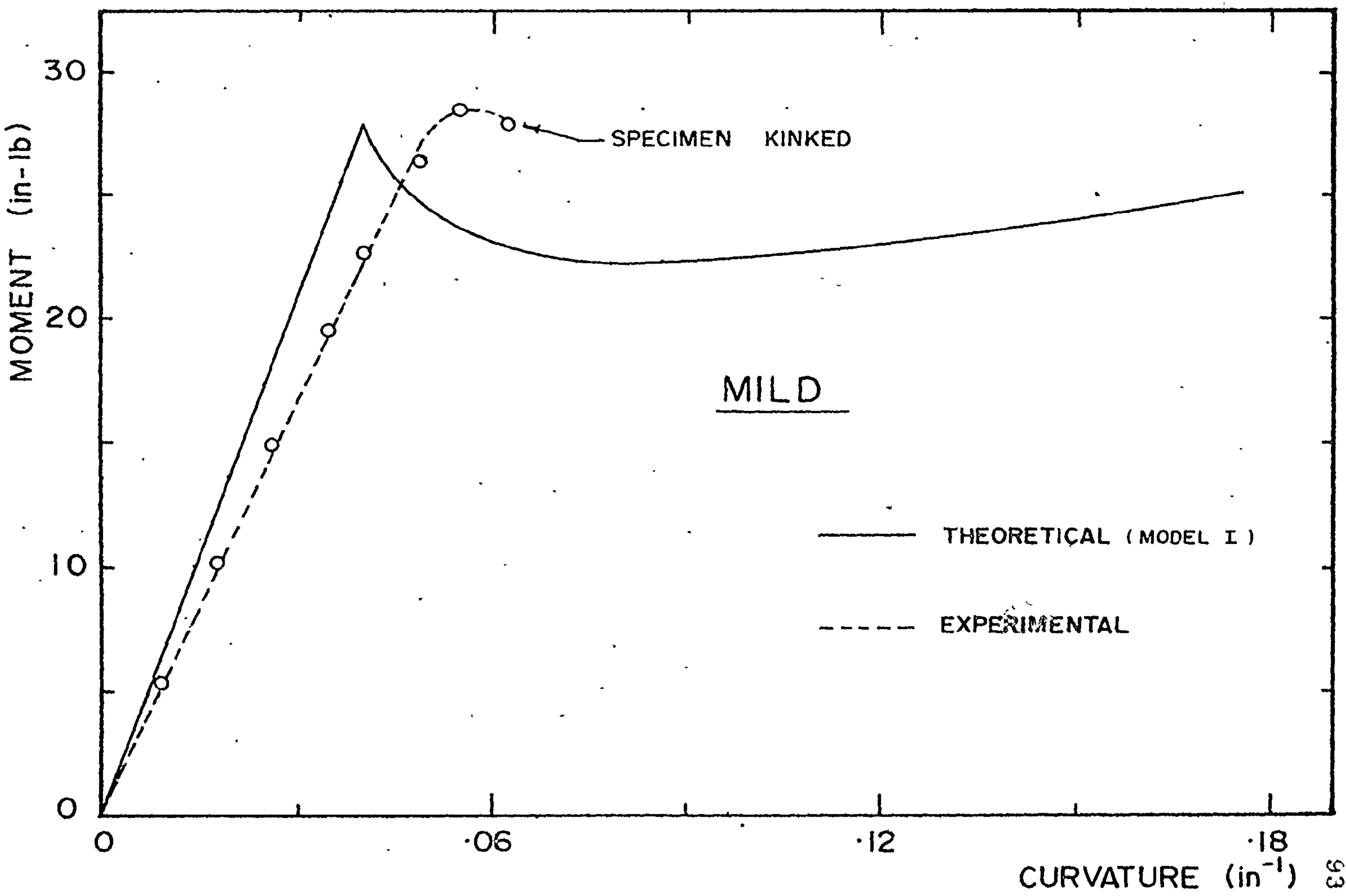

Fig. 6.6(g) - Comparison of experimental moment-curvature results with the theoretical curve from Model I for Mild steel in the as received condition

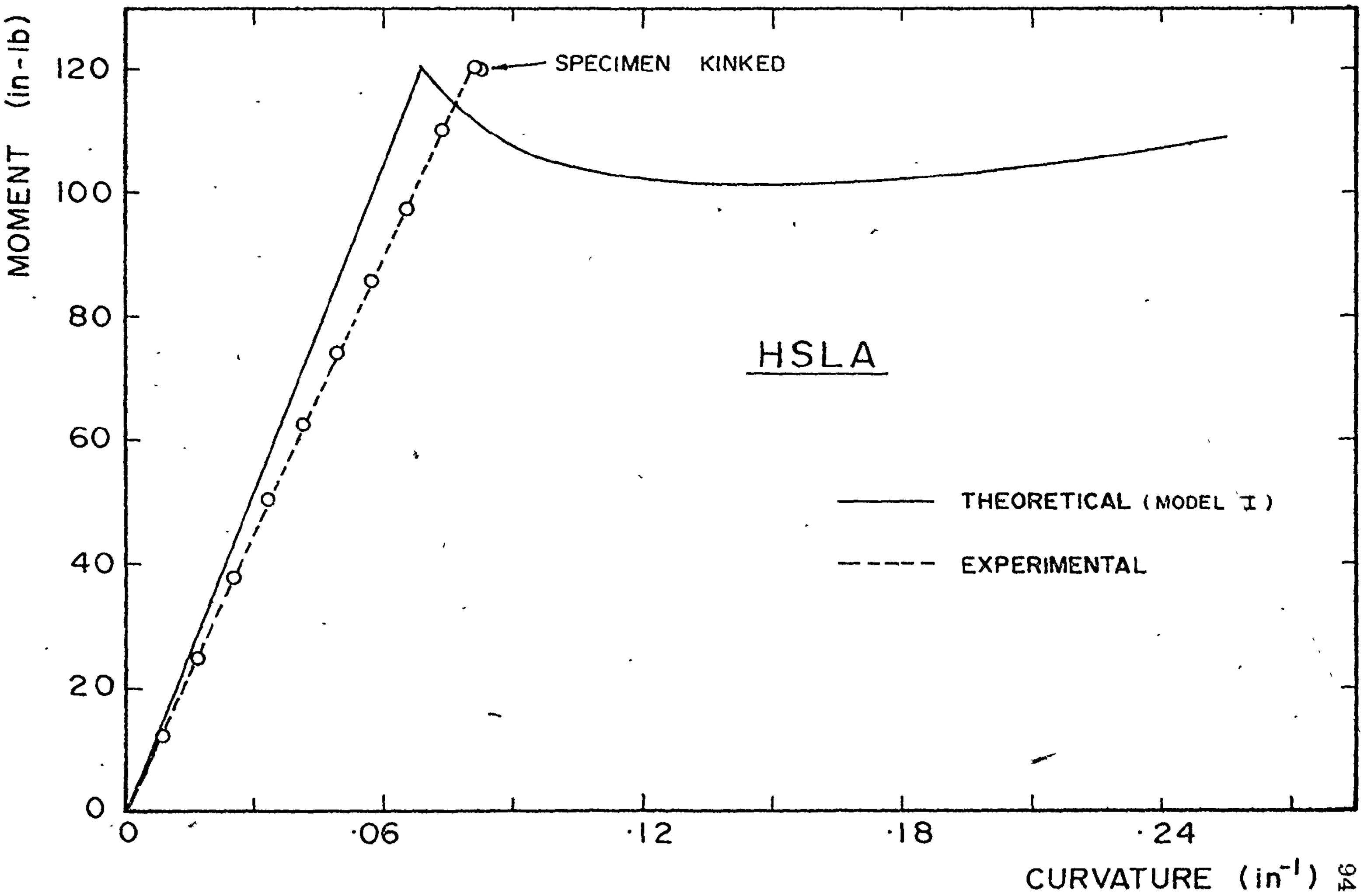

Fig. 6.6(h) - Comparison of experimental moment-curvature results with the theoretical curve from Model I for HSLA steel in the as received condition

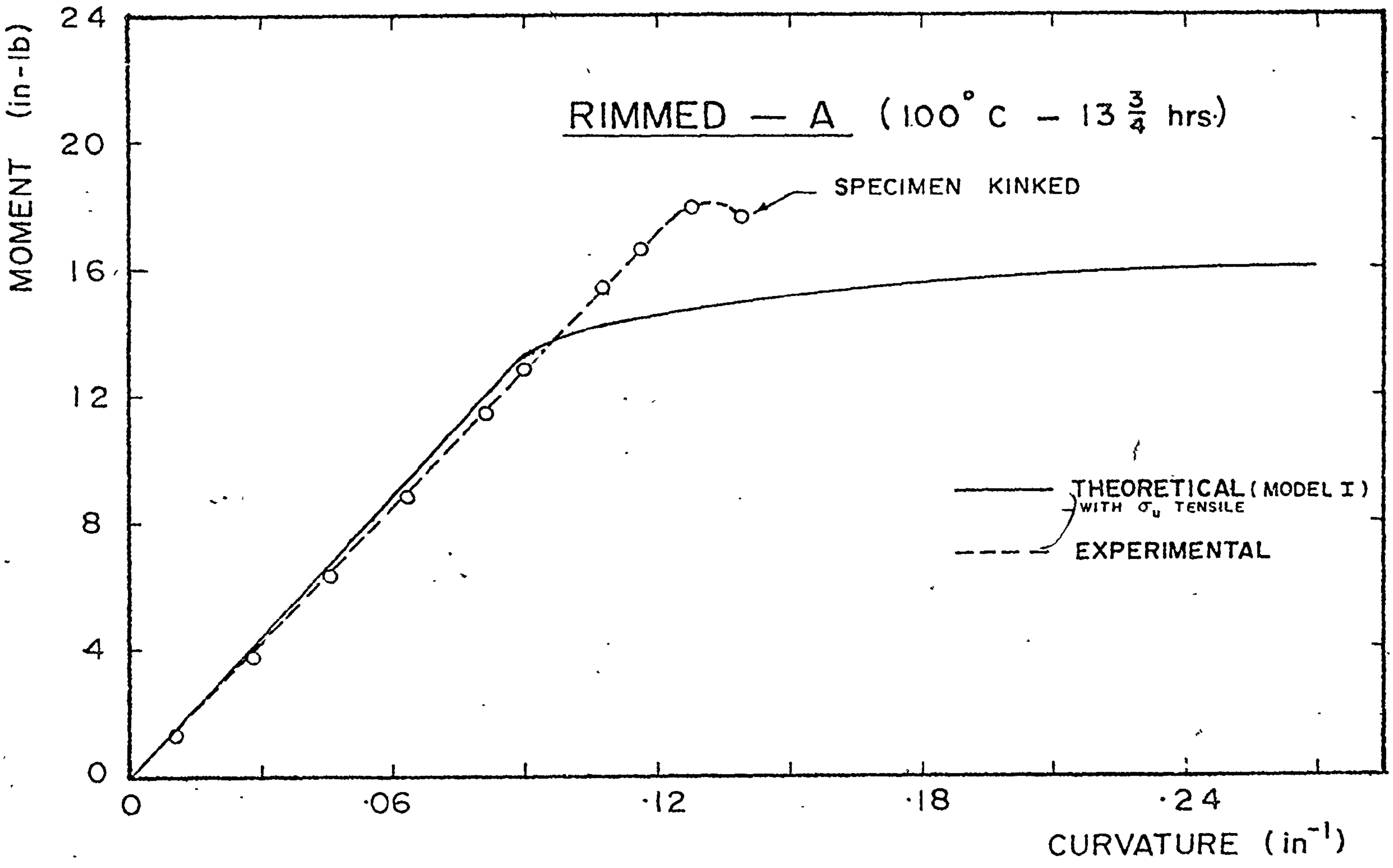

Fig. 6.7 - Comparison of experimental moment-curvature results with the theoretical curve from Model I, (using the experimental tensile upper yield stress value) for Rimmed steel-A, aged at 100°C for 13.75 hours

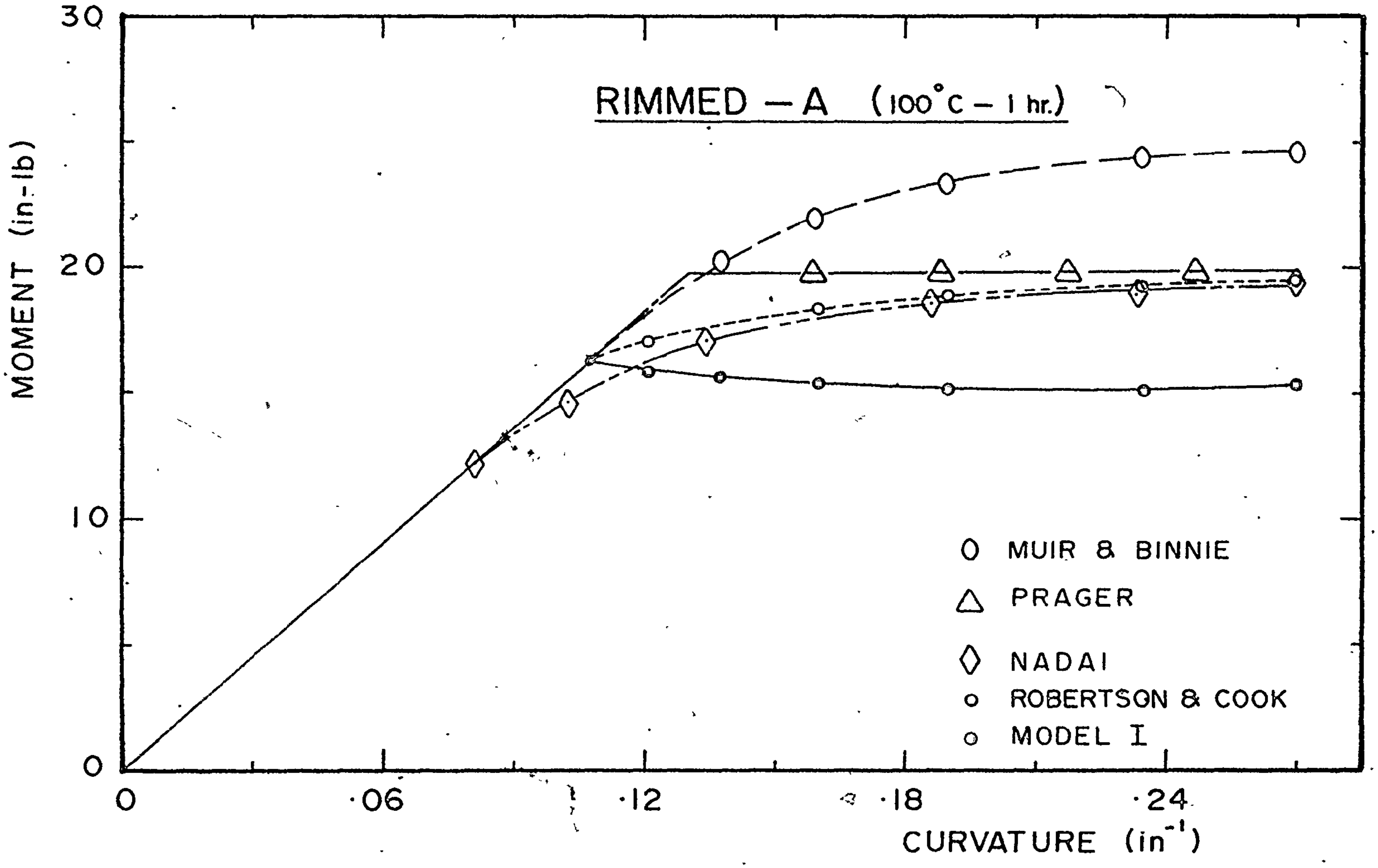

Fig. 6.8(a) - Comparison of theoretical curve from Model I with the curves from previous models for Rimmed steel-A, aged at 100°C for 1 hour

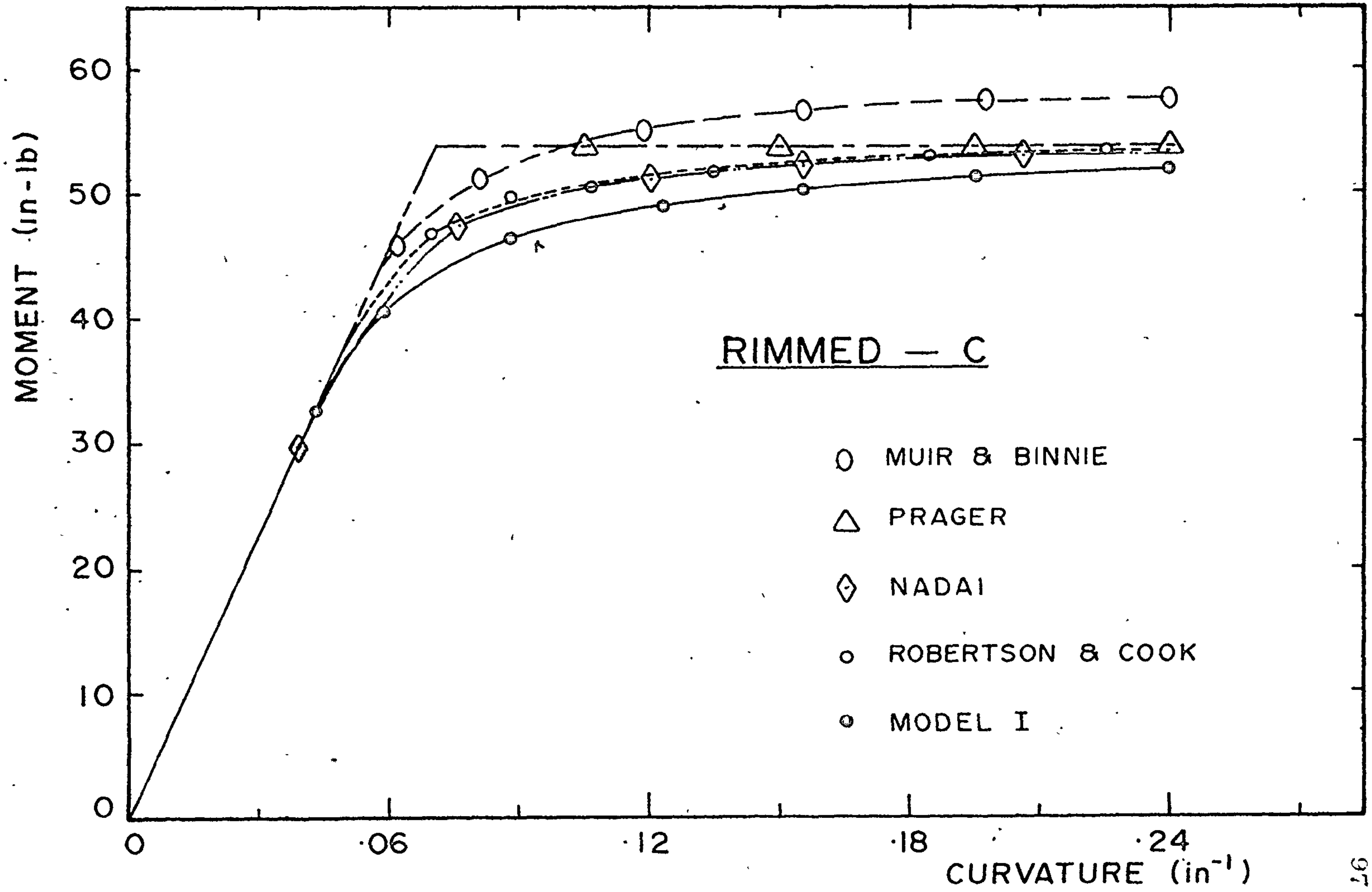

Fig. 6.8(b) - Comparison of theoretical curve from Model I with the curves from previous models for Rimmed steel-C in the as received condition

CHAPTER VII

CONCLUSIONS AND SUGGESTIONS

7.1 Conclusions

This work has been concerned with the behaviour of sheet steels which show discontinuity in elastic-plastic bending. Extensive experiments have been performed on five samples of steels and based on the experimental results obtained, the following conclusions can be made:

a) Of the two models suggested, Model I was found to be more plausible. The comparison of experimental and theoretical results from this model were in good agreement for all tests in that kinking or smooth bending in the bend test were invariably predicted correctly by this model.

b) The models suggested by previous investigators do not agree with experimental results.

c) The magnitude of the uniaxial tensile upper yield stress calculated from the bend test was in almost all cases greater than that obtained from the tensile test. This indicates that a more reliable test for determining the value of the true upper yield stress should be a pure bend test instead of the tensile test which is now being used.

d) The magnitude of the Lüder's strain does not determine whether the material can be bent smoothly or not.

e) The material parameter that was found to govern whether kinking will occur was the magnitude of ($\sigma_u - \sigma_f$). If this value was kept to a minimum, the material may be bent in a stable manner. One way of achieving this was by temper rolling the sheet. However, for one material, when this was done, surface markings appeared on both surfaces of the bent specimen. This effect could not be predicted from Model I.

7.2 Suggestions for Further Work

The experimental investigation carried out in this work has been limited to low carbon sheet steels, tested at a constant strain rate. To determine whether the proposed model truly predicts the behaviour of other discontinuously yielding materials, it is suggested that tests be performed on a wider range of materials and in different thicknesses to determine the effect of specimen geometry (b/t) on the material behaviour. Also, tests should be performed at different strain rates to see what effect this has on the behaviour of the material and the model.

APPENDIX A

CORRECTION TO THEORETICAL BENDING MOMENT FOR PLANE STRAIN BENDING

A.1 When Material is Totally Elastic

From the theory of elasticity, the relationship between stress and strain for the co-ordinate system shown in Figure A.1 is:

$$\begin{aligned} \varepsilon_x &= \frac{1}{E}\left[\sigma_x - \nu\,(\sigma_y + \sigma_z)\right] \\ \varepsilon_y &= \frac{1}{E}\left[\sigma_y - \nu\,(\sigma_z + \sigma_x)\right] \qquad \text{(A-1)} \\ \varepsilon_z &= \frac{1}{E}\left[\sigma_z - \nu\,(\sigma_x + \sigma_y)\right] \end{aligned}$$

where E = Young's modulus of elasticity

ν = Poisson's ratio

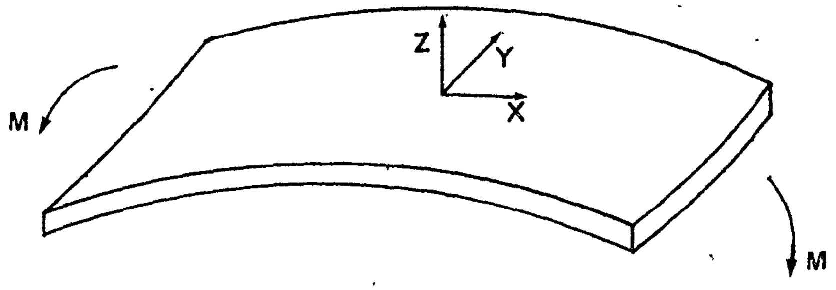

Fig. A.1 - Illustration of a beam in bending with the co-ordinate system used in the theoretical analysis.

For plane strain bending,

$$\varepsilon_y = 0 \qquad \text{and} \qquad \sigma_z = 0 \tag{A-2}$$

Therefore, equation (A-1) becomes:

$$\begin{aligned} \varepsilon_x &= \frac{1}{E}\left[\sigma_x - \nu\,\sigma_y\right] \\ \varepsilon_y &= 0 = \frac{1}{E}\left[\sigma_y - \nu\,\sigma_x\right] \\ \varepsilon_z &= \frac{1}{E}\left[-\nu\,(\sigma_x + \sigma_y)\right] \end{aligned} \tag{A-3}$$

Now, for a specimen subjected to a bending moment, M and at a radius of curvature R, the strain in the X-direction is given by:

$$\varepsilon_x = \frac{y}{R} \tag{A-4}$$

where y is the distance from the neutral axis.

Denoting the plane strain stress in the x-direction as σ_x^1, equation (A-3) gives:

$$\sigma_y = \nu \sigma_x^1 \tag{A-5}$$

and $$\sigma_x^1 = \frac{Ey}{R} + \nu \sigma_y \tag{A-6}$$

Substituting for σ_y in eqn. (A-6) and simplifying,

$$\sigma_x^1 = \frac{Ey}{R} \left(\frac{1}{1 - \nu^2} \right) \tag{A-7}$$

Now, from a tensile test in the elastic region, the material obeys Hooke's law and the tensile stress is given by:

$$\sigma_x = E\varepsilon = E \frac{y}{R} \tag{A-8}$$

Therefore, $$\sigma_x^1 = \left(\frac{1}{1 - \nu^2} \right) \cdot \sigma_x \tag{A-9}$$

Equation (A-9) is the relationship between the plane strain and uniaxial tensile stresses when anticlastic curvature is not allowed to take place.

However in bending of thin specimens, the anticlastic curvature is not completely neutralized and a correction has to be made to account for this. The anticlastic curvature gives rise to the distortion of the specimen as illustrated in an exaggerated manner in Figure A.2. R_2 is the anticlastic curvature and is a function of the ratio of (b/t) and the principal radius of curvature, R_1.

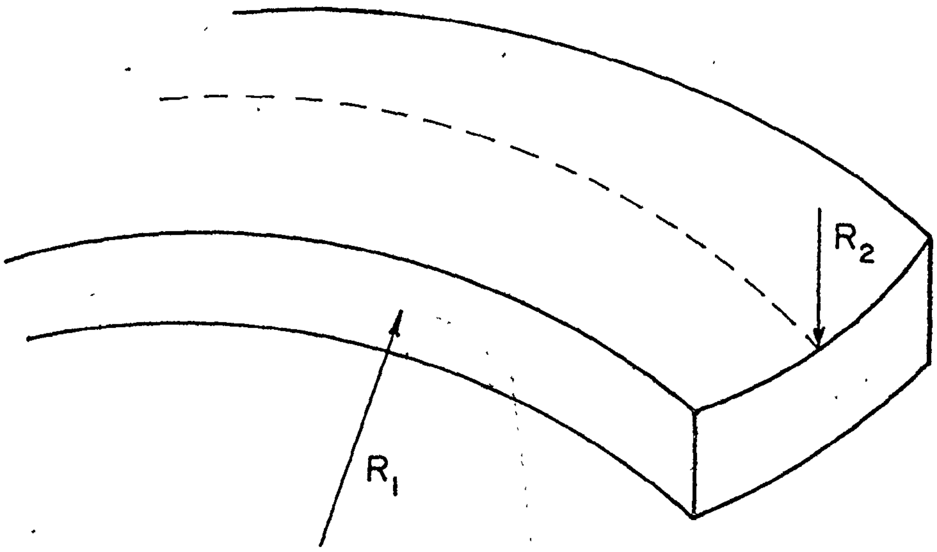

Fig. A.2 - Illustration of anticlastic curvature in a specimen with rectangular cross-section

The theory to account for anticlastic curvature in a rectangular specimen was developed by Ashwell [46] and for purely elastic bending,

$$M_{PSE} = M_E * \phi \qquad \text{(A-10)}$$

where M_{PSE} is the plane strain elastic component of bending moment, M_E is the uniaxial elastic component of bending moment and ϕ is the correction factor to account for anticlastic curvature.

According to Ashwell,

$$\phi = \frac{1}{1 - \nu^2} + \frac{3}{\alpha b} f(\alpha b) - \frac{2\sqrt{3}\,\nu}{b\sqrt{1 - \nu^2}} F(\alpha b) \qquad \text{(A-11)}$$

where:

$$\alpha b = \sqrt{\frac{3(1 - \nu^2) \cdot b}{Rt}}$$

$$f(\alpha b) = 2(B^2 + C^2)(\text{Sinh}\,\alpha b + \text{Sin}\,\alpha b) + (B^2 - C^2 + 2BC)\,\text{Cosh}\,\alpha b$$

$$\text{Sin}\,\alpha b + (B^2 + C^2 - 2BC)\,\text{Sinh}\,\alpha b\,\text{Cos}\,\alpha b + 2(B^2 - C^2)\,\alpha b$$

$$F(\alpha b) = (B + C)\,\text{Sinh}(\alpha b/2)\,\text{Cos}(\alpha b/2) - (B - C)\,\text{Cosh}(\alpha b/2)$$

$$\text{Sin}(\alpha b/2)$$

$$B = \frac{\nu}{\sqrt{3(1-\nu^2)}} \quad \frac{\sinh(\alpha b/2)\cos(\alpha b/2) - \cosh(\alpha b/2)\sin(\alpha b/2)}{\sinh \alpha b + \sin \alpha b}$$

$$C = \frac{\nu}{\sqrt{3(1-\nu^2)}} \quad \frac{\sinh(\alpha b/2)\cos(\alpha b/2) + \cosh(\alpha b/2)\sin(\alpha b/2)}{\sinh \alpha b + \sin \alpha b}$$

(A-12)

A.2 When Material is Totally Plastic

The plane strain correction factor to the theoretical bending moment when the material is totally plastic can be determined from the equivalent stresses in uniaxial tension and plane strain.

Using Hill's theory for anisotropy [47], the equivalent stress is given by:

$$\bar{\sigma} = \sqrt{\frac{3}{2}} \left[\frac{F(\sigma_y - \sigma_z)^2 + G(\sigma_z - \sigma_x)^2 + H(\sigma_x - \sigma_y)^2 + 2L\tau_{yz}^2 + 2M\tau_{zx}^2 + 2N\tau_{xy}^2}{F + G + H} \right]^{1/2}$$

(A-13)

where F, G, H, L, M, and N are constants.

Also, the components of plastic strain increments are:

$$d\varepsilon_x^p = d\lambda\,[H(\sigma_x - \sigma_y) + G(\sigma_x - \sigma_z)]$$

$$d\varepsilon_y^p = d\lambda\,[F(\sigma_y - \sigma_z) + H(\sigma_y - \sigma_x)] \qquad \text{(A-14)}$$

$$d\varepsilon_z^p = d\lambda\,[G(\sigma_z - \sigma_x) + F(\sigma_z - \sigma_y)]$$

For a specimen in pure tension with the co-ordinate system shown below,

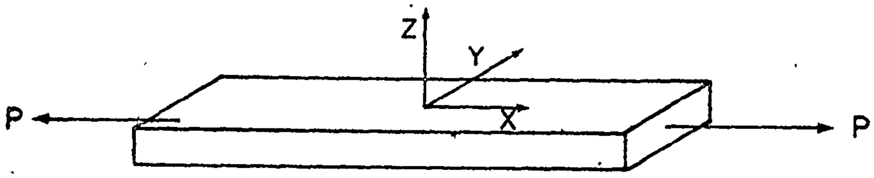

$$\sigma_y = \sigma_z = 0$$

and $$\tau_{xy} = \tau_{yz} = \tau_{zx} = 0 \qquad \text{(A-15)}$$

Substituting in equation (A-13) and simplifying,

$$\bar{\sigma} = \sqrt{\frac{3}{2}} \left[\frac{1 + H/G}{1 + F/G + H/G}\right]^{1/2} \cdot \sigma_x \qquad \text{(A-16)}$$

For a specimen cut in the x-direction of anistropy and pulled in pure tension,

$$d\varepsilon_x^{\,p} : d\varepsilon_y^{\,p} : d\varepsilon_z^{\,p} = (G + H) : -H : -G \qquad \text{(A-17)}$$

Now, the value of anistropy in the x-direction is:

$$r_x = \frac{d\varepsilon_y^{\,p}}{d\varepsilon_z^{\,p}} = \frac{H}{G} \qquad \text{(A-18)}$$

Similarly, for a specimen cut in the y-direction of anisotropy,

$$d\varepsilon_x^p : d\varepsilon_y^p : d\varepsilon_z^p = -H : (F + H) : F \qquad (A\text{-}19)$$

Therefore, $$r_y = \frac{d\varepsilon_x^p}{d\varepsilon_z^p} = \frac{H}{F} \qquad (A\text{-}20)$$

Re-writing equation (A-16), the equivalent stress for a specimen in pure tension is:

$$\bar{\sigma} = \sqrt{\frac{3}{2}} \left[\frac{1 + r_x}{1 + \frac{r_x}{r_y} + r_x} \right]^{1/2} \cdot \sigma_x \qquad (A\text{-}21)$$

For a specimen in plane strain bending as in Figure A.1,

$$\begin{aligned} \varepsilon_y^p &= 0 \\ \sigma_z &= 0 \end{aligned} \qquad (A\text{-}22)$$

and $$\tau_{xy} = \tau_{yz} = \tau_{zx} = 0$$

Since $\varepsilon_y^p = 0$, $d\varepsilon_y^p = 0$ also

Therefore, from equation (A-14),

$$\sigma_y = \frac{H}{(F + H)} \cdot \sigma_x^1 \tag{A-23}$$

Substituting for σ_y in equation (A-13), and simplifying,

$$\bar{\sigma} = \sqrt{\frac{3}{2}} \left[\frac{1 + H/G + H/F}{(1 + G/F + H/F)\ (F/G + H/G)} \right]^{1/2} \cdot \sigma_x^1 \tag{A-24}$$

Substituting for the r-values,

$$\bar{\sigma} = \sqrt{\frac{3}{2}} \left[\frac{1 + r_x + r_y}{\left(1 + \frac{r_y}{r_x} + r_y\right) \left(r_x + \frac{r_x}{r_y}\right)} \right]^{1/2} \cdot \sigma_x^1 \tag{A-25}$$

Comparing equations (A-21) and (A-25),

$$\sqrt{\frac{3}{2}} \left[\frac{1 + r_x}{1 + \frac{r_x}{r_y} + r_x} \right]^{1/2} \cdot \sigma_x = \sqrt{\frac{3}{2}} \left[\frac{1 + r_x + r_y}{\left(1 + \frac{r_y}{r_x} + r_y\right) \left(r_x + \frac{r_x}{r_y}\right)} \right]^{1/2} \cdot \sigma_x^1 \tag{A-26}$$

Therefore, the relationship between plane strain and uniaxial tensile stresses in the plastic region can be denoted by:

$$\sigma_x^1 = (\text{PPSC}) \cdot \sigma_x \tag{A-27}$$

where

$$\mathrm{PPSC} = \left[\frac{1 + r_x}{\left(1 + \frac{r_x}{r_y} + r_x\right)}\right]^{1/2} \cdot \left[\frac{\left(1 + \frac{r_y}{r_x} + r_y\right)\left(r_x + \frac{r_x}{r_y}\right)}{1 + r_x + r_y}\right]^{1/2} \qquad \text{(A-28)}$$

Thus, by knowing the r-values at 0° and 90° to the rolling direction of the sheet, the plastic component of the plane strain bending moment can be determined.

APPENDIX B

CURVATURE CALIBRATION

It is assumed that the surface of the material has uniform curvature and forms an arc of a circle. From a spherometer arrangement, the radius of curvature can be obtained. The diagram below shows the geometrical configuration after some bending moment, M. The distance h is the dial gauge reading, 2a is the distance between the spherometer legs and R_o is the radius of curvature of the outer surface.

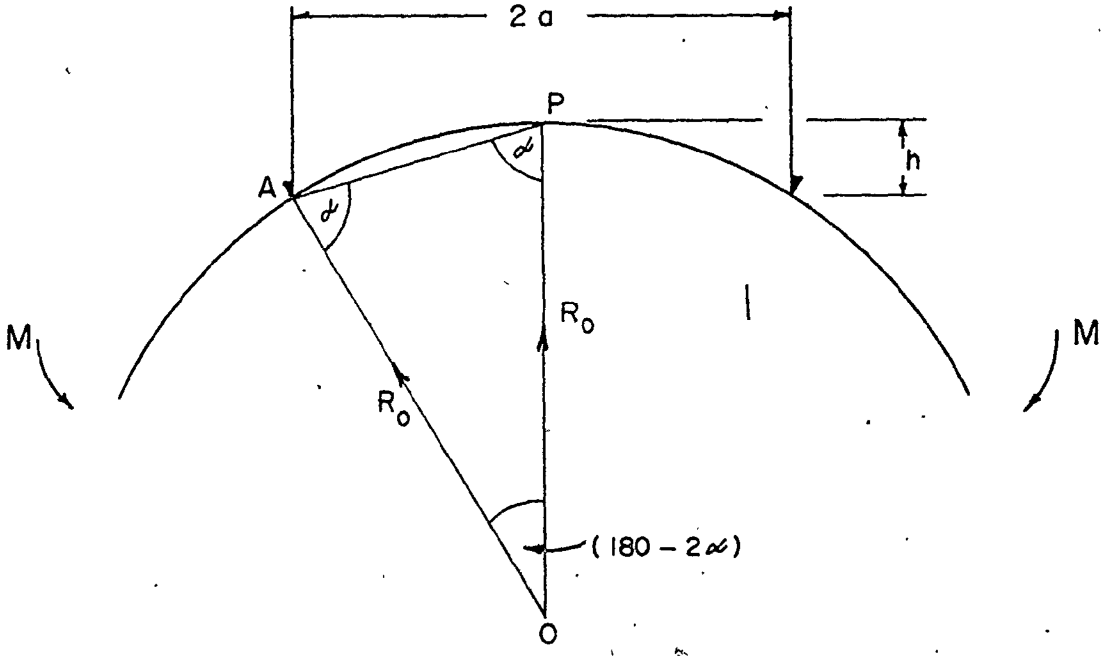

From the geometrical configuration,

$$AP = a^2 + h^2 \tag{B-1}$$

Applying the Sine Rule to triangle OAP,

$$\frac{R_o}{\text{Sin}\ \alpha} = \frac{AP}{\text{Sin}\ (180-2\alpha)} \tag{B-2}$$

Substituting for AP and simplifying,

$$R_o = \frac{a^2 + h^2}{2h} \tag{B-3}$$

Since the neutral axis is assumed to be at the centre of the testpiece, the radius of curvature at the neutral axis, R is given by:

$$R = (R_o - t/2) = \frac{a^2 + h^2}{2h} - \frac{t}{2} \tag{B-4}$$

where t is the thickness of the specimen.

The calibration data is given in Table B-1 and the calibration curve is shown in Figure B-1.

TABLE B-1 - Curvature Calibration Data

Crosshead extension (in.)	Gauge reading, h (in.)	R (in.)	1/R (in.$^{-1}$)
0.044	0.0035	64.3	0.016
0.064	0.0054	41.7	0.024
0.084	0.0075	30.0	0.033
0.104	0.0094	23.9	0.042
0.144	0.0144	15.6	0.064
0.184	0.0200	11.2	0.089
0.224	0.0245	9.2	0.109
0.264	0.0304	7.4	0.135
0.304	0.0355	6.3	0.158
0.334	0.0392	5.7	0.174
0.364	0.0430	5.2	0.191
0.404	0.0475	4.7	0.211
0.484	0.0565	4.0	0.251
0.514	0.0610	3.7	0.271
0.554	0.0643	3.5	0.285

* For the spherometer used, 2a = 1.342"

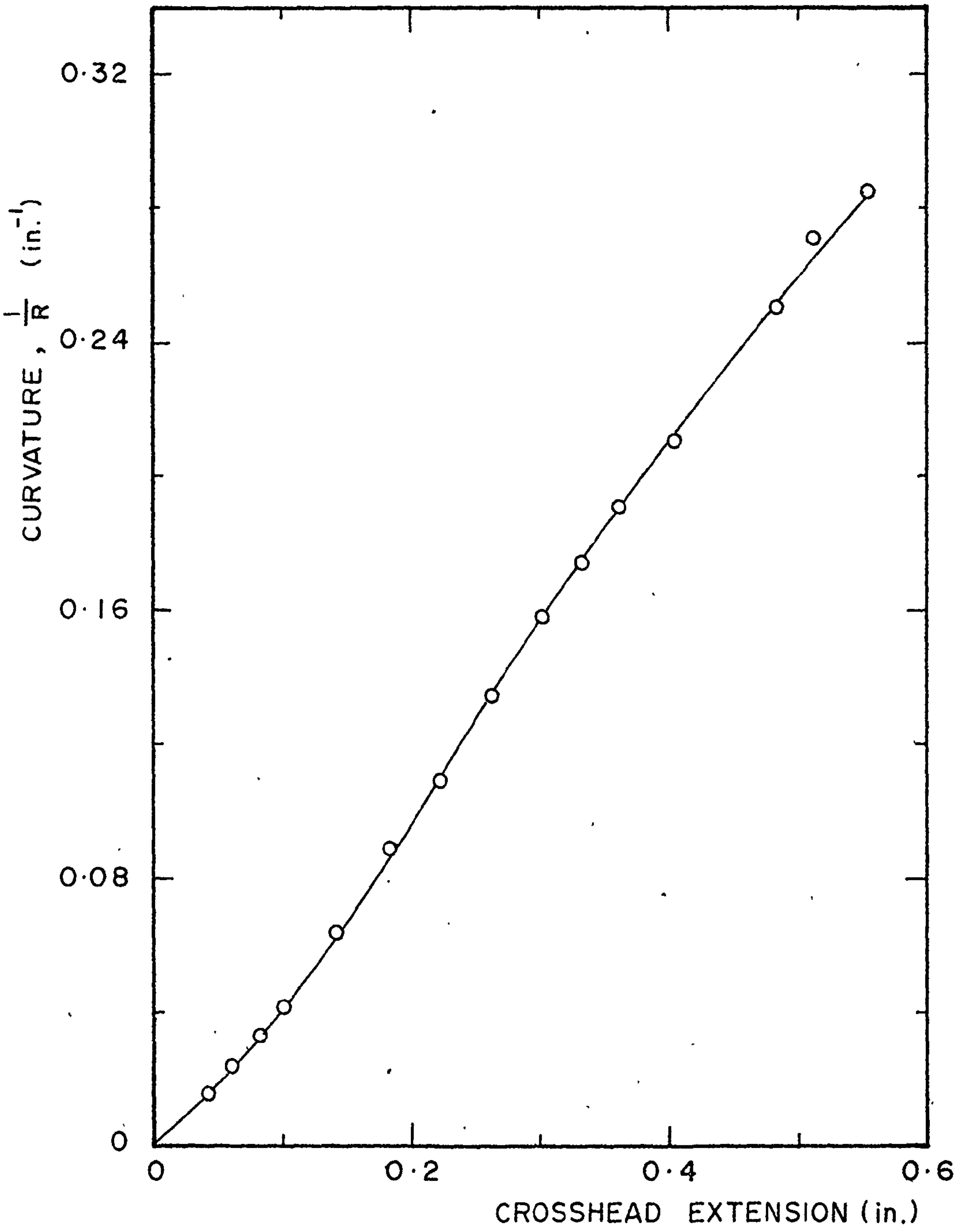

Fig. B-1 - Curvature calibration curve

APPENDIX C

PRELIMINARY EXPERIMENTS

Tensile and bend tests were performed on AKDQ steel which is a continuously yielding material and the true stress-true strain tensile curve is given in Figure C-1. Table C-1 gives the values of the material parameters and the plastic plane strain correction factor (PPSC).

Table C-1 - Material parameters for AKDQ steel

Yield stress at 0.2% strain (ksi)	K (ksi)	ε_o	n	$\bar{r}_o$	$\bar{r}_{90}$	PPSC
26.4	72.852	0.0044	0.231	1.96	2.34	1.36

Since the material is continuously yielding, the stress distribution in bending is as shown in Figure C.2 where σ_y is the yield stress at 0.2% strain.

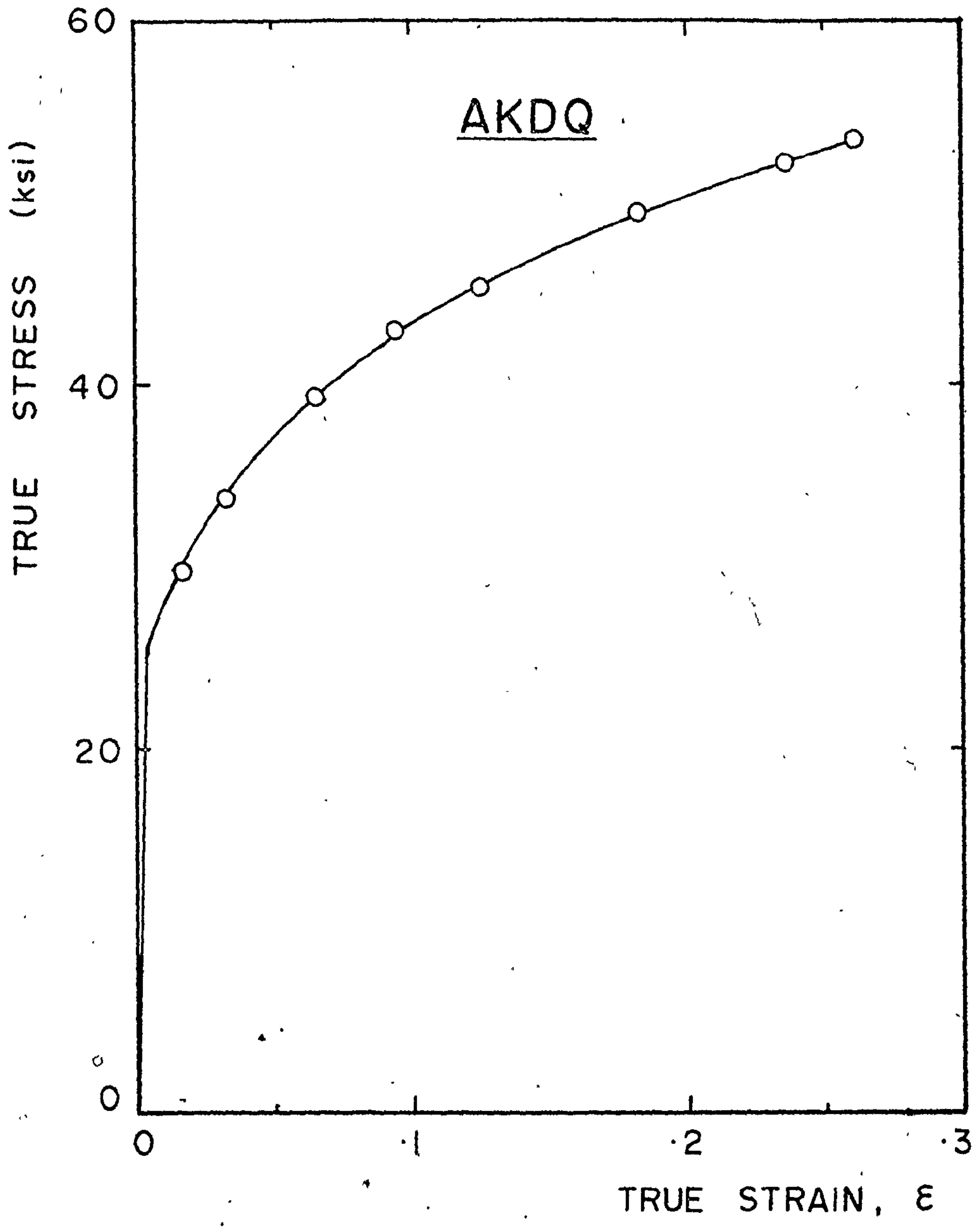

Fig. C.1 - Experimental tensile true stress-true strain diagram for AKDQ steel in the as received condition

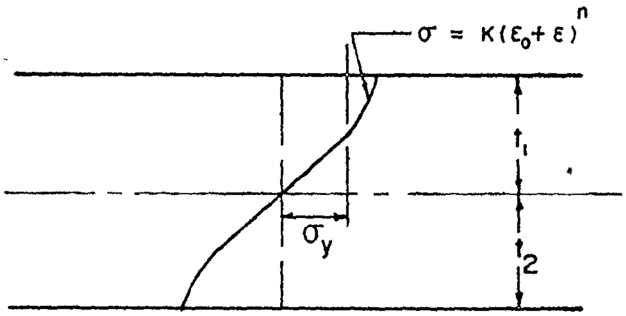

Fig. C.2 - Stress distribution for continuously yielding material in bending

Figure C.3 shows the comparison between the experimental and theoretical results.

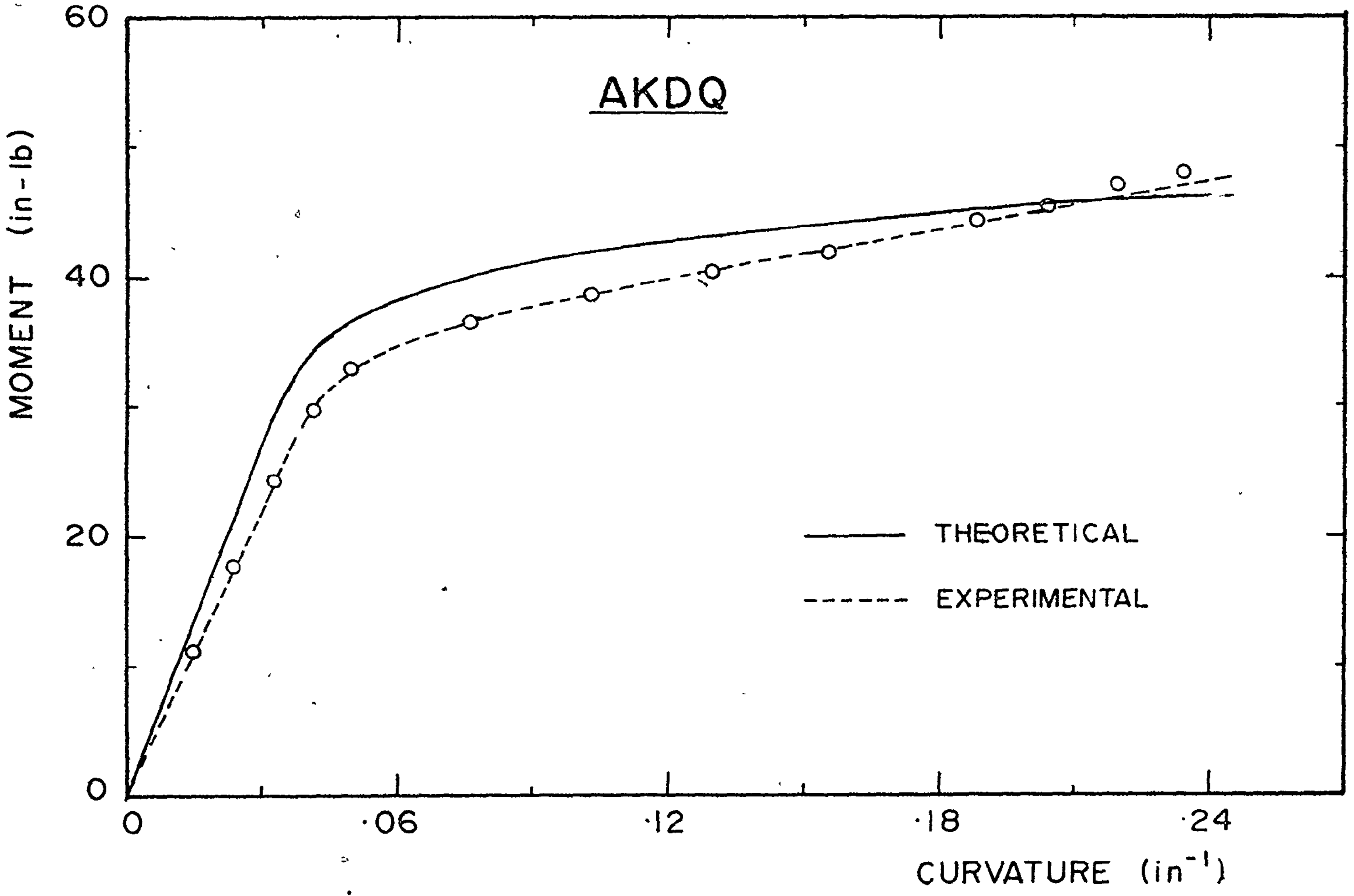

Fig. C-3 - Comparison of experimental and theoretical bending moment-curvature results for AKDQ steel

APPENDIX D

DETERMINATION OF BENDING MOMENT FROM EXPERIMENTAL DATA

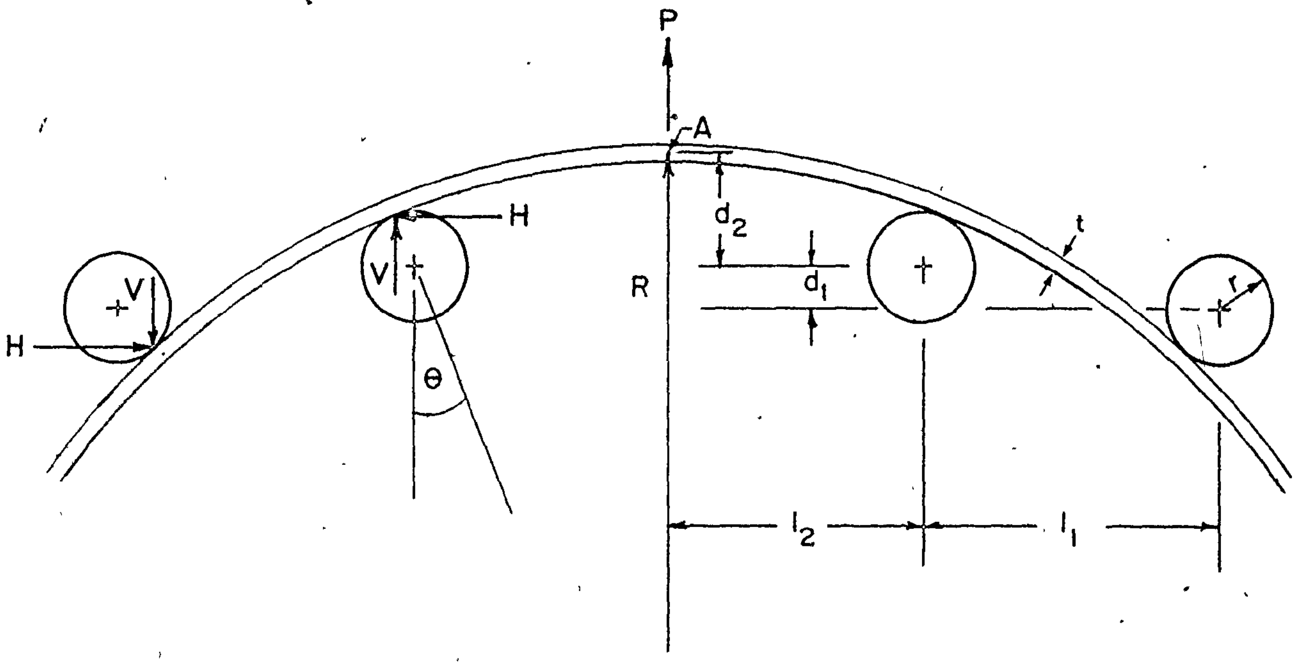

Fig. D.1 - Geometrical configuration of testpiece in bending rig

When the specimen is subjected to pure bending, it is assumed that the test section forms an arc of a circle of radius of curvature R along the neutral axis.

The geometrical configuration of the specimen in bending is as shown in Figure D.1 where:

R = radius of curvature at the neutral axis

r = radius of curvature of bending rig rollers

t = thickness of specimen

V = vertical component of force at point of contact

H = horizontal component of force at point of contact

P = load recorded on chart

The bending moment at A is given by:

$$M_A = V\,(l_1 + l_2 - r\ \mathrm{Sin}\ \theta) - V\,(l_2 + r\ \mathrm{Sin}\ \theta) + H\,(d_1 + d_2 + t/2 + r\ \mathrm{Cos}\ \theta) - H\,(d_2 + t/2 - r\ \mathrm{Cos}\ \theta) \qquad \text{(D-1)}$$

Simplifying,

$$M_A = V\,(l_1 - 2r\ \mathrm{Sin}\ \theta) + H\,(d_1 + 2r\ \mathrm{Cos}\ \theta) \qquad \text{(D-2)}$$

Now, from Figure D.1, $\theta = \mathrm{Sin}^{-1} \dfrac{l_2}{(R - r - t/2)}$ (D-3)

and from force equilibrium,

$$V = \frac{P}{2}, \qquad H = \frac{P}{2}\ \mathrm{Tan}\ \theta \qquad \text{(D-4)}$$

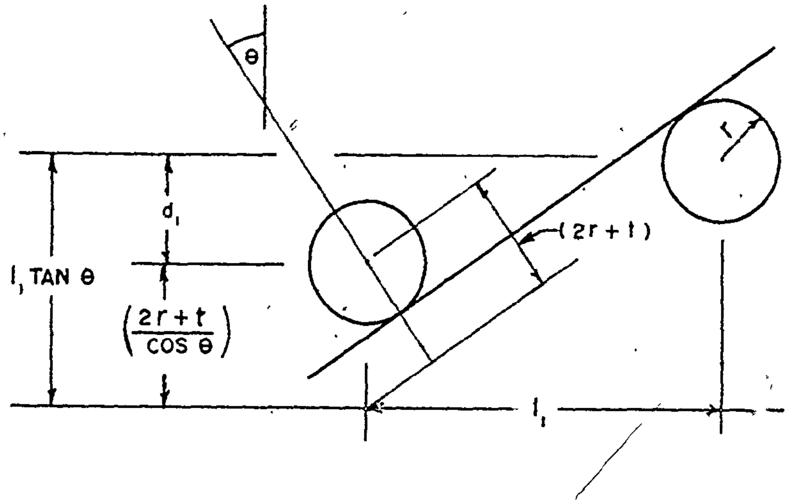

Also, from the above diagram:

$$d_1 = l_1 \operatorname{Tan} \theta - \frac{2r + t}{\operatorname{Cos} \theta} \qquad \text{(D-5)}$$

Substituting for d_1, V and H in equation (D-2) and simplifying,

$$M_A = \frac{P \{l_1 - (2r + t) \operatorname{Sin} \theta\}}{2 \operatorname{Cos}^2 \theta} \qquad \text{(D-6)}$$

Now, R is obtained from the calibration curve given in Appendix B and from equation (D-3), θ can be calculated. Hence, the bending moment can be obtained.

APPENDIX E

EXPERIMENTAL TRUE STRESS-TRUE STRAIN CURVES

Figures E.1(a) to 1(j) show the curves for Rimmed steel-A in the as received and aged conditions.

Figures E.2(a) to 2(d) show the curves for Rimmed steel-B in the as received and aged conditions.

Figures E.3(a) to 3(f) show the curves for Rimmed steel-B' in the as rolled and aged conditions.

Figures E.4(a) to 4(f) show the curves for Rimmed steel-C in the as received and aged conditions.

Figures E.5(a) to 5(e) show the curves for Mild steel in the as received and aged conditions.

Figures E.6(a) and (b) show the curves for HSLA steel in the as received and aged conditions.

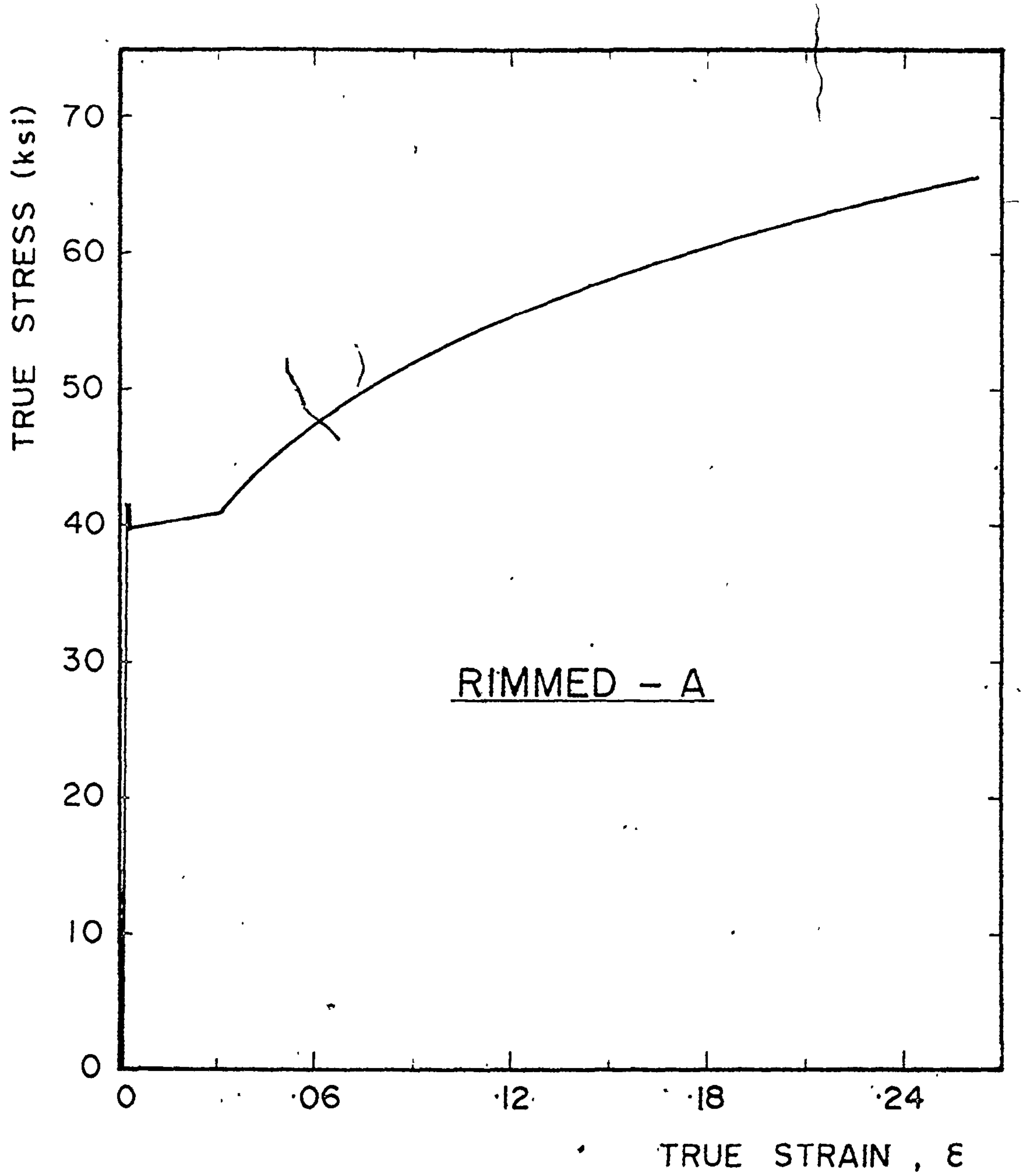

Fig. E.1(a) - Experimental tensile true stress-true strain diagram for Rimmed steel-A in the as received condition

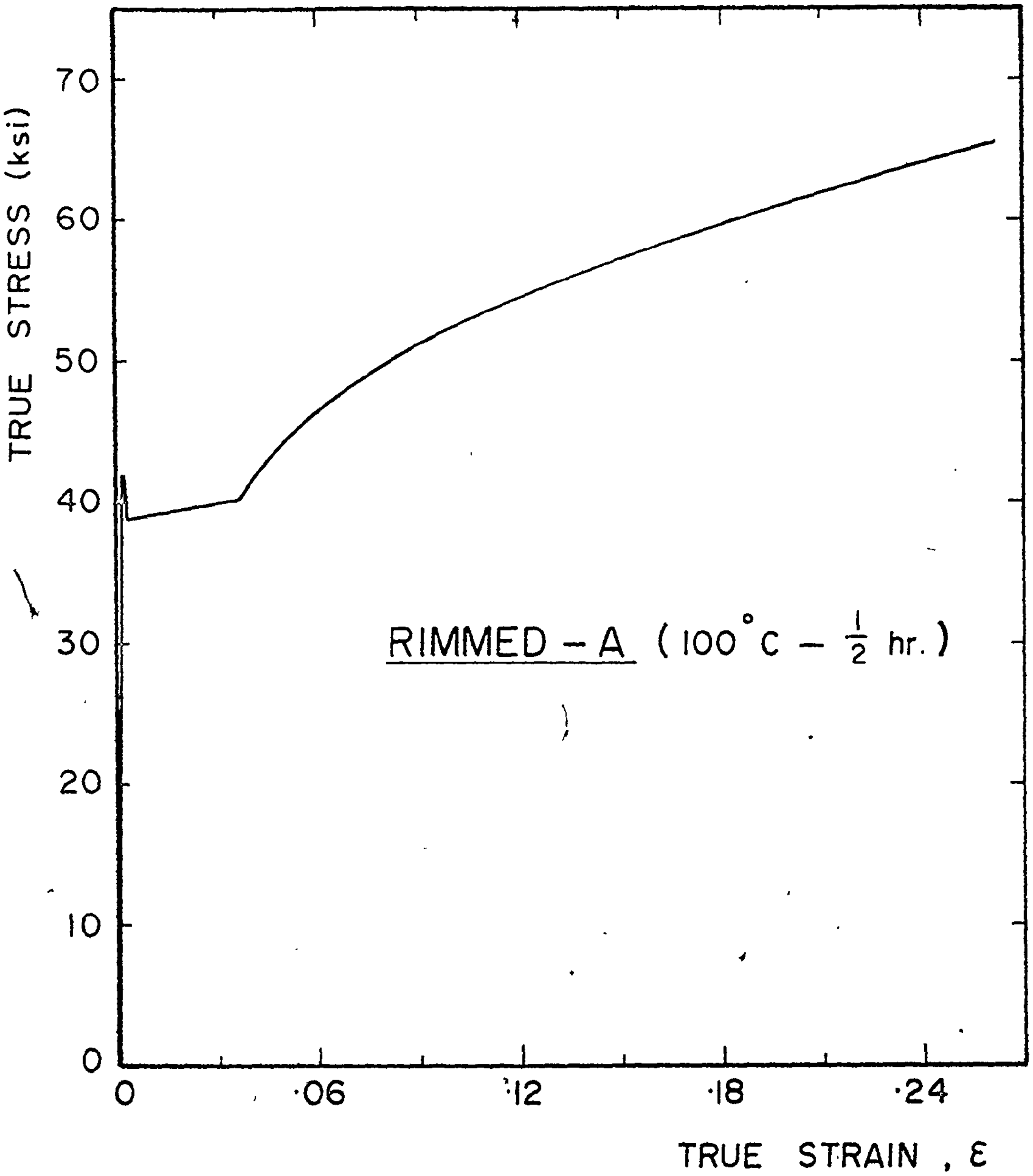

Fig. E.1(b) - Experimental tensile true stress-true strain diagram for Rimmed steel-A, aged at 100°C for 0.5 hours

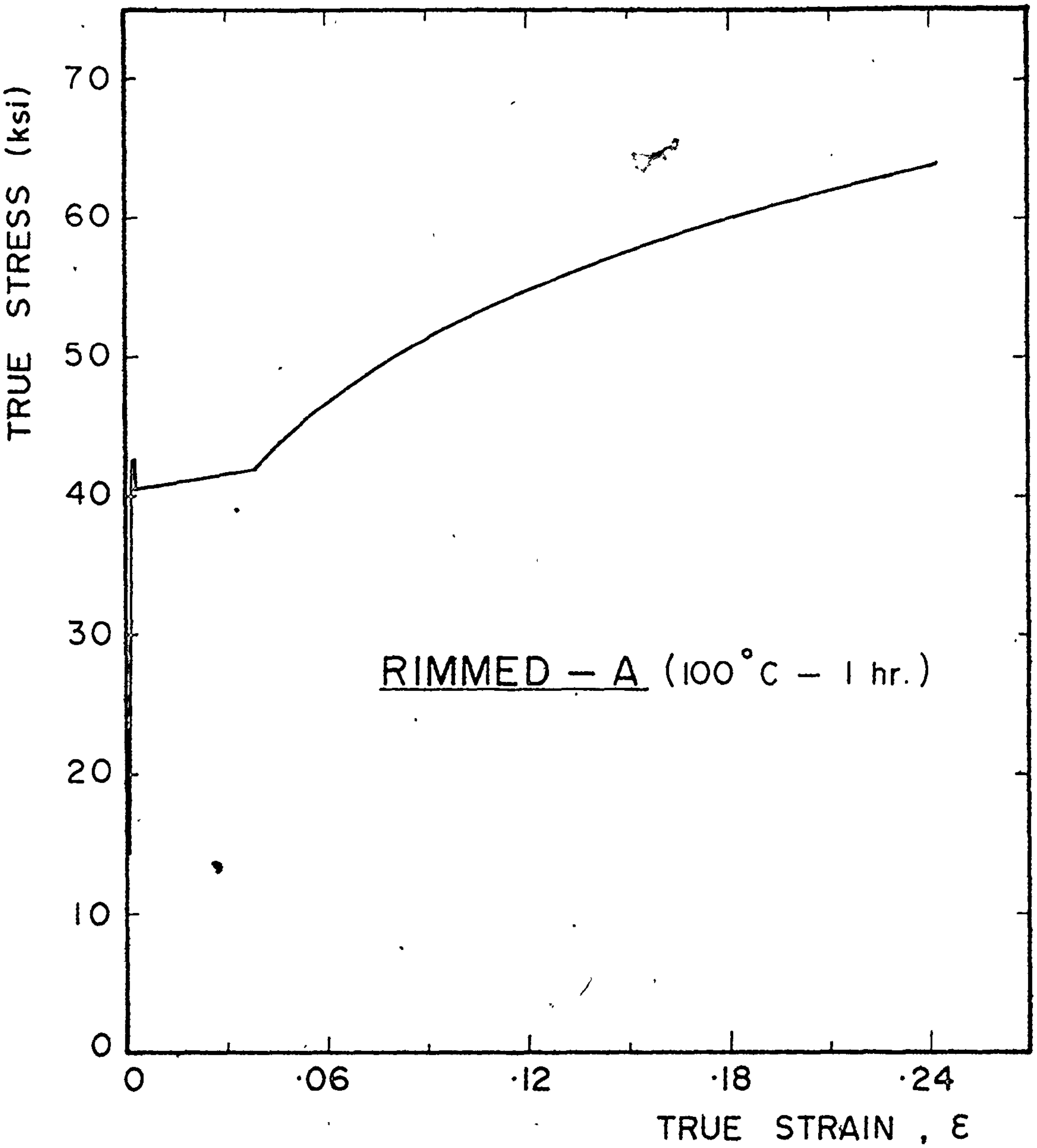

Fig. E.1(c) - Experimental tensile true stress-true strain diagram for Rimmed steel-A, aged at 100°C for 1 hour

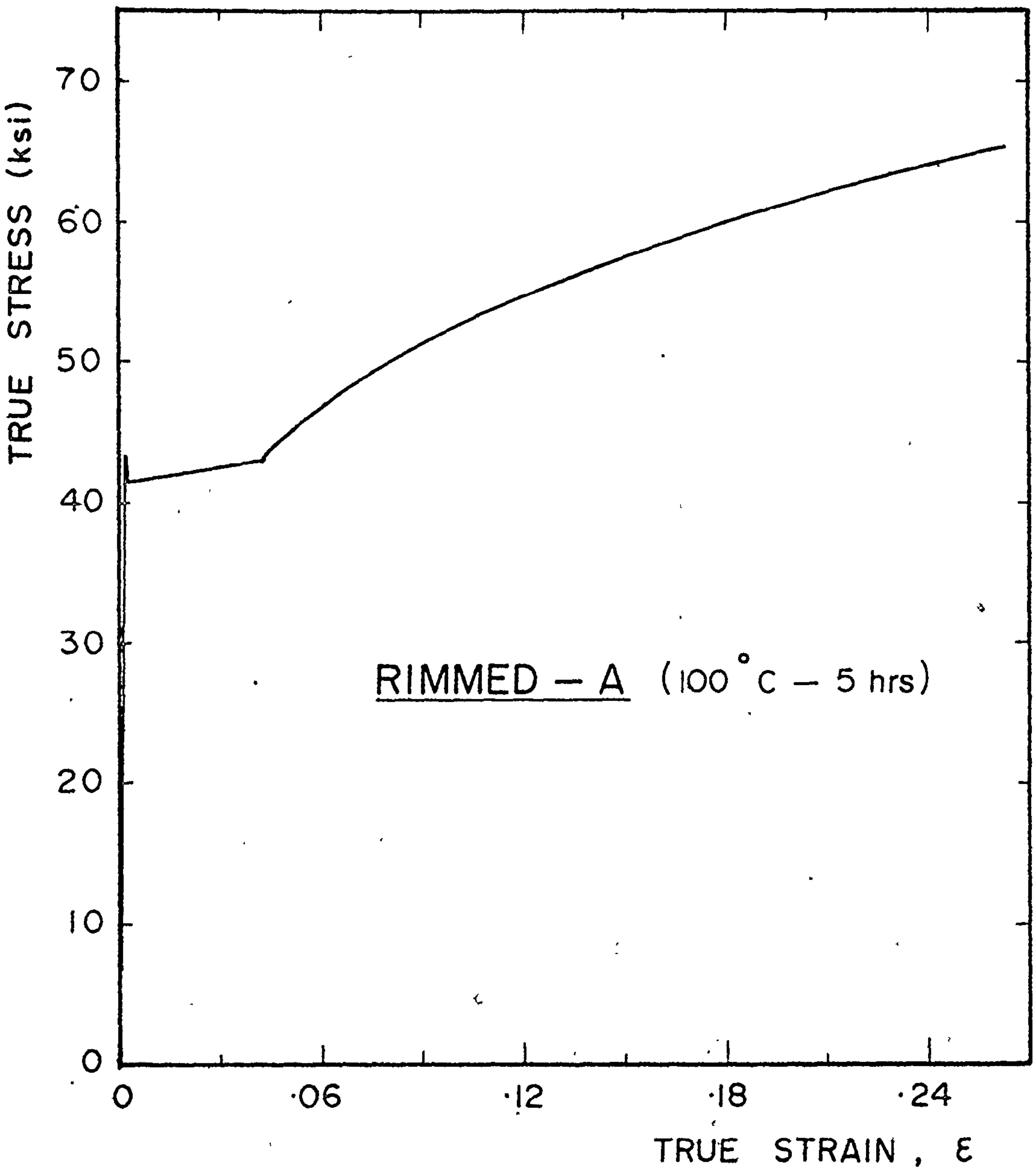

Fig. E.1(d) - Experimental tensile true stress-true strain diagram for Rimmed steel-A, aged at 100°C for 5 hours

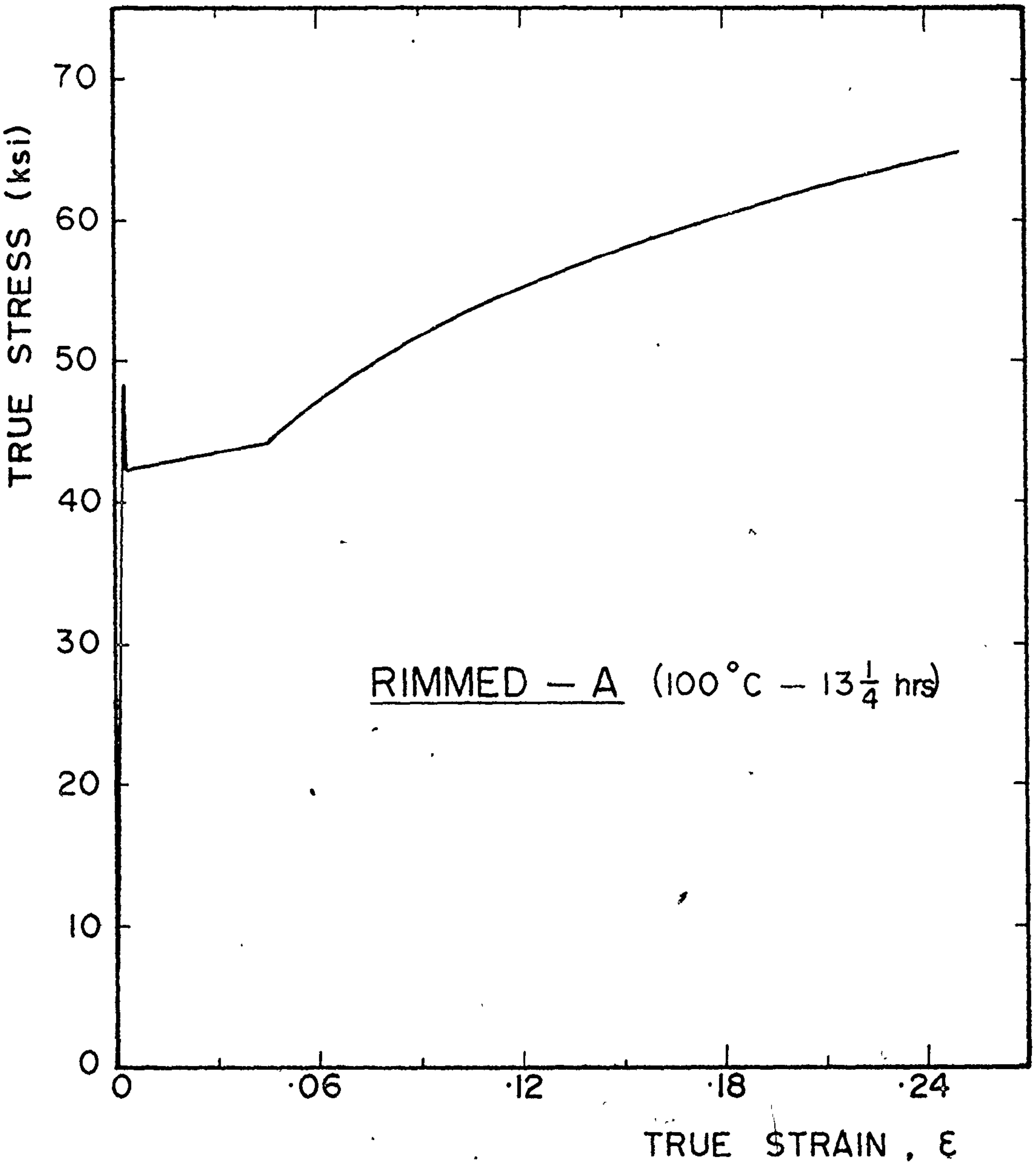

Fig. E.1(e) - Experimental tensile true stress-true strain diagram for Rimmed steel-A, aged at 100°C for 13.25 hours

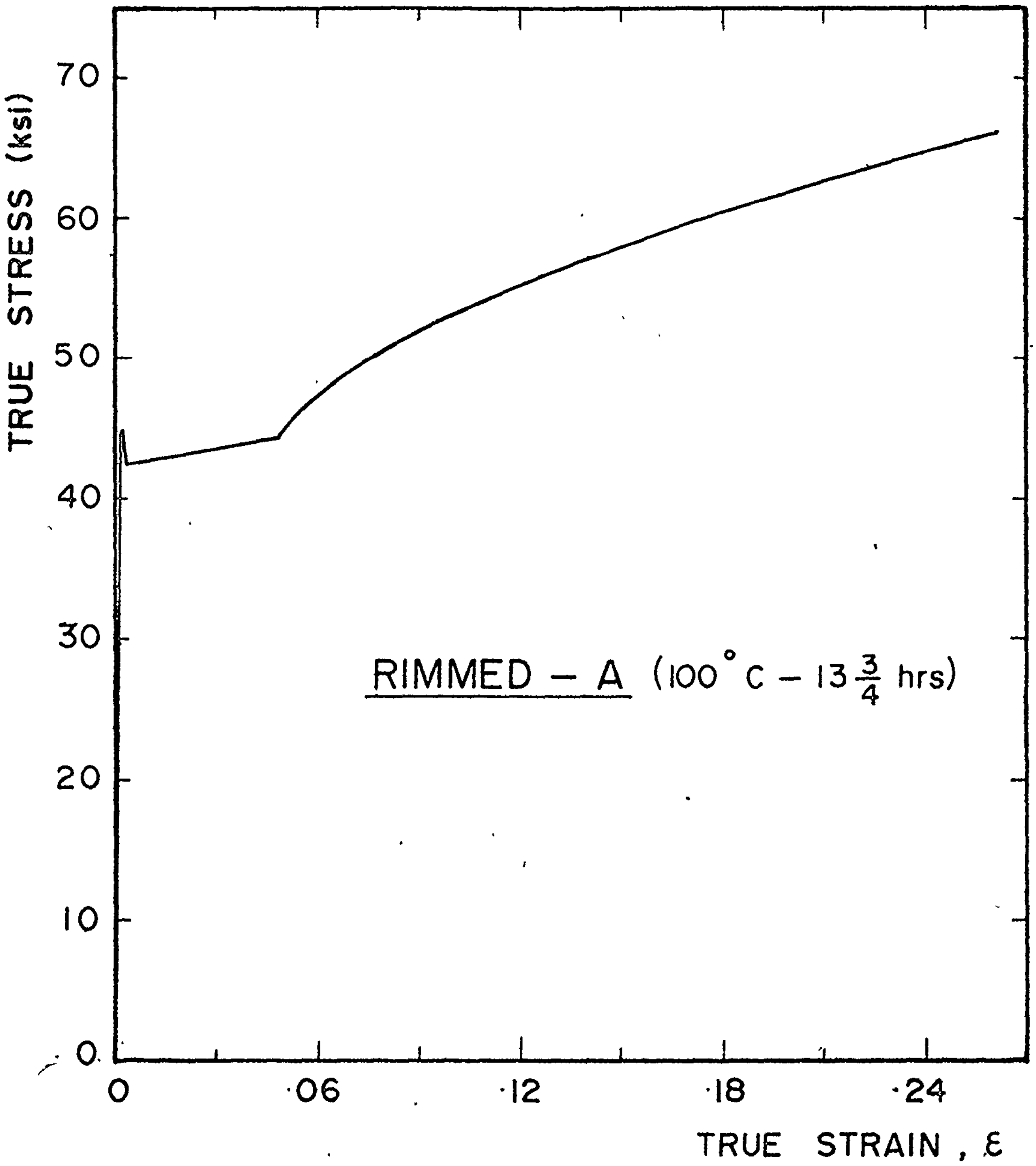

Fig. E.1(f) - Experimental tensile true stress-true strain diagram for Rimmed steel-A, aged at 100°C for 13.75 hours

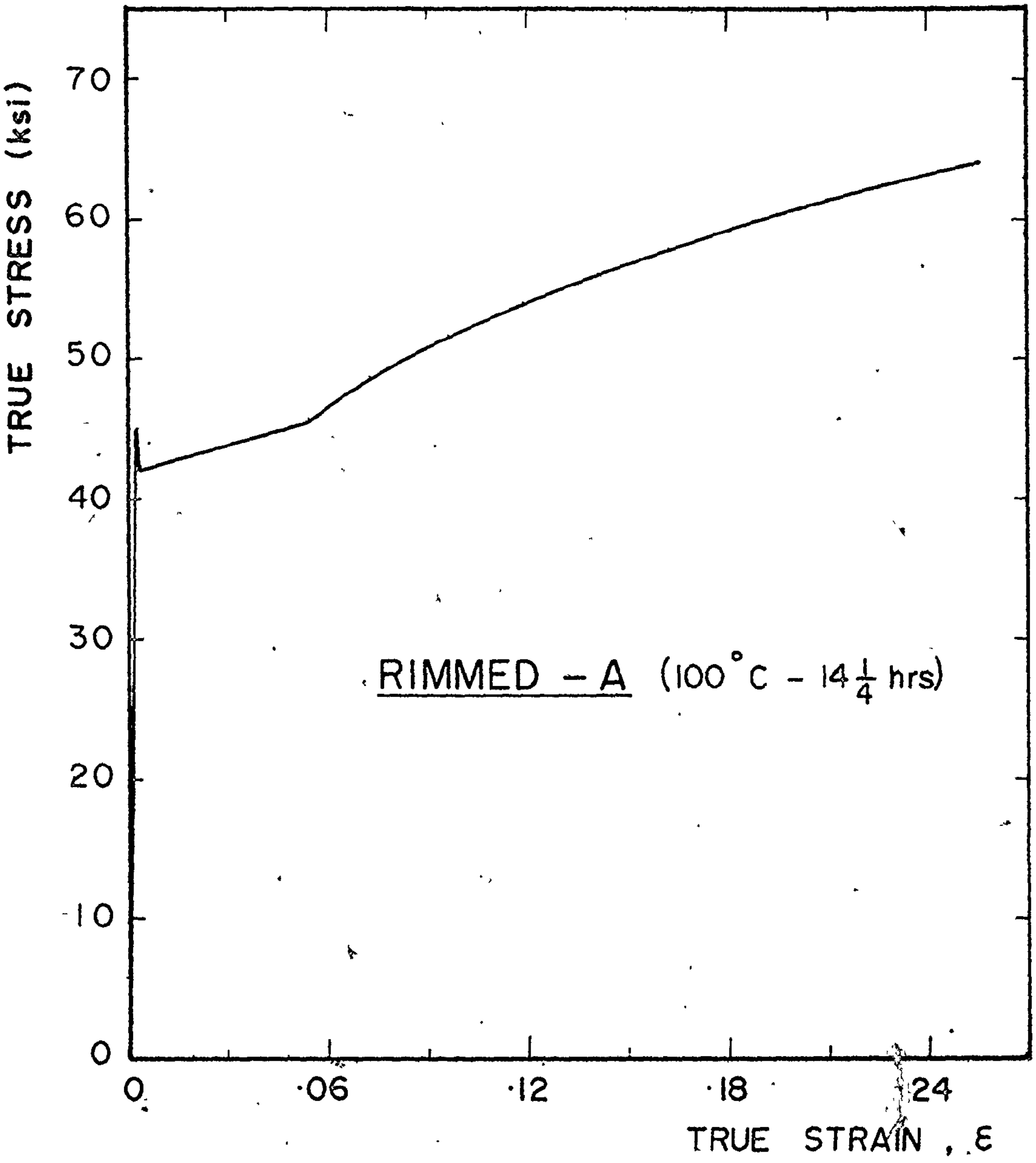

Fig. E.1(g) - Experimental tensile true stress-true strain diagram for Rimmed steel-A, aged at 100°C for 14.25 hours

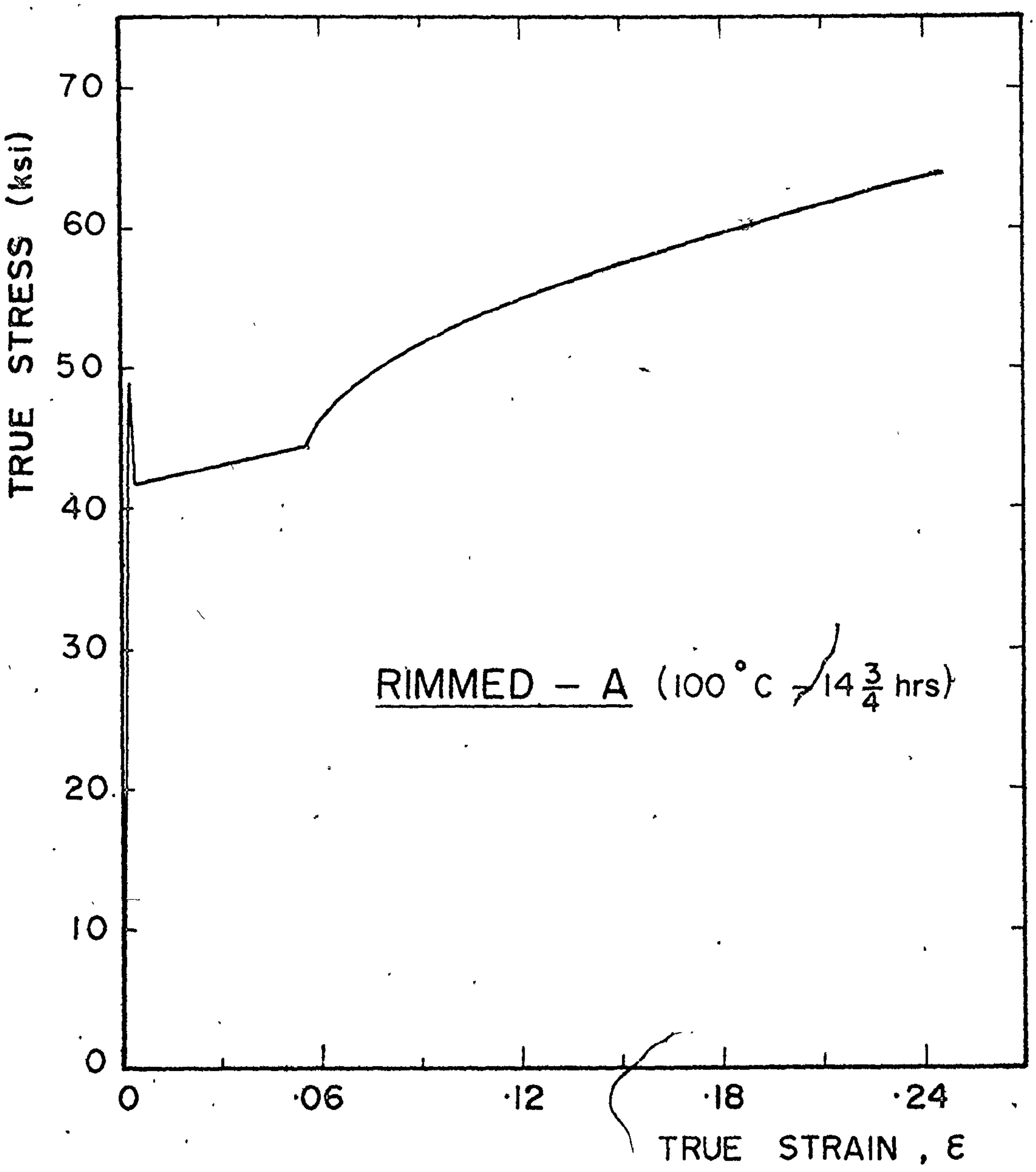

Fig. E.1(h) - Experimental tensile true stress-true strain diagram for Rimmed Steel-A, aged at 100°C for 14.75 hours

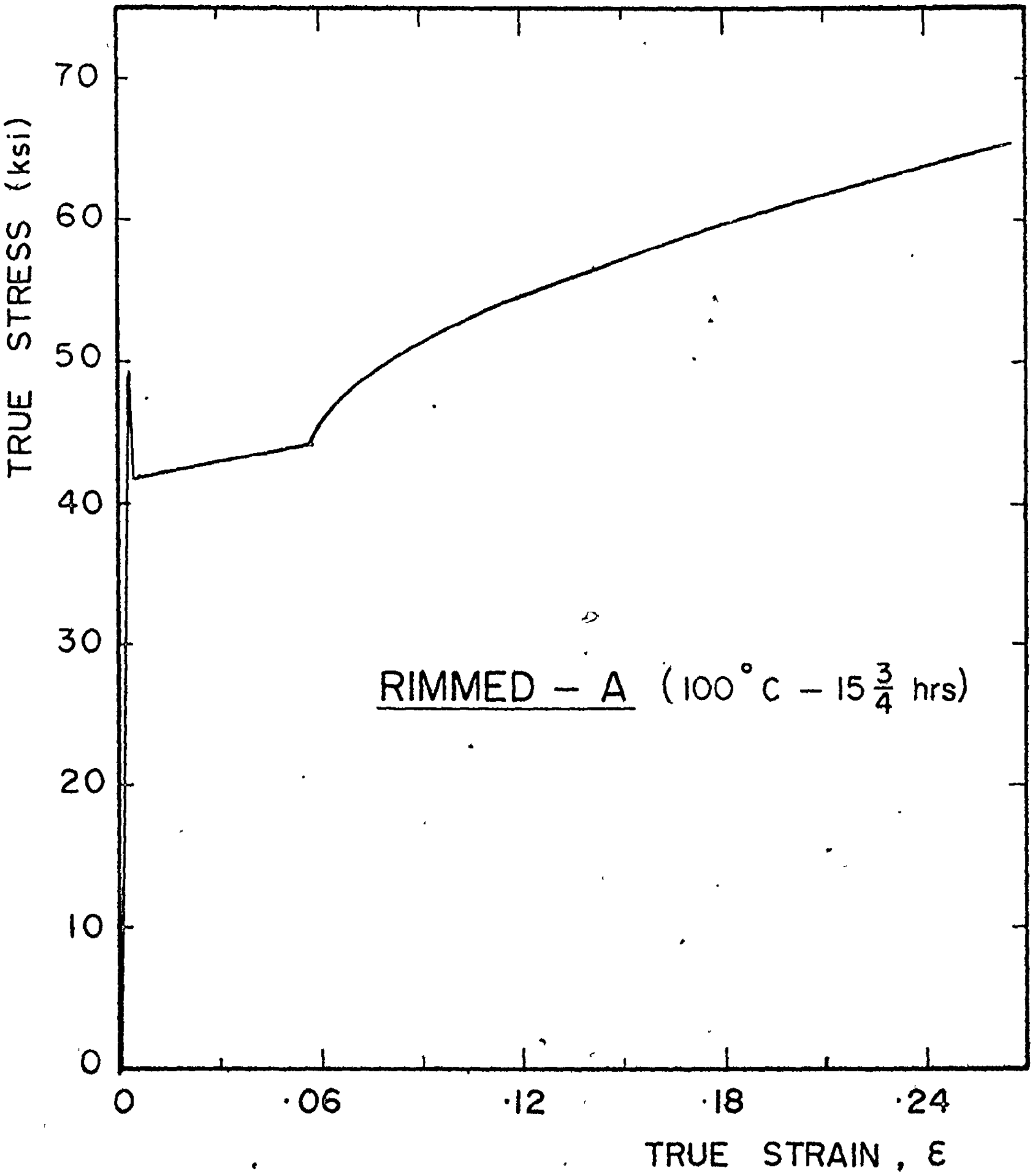

Fig. E.1(i) - Experimental tensile true stress-true strain diagram for Rimmed steel-A, aged at 100°C for 15.75 hours

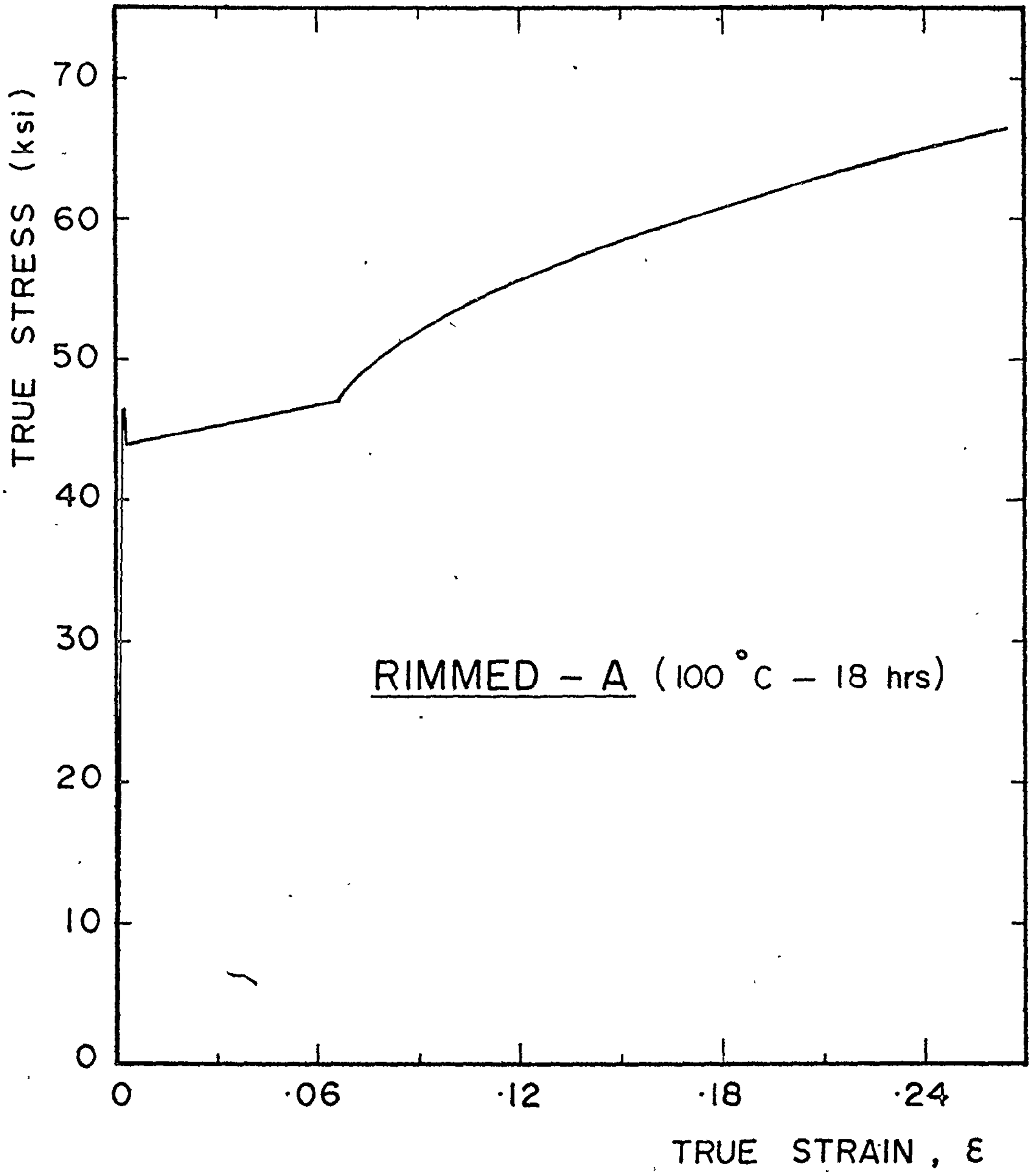

Fig. E.1(j) - Experimental tensile true stress-true strain diagram for Rimmed steel-A, aged at 100°C for 18 hours

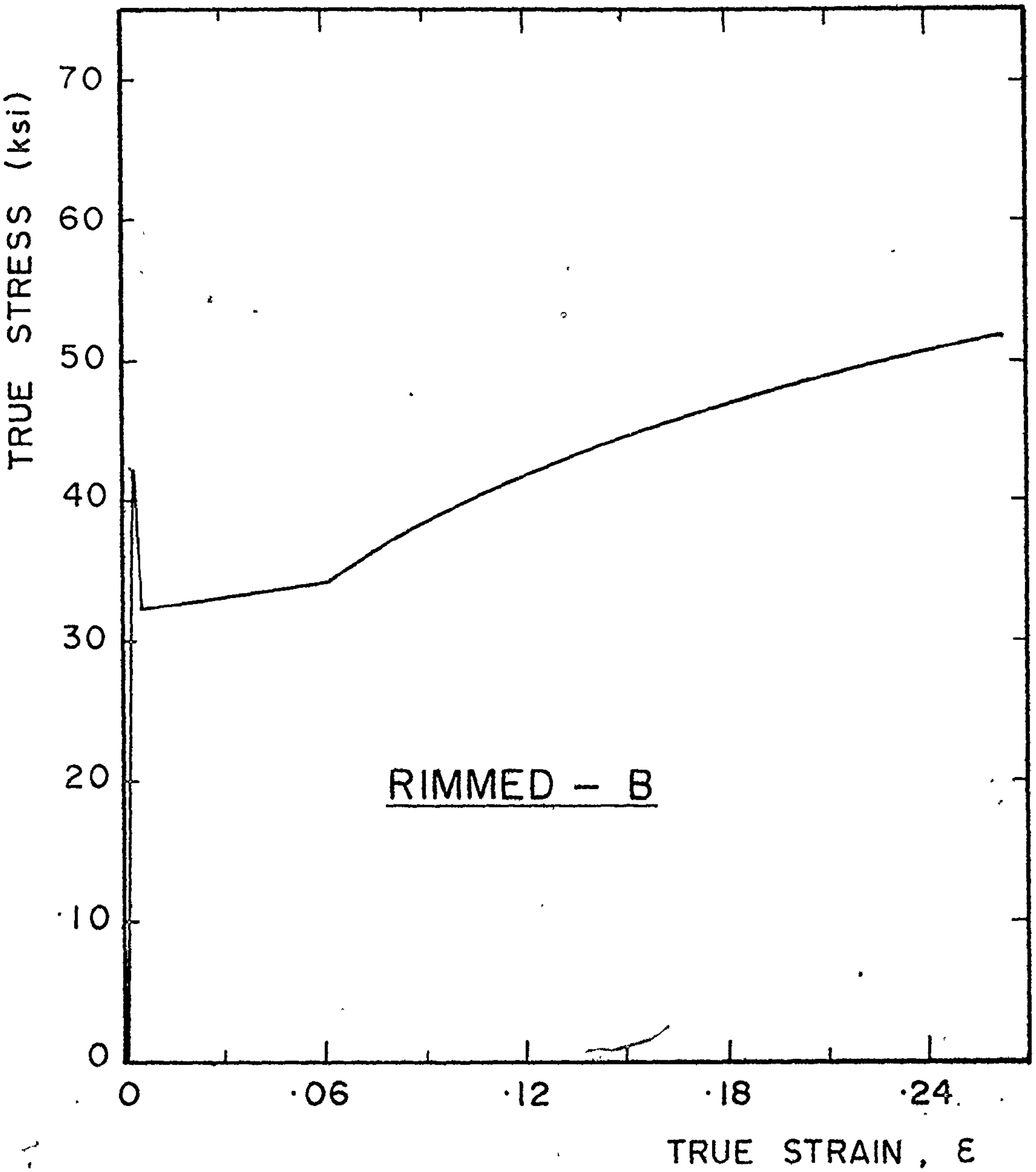

Fig. E.2(a) - Experimental tensile true stress-true strain diagram for Rimmed steel-B in the as received condition

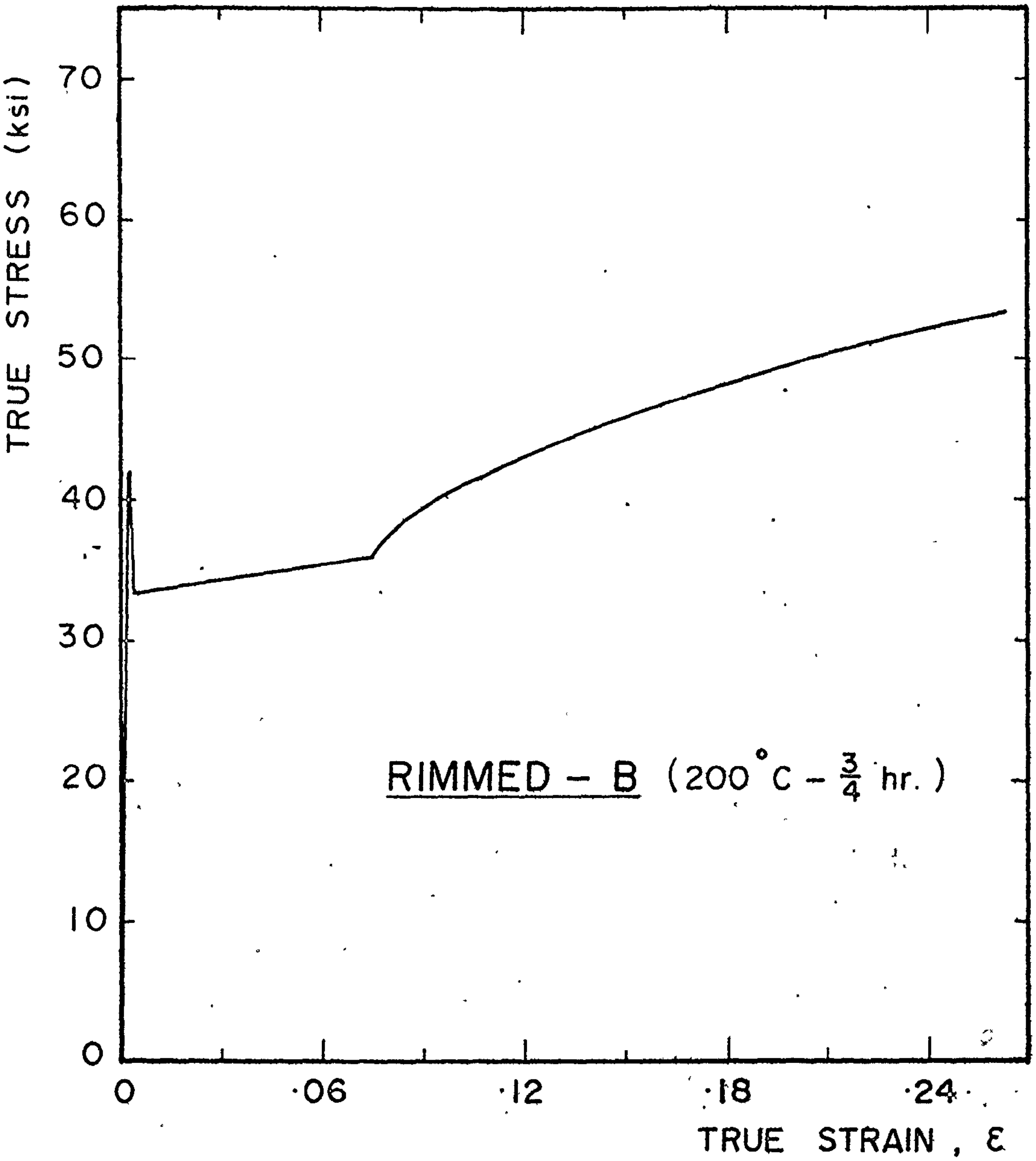

Fig. E.2(b) - Experimental tensile true stress-true strain diagram for Rimmed steel-B, aged at 200°C for 0.75 hours

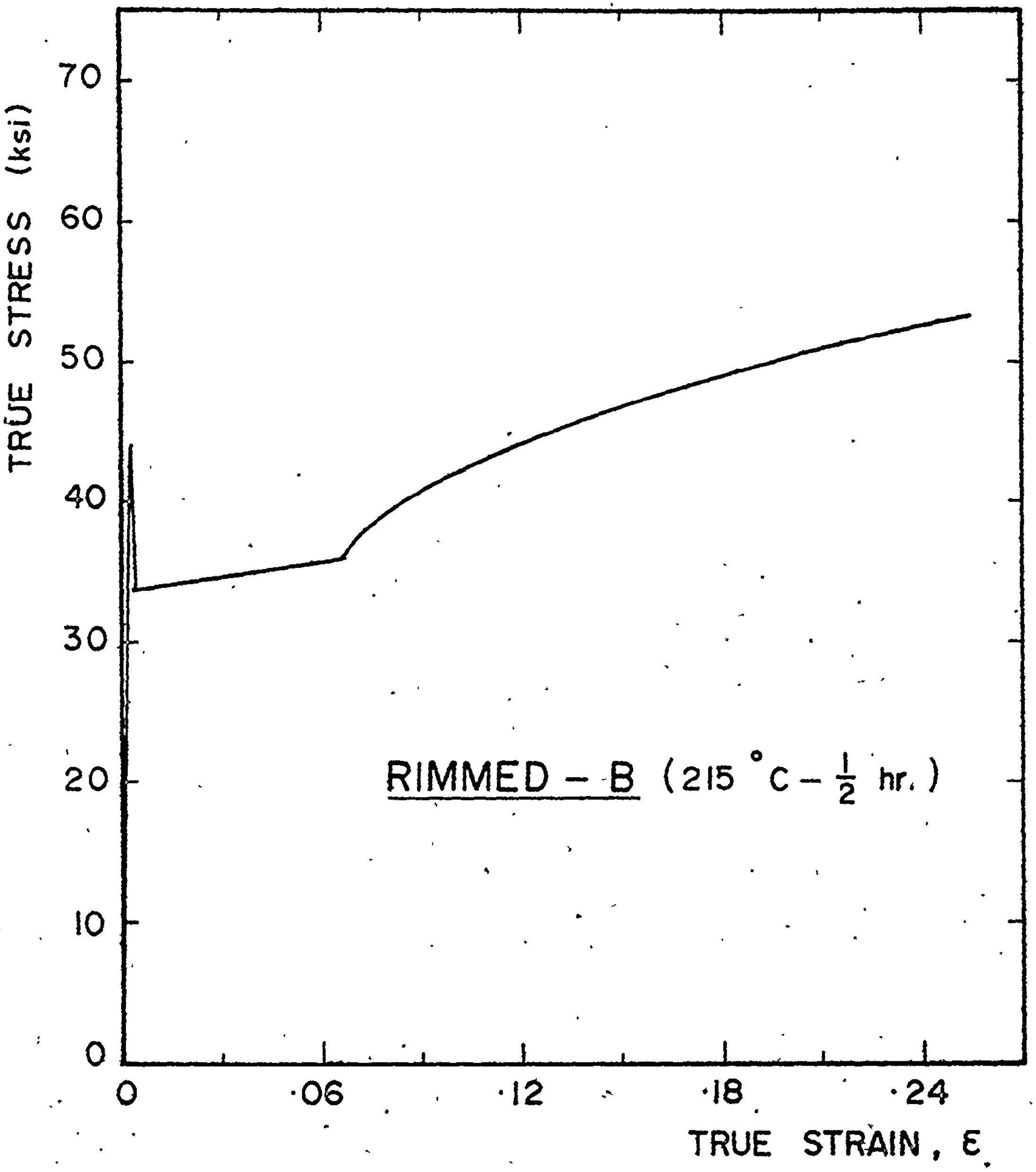

Fig. E.2(c) - Experimental tensile true stress-true strain diagram for Rimmed steel-B, aged at 215°C for 0.5 hours

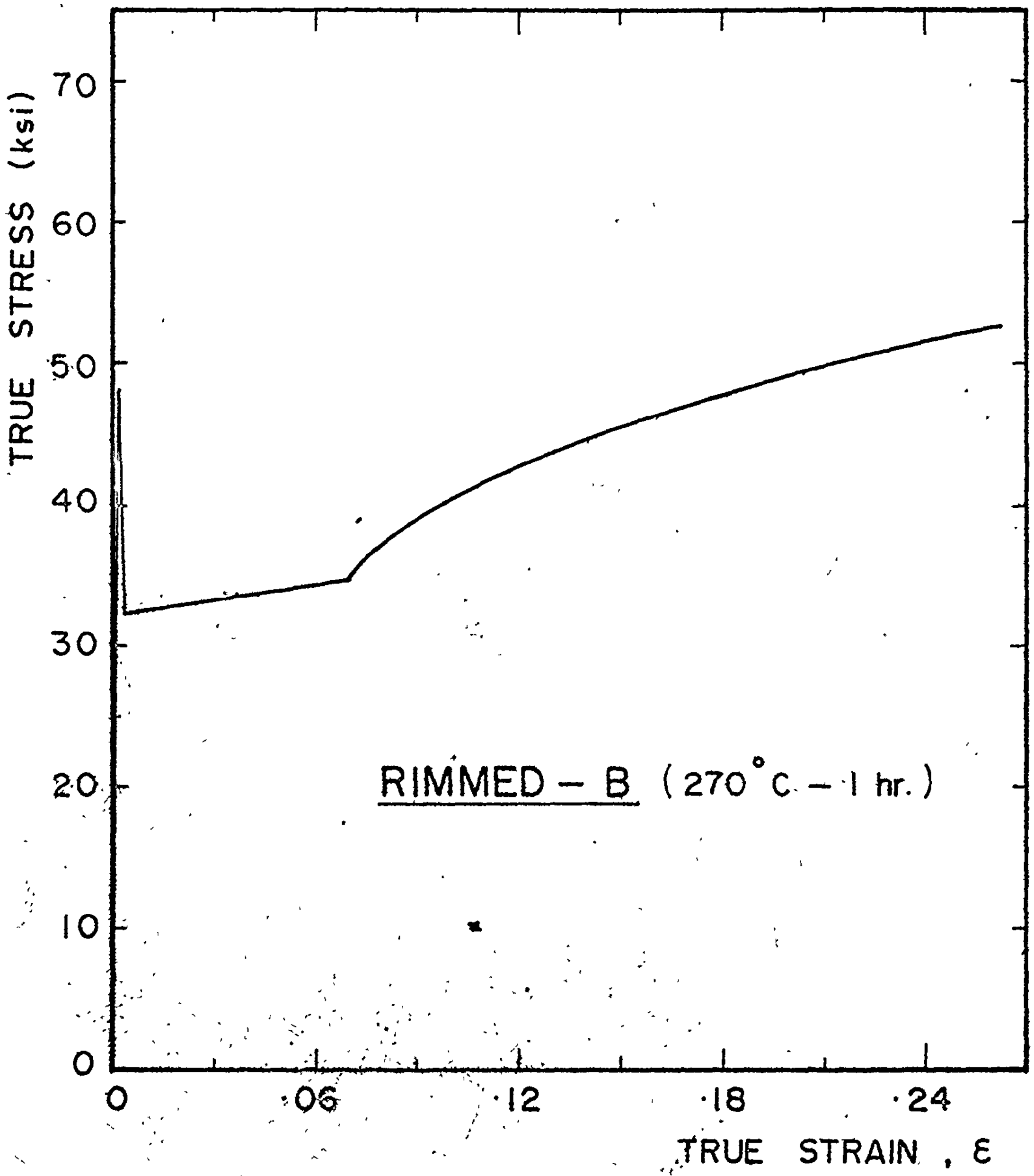

Fig. E.2(d) - Experimental tensile true stress-true strain diagram for Rimmed steel-B, aged at 270°C for 1 hour

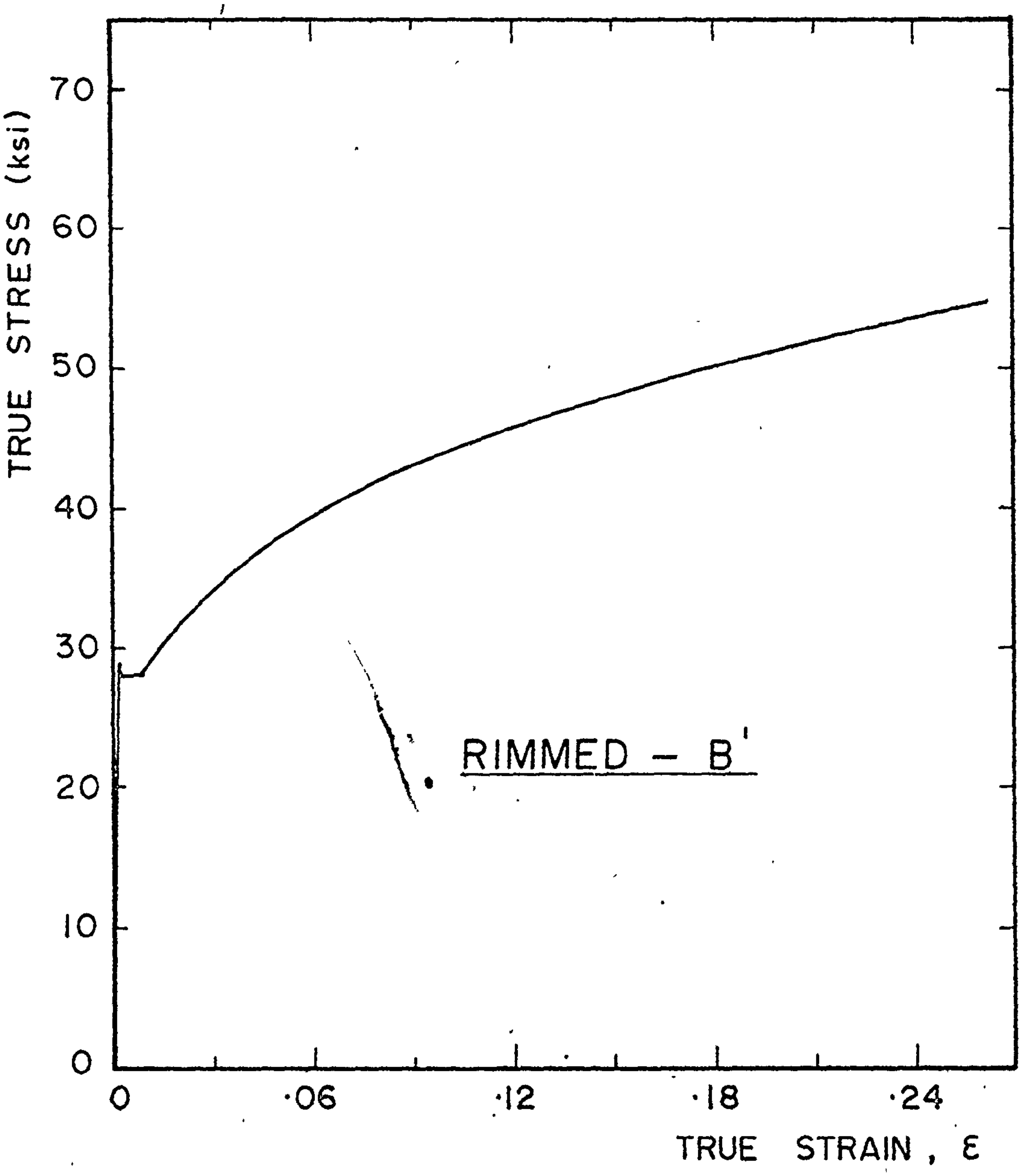

Fig. E.3(a) - Experimental tensile true stress-true strain diagram for Rimmed steel-B'

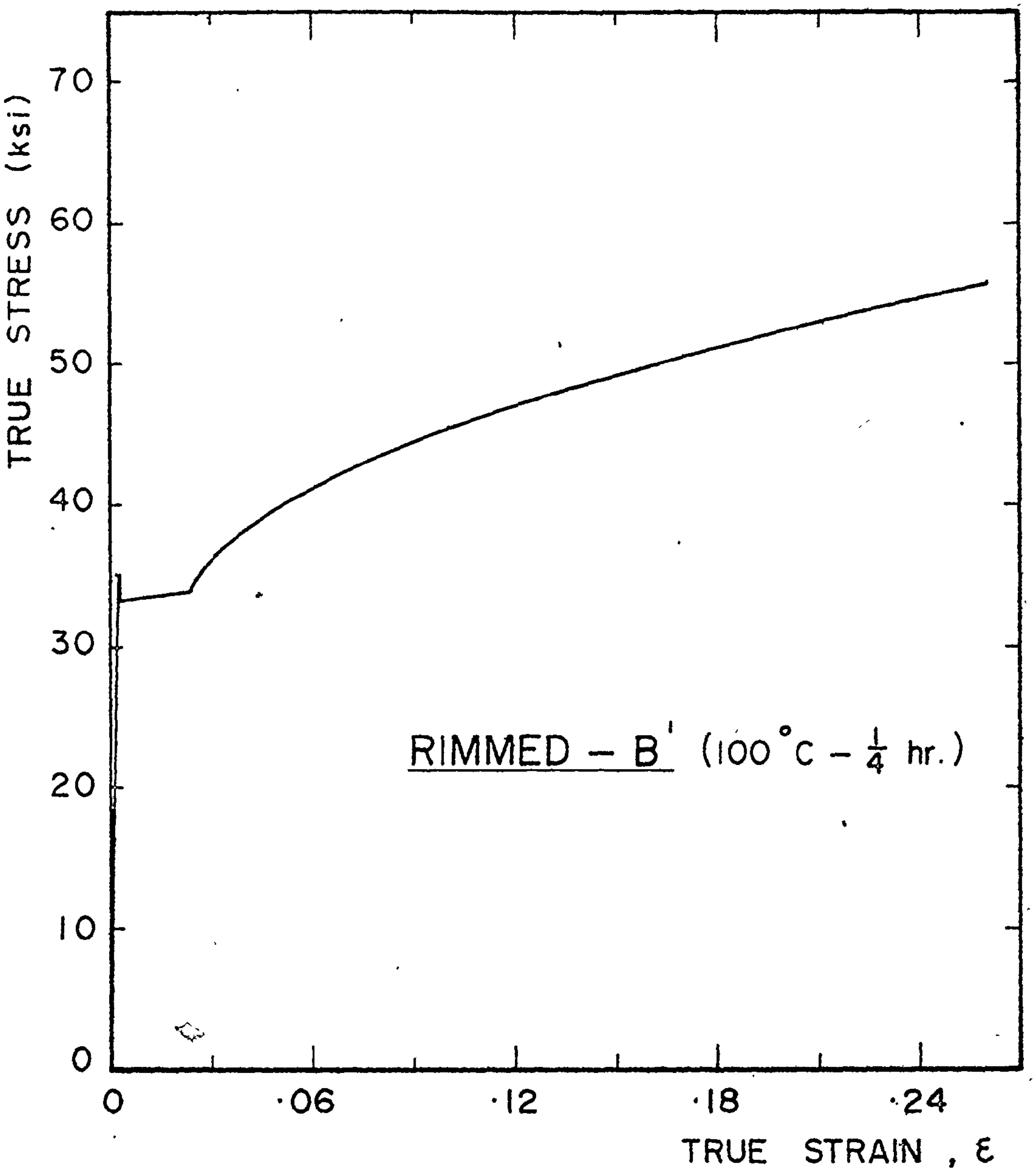

Fig. E.3(b) - Experimental tensile true stress-true strain diagram for Rimmed steel-B', aged at 100°C for 0.25 hours

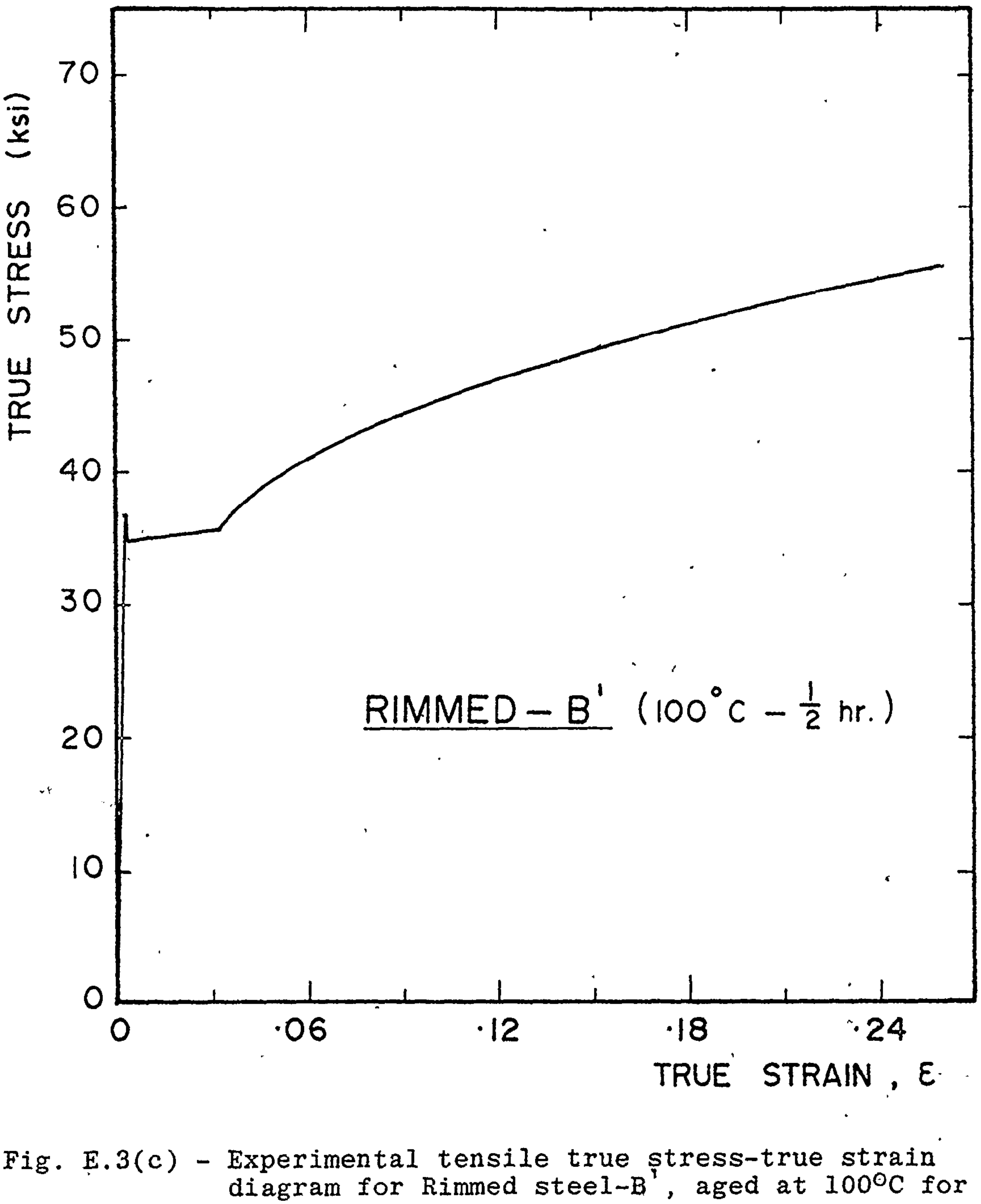

Fig. E.3(c) - Experimental tensile true stress-true strain diagram for Rimmed steel-B', aged at 100°C for 0.5 hours

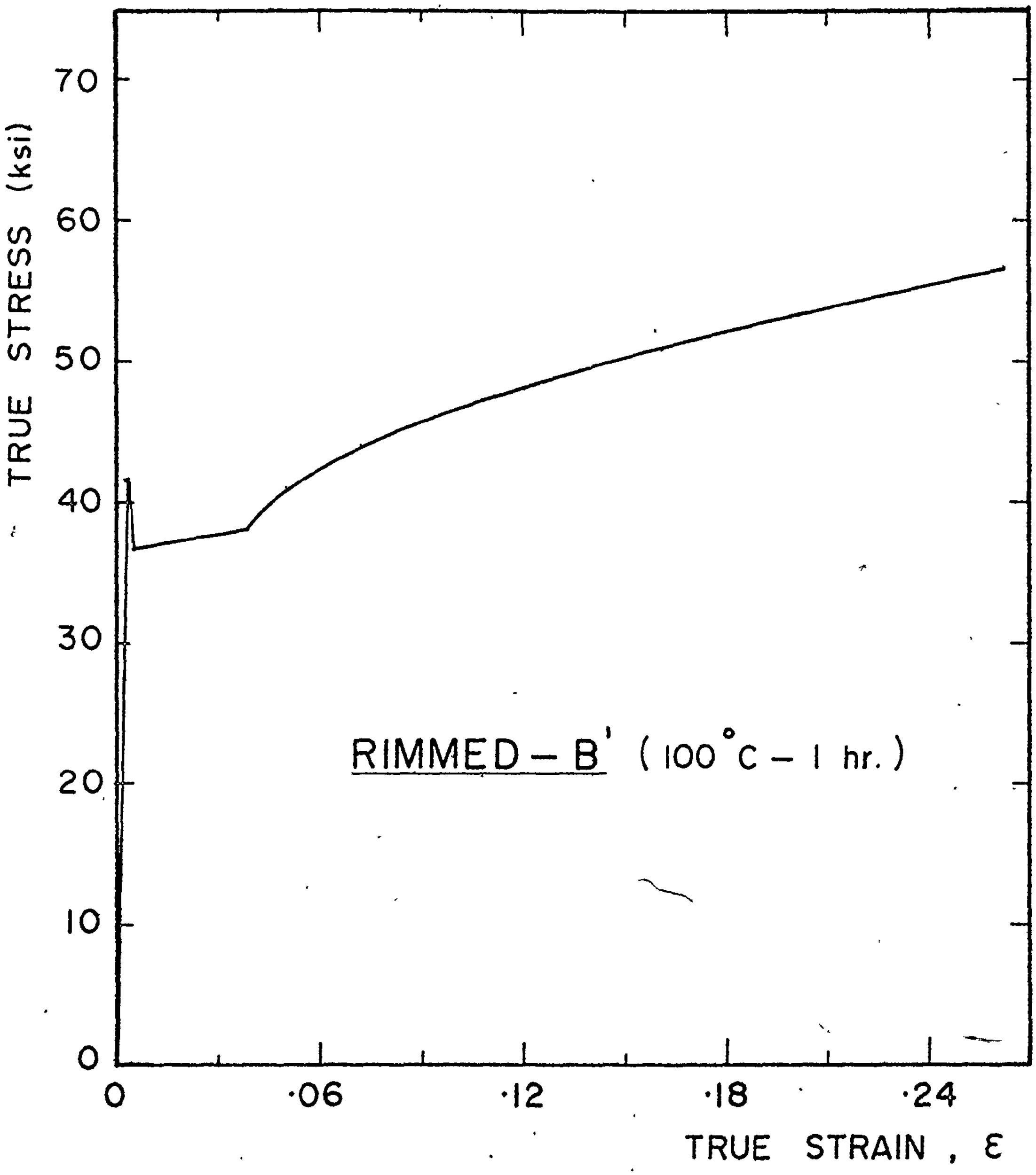

Fig. E.3(d) - Experimental tensile true stress-true strain diagram for Rimmed steel-B', aged at 100°C for 1 hour

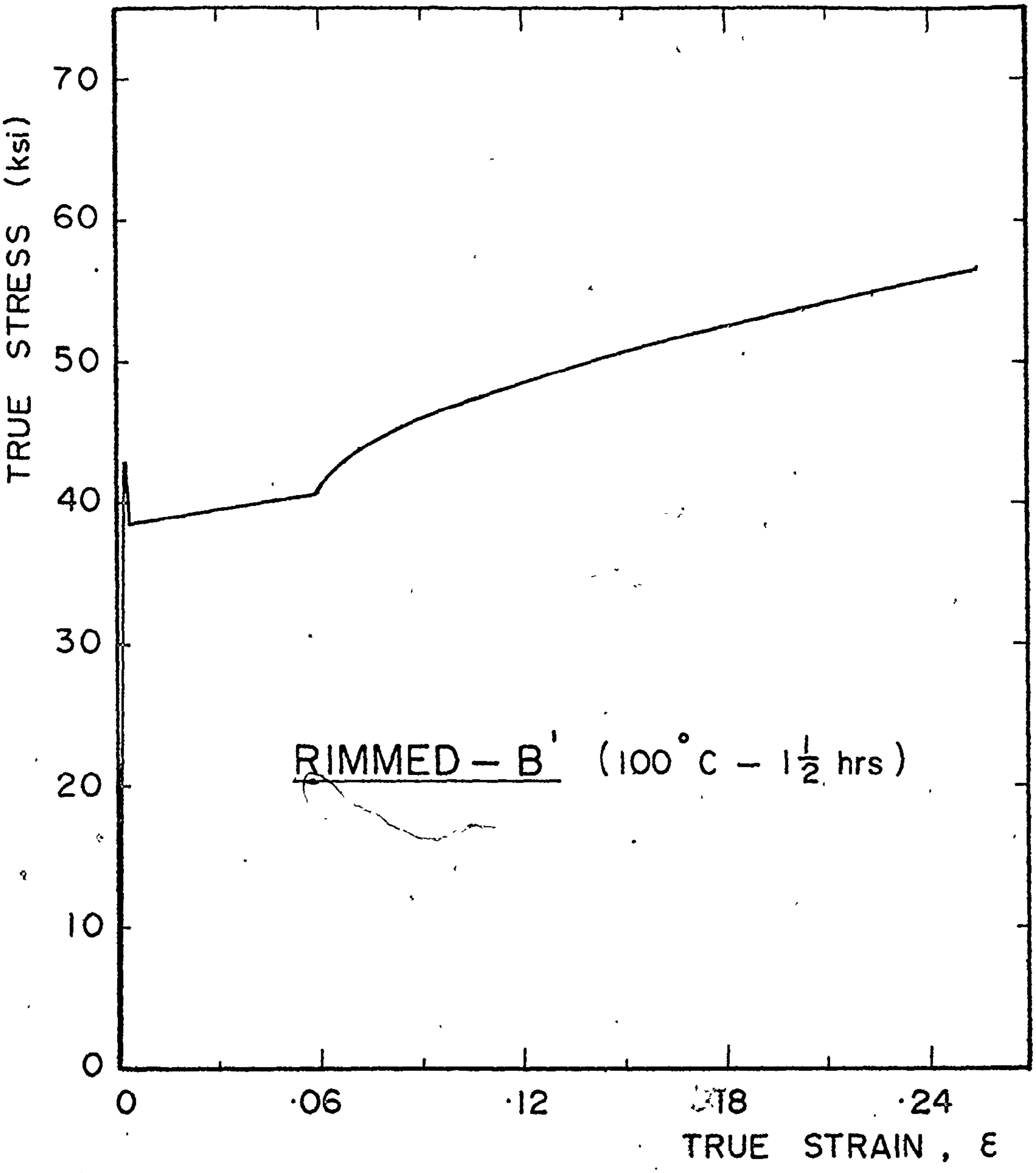

Fig. E.3(e) - Experimental tensile true stress-true strain diagram for Rimmed steel-B', aged at 100^{O}C for 1.5 hours

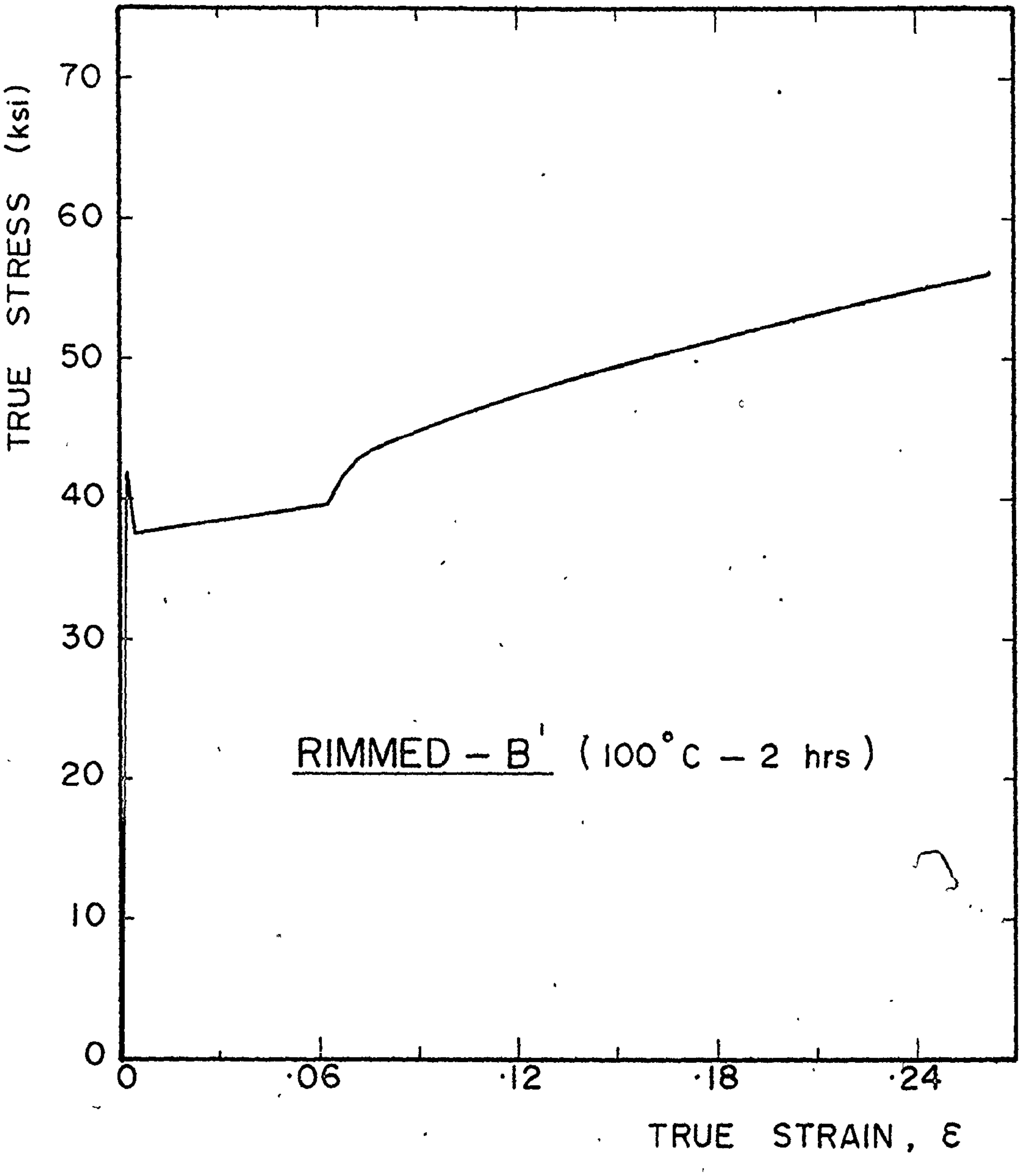

Fig. E.3(f) - Experimental tensile true stress-true strain diagram for Rimmed steel-B', aged at 100°C for 2 hours.

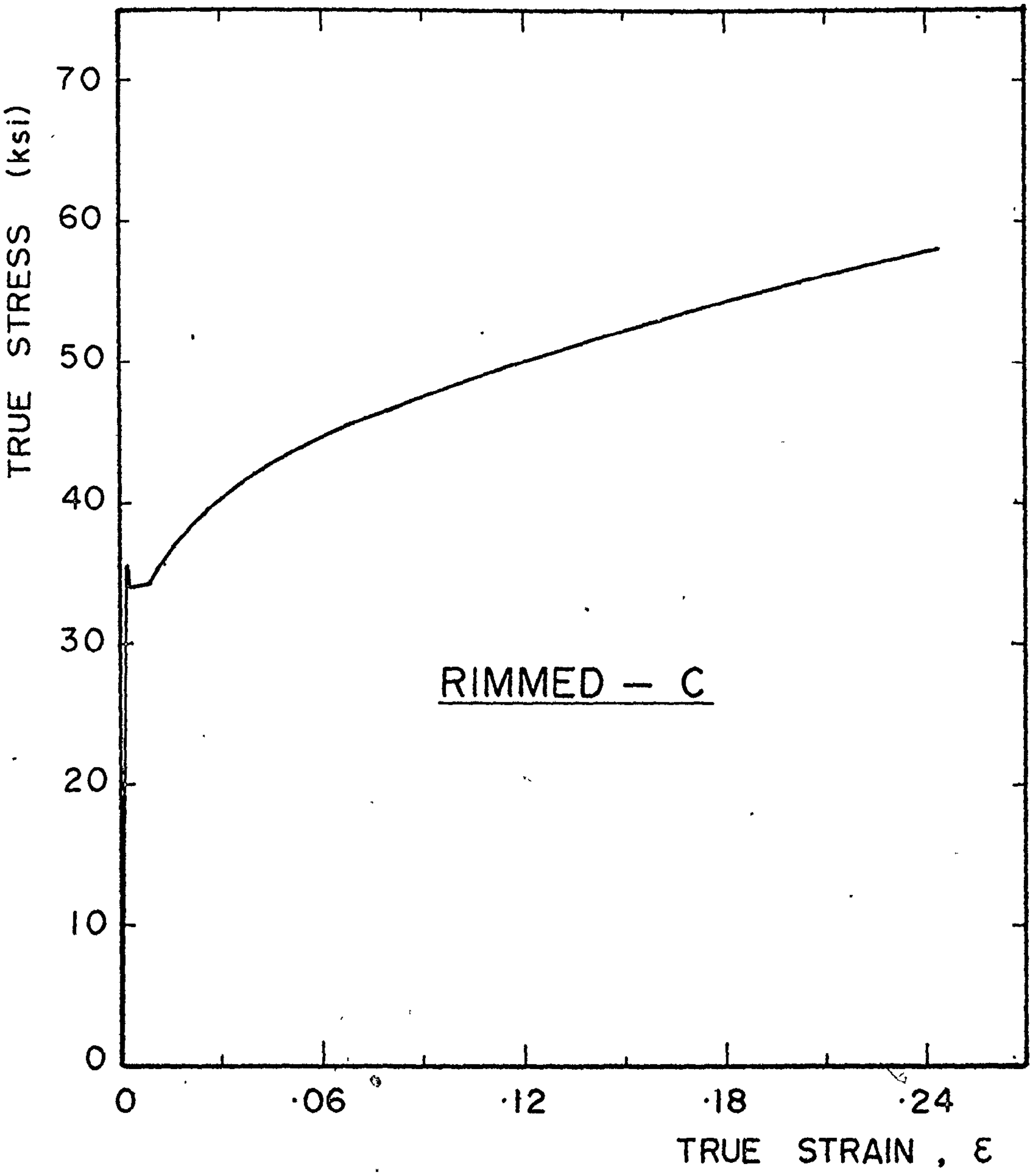

Fig. E.4(a) - Experimental tensile true stress-true strain diagram for Rimmed steel-C in the as received condition

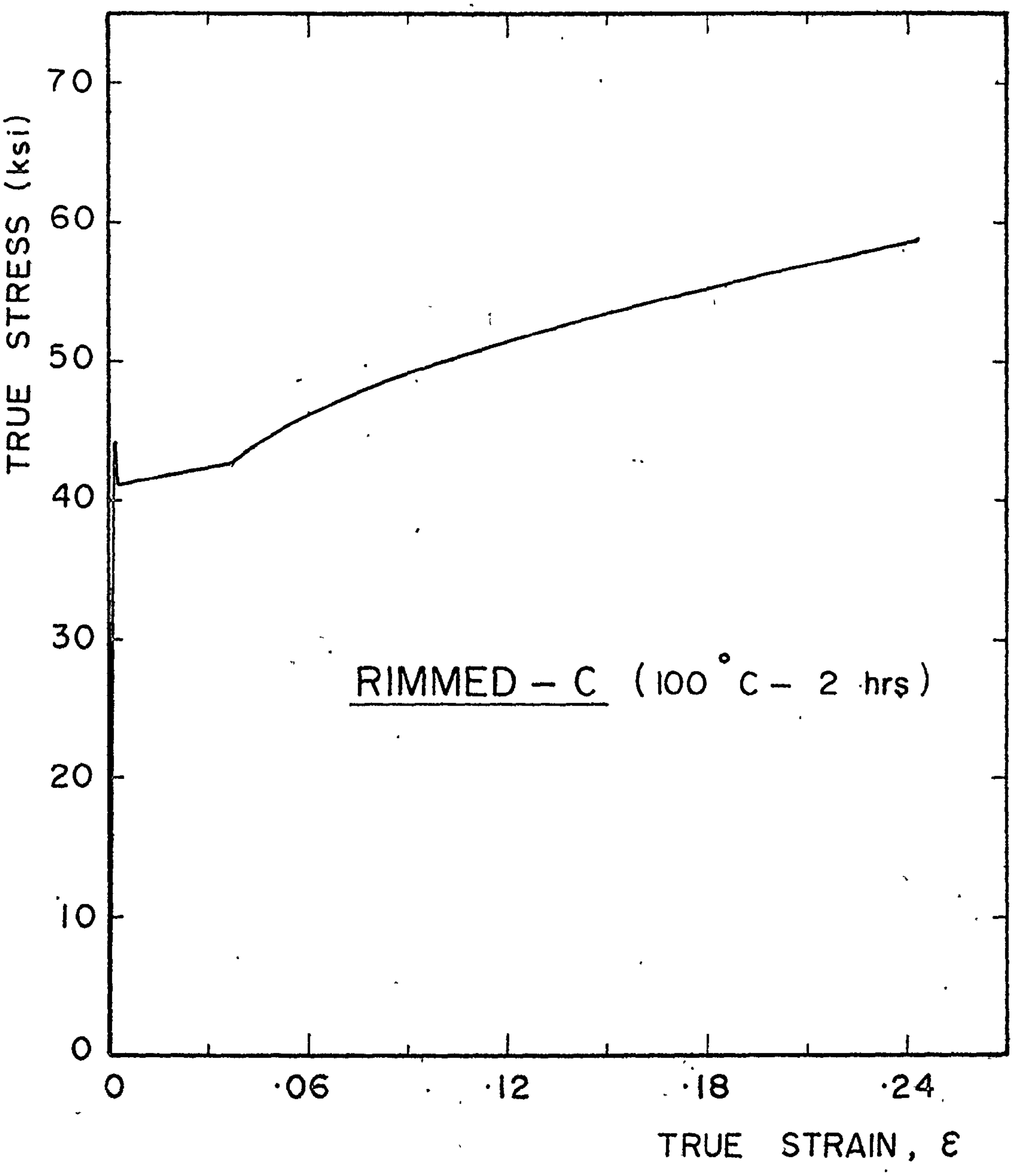

Fig. E.4(b) - Experimental tensile true stress-true strain diagram for Rimmed steel-C, aged at 100°C for 2 hours

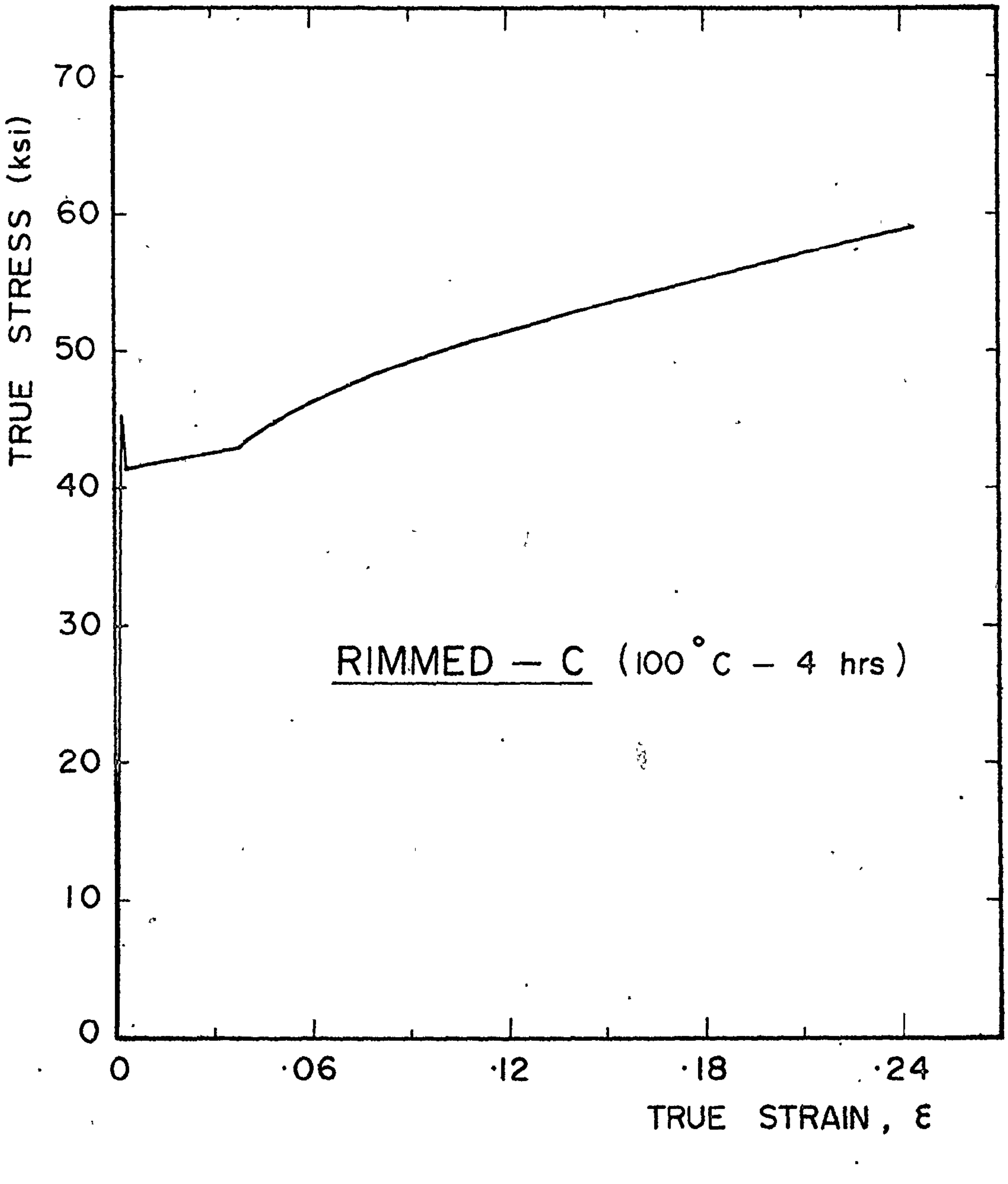

Fig. E.4(c) - Experimental tensile true stress-true strain diagram for Rimmed steel-C, aged at 100°C for 4 hours

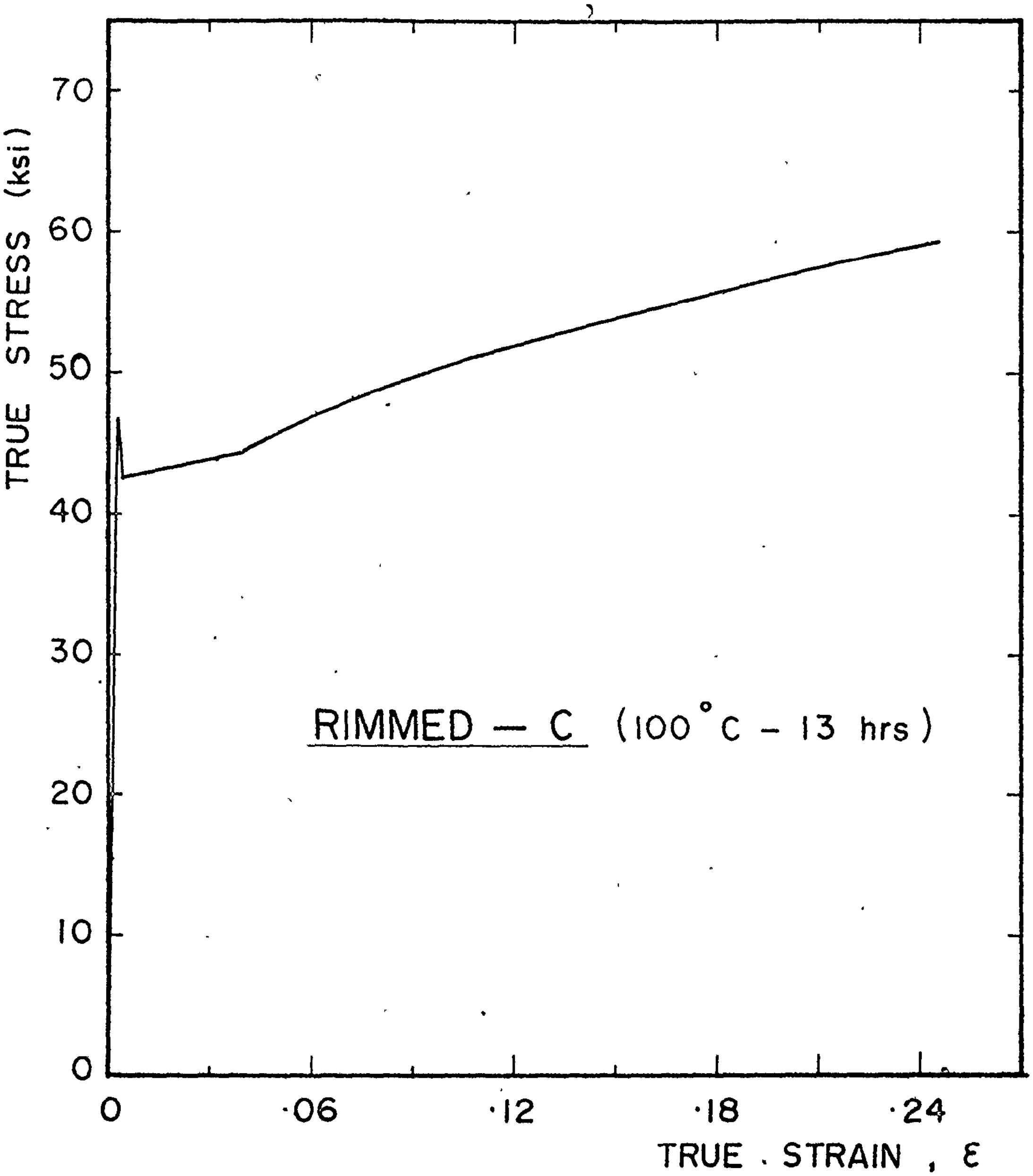

Fig. E.4(d) - Experimental tensile true stress-true strain diagram for Rimmed steel-C, aged at 100°C for 13 hours

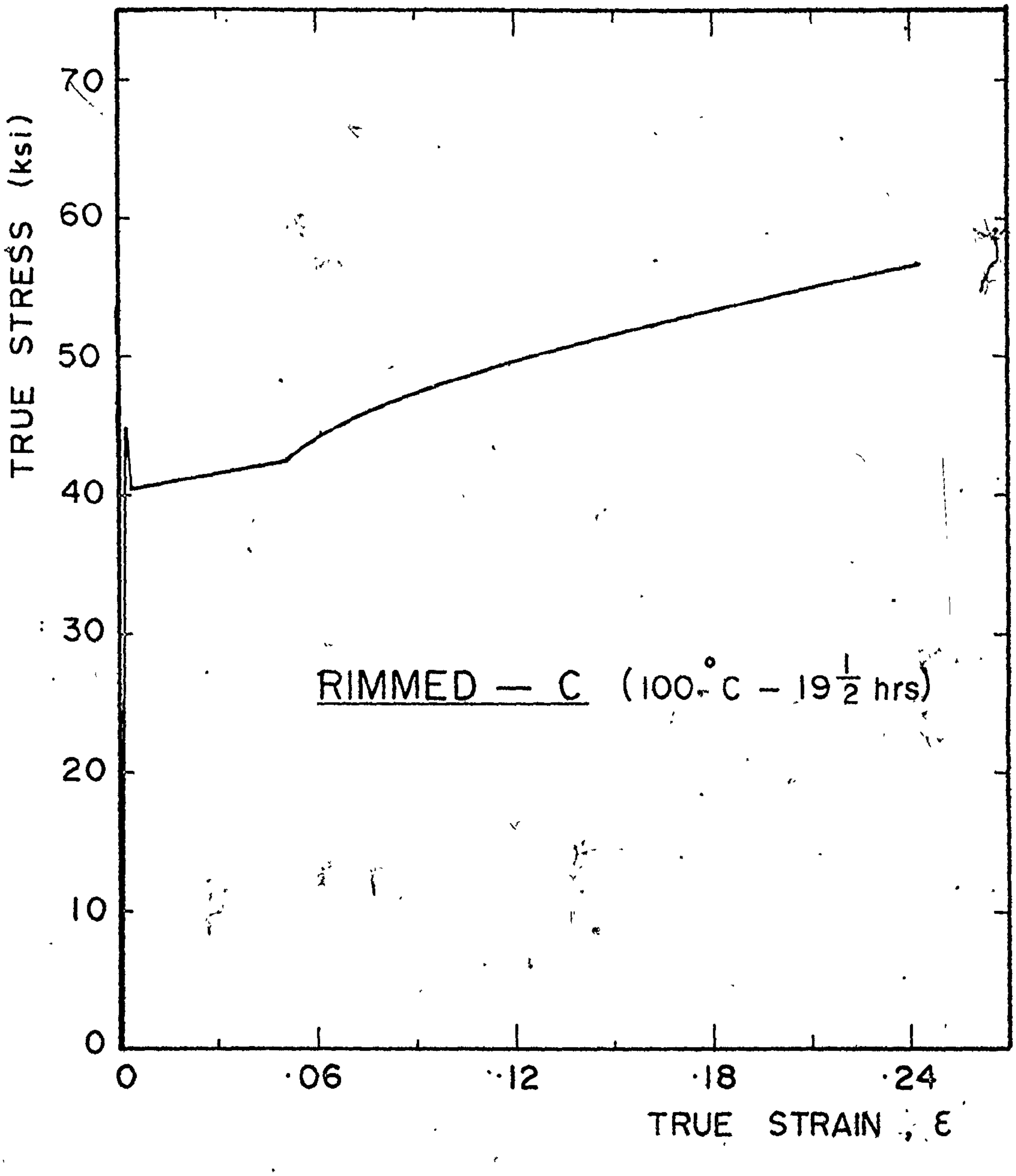

Fig. E.4(e) - Experimental tensile true stress-true strain diagram for Rimmed steel-C, aged at 100°C for 19.5 hours

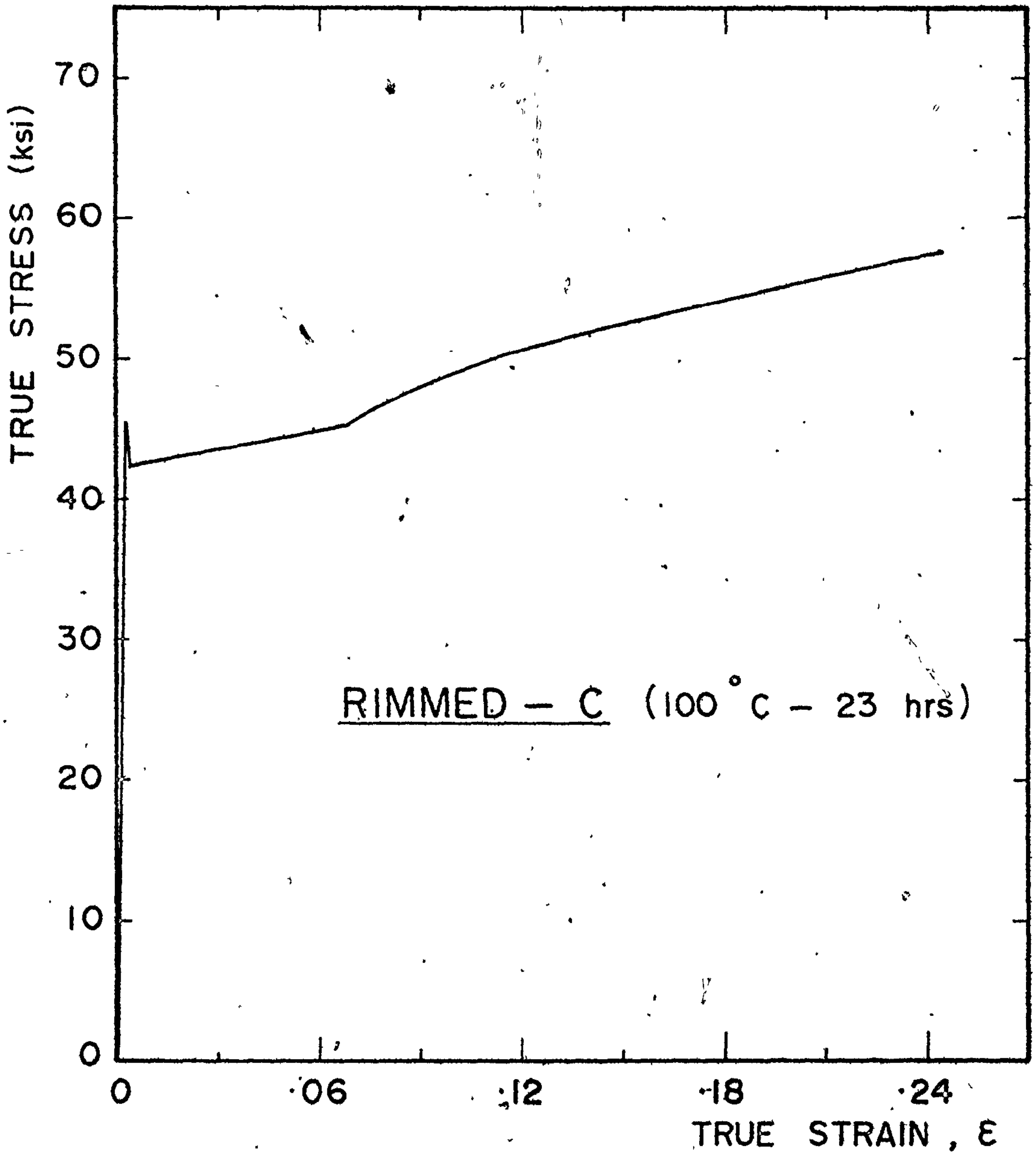

Fig. E.4(f) - Experimental tensile true stress-true strain diagram for Rimmed steel-C, aged at 100°C for 23 hours

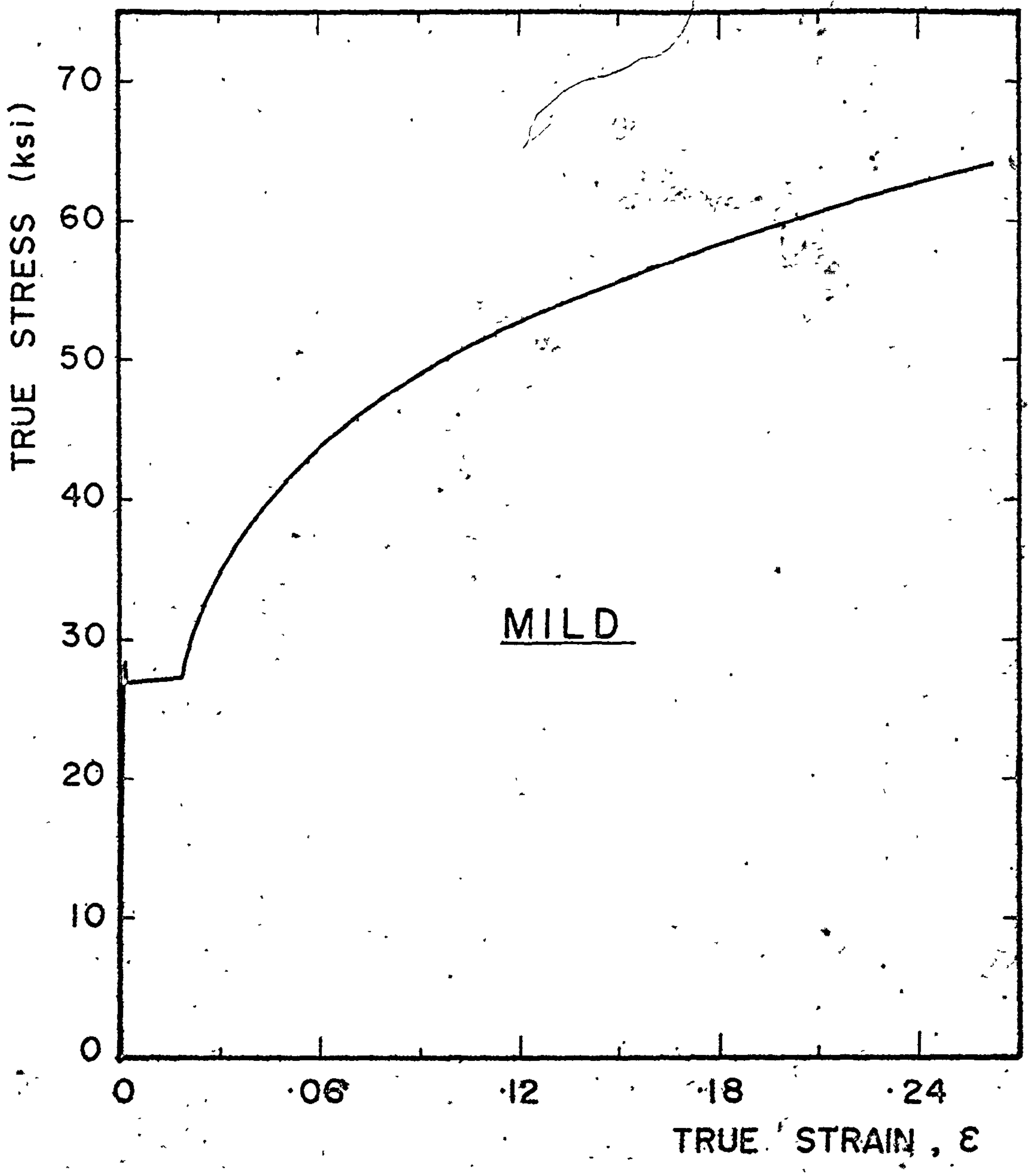

Fig. E.5(a) - Experimental tensile true stress-true strain diagram for Mild steel in the as received condition

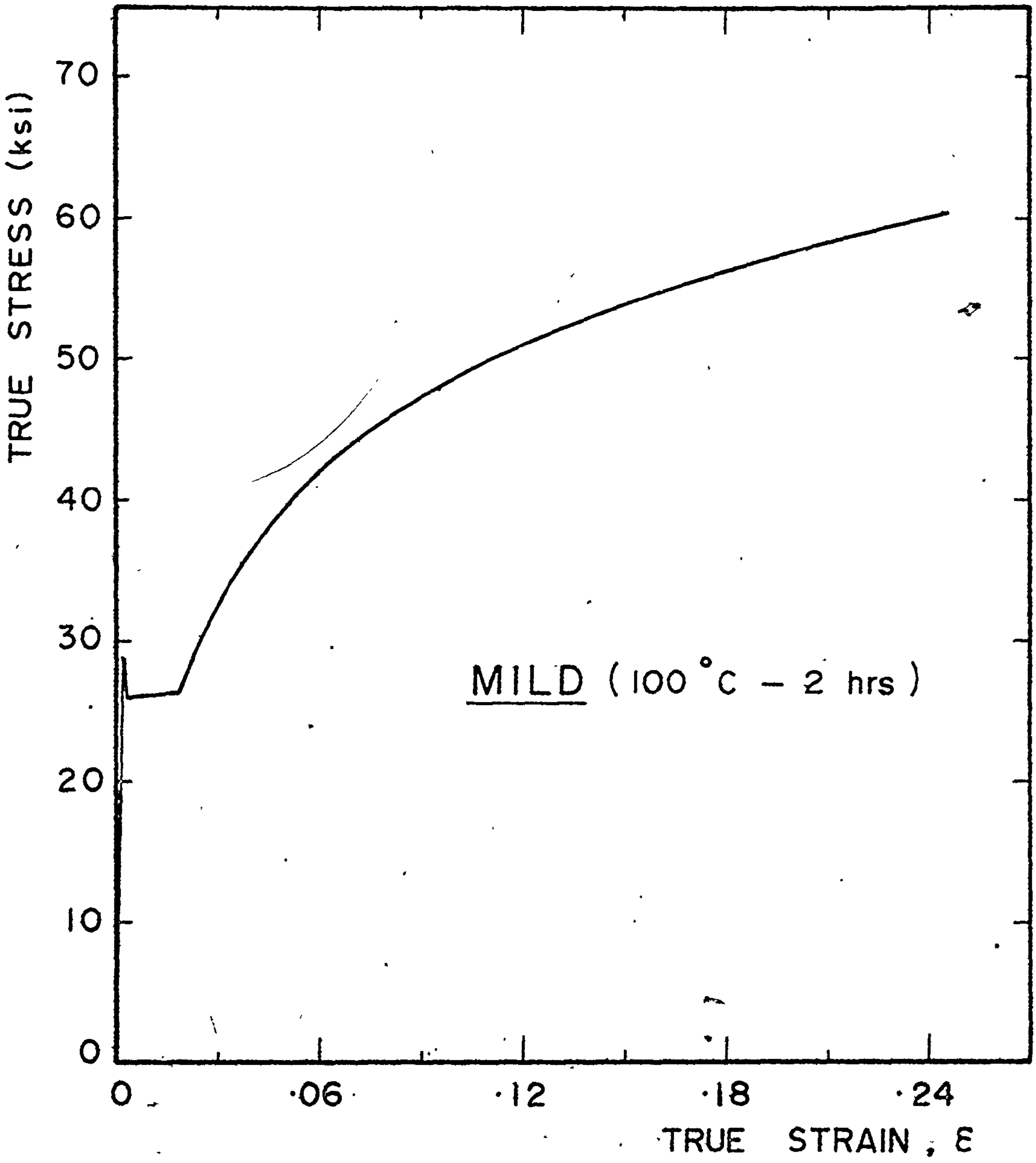

Fig. E.5(b) - Experimental tensile true stress-true strain diagram for Mild steel, aged at 100°C for 2 hours

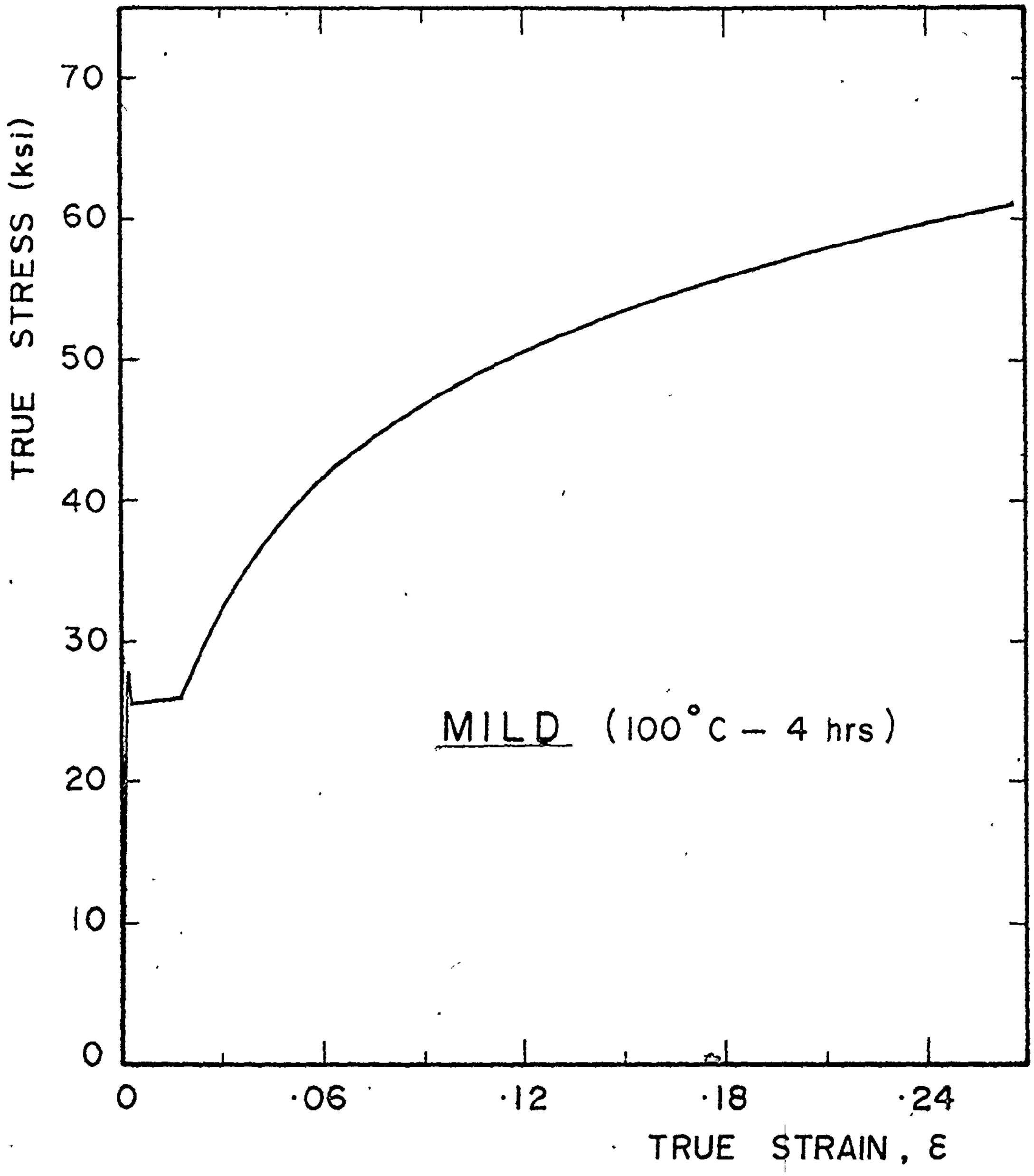

Fig. E.5(c) - Experimental tensile true stress-true strain diagram for Mild steel, aged at 100°C for 4 hours

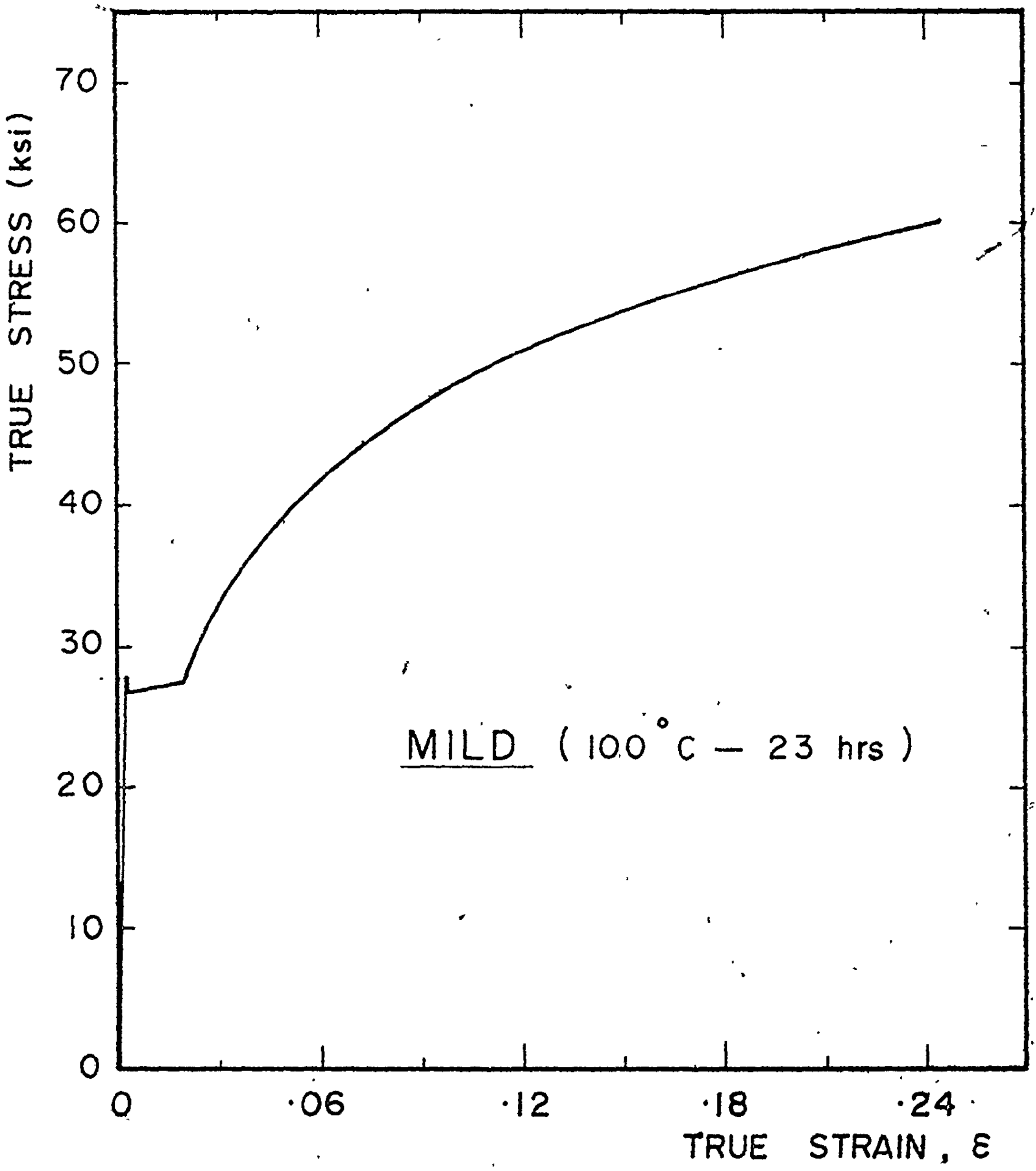

Fig. E.5(d) - Experimental tensile true stress-true strain diagram for Mild steel, aged at 100°C for 23 hours

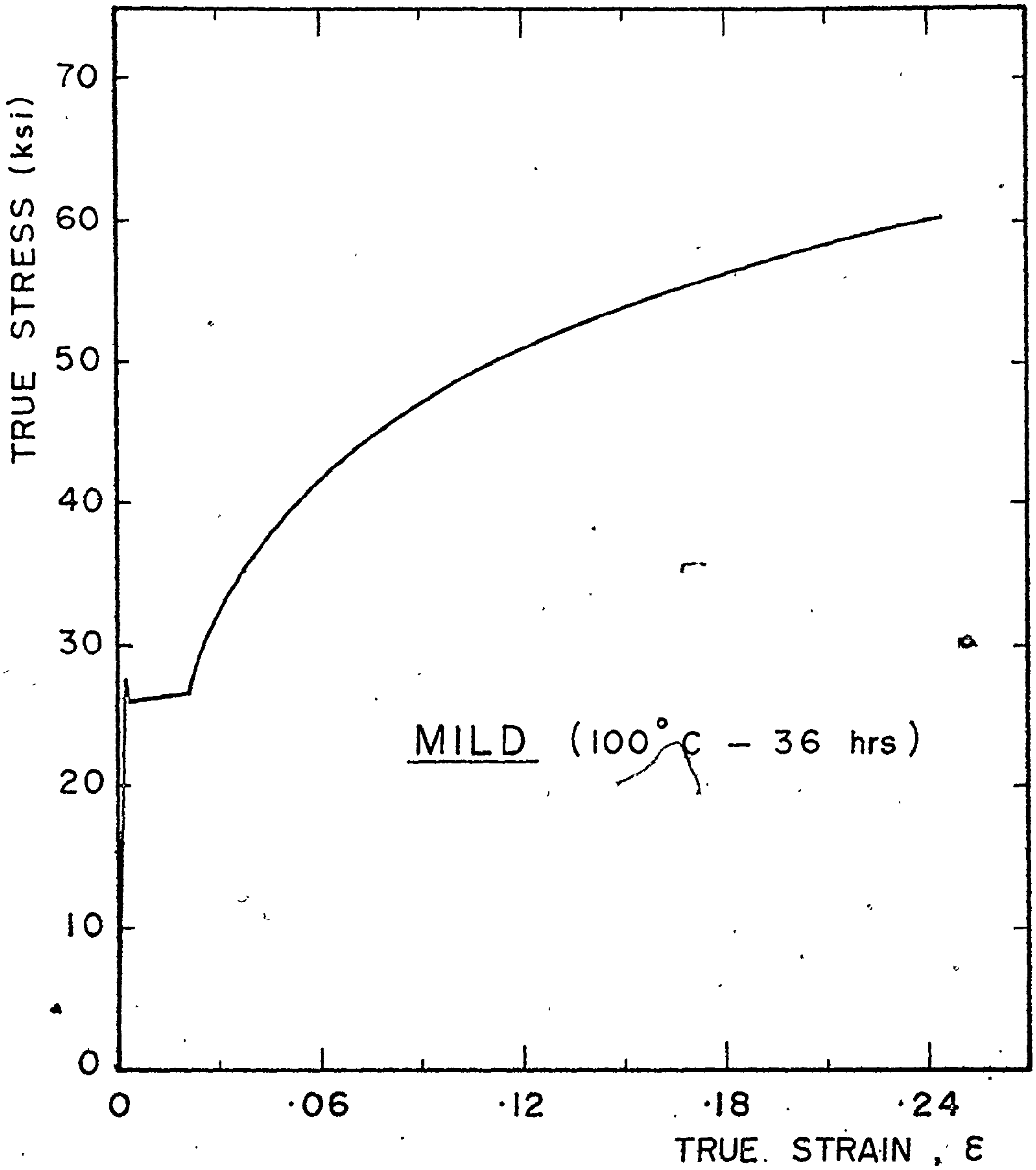

Fig. E.5(e) - Experimental tensile true stress-true strain diagram for Mild steel, aged at 100°C for 36 hours

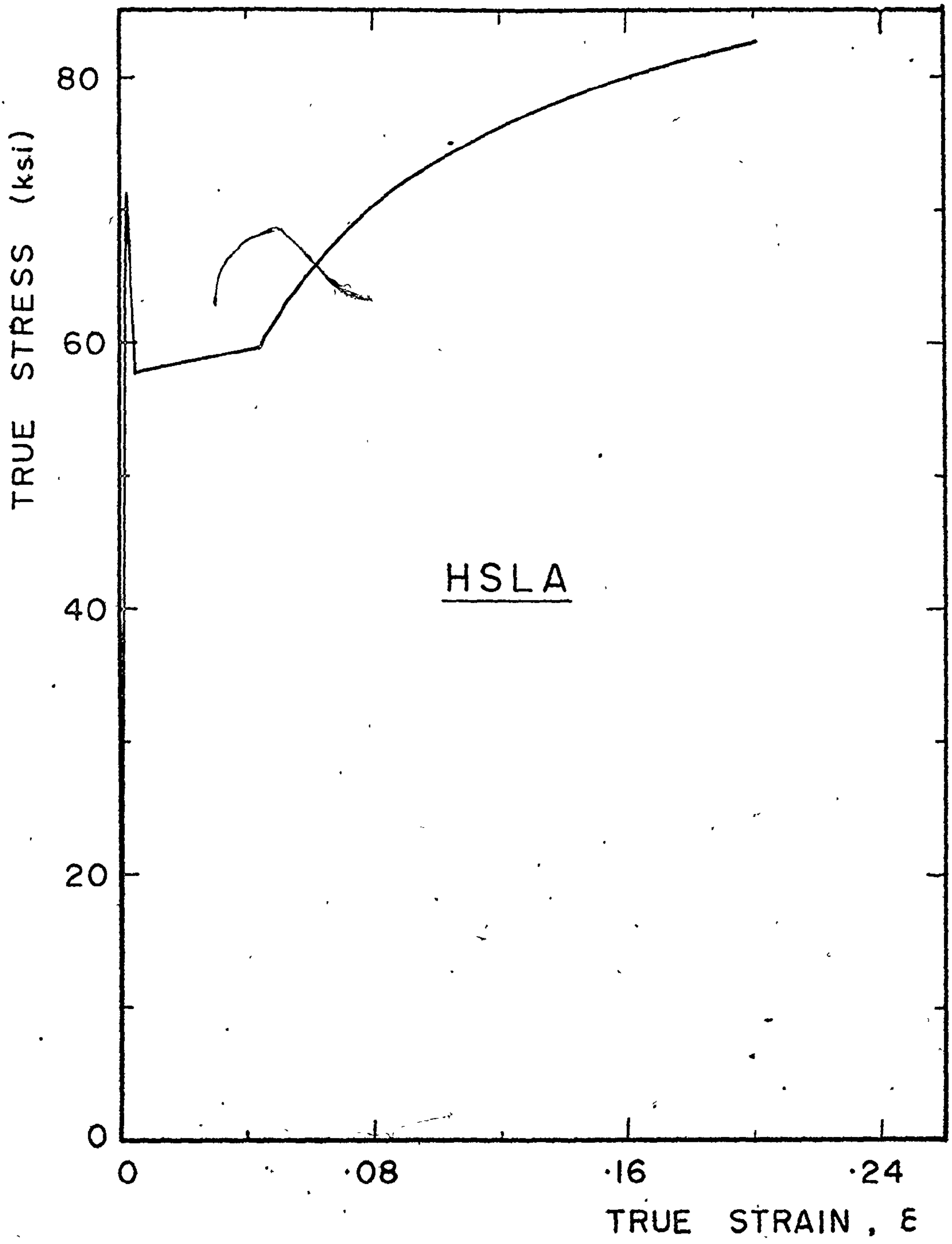

Fig. E.6(a) - Experimental tensile true stress-true strain diagram for HSLA steel in the as received condition

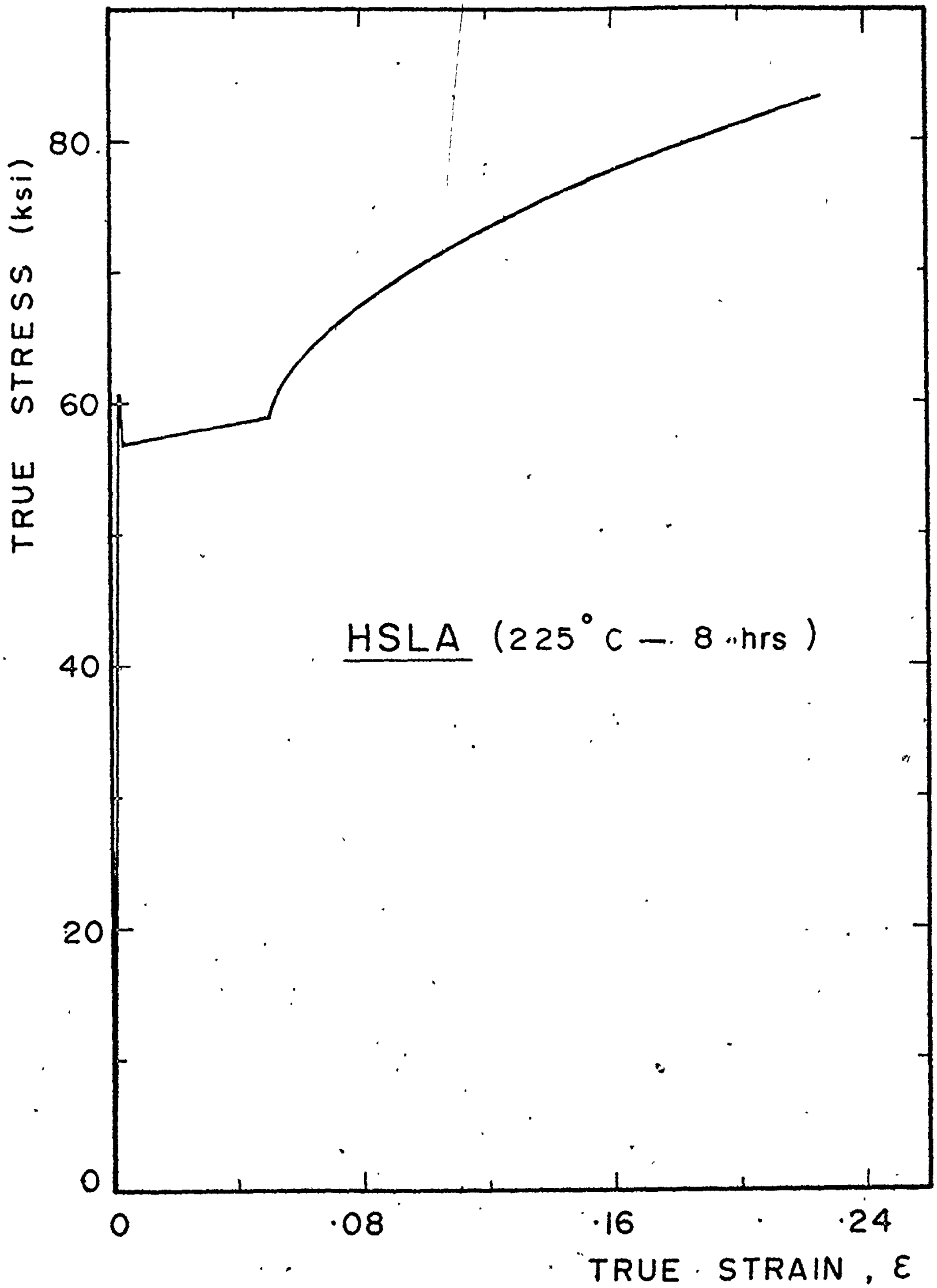

Fig. E.6(b) - Experimental tensile true stress-true strain diagram for HSLA steel, aged at 225°C for 8 hours

APPENDIX F

COMPARISON OF EXPERIMENTAL RESULTS WITH THE THEORETICAL CURVE GENERATED FROM MODEL I

Figures F.1(a) to 1(h) show the curves for aged Rimmed steel-A.

Figures F.2(a) to 2(c) show the curves for aged Rimmed steel-B.

Figures F.3(a) to 3(e) show the curves for Rimmed steel-B' in the as received and aged conditions.

Figure F.4(a) to 4(d) show the curves for aged Rimmed steel-C.

Figures F.5(a) to 5(d) show the curves for aged Mild steel.

Figure F.6 shows the curve for aged HSLA steel.

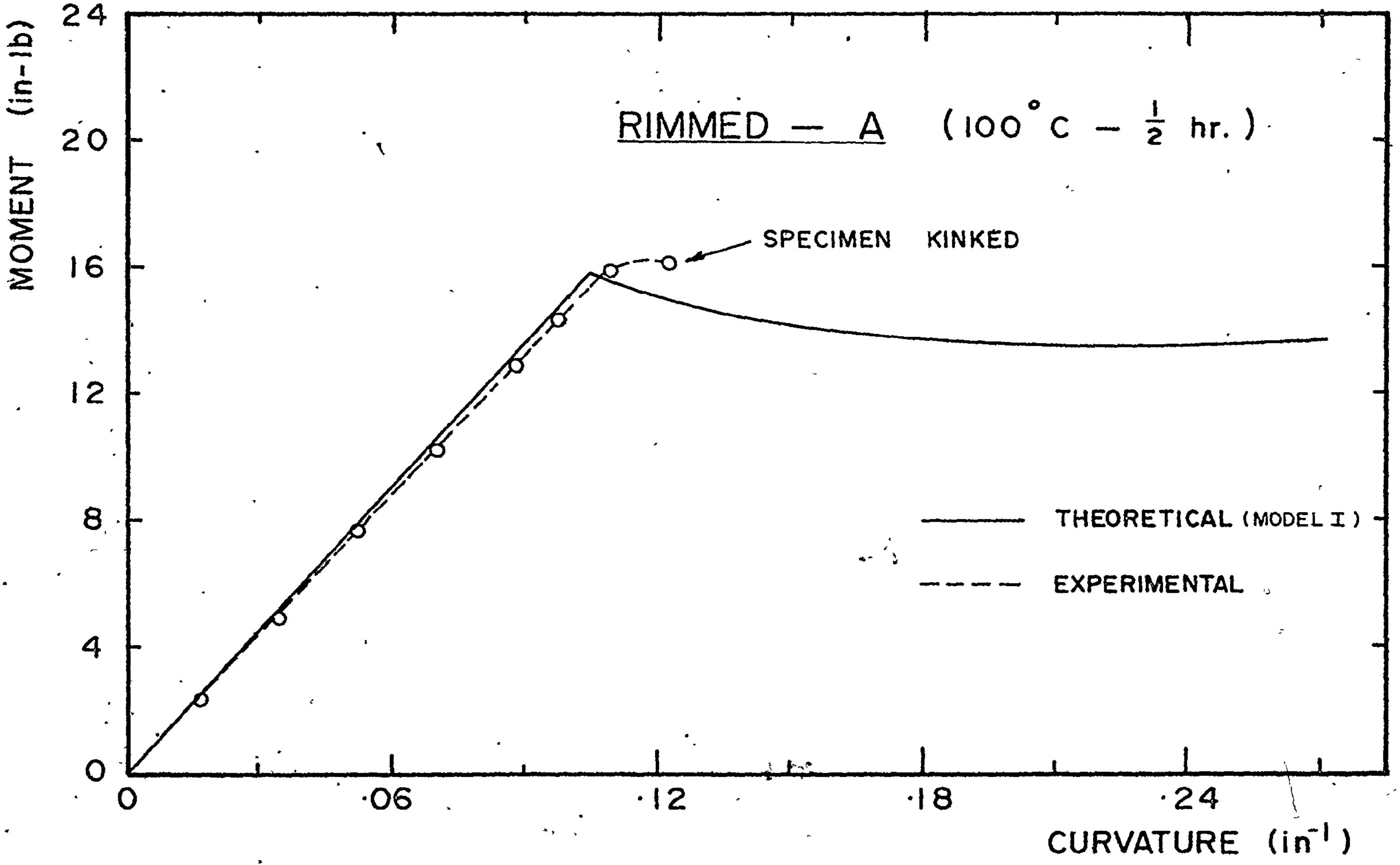

Fig. F.1(a) - Comparison of experimental moment-curvature results with the theoretical curve from Model I for Rimmed steel-A, aged at 100°C for 0.5 hours

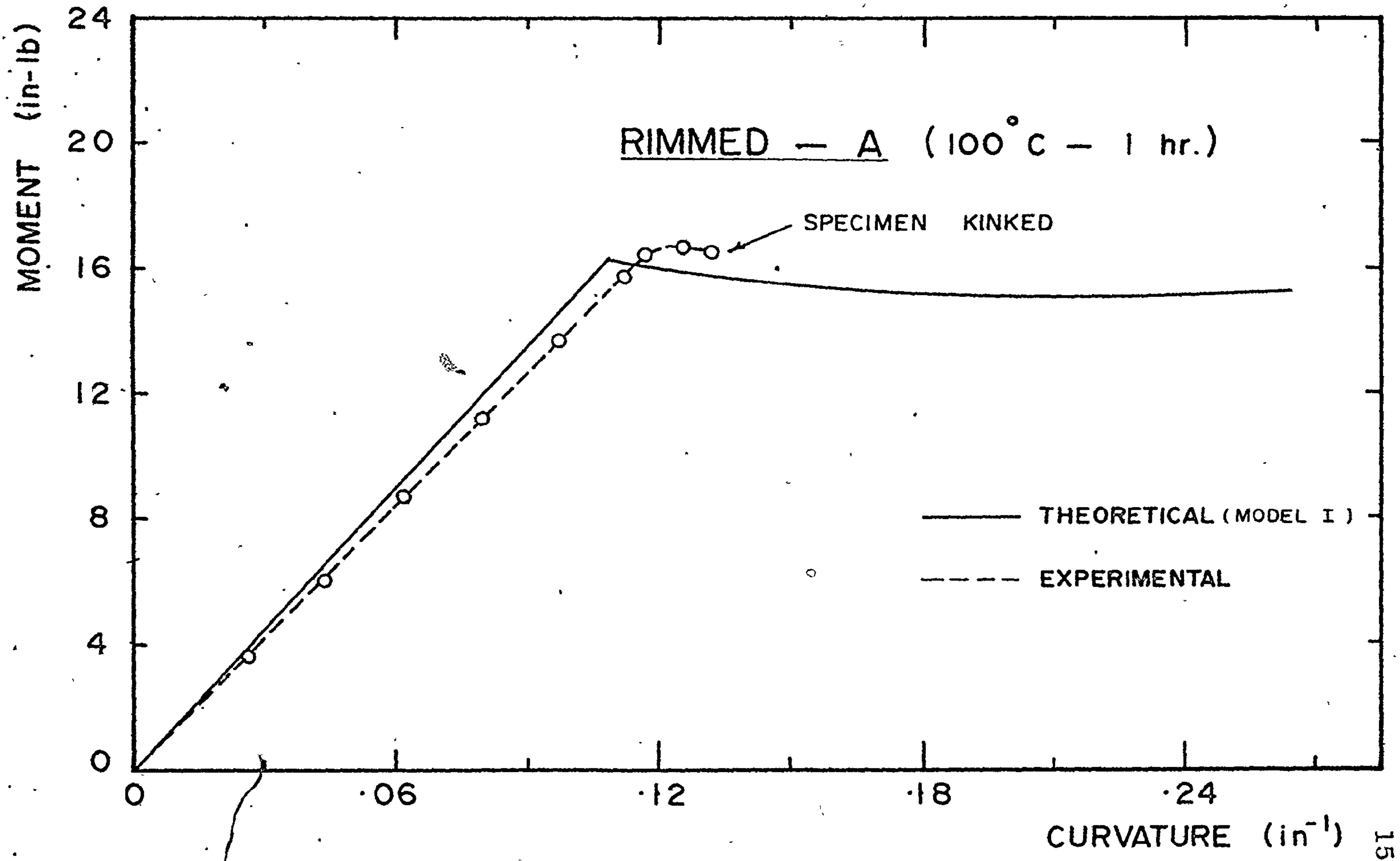

Fig. F.1(b) - Comparison of experimental moment-curvature results with the theoretical curve from Model I for Rimmed steel-A, aged at 100°C for 1 hour

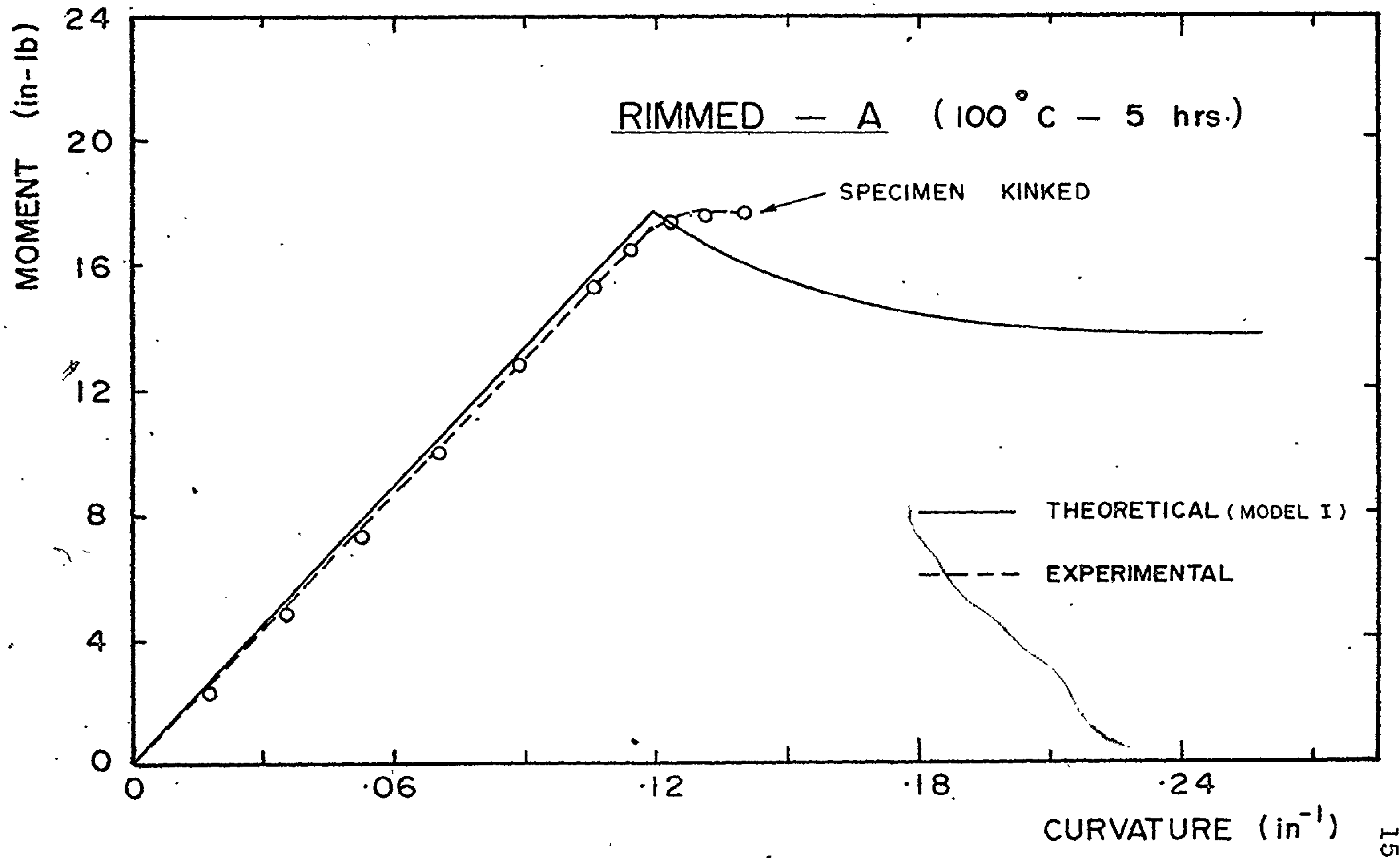

Fig. F.1(c) - Comparison of experimental moment-curvature results with the theoretical curve from Model I for Rimmed steel-A, aged at 100^{o}C for 5 hours

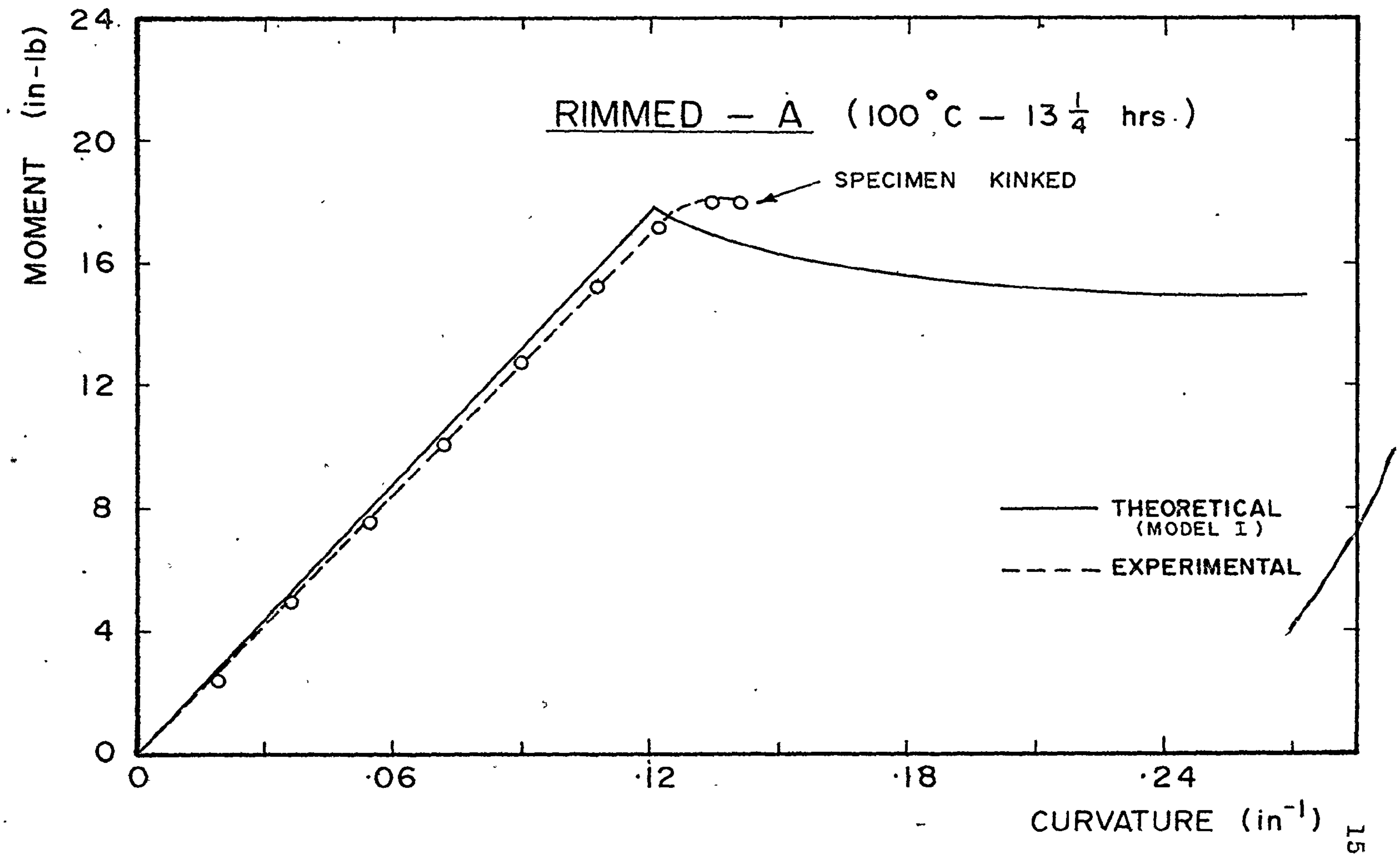

Fig. F.1(d) - Comparison of experimental moment-curvature results with the theoretical curve from Model I for Rimmed steel-A, aged at 100°C for 13.25 hours

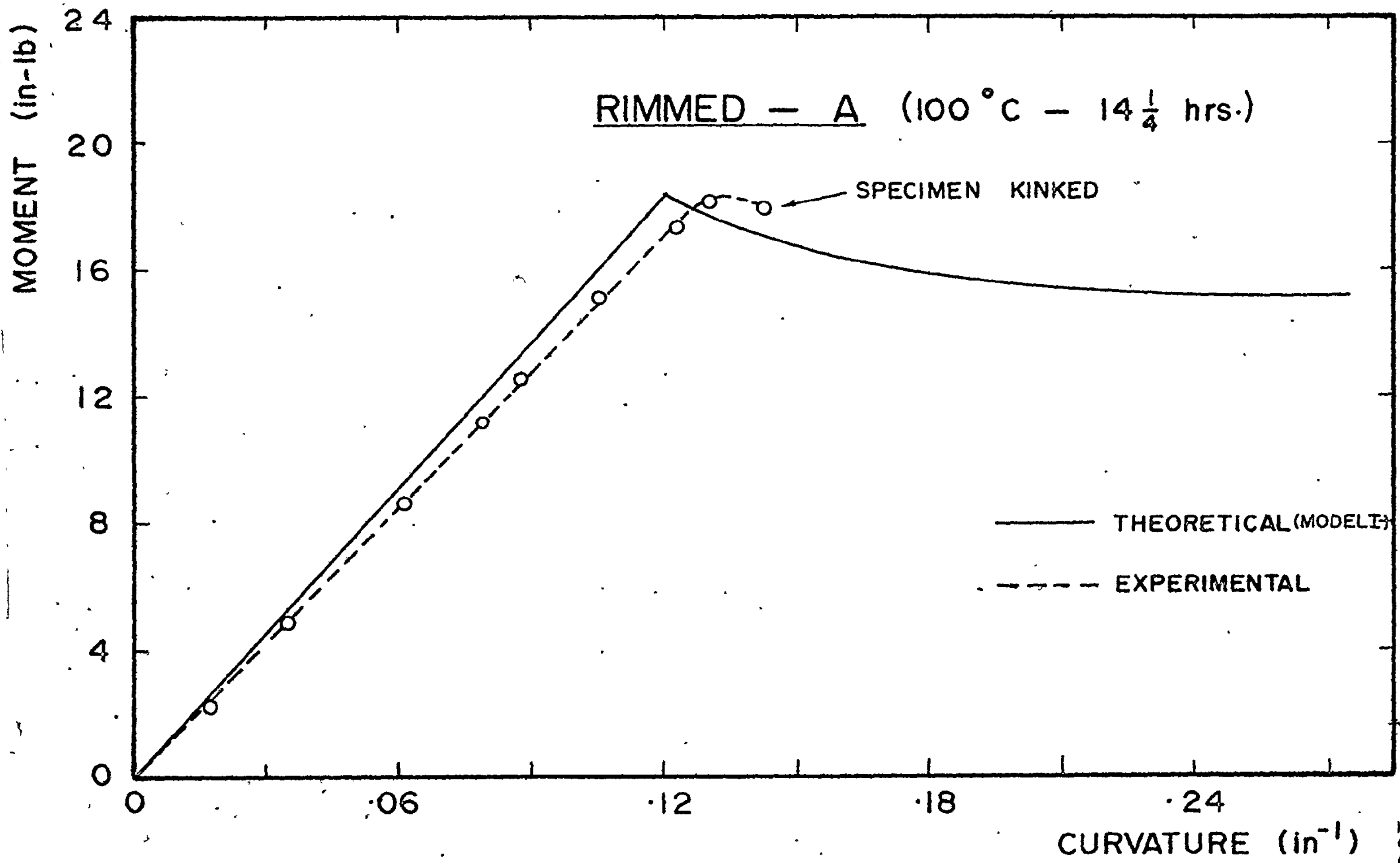

Fig. F.1(e) - Comparison of experimental moment-curvature results with the theoretical curve from Model I for Rimmed steel-A, aged at 100°C for 14.25 hours

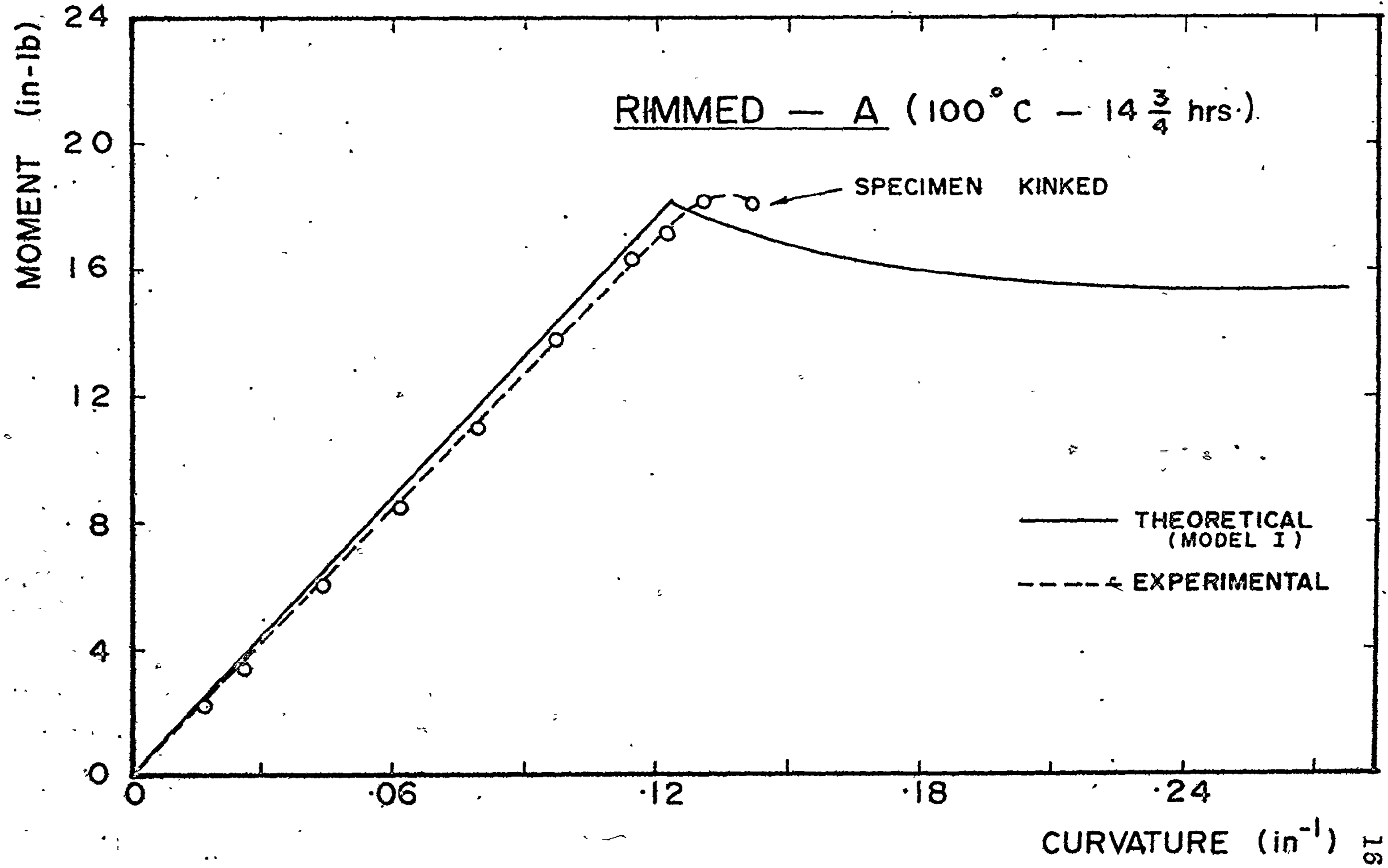

Fig. F.1(f) - Comparison of experimental moment-curvature results with the theoretical curve from Model I for Rimmed steel-A, aged at 100°C for 14.75 hours

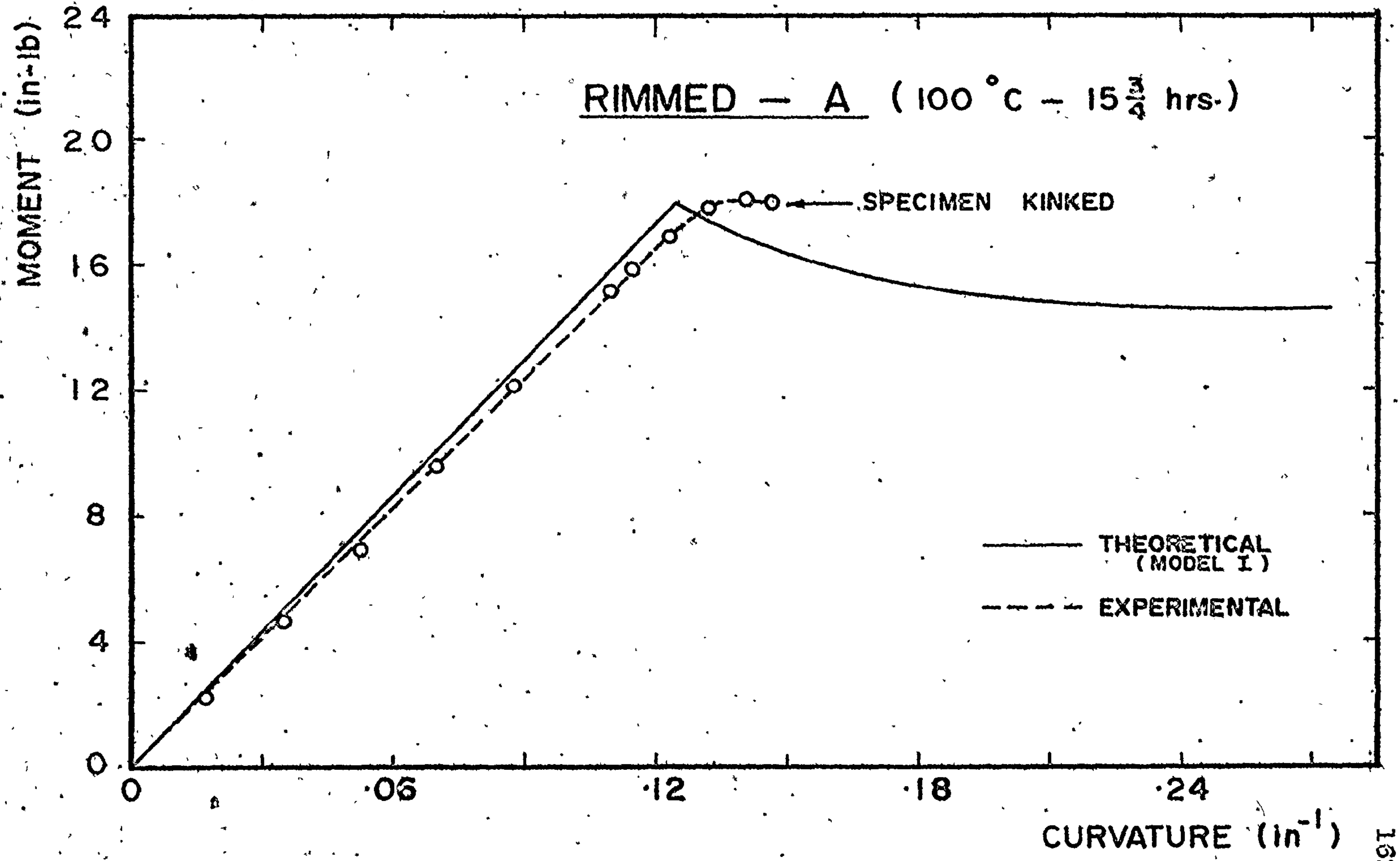

Fig. F.1(g) - Comparison of experimental moment-curvature results with the theoretical curve from Model I for Rimmed steel-A, aged at 100°C for 15.75 hours

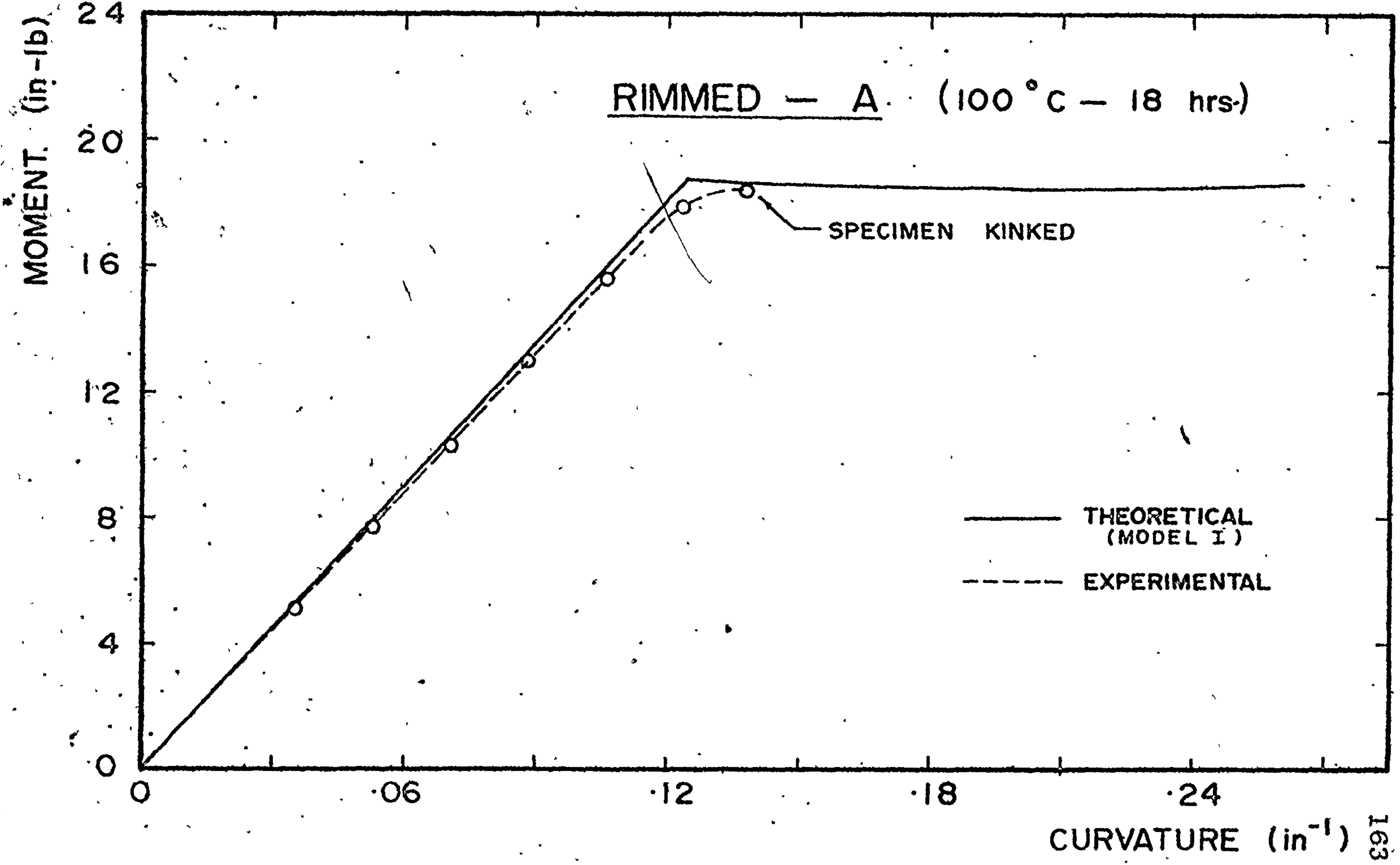

Fig. F.1(h) : Comparison of experimental moment-curvature results with the theoretical curve from Model I for Rimmed steel-A, aged at 100°C for 18 hours

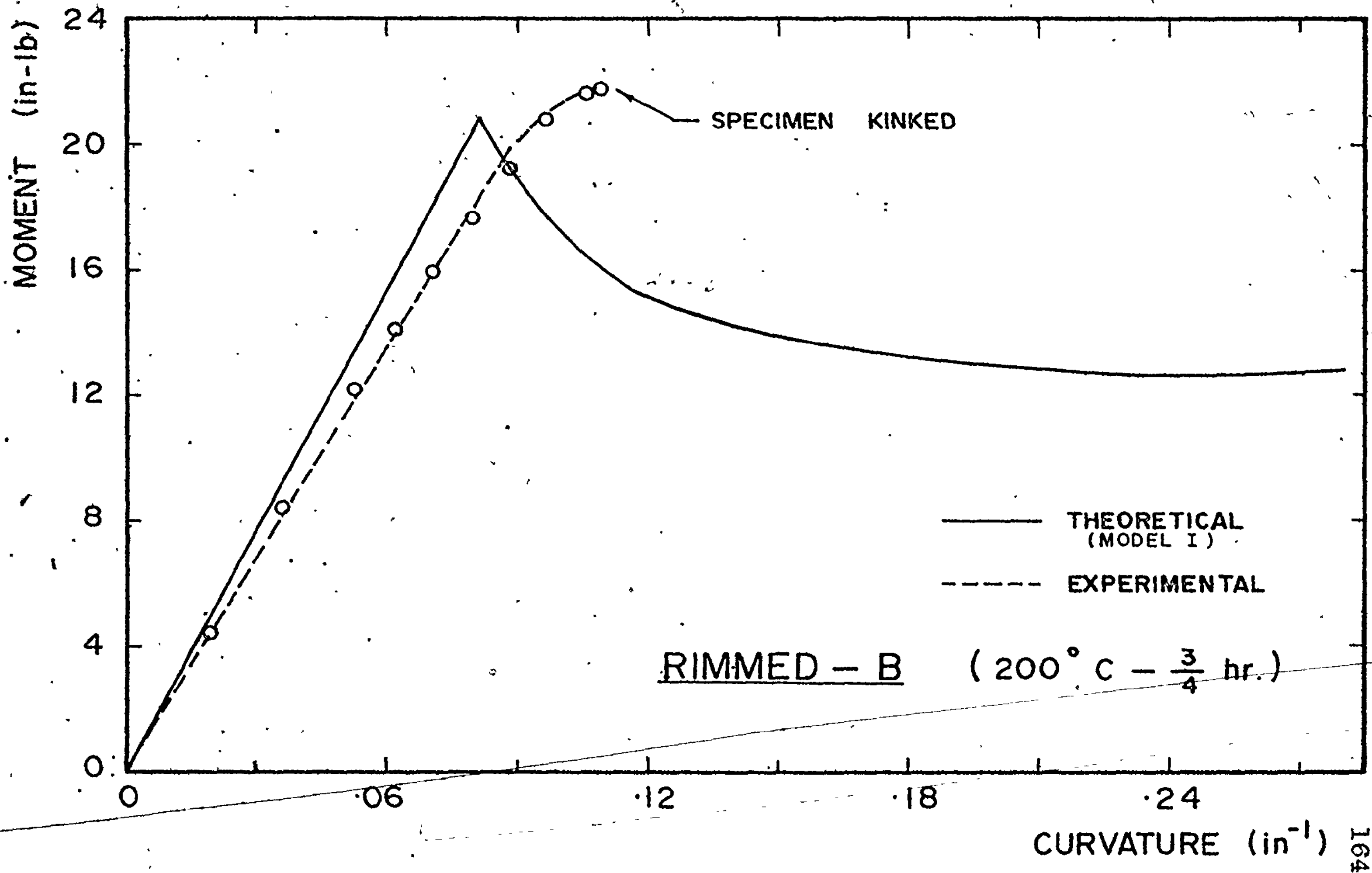

Fig. F.2(a) - Comparison of experimental moment-curvature results with the theoretical curve from Model I for Rimmed steel-B, aged at 200°C for 0.75 hours

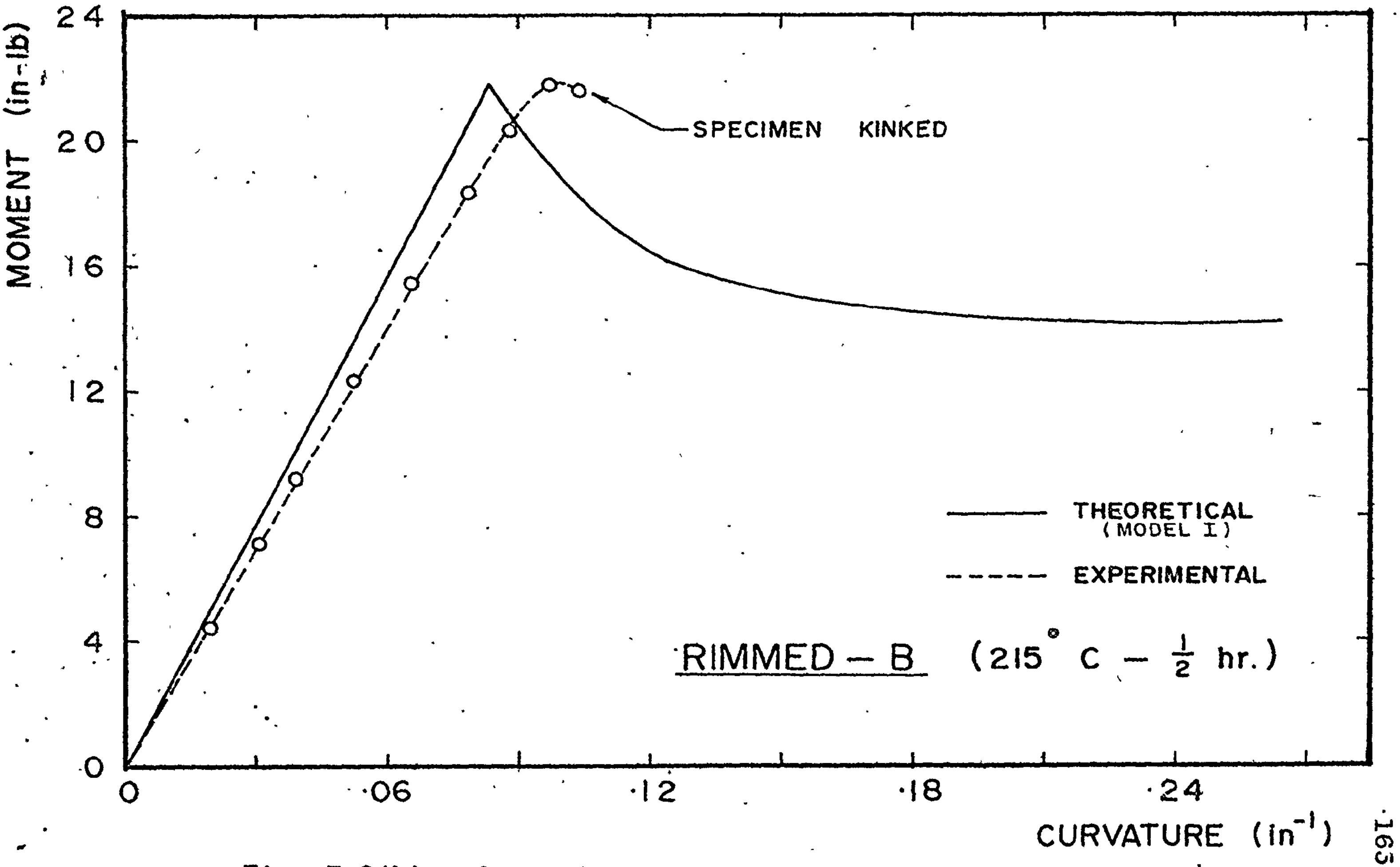

Fig. F.2(b) - Comparison of experimental moment-curvature results with the theoretical curve from Model I for Rimmed steel-B, aged at 215°C for 0.5 hours

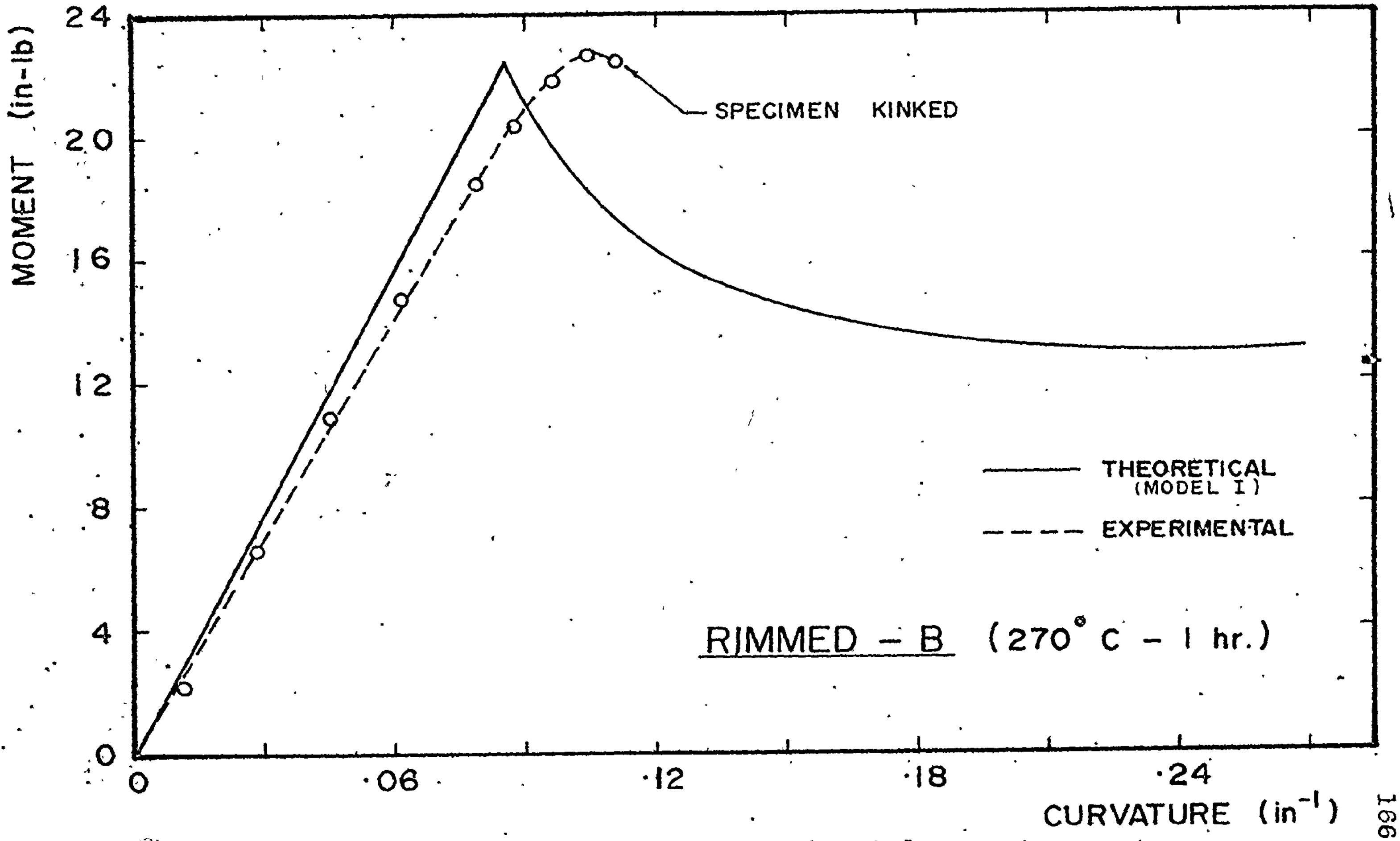

Fig. F.2(c) - Comparison of experimental moment-curvature results with the theoretical curve from Model I for Rimmed steel-B, aged at 270°C for 1 hour

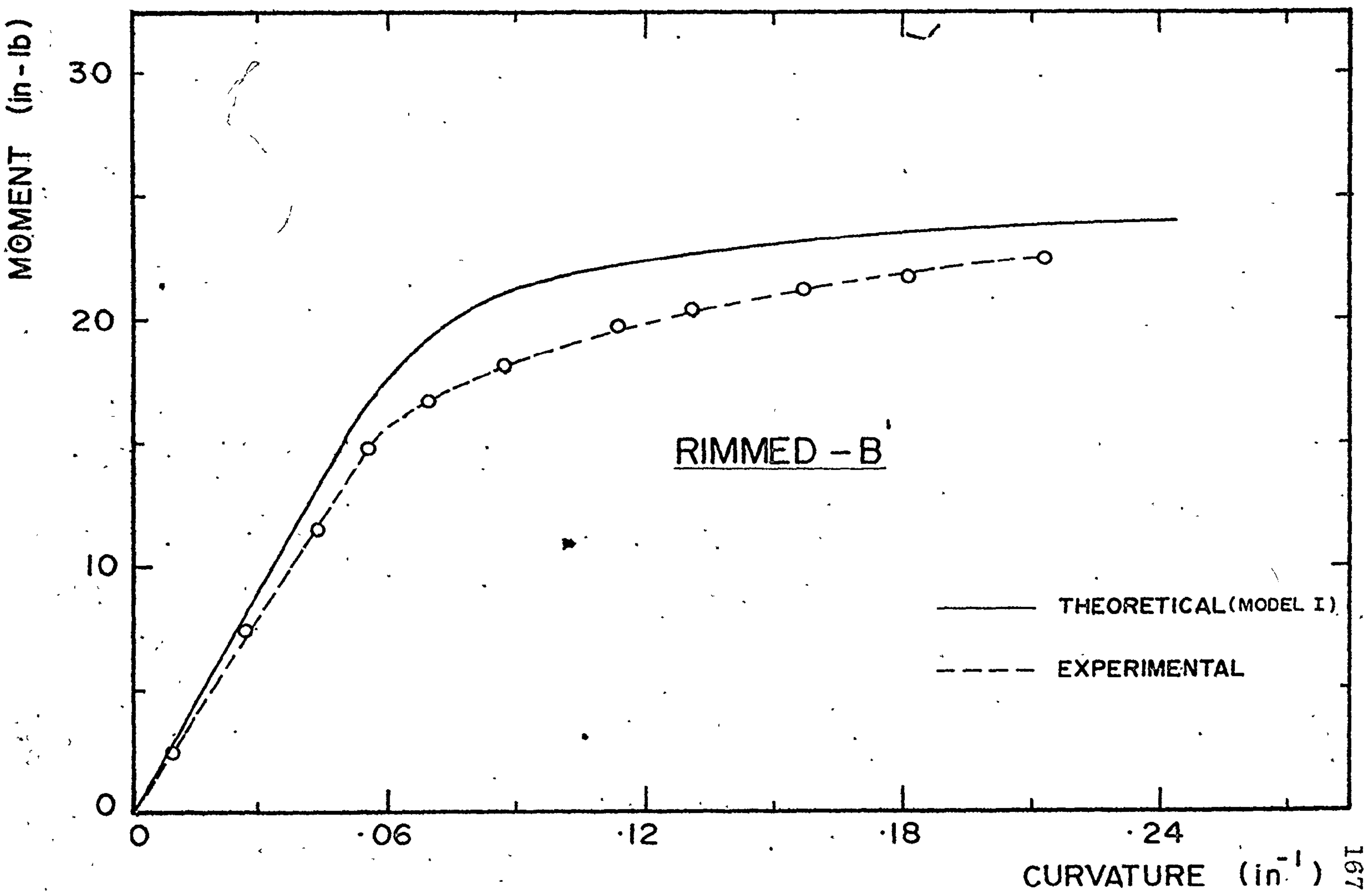

Fig. F.3(a) - Comparison of experimental moment-curvature results with the theoretical curve from Model I for Rimmed steel-B'.

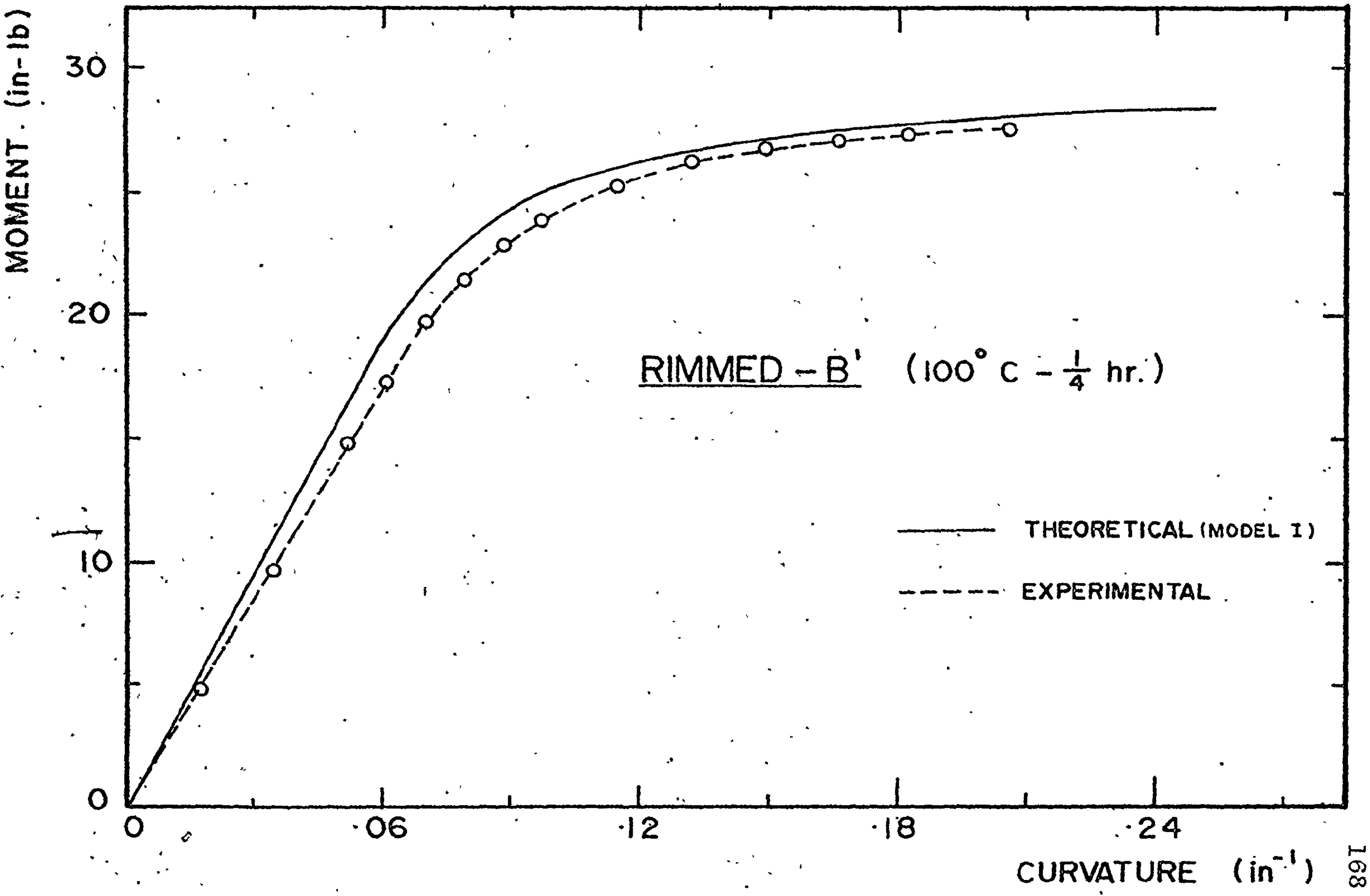

Fig. F.3(b) - Comparison of experimental moment-curvature results with the theoretical curve from Model I for Rimmed steel-B', aged at 100°C for 0.25 hours

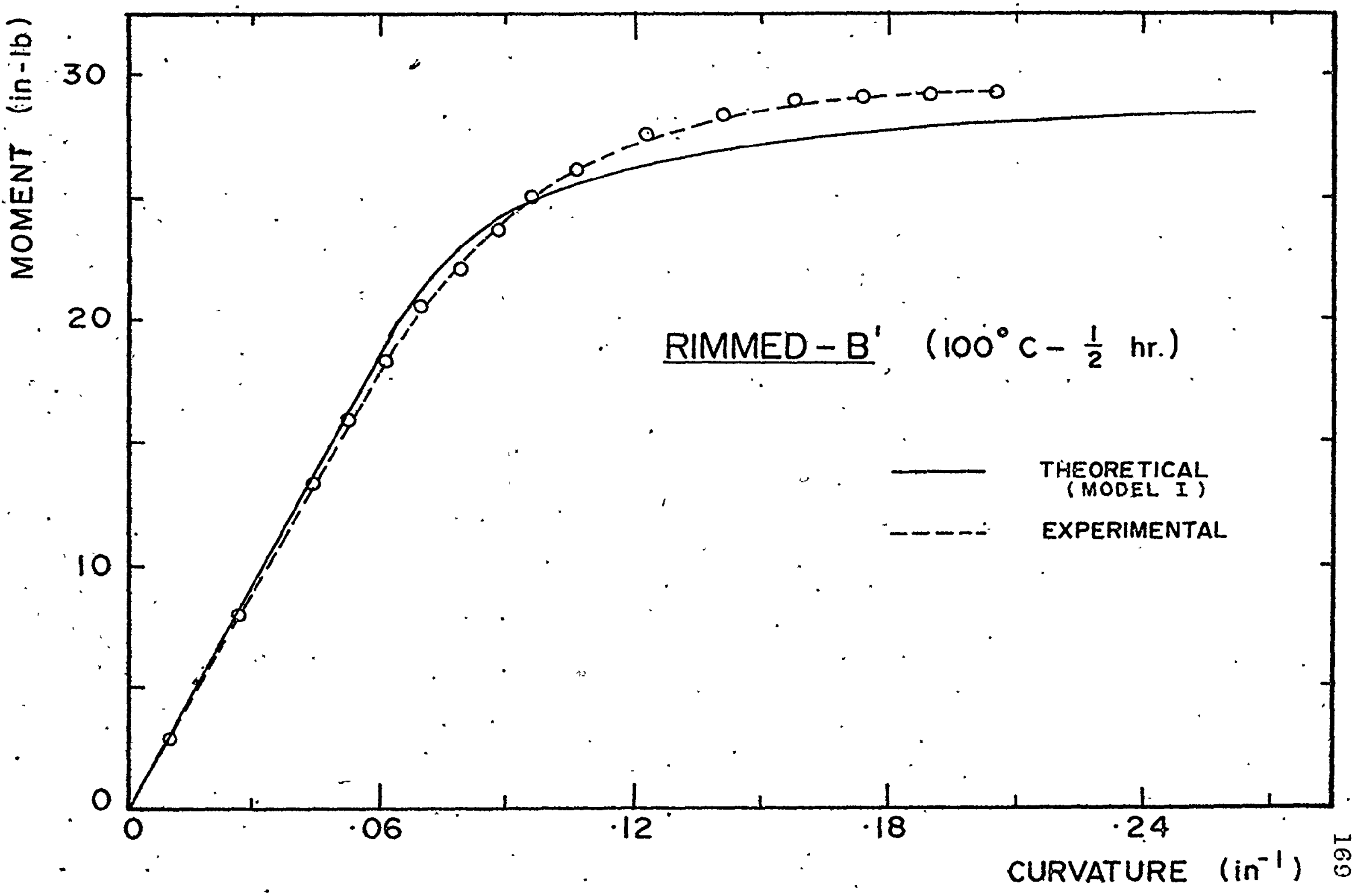

Fig. F.3(c) - Comparison of experimental moment-curvature results with the theoretical curve from Model I for Rimmed steel-B', aged at 100°C for 0.5 hours

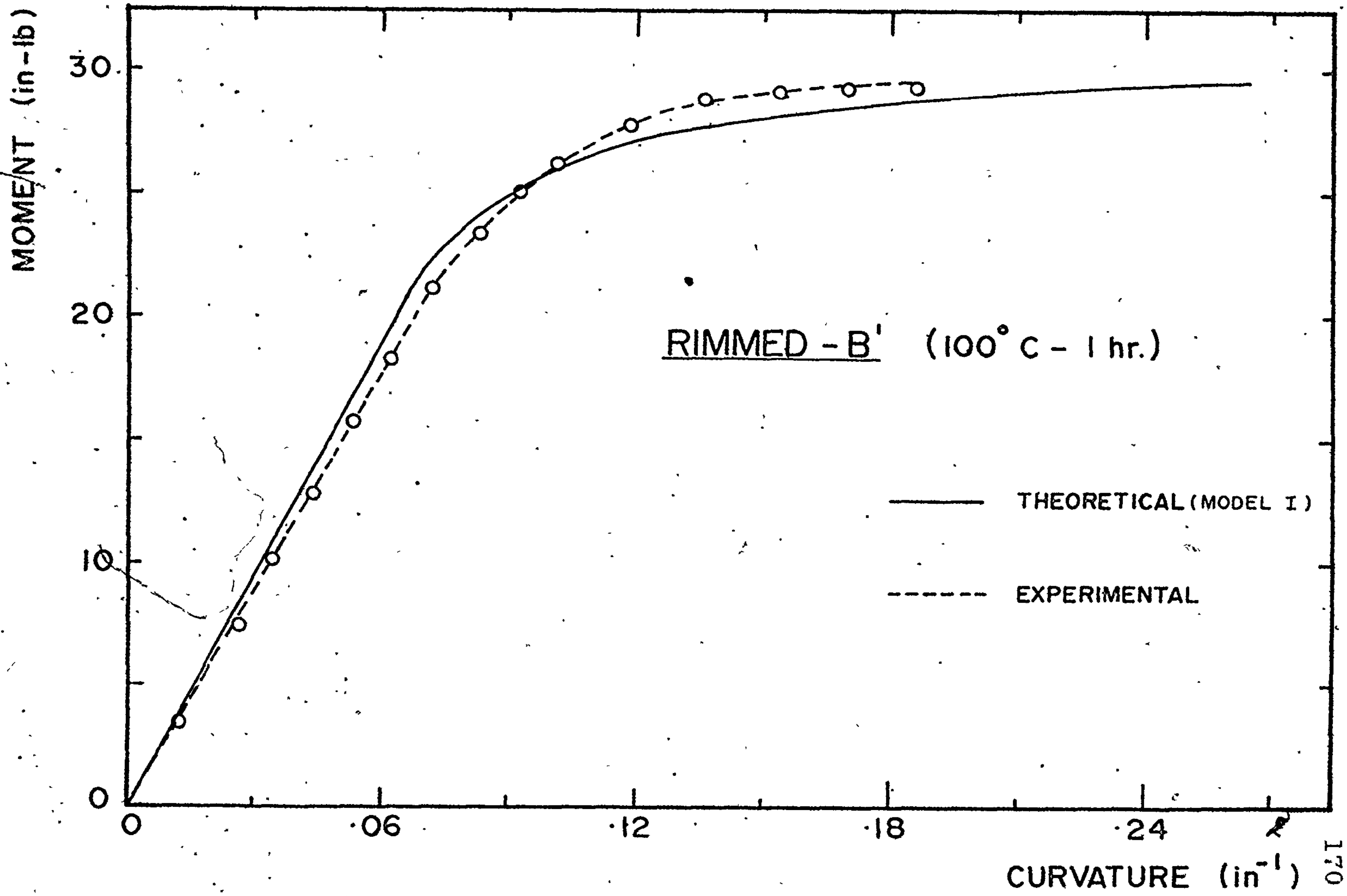

Fig. F.3(d) - Comparison of experimental moment-curvature results with the theoretical curve from Model I for Rimmed steel-B', aged at 100°C for 1 hour

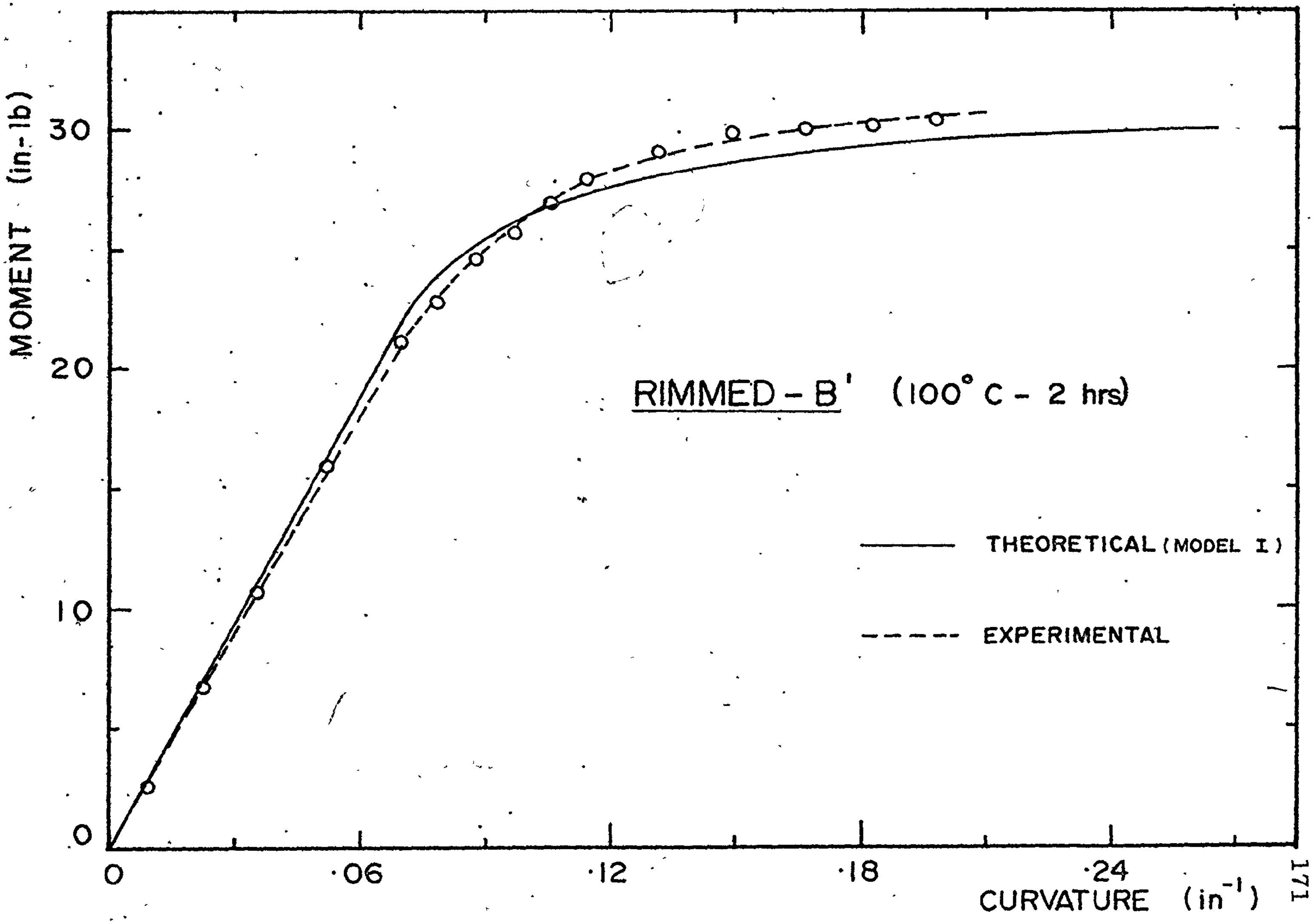

Fig. F.3(e) - Comparison of experimental moment-curvature results with the theoretical curve from Model I for Rimmed steel-B', aged at 100°C for 2 hours

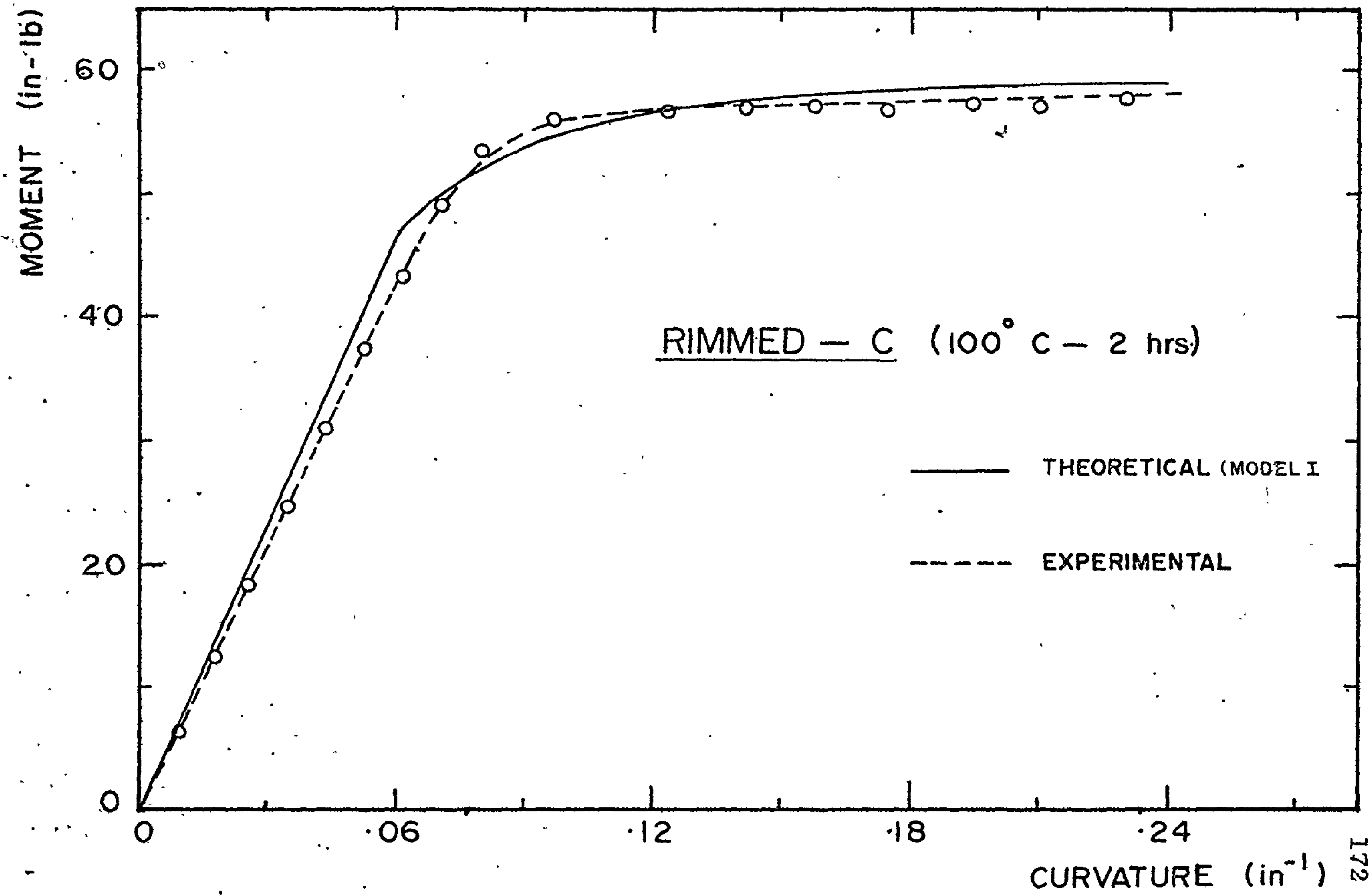

Fig. F.4(a) - Comparison of experimental moment-curvature results with the theoretical curve from Model I for Rimmed steel-C, aged at 100°C for 2 hours

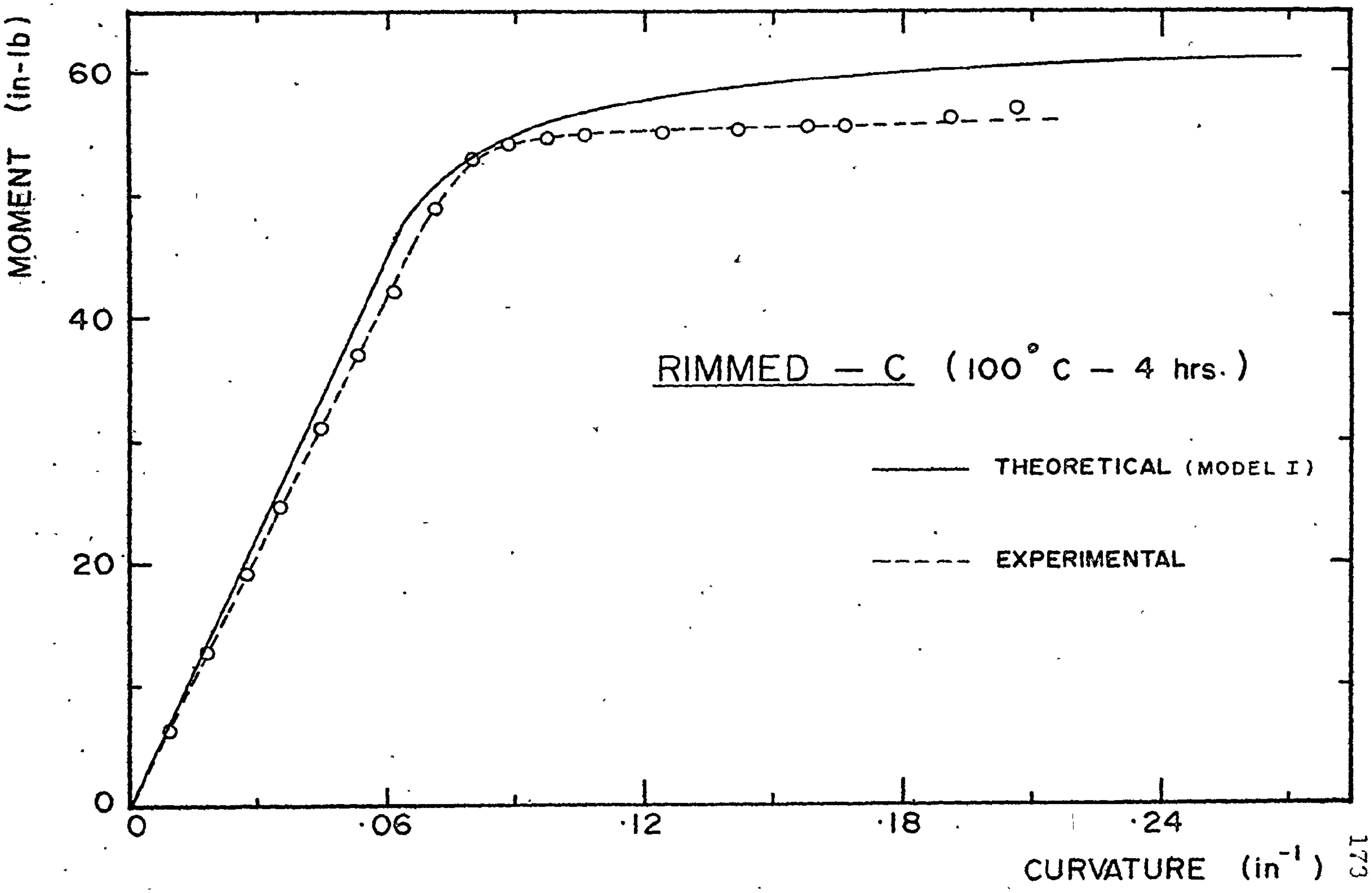

Fig. F.4(b) - Comparison of experimental moment-curvature results with the theoretical curve from Model I for Rimmed steel-C, aged at 100°C for 4 hours

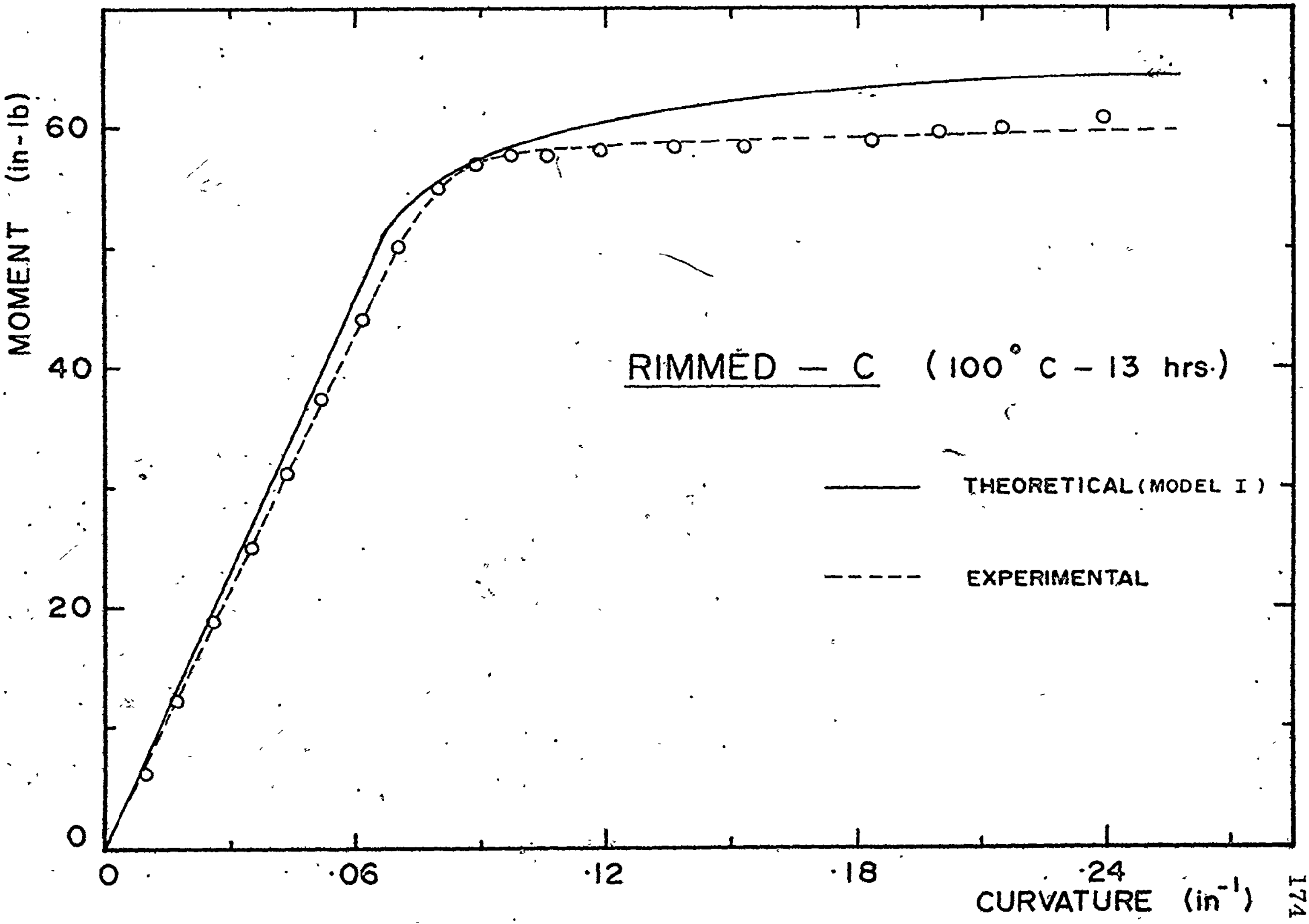

Fig. F.4(c) - Comparison of experimental moment-curvature results with the theoretical curve from Model I for Rimmed steel-C, aged at 100°C for 13 hours

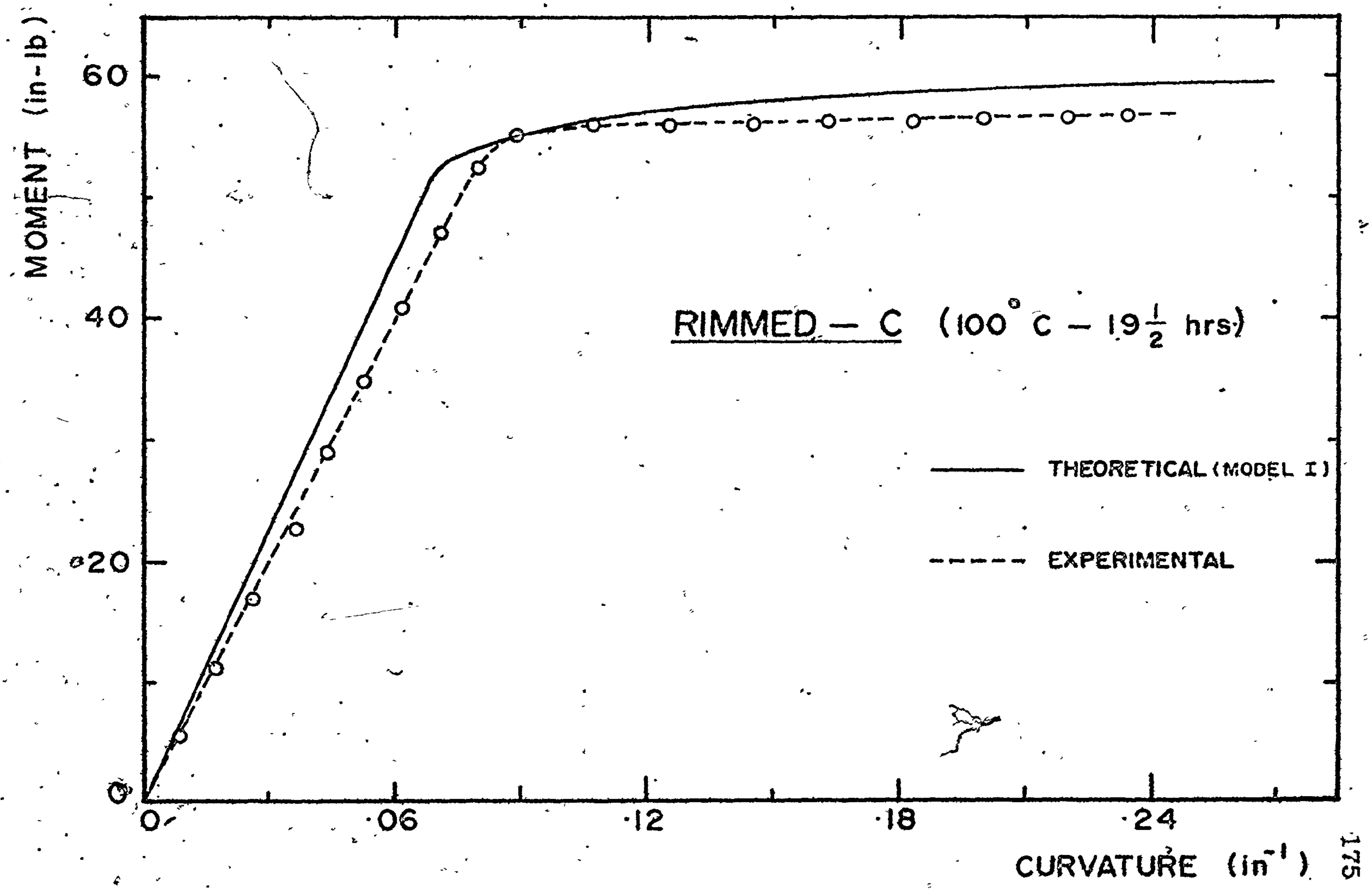

Fig. F.4(d) - Comparison of experimental moment-curvature results with the theoretical curve from Model I for Rimmed steel-C, aged at 100°C for 19.5 hours

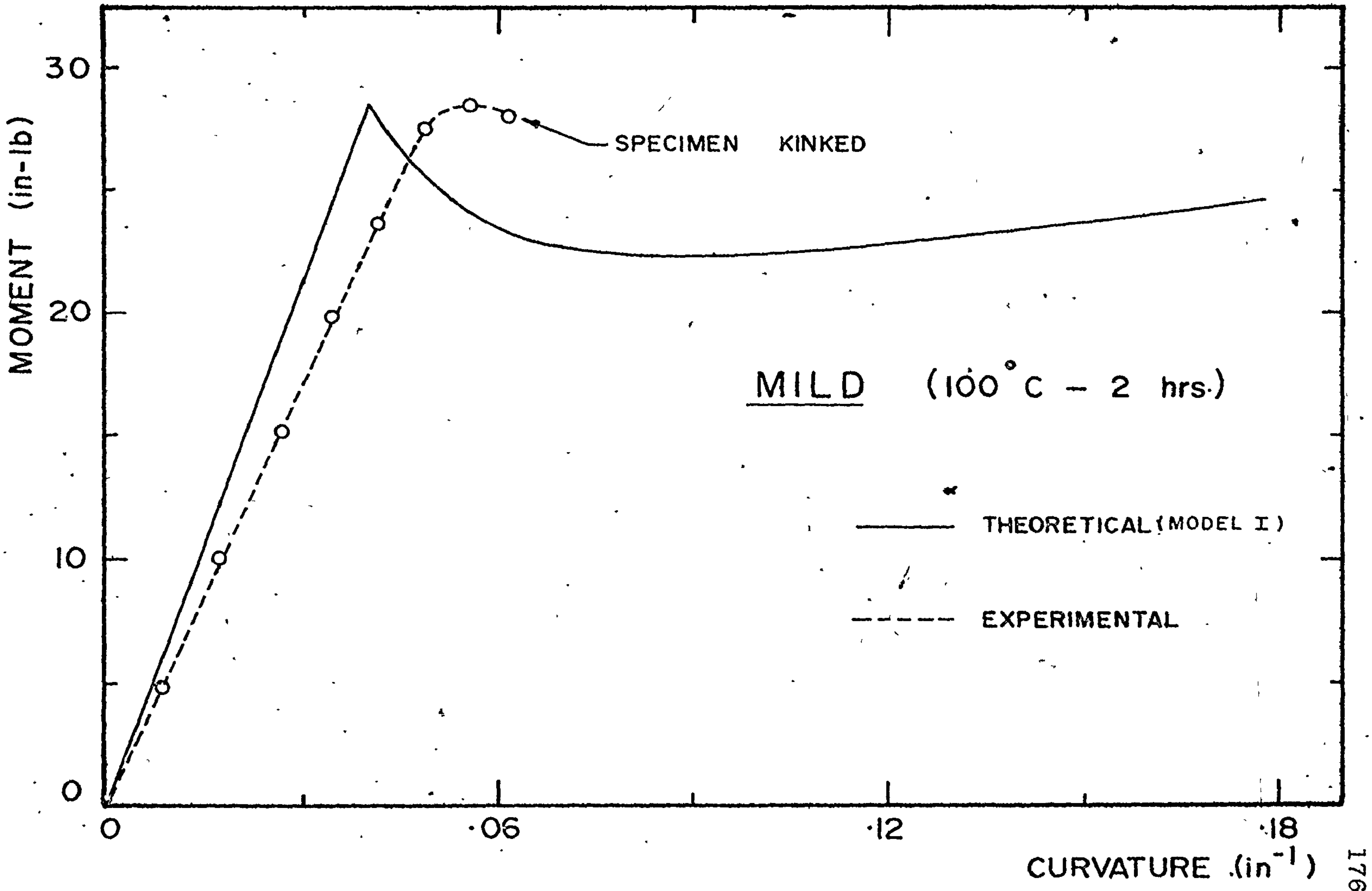

Fig. F.5(a) - Comparison of experimental moment-curvature results with the theoretical curve for Mild steel, aged at 100°C for 2 hours

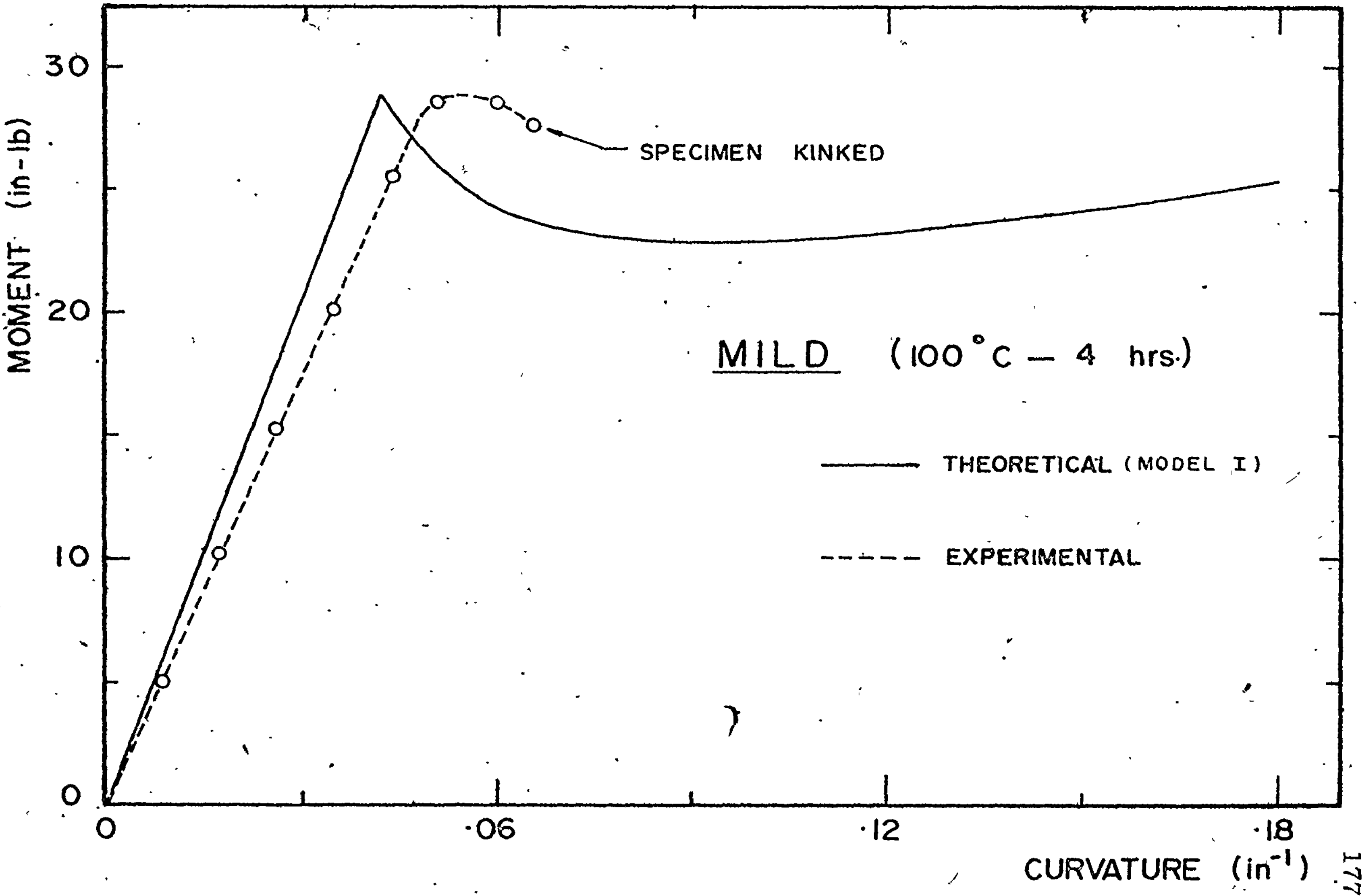

Fig. F.5(b) - Comparison of experimental moment-curvature results with the theoretical curve for Mild steel, aged at 100°C for 4 hours

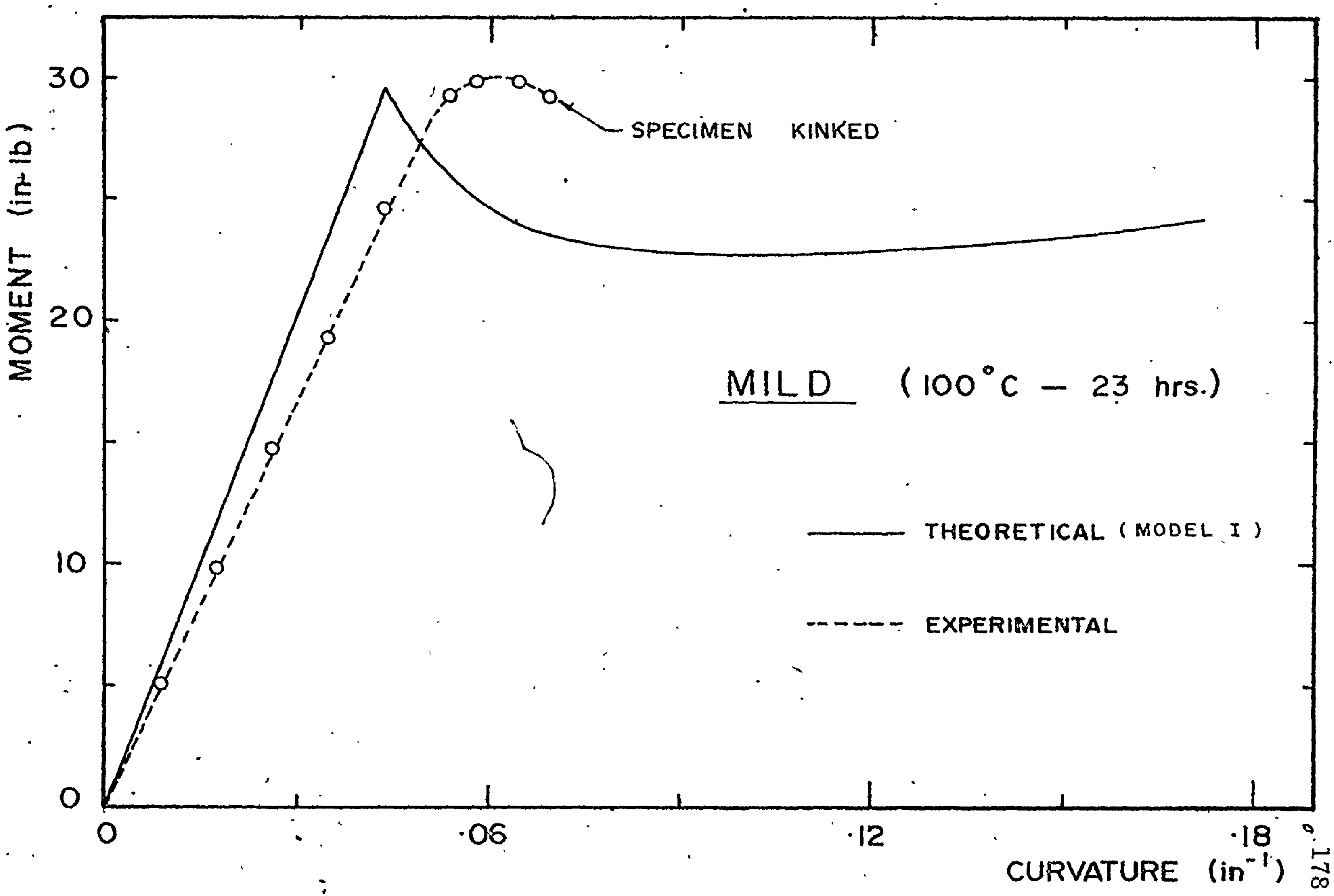

Fig. F.5(c) - Comparison of experimental moment-curvature results with the theoretical curve for Mild steel, aged at 100°C for 23 hours

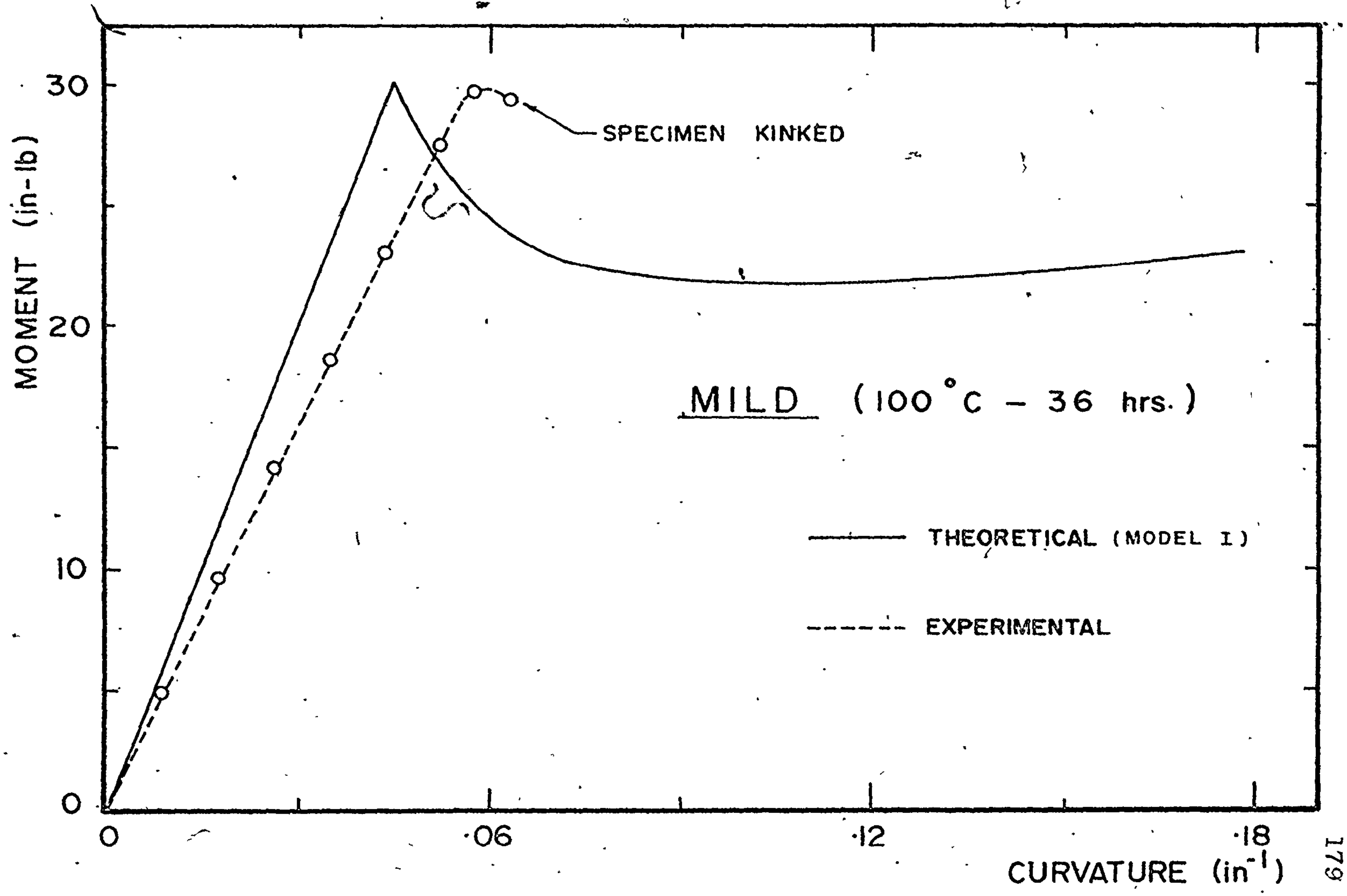

Fig. F.5(d) - Comparison of experimental moment-curvature results with the theoretical curve for Mild steel, aged at 100°C for 36 hours

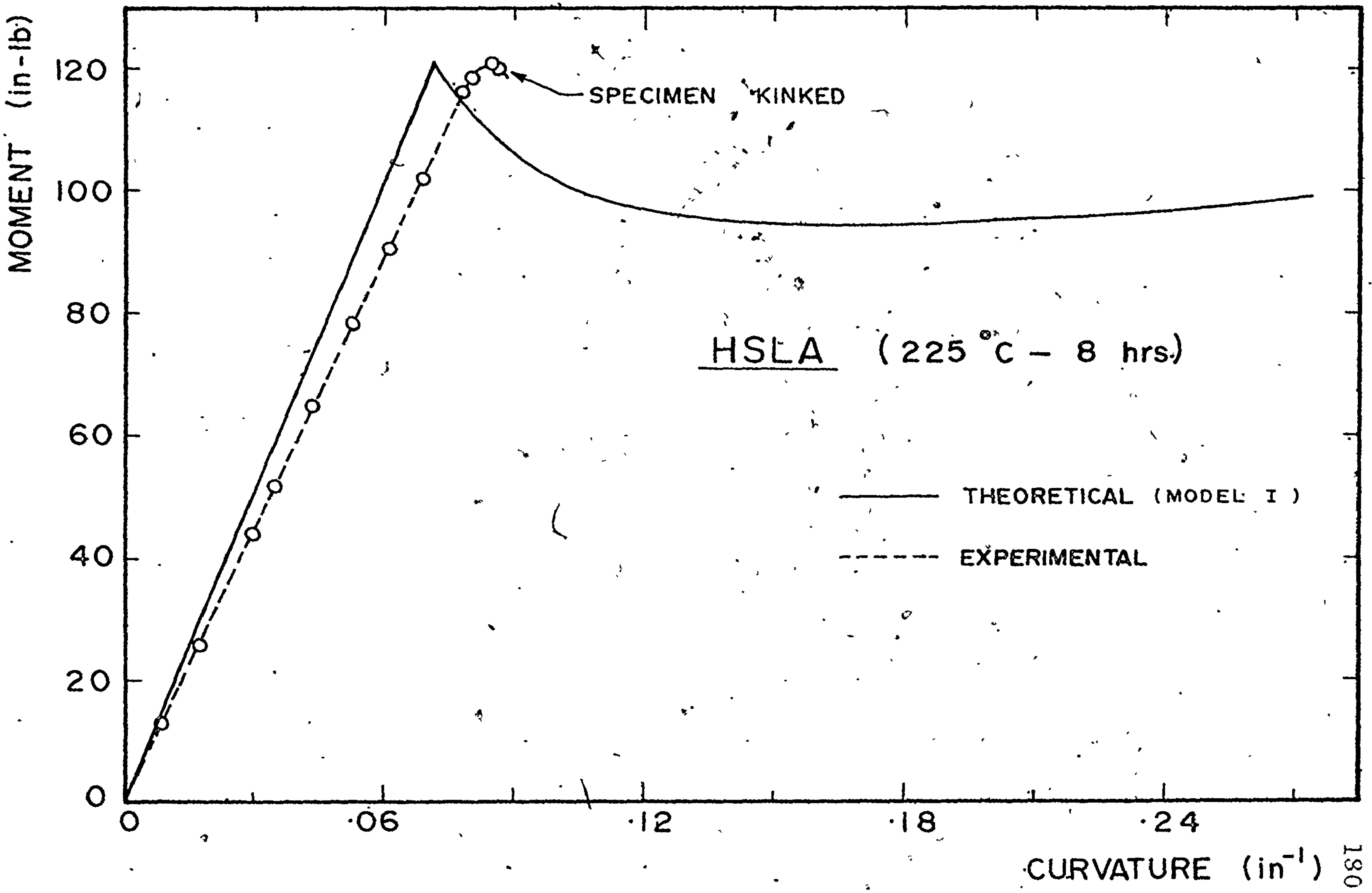

Fig. F.6 – Comparison of experimental moment-curvature results with the theoretical curve for HSLA steel, aged at 225°C for 8 hours

REFERENCES

1. Johnson, W. and Mellor, P. B., Engineering Plasticity, Van Nostrand Reinhold Co., London, 130 (1978).

2. Van Rooyen, G. T., Mater. Sci. Eng., 3, 105 (1968).

3. Gupta, I., and Garofalo, F., Mater. Sci. Eng., 5, 271 (1969).

4. Imamura, J. and Taoka, T., Trans. ISIJ, 11, 191 (1971).

5. Garofalo, F., Met. Trans., 2, 2315 (1971).

6. Prewo, K. et al, Met. Trans., 3, 2261 (1972).

7. Fujita, H. and Miyazaki, S., Acta Met., 26, 1273 (1978).

8. Enomoto, M. and Furubayashi, E., Scripta Met., 13, 113 (1979).

9. Conrad, H. and Stone, G., J. Mech. Phys. Solids, 12, 139 (1964).

10. Morris, J. G., Mater. Sci. Eng., 5, 299 (1969).

11. Lloyd, D. J. and Morris, L. R., Acta Met., 25, 857 (1977).

12. McCormick, P. G., Acta Met., 22, 489 (1974).

13. Hart, E. W., Acta Met., 3, 146 (1955).

14. Fisher, J. C. and Rogers, H. C., Acta Met., 4, 180 (1956).

15. Butler, J. F., J. Mech. Phys. Solids, 12, 139 (1962).

16. Hall, E. O., Proc. Phys. Soc. Lond., B64, 742 (1951).

17. Petch, N. J., J. Iron Steel Inst., 25, 174 (1953).

18. Morrison, W. B., Trans. ASM, 59, 824 (1966).

19. Van Rooyen, G. T., Mater. Sci. Eng., 7, 37 (1971).

20. Cottrell, A. H. and Bilby, B. A., Proc. Phys. Soc. Lond., A62, 49 (1949).

21. Low, J. R. and Gensamer, M., Trans. AIME, 158, 207 (1944).

22. Johnson, W. G. and Gilman, J. J., J. Appl. Phys., 30, 129 (1959).

23. Hahn, G. T., Acta Met., 10, 727 (1962).

24. Moon, D. W., Mater. Sci. Eng., 8, 235 (1971).

25. Sylwestrowicz, W. and Hall, E. O., Proc. Phys. Soc. Lond., B64, 495 (1951).

26. Lomer, W. H., J. Mech. Phys. Solids, 1, 64 (1952).

27. Le blois Cl. and Massonnet, Ch., Int. J. Mech. Sci., 14, 95 (1972).

28. Abel, A. and Muir, H., Acta Met., 21, 93 (1973).

29. Takada, I. and Sugie, E., Trans. ISIJ, 16, 531 (1976).

30. Uko, D. K., Ph.D. Thesis, McMaster University, Hamilton, Canada (1978).

31. Ewing, A., The Strength of Materials, 109 (1903).

32. Robertson, A. and Cook, G., Proc. Roy. Soc., A88, 462 (1913).

33. Muir, J. and Binnie, D., Engineering, 122, 743 (1926).

34. Kennedy, A. B. W., Engineering, 115, 736 (1923).

35. Nadai, A., Plasticity, McGraw-Hill, New York, 173, (1931).

36. Prager, W., Die Flieszgrenze bei behinderter Formanderung, Forsch Ing. Wes., 4, 95 (1933).

37. Thum, A. and Wunderlich, F., Forsch Ged. d. Ingenienrwesens, 3, 95 (1932).

38. Kuntze, W., Stahlbau, 6, 49 (1933).

39. Rinagl, F., Prelim. Publn. Second Congr. Inter. Assn. Bridge Struct. Engr., Berlin, 1561 (1936).

40. Morrison, J. L. M., Proc. Instn. Mech. Engrs., 142, 193 (1939).

41. Roderick, J. W. and Phillips, I. H., Engineering Structures, Butterworths, London, 9 (1949).

42. Nakanishi, F., Proc. World Eng. Congr., Tokyo, 3 (1929).

43. Peterson, F. G., Trans. Amer. Soc. Civ. Engrs., 112, 1201 (1947).

44. Haigh, B. P., Engineering, 138, 461 (1934).

45. Volterra, E., J. Instn. Civ. Engrs., 20, 1 (1942-43).

46. Ashwell, D. G., J. Roy. Aeronaut. Soc., 54, 708 (1950).

47. Hill, R., The Mathematical Theory of Plasticity, Oxford University Press, London, 317 (1950).